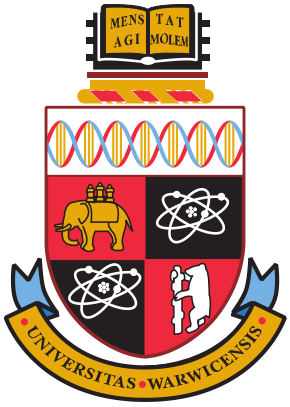

Probing the Geometrical and Electronic Structure of Two-Dimensional Charge Transfer Networks on Metal Surfaces

by

Philip Blowey

A thesis submitted in partial fulfilment of the requirements for the degree of Doctor of Philosophy in Physics

University of Warwick, Department of Physics

June 2018

Contents

List of figures

List of tables

Acknowledgements

First and foremost, I would like to thank my PhD supervisors, Professor Giovanni Costantini and Professor Phil Woodruff, for giving me the opportunity to work on such an interesting project. I am very grateful for the invaluable support and guidance they have given me throughout the last four years and it is an honour to have worked with such excellent scientists.

I would also like to thank Dr. Luke Rochford for his valuable knowledge and the substantial amount of time and effort that he has invested in this project. Whether it was ensuring that I had everything I needed to get me up and running, teaching me the ways of UHV science or providing useful ideas and suggestions, he has always been on hand to help throughout my PhD and, needless to say, this work would not have been possible without him. My gratitude also goes to Dr. David Duncan, who taught me a lot about synchrotron surface science and made sure that the many beamtimes throughout this project have run smoothly (a difficult task indeed!). He has been such an inspiration with his tremendous work ethic and knowledge of surface science and I hope he can now finally have a good night sleep without being woken up by a certain PhD student who can't get his measurements to work!

My appreciation also extends to Dan, James and Paul, as well as those mentioned above, who have, on multiple occasions, given up their time to join me on the beamline and have made each beamtime such a pleasant experience. I would also like to thank the I09 beamline staff, Tien-Lin, Pardeep and Dave, who operate a fantastic facility have always been extraordinarily accommodating of us. I must also thank Harry, Jon and Luis as well as Dan and James again for being such great groupmates. I would also like to acknowledge the DFT collaborators Simone Velari, Alessandro de Vita and Reinhard Maurer, whose calculations and ideas have been hugely helpful in this project. I am also grateful to Diamond Light Source and EPSRC for project funding.

For their continued and unquestioning support, I would like to thank my family; I would not have been able to get to where I am today without them and for this I am eternally grateful. Special thanks must also go to my partner Aimée who manages to make every day perfect, even with the very difficult and grumpy roommate she has had these last few months. She has always believed in me and I am very lucky to have her in my life.

Finally, I would like to thank you for taking the time to read this.

Declarations

This thesis has been submitted to the University of Warwick in partial fulfilment of the requirements for the degree of Doctor of Philosophy in Physics. The work presented here is my own, except where specifically stated otherwise, and was performed between September 2014 and March 2018 under the supervision of Professor Giovanni Costantini and Professor Phil Woodruff. This thesis has not been previously submitted to any institution for a higher degree. Chapters 4 and 5 contain the results of density functional theory calculations performed by collaborators. This is explicitly stated in the text and details of these calculations can be found in section 2.8. Due to the 24-hour use of the I09 beamline, the experiments conducted at this facility (i.e. the NIXSW and XPS experiments, as detailed in section 2.8) were performed by a team of people including, and led by, myself. The analysis and interpretation of all the data obtained from these experiments were performed solely by me.

Some of the work presented in this thesis has been and will be published in the following articles:

- P.J. Blowey, R.J. Maurer, L.A. Rochford, D.A. Duncan, P.T.P. Ryan, T.-L. Lee, P.K. Thakur, G. Costantini, D.P. Woodruff, *Testing the potential of two-dimensional charge-transfer networks to control the electronic structure of metal-organic interfaces*, in preparation.
- P.J. Blowey, R.J. Maurer, L.A. Rochford, D.A. Duncan, D.A. Warr, J. Lawrence, T.-L. Lee, P.K. Thakur, G. Costantini, D.P. Woodruff, *Conformational adsorption changes of electron acceptor molecules on metal surfaces*, in preparation.
- P.J. Blowey, R.J. Maurer, L.A. Rochford, D.A. Duncan, D.A. Warr, P.T.P. Ryan, T.-L. Lee, P.K. Thakur, G. Costantini, D.P. Woodruff, *The structure of TCNQ/alkali metal charge-transfer networks on metal surfaces*, in preparation.
- P.J. Blowey, S. Velari, L.A. Rochford, D.A. Duncan, D.A. Warr, T.-L. Lee, A. De Vita, G. Costantini, D.P. Woodruff, *Re-evaluating how charge transfer modifies the conformation of adsorbed molecules*, accepted by Nanoscale.
- P.J. Blowey, L.A. Rochford, D.A. Duncan, D.A. Warr, T.-L. Lee, D.P. Woodruff, G. Costantini, *Probing the interplay between geometric and electronic structure in a two-dimensional K-TCNQ charge transfer network*, Faraday Discussions, 204 (2017), 97-110.

A full publication list is shown in Appendix A.

Philip Blowey, June 2018.

Abstract

Due to its ability to form conductive organic salts, the prototypical electron acceptor molecule 7,7,8,8-tetracyanoquinodimethane (TCNQ) has attracted considerable interest in the field of organic electronics. This has motivated numerous surface science studies of TCNQ and related molecules, with an aim to understand the molecule-substrate interface and, in particular, the nature of any charge transfer. Although charge transfer is strongly dependent on subtle aspects of the molecular adsorption geometry, there is a dearth of detailed structural investigations for these systems.

In this thesis, a variety of surface science techniques were used to characterise model systems of TCNQ adsorbed on coinage metal substrates with the aim to identify key relationships between the adsorption structure and the electronic properties of the surface. Particular focus was given to studying two-dimensional charge-transfer networks formed by TCNQ and alkali metals on the surface of Ag. Scanning tunnelling microscopy and low energy electron diffraction were used to characterise the packing and ordering of molecules and to ascertain whether the adsorbed layer is commensurate with respect to the underlying substrate. X-ray and ultraviolet photoelectron spectroscopy were used to provide complementary information on the chemical composition and electronic properties of the surface. Most significantly, the normal incident X-ray standing wave (NIXSW) technique was used to obtain precise quantitative structural measurements of the surface.

On the surfaces of coinage metals, TCNQ is generally believed to adsorb in a significantly bent conformation, with all four cyano groups pointing down towards the substrate. The NIXSW measurements in this thesis show that the conformation adopted by TCNQ on Ag(100) is consistent with this, but on Ag(111), TCNQ adopts a considerably different conformation that was found, through comparison with density functional theory calculations, to result from the participation of Ag adatoms within the surface structure. These results also highlight the need for using both experimental and theoretical quantitative structural methods to obtain a reliable understanding of metal-organic interfaces and that some previously studied systems may need to be re-investigated.

On both the (111) and (100) surfaces of Ag, a wide variety of TCNQ/alkali metal network structures were formed with Cs, K and Na. NIXSW measurements obtained from a subset of these structures show that the alkali metals adsorb at elevated heights above the TCNQ molecules. In comparable structures, K adsorbs closer to the surface than Cs and causes a smaller shift to the surface work function. The alkali metal adsorption height was also found to decrease as its coverage relative to TCNQ increased.

List of abbreviations

AIMD	*Ab initio* molecular dynamics
DFT	Density functional theory
DOS	Density of states
ETL	Electron transport layer
F4-TCNQ	2,3,5,6-tetrafluoro-7,7,8,8-tetracyanoquinodimethane
fcc	Face centred cubic
hcp	Hexagonal close packing
HOMO	Highest occupied molecular orbital
HTL	Hole transport layer
ICT	Integer charge transfer
IMFP	Inelastic mean free path
LEED	Low energy electron diffraction
LUMO	Lowest unoccupied molecular orbital
MCP	Microchannel plate
ML	Monolayer
NEXAFS	Near edge X-ray absorption fine structure
NIXSW	Normal incidence X-ray standing wave
OED	Organic electronic device
OFET	Organic field-effect transistor
OLED	Organic light emitting diode
OMBD	Organic molecular beam deposition
OPV	Organic photovoltaic
rms	Root mean square
RT	Room temperature
SECO	Secondary electron cutoff
STM	Scanning tunnelling microscope/microscopy
TCNE	Tetracyanoethylene
TCNQ	7,7,8,8-tetracyanoquinodimethane
TISE	Time-independent Schrödinger equation
UHV	Ultra-high vacuum
UPS	Ultraviolet photoelectron spectroscopy
UV	Ultraviolet

vdW	van der Waals
VL	Vacuum level
XPS	X-ray photoelectron spectroscopy
XSW	X-ray standing wave
1D	One-dimensional
2D	Two-dimensional

1. Introduction

1.1 General introduction

Organic semiconductor molecules have attracted considerable interest, owing to their promising performance in a range of applications such as organic light emitting diodes (OLEDs),[1, 2] organic photovoltaics[3-5] (OPVs) and organic field effect transistors (OFETs).[6, 7] These organic electronic devices (OEDs), which typically comprise ultra-thin films of π-conjugated organic molecules deposited onto conductive electrodes, offer several advantages over their inorganic counterparts.[8, 9] One such advantage is that OEDs can be fabricated using techniques such as vacuum deposition, spin coating or direct printing onto substrates.[9] OEDs can be prepared on more flexible and lightweight materials at a low cost using these techniques and this has already seen some commercial success for a range of portable devices.[8] Furthermore, using organic compounds offers a larger scope for chemical modification, potentially enabling new and complex functionalities that cannot be achieved with inorganic devices.[8, 9] Despite this, OEDs still face challenges to meet the demands of current electronic applications with further optimisation needed to improve device performance[5] and to reduce the susceptibility of devices to degradation under ambient conditions.[10]

A key component of OEDs is the interface formed between the active organic material and the conducting electrode, which can be a major determining factor of device performance.[11, 12] For instance, the alignment of energy levels across the interface can significantly affect organic photovoltaic device efficiency as this defines the height of charge transport energy barriers.[11, 12] A logical approach to improve efficiency would therefore be to chemically modify the organic semiconductor molecules in order to achieve the desired energy level alignment across the interface and minimise the energy cost associated with charge transport to and from the electrode. However, in practice, making changes to one aspect of the organic semiconductor's properties can have unforeseen effects on, for example, the molecular interactions at the interface which define the organic film morphology and in turn can have a notable effect on the electronic properties of the device.[9] As a result of this, it is essential to understand the metal-organic interface from an electronic and structural perspective to assess the full impact of any chemical modifications made to the organic semiconductor material.[13-15] To this effect, a significant research effort has been dedicated to understanding the metal-organic interface and its consequence on OED performance. Ideally, it would be possible to study these metal-organic interfaces in real OED architectures, however this is beyond the capability of current methodology. Instead, monolayers or thin films of organic semiconductor materials are typically studied on low index coinage metal (Cu, Ag, Au) surfaces as model systems to represent the interface between an electrode and the active organic

material.[14, 15] To characterise these model systems, a variety of complementary surface analysis techniques are used to probe the atomic-scale structure and electronic properties of the interface (*e.g.* Mercurio *et al.*[16] and Tseng *et al.*[17]). One key requirement of surface characterisation is the ability to probe only the top most layers of the system in isolation from the bulk of the substrate. This surface specificity is usually attained by using low-energy (i.e. < 1 keV) electrons as either the probe or the detection signal (or a combination of both).[18, 19] Electrons in this energy range have a characteristically short (~1 nm) inelastic mean free path (IMFP) in condensed matter and therefore can only travel a few atomic layers before being scattered inelastically. The elastic portion of the measured signal will therefore only correspond to the first few layers of the surface. Surface characterisation techniques exploit this by isolating the elastic signal from the inelastic background to obtain surface specific information. A consequence of using low energy electrons, however, is that experiments must be performed under ultra-high vacuum (UHV) conditions because the electrons can only travel very short distances (~1 μm) in air at ambient pressures. Furthermore, the high surface specificity of the techniques imposes strict requirements on sample cleanliness that can only be achieved in UHV.[20]

In this thesis, the electronic properties and atomic-scale structures of an organic semiconductor molecule were studied on the surfaces of coinage metals. A particular focus was given to obtaining quantitative structural information, which involves measuring highly precise atomic coordinates and bondlengths within the molecular adsorption structure.[21, 22] From this, valuable insight can be gained, allowing important driving forces and interactions that determine how molecules adsorb onto the surface to be identified. Precise experimentally measured adsorption structures are also of great interest in theoretical chemistry, providing references to which computational density functional theory (DFT) codes can be benchmarked and parameterised against.[23, 24] Currently, for inorganic systems, DFT codes are capable of accurately modelling interfaces, also offering predictive capability for systems that have not been measured experimentally.[25, 26] However, pure DFT codes are not suitable for calculations involving organic adsorbates as they do not provide a description of long-range dispersion interactions that are significant in these systems.[24, 25] To overcome this, a number of functionals, designed to correct for dispersion interactions, are in development,[27-33] which require precise experimental structural measurements for a variety of systems to benchmark these codes against.[24, 34] Whilst there has been some success in developing dispersion corrections that can accurately reproduce experimentally measured adsorption structures, the efficacy of the corrections can vary between systems, which limits the predictive power of the technique significantly.[34] As a result, there is an ongoing effort to develop codes that are less reliant on empirical data and perform consistently for a wide range of systems.[30, 34, 35] Nonetheless, DFT can still be used to obtain valuable complementary information, particularly as it can provide further understanding of properties that are difficult to measure experimentally (*e.g.* the

relative stability of adsorption structures).[25] However, despite the valuable insight into molecular adsorbate systems that is on offer, there is a dearth of experimental quantitative surface structure measurements in the literature. This owes partly to the demanding requirements of quantitative structural measurements, which often require the use of synchrotron radiation[21, 22], computationally intensive model fitting routines[19, 36] or both.[22, 37]

This work focusses on the archetypal electron acceptor molecule, 7,7,8,8-tetracyanoquinodimethane (TCNQ) adsorbed both by itself and in two-dimensional (2D) charge transfer networks formed with codeposited alkali metals on low-index coinage metal surfaces. Scanning tunnelling microscopy (STM) and low energy electron diffraction (LEED) were used to characterise the packing and ordering of molecules within the surface plane and to ascertain whether the molecular overlayer is commensurate with respect to the underlying substrate. X-ray and ultraviolet photoelectron spectroscopy (XPS, UPS) were used to provide complementary information on the chemical composition and electronic properties of the surface. Most significantly, the normal incident X-ray standing wave technique (NIXSW) was used to obtain quantitative structural information, such as the molecule-substrate spacing and the adsorption conformation of the molecules.

1.2 Interactions of molecules on surfaces

When an organic molecule is brought into contact with a metal surface, a wide range of interactions can occur, both between neighbouring molecules and between the molecules and the surface, which dictate the nature of the adsorption structure.[38, 39] In this section, the various types of interaction that occur at the metal-organic interface and their impact on the molecular adsorption structure will be discussed.

The interactions between an adsorbate and a surface can be broadly divided into two categories: physisorption and chemisorption. Physisorption describes systems in which adsorbates are weakly bound to a surface by long-range van der Waals (vdW) forces. Figure 1.2.1 shows the potential energy curve for physisorption as an adsorbate approaches a surface.[40] At larger distances from the surface, the adsorbate is weakly attracted to the surface by vdW forces, with the interaction strength increasing as it is brought closer to the surface until, at short adsorbate-substrate separations, Pauli-repulsions between the adsorbate and surface density of states (DOS) begin to dominate, causing a sharp increase in potential energy. Due to these competing interactions, the potential energy reaches a minimum at a distance equal to the combined sum of vdW radii for the adsorbate and substrate atoms.[41] For a physisorbed system, in which vdW forces are the main interaction, this would be the expected distance between the adsorbate and substrate atoms. For chemisorbed systems, the adsorbate and substrate wavefunctions hybridise leading to the formation of chemical bonds, in addition to the vdW

interactions. Here, the bonding is significantly stronger than the weak vdW interactions (as depicted in Figure 1.2.1) and thus the adsorbate substrate separation will be shorter than the sum of vdW radii and instead would be expected to be equal to the sum of the surface and adsorbate atom's covalent radii.[42]

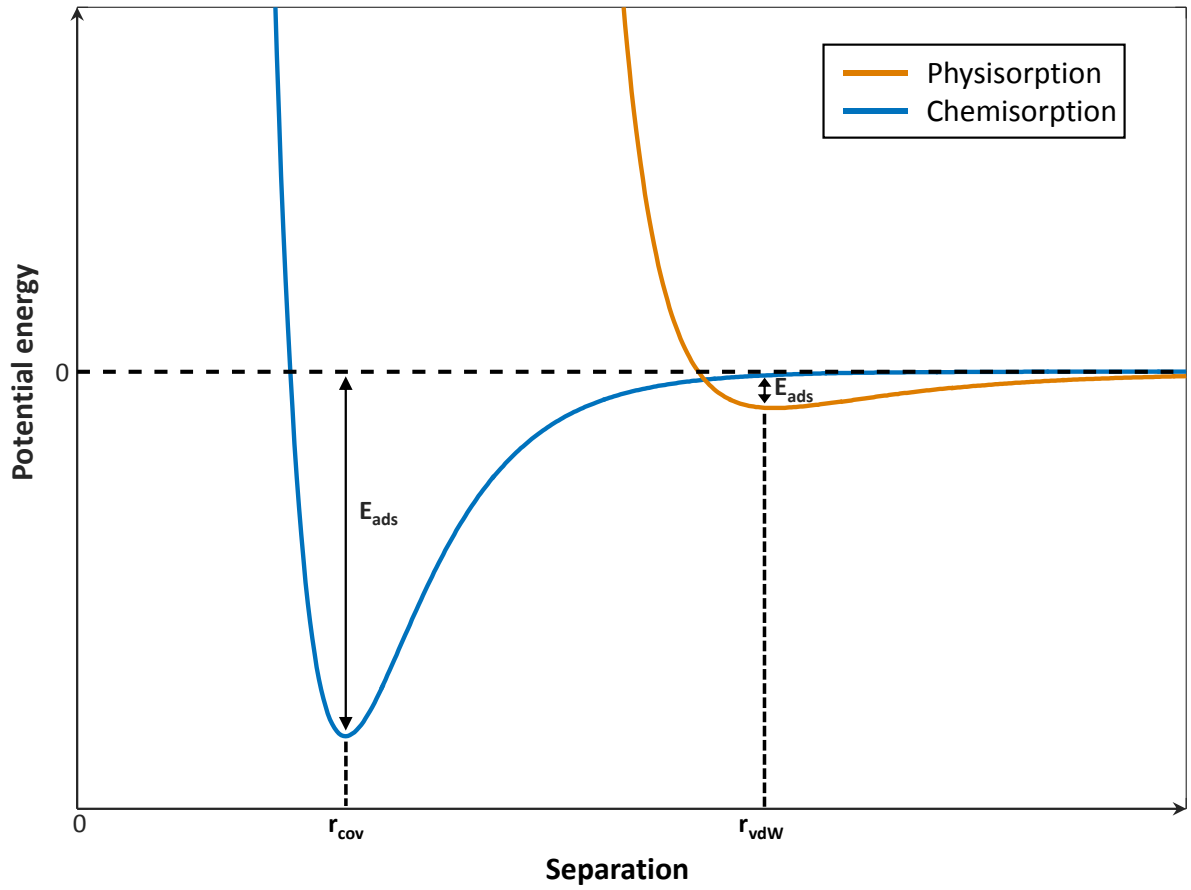

Figure 1.2.1 – Schematic potential energy curves for a molecule interacting with a surface. The orange line depicts a Lennard-Jones potential,[40] which models vdW interactions between two species and is used here to represent physisorption. The blue line depicts a Morse potential[43] which is used to model chemical bonds and is used here to represent chemisorption. The adsorption energy (E_{ads}) for each model is indicated at the minimum of each potential well. The distances corresponding to the sum of covalent radii (r_{cov}) and the sum of vdW radii (r_{vdW}) are also displayed.

Although the difference between the two types of adsorption nominally refers to the character of adsorbate-substrate interactions, they are often characterised by the adsorption strength which is typically an order of magnitude stronger for chemisorption than physisorption.[44] As a result, the correlation between interaction strength and bond length is used to qualitatively describe the nature of adsorption from structural information.[23, 45] This is especially prevalent as chemisorption and

physisorption are only limiting cases with the adsorption character for many systems falling somewhere in between.[23, 46]

In addition to the interactions between the adsorbed molecules and the surface, intermolecular forces between the adsorbates can also have a big impact on the adsorption structure.[38, 39, 47] The realisation that organic molecules form ordered structures through non-covalent interactions (e.g. vdW forces, hydrogen bonding, halogen bonding etc.), led to the onset of a new field known as supramolecular chemistry.[48] This effect is also observed on surfaces in which local intermolecular forces direct the molecules into ordered packing arrangements in a process known as 'supramolecular self-assembly,' which refers to how the molecules arrange into well-ordered structures on the surface with little or no external input.[38, 39, 47] Here, the intermolecular forces are largely dictated by the positions and types of functional groups within the molecule. By making synthetic chemical modifications to the molecules to promote specific intermolecular interactions, self-assembly can be exploited to engineer desired surface structures.[39, 47] This offers a convenient method to form functional nanoarchitectures with relatively high precision in a 'bottom-up' approach that is highly compatible with established device processing techniques such as UHV sublimation or spin-coating.[9, 39] This is highly advantageous over other methods for forming nanostructures that rely on the precise positioning of individual atoms and molecules (such as STM tip manipulation or optical tweezing) and are ultimately not viable for the large-scale fabrication of devices for practical applications.[38]

Whilst attempts to engineer nanostructures by designing molecules with desirable intermolecular interactions are promising, the role of the substrate in determining the molecular arrangement cannot be neglected.[38, 39] Generally, the resulting 2D arrangement of organic molecules on a surface depends on a mixture of molecule-substrate and intermolecular interactions. For molecules that interact via weak, non-covalent, intermolecular forces, it is usually the molecule-substrate interactions that determine the adsorption geometry although the molecule-molecule interactions will have some influence on the resulting self-assembly.[38] However, in cases where molecules can form strong directional intermolecular bonds, such as hydrogen or halogen bonds, and exhibit only weak physisorption to the substrate, the supramolecular assembly will largely be determined by the molecule-molecule interactions.[47, 49]

The molecule-substrate interaction can affect the adsorption structure in numerous ways. For example, physisorbed molecules will preferentially adsorb in geometries that increase contact between the molecule and the surface to maximise vdW interactions.[38] As a result, many planar molecules with conjugated π-systems tend to adsorb in a flat geometry.[50, 51] Organic molecules, particularly those that contain heteroatoms (such as nitrogen, oxygen and sulfur) may also chemisorb to the substrate forming

strong covalent or dative bonds.[45, 52] Consequently, this promotes adsorption in sites that optimise the formation of these chemical bonds and thus the assembly is likely to be dictated by the footprint of the underlying substrate. Furthermore, in some cases, the strong nature of bonds formed may even induce distortions or reconstructions to the underlying substrate lattice.[53] A common example of this is the Au(111) surface, which when clean adopts a $22 \times \sqrt{3}$ herringbone reconstruction that is often lifted when strongly binding molecules are adsorbed on top.[54, 55]

One additional method of directing the molecular arrangements on a surface is through the coadsorption of metal atoms.[38, 56-58] This allows the molecule to form coordinative or ionic bonds with the metal atoms to form 2D networks on the surface.[59] Here, the bonding between the molecules and the metal atoms has a significant effect on the molecular assembly, in particular with coordinative bonds, which, due to their highly directional nature, will promote very specific molecular orientations.[59] In some systems, it has also been suggested that molecules can form 2D networks with adatoms abstracted from the underlying substrate, which play a similar determining role in the surface structure.[60-62]

1.3 Energy level alignment at the metal-organic interface

The performance of OEDs is highly dependent on the energy-level alignment across the interface between the metallic electrodes and the active organic material.[11, 12] Poor alignment of energy levels across these interfaces is detrimental to device efficiency as it creates energy barriers for charge transport[12] or, in the case of organic photovoltaic devices, reduces the open circuit voltage.[63] To illustrate this, Figure 1.3.1 depicts the energy levels at the various interfaces between layers in OPV and OLED devices. In OPVs, photons are absorbed by a photoactive organic material to produce an electron-hole pair, with the charge-carriers then transported away to the respective electrodes.[64] OLEDs are based on the same process but in reverse, recombining the electron-hole pair within an emitter material to produce photons.[65] In order to reduce energy losses, these devices often feature intermediate layers between the electrodes and the active organic material, known as electron transport layers (ETLs) and hole transport layers (HTLs), to improve the energy level alignment across the interfaces either by bridging the energy gap or by tuning the electrode work function.[64] Furthermore, the energy levels of these layers are designed to promote charge transport in the desired direction (indicated by the blue and orange arrows in Figure 1.3.1) to prevent the unwanted recombination of electron-hole pairs, which reduces device efficiency.[64]

When π-conjugated organic molecules are adsorbed onto metal surfaces, a wide-range of effects can occur which determine the electronic properties of the metal-organic interface.[11] In this section, the basic concepts of these effects will be discussed, with a particular focus on those most relevant to the

systems studied in this work. A more comprehensive description of the electronic properties of metal-organic interfaces can be found in review papers on this topic.[11, 12]

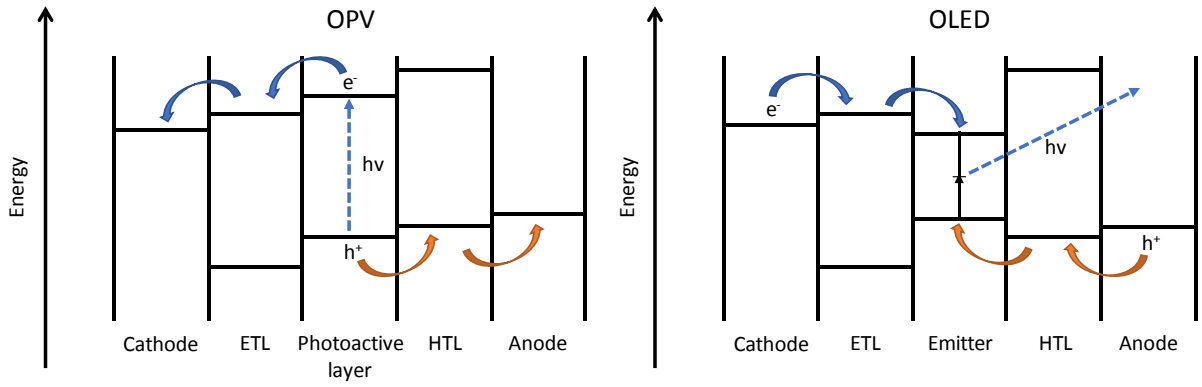

Figure 1.3.1 – Energy level diagrams of typical OPV and OLED device architectures. In an OPV, a photon (hv) is absorbed by the photoactive layer to produce an electron-hole pair. In an OLED, an electron-hole pair is recombined in an emitter material to produce a photon. The blue and orange arrows depict the desired direction of electron (e^-) and hole (h^+) transport respectively.

A key concept when discussing the electronic properties of the metal-organic interface is the work function (Φ), which is the minimum energy required to remove an electron from a solid and can be expressed as:

$$\Phi = VL(s) - E_F \qquad [1.3.1]$$

corresponding to the energy difference between the vacuum level (VL, the energy state of a free electron at rest outside of the solid) and the Fermi level (E_F, the highest occupied energy state in the solid). A key distinction is that here the vacuum level is not an invariant reference point for an electron at rest at an infinite distance from the surface (denoted as VL(∞)) but actually corresponds to the energy of an electron at rest just outside of the solid (denoted as VL(s)), where the electron energy is still affected by the potential of the surface.[12] This effect is highlighted by the well-established variance of work function for different surfaces of a metal single crystal. Because the metal single crystal has a constant Fermi level throughout, yet different surfaces have different work functions, the variance in work function must therefore be due to the surface dependence of the vacuum level.[12] For a metal, the difference in energy between VL(∞) and VL(s) is mostly caused by the surface dipole layer which results from electron density tailing-out of the surface into the vacuum.[11, 12] This tailing effect makes the vacuum side of the surface negatively charged, with the subsequent deficiency of electrons inside

the surface creating a positive charge, thus forming a surface dipole layer.[11, 12] For the different surfaces of a single metal crystal, the tailing of electron density occurs to different extents, thus creating surface dependent work functions.[12]

When a molecule approaches a metal surface, it interacts initially via long range vdW dispersion forces, with the electron density that tails out of the surface.[11] This causes the electron density to be 'pushed-back' into the surface thus reducing the surface dipole and, in turn, the workfunction.[11] The impact of this effect is generally dependent on the magnitude of the surface dipole, with greater work function changes observed for substrates with a large surface dipole potential energy.[11] Since the push-back effect is the result of vdW dispersion interaction, it occurs for all adsorbates and thus its effect on the work function must be considered when determining the interfacial energy level alignment. This is demonstrated by the deposition of wide gap insulators onto inert substrates such as gold, which do not participate in charge transfer or form chemical bonds with the substrate yet show a reduction in the work function, indicating that the work function shift is the result of physical processes.[11, 12]

In addition to the push-back effect, the interfacial dipole will also be influenced by the presence of polar functional groups within the molecule.[66] Polar bonds within the molecule will act as dipoles on the surface and thus will alter the vacuum level, although the impact of these molecular dipolar effects will largely depend on the molecular geometry on the surface and *vice versa*. One important consideration here is the surface image charge, which is the reorganisation of the highly mobile electron density within the metal substrate to stabilise the charges in the adsorbates by producing charges of comparable magnitude and opposite polarity.[67] As a result, only polar bonds which are oriented with some component perpendicular to the surface will have an effect as any dipoles parallel to the surface will be negated by the image charge.

Another electronic process that may occur at the metal-organic interface is charge transfer between the molecule and the substrate. This can occur either via the transfer of electrons across the interface, termed integer charge transfer (ICT), or as a partial charge transfer process resulting from the non-uniform distribution of electron density in chemical bonds formed between the molecule and surface.[11] In the former case, the nature of this effect is dependent on the energy of the molecular states in comparison to the Fermi energy of the metal.[11] Figure 1.3.2 compares schematic energy level diagrams of a metal and an organic semiconductor molecule when the molecule is far from the surface (Figure 1.3.2a) and when it is adsorbed on the surface (Figure 1.3.2b). In contrast to the band structure of the metal, the organic semiconductor states are localised on each molecule. In Figure 1.3.2 the highest occupied molecular orbital (HOMO) and lowest unoccupied molecular orbitals (LUMO) are shown, and are the respective states analogous to the valence and conduction bands in band theory, with the energy

difference of these two states (E_g) the molecular equivalent of a band gap. The Fermi level for the molecule here is defined as the midpoint between the HOMO and LUMO. The energy required to excite an electron from the HOMO to the VL is the ionisation energy (E_i) and the energy between the VL and the LUMO is the electron affinity (E_a). When the molecule is far from the surface it does not 'feel' the surface dipole layer and thus the local VL corresponds to VL(∞).[12] However, when the molecule is adsorbed on the surface, the molecule shares a VL with the metal and the molecular energy states shift accordingly.[12]

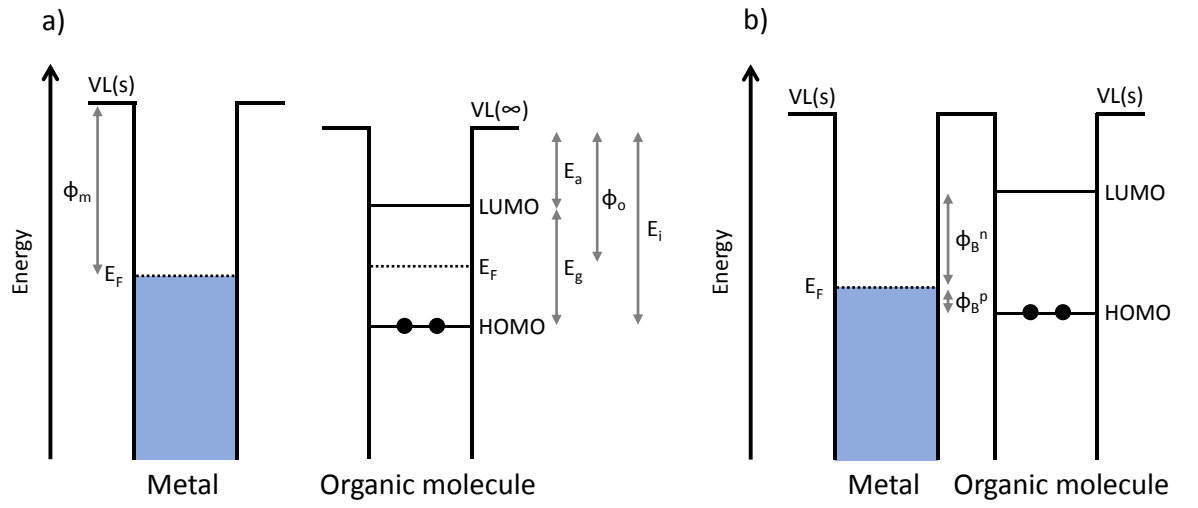

Figure 1.3.2 – Schematic diagrams of the energy levels within a metal and an organic semiconductor molecule when the molecule is far from the surface (a) and when the molecule is adsorbed on the surface (b). The terms marked on each diagram are explained in the main text.

Figure 1.3.2b depicts the energy states of the metal-organic interface that does not exhibit any charge transfer. Here the charge injection barriers (Φ_B^p and Φ_B^n) are defined by the energy differences between the metal work function Φ_m and the energy of the adsorbate HOMO and LUMO.[12] However, under different circumstances depending on the relative values of the energy levels across the interface, charge transfer occurs until equilibrium is reached between the two phases. Nominally, the extent and direction of charge transfer will depend on how the metal work function compares to the ionisation energy, for molecule-to-substrate electron transfer, or the electron affinity, in the case of substrate-to-molecule electron transfer.[11] However, as molecules become charged on the surface, electronic rearrangements and molecular relaxations will have a stabilising effect thus modifying the effective HOMO and LUMO energies for the charge transfer states (denoted by E_{CT+} for molecule-to-substrate electron transfer and E_{CT-} for substrate-to-molecule electron transfer).[11, 68] Figure 1.3.3 illustrates the charge transfer process for three possible scenarios from the ICT model proposed by Braun *et al.*,[11] which depends on the

relative values of Φ_m, E_{CT+} and E_{CT-}. When $\Phi_m < E_{CT+}$ (Figure 1.3.3a), electrons are transferred from the molecules to the substrate, until equilibrium is achieved between E_F and E_{CT+} in a regime known as Fermi level pinning. Under this regime, the work function of the metal organic interface (Φ_{mo}) is independent of the substrate and is equal to E_{CT+}. Fermi level pinning is also achieved when $\Phi_m > E_{CT-}$ (Figure 1.3.3c), in which electrons are transferred from the substrate into the LUMO of the molecules until E_F is in equilibrium with E_{CT-}. Again, Φ_{mo} is independent of the substrate and is equal to E_{CT-}. When Φ_m lies between E_{CT+} and E_{CT-} (Figure 1.3.3b), vacuum level alignment is achieved between the molecule and substrate but charge transfer does not occur and thus Φ_{mo} is simply equal to Φ_m.

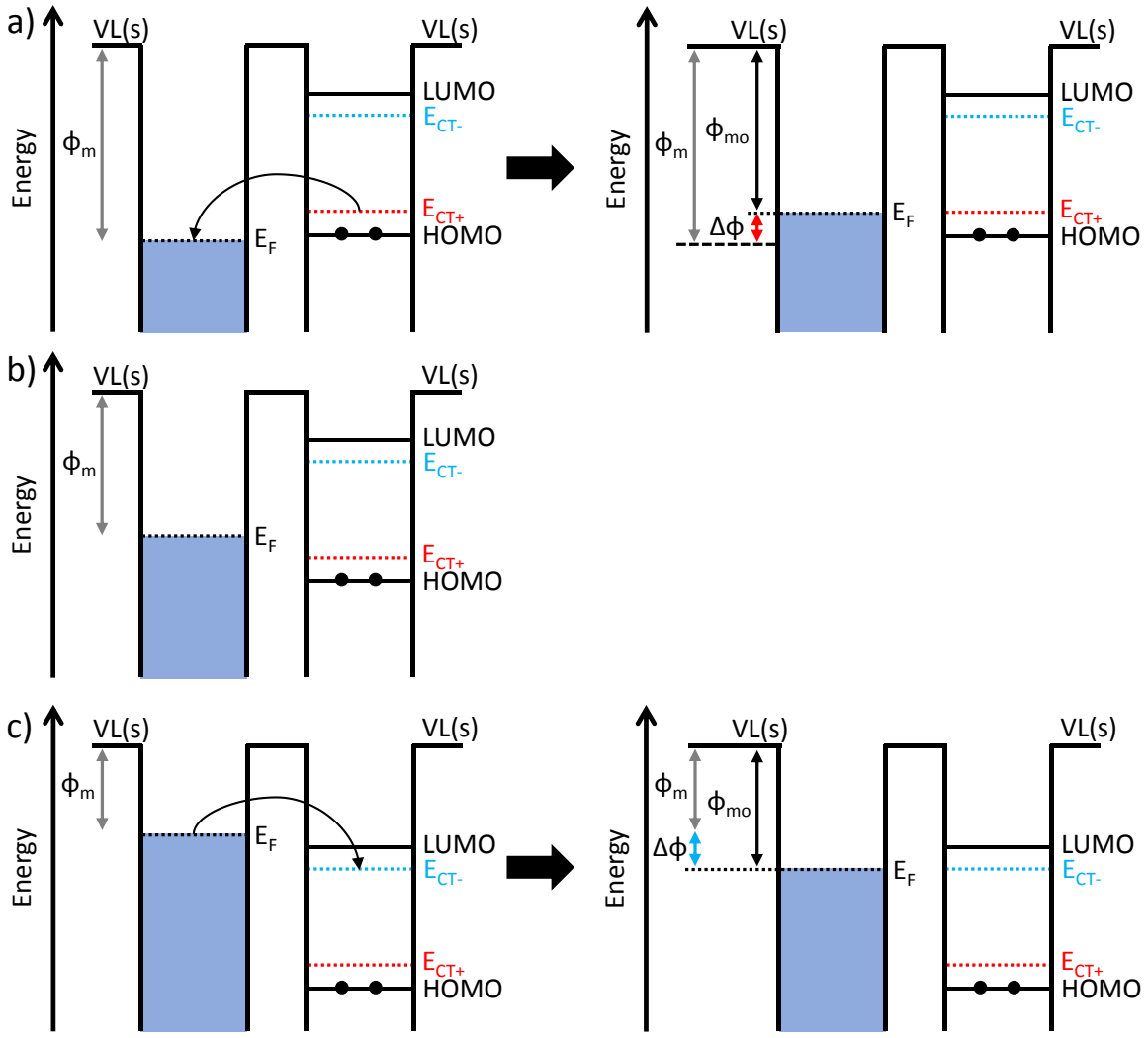

Figure 1.3.3 - Schematic of the integer charge transfer model when an organic semiconductor molecule is adsorbed onto a metal surface in three different scenarios adapted from Braun et al.[11] a) $\varphi_m > E_{CT+}$ The metal E_F is pinned to E_{CT+} as electrons are transferred from the molecules to the substrate. b) $E_{CT+} < \varphi_m < E_{CT-}$, VL alignment is achieved without charge transfer between the two phases. c) $\varphi_m < E_{CT-}$ The metal E_F is pinned to E_{CT-} as electrons are transferred from the substrate to the molecule.

The ICT model assumes that there is minimal hybridisation of the molecular and metallic energy states (i.e. non-covalent interaction).[11] However, if there is chemisorption at the metal organic interface, the description of charge transfer becomes significantly more complex, with additional factors affecting the interfacial energy level alignment.[11] The formation of chemical bonds at the interface causes a rearrangement of electron density which can result in net charge transfer, creating an interface dipole that shifts the surface work function.[11] Like the ICT model, the direction of charge transfer will largely be determined by the electron affinity and ionisation energy of the molecule relative the metal's work function.[11] However, this picture is complicated by the hybridisation of the HOMO and LUMO with energy states in the surface, which subsequently modifies their energies.[11, 69] Furthermore, the extent of charge transfer is not only dependent on relative energies but is also affected by the metal's hardness – a property that is inversely proportional to the DOS at the Fermi level – with the charge accepting ability of metals reducing with increasing hardness.[11, 69] Additionally, adsorption induced changes to the molecule may also impact on the nature of the chemical bonding and thus the nature of charge transfer may also vary depending on the adsorption site.[69, 70] Because of these factors, the energy level alignment for chemisorbed metal-organic interfaces is difficult to model.

2. Experimental techniques

2.1 Ultra-high vacuum in surface science

All of the experimental techniques used in this work were performed under UHV conditions (pressure < 10^{-9} mbar). Whilst this imposes strict demands on the experimental conditions and requires the use of cumbersome equipment, UHV offers many benefits to the study of molecules on surfaces. A large proportion of surface science techniques use low-energy electrons, either as a probe or a detecting medium, exploiting their short IMFP to obtain surface specific information. Operating under UHV conditions prevents electrons from inelastically scattering with ambient gasses, which would interfere with the measured signal and enables the preparation of atomically clean surfaces.[71, 72] Generally, under ambient conditions, even the relatively noble surfaces of coinage metals become coated by a layer of hydrocarbons, water and other background gas molecules.[20, 73] The presence of these contaminants affects both the electronic properties of the surface[11] and the formation of molecular films.[71, 72] Due to the high sensitivity of surface characterisation techniques, any contaminants on the surface will also supress or contribute to the measured signal.[20, 73] Therefore, to be able to isolate the properties of the desired adsorbate, surface cleanliness is essential.

Achieving UHV requires the use of specialist vacuum chambers and vacuum pumps with high pumping speeds. One major problem with UHV systems is outgassing, which is the unwanted release of gas from materials within the vacuum chamber that compromises the vacuum quality.[73] Materials with relatively high vapour pressures will outgas under UHV conditions so their use is limited and vacuum chambers are typically constructed from carefully selected low vapour pressure materials (e.g. zinc-free stainless steel, glass and ceramics).[20, 73] Additionally, outgassing can occur due to gas molecules desorbing from the interior surfaces of the UHV chamber.[20, 73] When the chamber is initially evacuated after being exposed to ambient pressures, the interior surfaces remain coated with hydrocarbons, water molecules and other ambient gas molecules. [20, 73] Over time, these molecules desorb into the vacuum, raising the pressure. [20, 73] To overcome this, UHV chambers are baked to temperatures in excess of 120 °C after evacuation to accelerate the desorption of residual gas molecules from the chamber walls.[20, 73]

Atomically clean surfaces are obtained through *in situ* preparation of samples under UHV conditions. Typically, the cleaning procedure comprises cycles of bombarding the surface with inert gas ions (e.g. Ar^+) followed by subsequent high-temperature annealing of the sample.[71, 72] The Ar^+ ion bombardment creates controlled sputter damage to the topmost layers of metal surfaces and also removes impurities such as oxide layers or adsorbed hydrocarbons, which are then expelled into the vacuum and are pumped

away. [71, 72] The high-temperature annealing step then provides sufficient thermal energy for the metal atoms to become mobile, smoothing out the sputter damage and generating large contaminant-free terraces of atoms on the surface. [71, 72] Once a clean surface is obtained, organic molecules can then be deposited on top through UHV organic molecular beam deposition (OMBD).[74, 75] OMBD consists of heating a powder of the desired organic compound in vacuum, causing it to sublime. [74, 75] Under UHV conditions, the sublimed molecules have a large IMFP and thus travel long distances without interacting with other gas molecules. As a result, the molecules travel in a beam, reaching all surfaces that are in the line-of-sight of the heated powder. [74, 75] By using apertures and shutters, the molecular beam can be directed onto the sample surface to minimise unwanted deposition onto the UHV chamber walls.

2.2 Low-energy electron diffraction

LEED is a technique that probes the long range 2D order of crystalline solid surfaces with intrinsically high surface specificity. The first example of LEED was shown in 1927 by C. Davisson and L. H. Germer in an experiment that also demonstrated the wavelike behaviour of electrons for the first time.[76] The experiment consisted of a monoenergetic beam of electrons aimed at a single Ni crystal surface from which it was observed that the electrons were elastically scattered in preferred directions relating to the periodic arrangement of the Ni atoms within the crystal structure. However, it wasn't until the 1960s with the development of modern UHV equipment and optics capable of displaying the diffraction patterns in real time that LEED began to see widespread use in surface science. In this section, the basic theory underpinning LEED will be introduced and discussed. A more complete overview of the principles can be found elsewhere.[19, 36, 77]

In a LEED experiment, an electron beam with a well-defined kinetic energy, typically in the energy range of 10-300 eV is focussed onto a sample. Electrons in this energy range have a de Broglie wavelength of the order of ~1 Å and thus are ideal for diffracting from a crystalline solid. Using electrons in this energy range also provides high surface specificity, isolating structural information of the surface from that of the bulk. The surface specificity is brought about by the short IMFP of electrons at these energies (see Figure 2.2.1), which in an inorganic solid is of the order of 1 nm. This means that elastically scattered electrons, which can be isolated from the inelastic background using a retarding field, are only likely to come from the top few atomic layers of the surface. Furthermore, the high backscattering cross-section of electrons means that a large proportion of the incident electron flux will be scattered back out of the crystal and will not reach layers deeper into the bulk. If the sample surface contains regions with long-range order, the incident electrons will be back-scattered, producing a pattern that is a projection of the reciprocal mesh, which is inversely proportional to the real space unit

mesh of the surface structure. The symmetry and periodicity of the real-space surface structure can therefore be extracted from the LEED pattern.

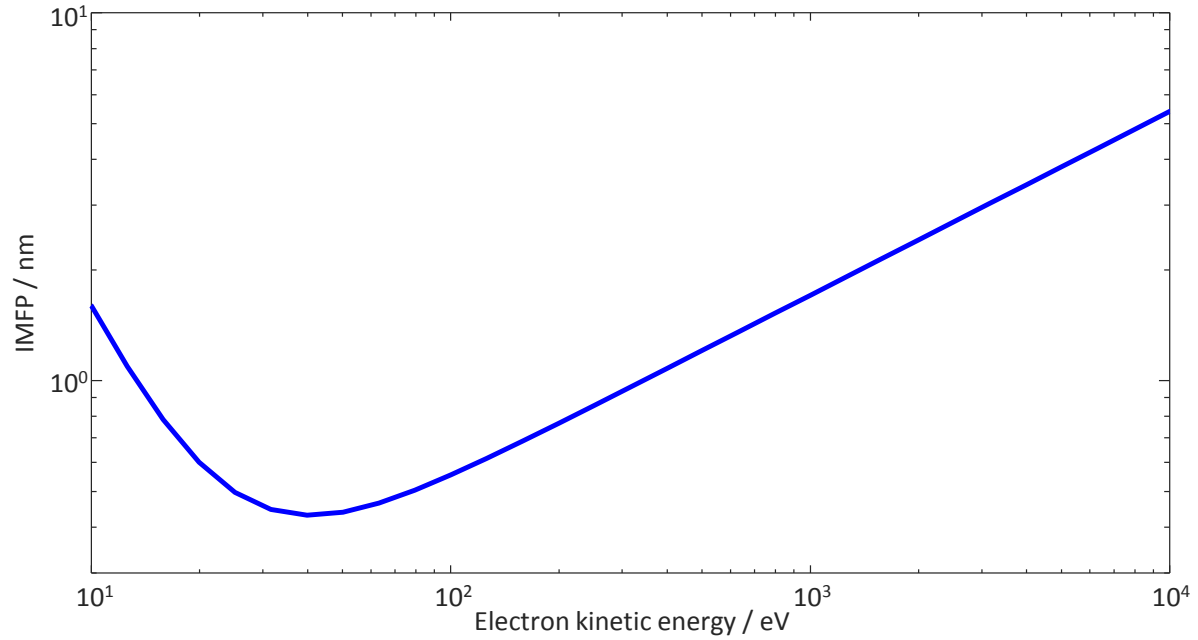

Figure 2.2.1 – Universal IMFP curve of electrons in condensed matter as a function of electron kinetic energy based on equations proposed by Seah and Dench.[78]

To describe the structural information obtainable by LEED, it is important to define surface structure notation. For adsorbate layers, it is usual practice to express the surface structure as a relationship between the adsorbate lattice vectors ($\mathbf{b_1}$ and $\mathbf{b_2}$) and the substrate lattice vectors ($\mathbf{a_1}$ and $\mathbf{a_2}$). One example is Wood's notation, which gives a simple description of the surface structure but is limited to adsorption structures that are commensurate to the underlying substrate with the angle between $\mathbf{b_1}$ and $\mathbf{b_2}$ the same as that between $\mathbf{a_1}$ and $\mathbf{a_2}$. Wood's notation expresses the surface structure by the ratio between the adsorbate and substrate lattice vector lengths along with the azimuthal angle (θ) between them in the format of $\left(\frac{|\boldsymbol{b_1}|}{|\boldsymbol{a_1}|} \times \frac{|\boldsymbol{b_2}|}{|\boldsymbol{a_2}|}\right) R\theta$. More complicated overlayer structures can be expressed as a transformation matrix of the substrate lattice vectors taking the form of:

$$\begin{pmatrix} \boldsymbol{b_1} \\ \boldsymbol{b_2} \end{pmatrix} = \begin{pmatrix} * & * \\ * & * \end{pmatrix} \begin{pmatrix} \boldsymbol{a_1} \\ \boldsymbol{a_2} \end{pmatrix} \qquad [2.2.1]$$

Examples of these two types of notation are shown in Figure 2.2.2.

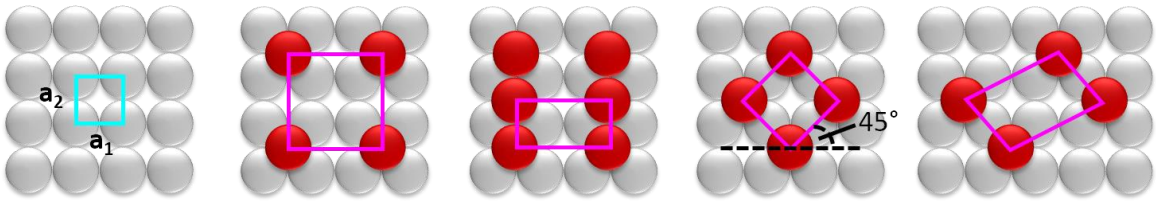

Wood's notation:	(2×2)	(2×1)	$(\sqrt{2} \times \sqrt{2})R45$	-
Matrix notation:	$\begin{pmatrix} 2 & 0 \\ 0 & 2 \end{pmatrix}$	$\begin{pmatrix} 2 & 0 \\ 0 & 1 \end{pmatrix}$	$\begin{pmatrix} 1 & 1 \\ -1 & 1 \end{pmatrix}$	$\begin{pmatrix} 2 & 1 \\ -1 & 1 \end{pmatrix}$

Figure 2.2.2 – Example surface structures for adsorbate atoms shown on an Ag(100) surface. The grey circles represent Ag atoms and the red circles correspond to adsorbate atoms. The Ag substrate unit mesh (cyan square) is indicated in the left-most panel and the adsorbate unit mesh (purple square) is shown for each of the adsorption structures. Below each panel, the Wood's notation and matrix notation of each adsorption structure is given. Note that because the internal angle of the unit mesh for the right-most structure does not equal that of the substrate (i.e. 90°), it cannot be described using Wood's notation.

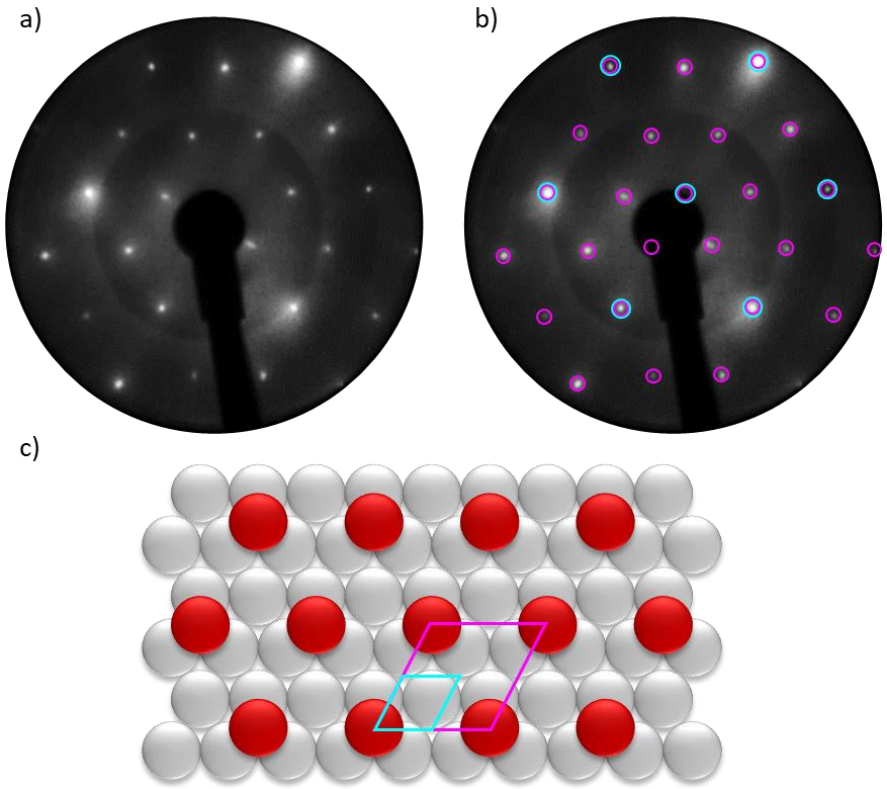

Figure 2.2.3 – Comparison of a LEED pattern with its corresponding real-space surface unit mesh. a) Example LEED pattern of the (2x2) phase formed by Cs adsorbed on Ag(111), recorded with an electron kinetic energy of 135 eV. b) The experimental LEED pattern with the beam positions for the Ag(111) substrate (cyan) and the (2x2) Cs structure (purple) overlaid. c) A real space depiction of the (2x2) Cs-Ag(111) adsorption phase with the unit meshes for the Ag(111) substrate (cyan) and Cs overlayer (purple) highlighted.

Figure 2.2.3 shows an example LEED pattern for the (2x2) structure formed by Cs atoms adsorbed on an Ag(111) substrate. Note that in real space structure, the (2x2) Cs overlayer unit mesh vectors are twice the length of the Ag(111) substrate unit mesh vectors, however in the LEED pattern (reciprocal space), the Cs overlayer beams are separated by half the distance of the substrate beams.

LEED patterns comprise a series of diffracted beams that can be explained by conservation of energy and momentum with the recoil momentum of the surface given in units of the reciprocal lattice vectors. For an electron that is elastically scattered, the magnitude of the incident beam wavevector $\boldsymbol{k}$ must equal that of the diffracted beam $\boldsymbol{k'}$:

$$k^2 = k'^2 \qquad [2.2.2]$$

For diffraction from a surface, which has two-dimensional periodicity, only the component of the wavevector that is parallel to the surface is conserved. With ∥ and ⊥ denoting the components parallel and perpendicular to the surface respectively, this gives:

$$k_{\parallel}{}^2 + k_{\perp}{}^2 = k'_{\parallel}{}^2 + k'_{\perp}{}^2 \qquad [2.2.3]$$

and conservation of momentum gives:

$$\boldsymbol{k}_{\parallel}{}' = \boldsymbol{k}_{\parallel} + \boldsymbol{g}_{hk} \qquad [2.2.4]$$

where $\boldsymbol{g}_{hk}$ is a reciprocal mesh vector,

$$\boldsymbol{g}_{hk} = h\boldsymbol{a}^* + k\boldsymbol{b}^* \qquad [2.2.5]$$

where h and k are a set of integers called Miller indices and $\boldsymbol{a}^*$ and $\boldsymbol{b}^*$ are reciprocal lattice vectors related to the real surface lattice vectors $\boldsymbol{a}$ and $\boldsymbol{b}$ by:

$$\boldsymbol{a}^* = 2\pi\frac{\boldsymbol{b}\times\boldsymbol{n}}{A}, \qquad \boldsymbol{b}^* = 2\pi\frac{\boldsymbol{n}\times\boldsymbol{a}}{A}, \qquad A = \boldsymbol{a}\cdot\boldsymbol{b}\times\boldsymbol{n} \qquad [2.2.6]$$

where ***n*** is a unit vector normal to the surface. The diffraction conditions are therefore satisfied for points on the reciprocal surface mesh. These equations can also be represented graphically with the construction of the Ewald sphere which is depicted in Figure 2.2.4. For scattering from a surface, the Ewald sphere is superimposed on a set of reciprocal lattice rods which extend infinitely, perpendicular to the surface and pass through the points of the reciprocal mesh. The Ewald sphere is constructed by drawing a wavevector, ***k***, which terminates at the origin of the reciprocal mesh and by building sphere of radius *k* about the beginning of vector ***k***. Each point on the sphere that intercepts one of the reciprocal lattice rods corresponds to a diffracted beam ***k'***. Note that there are two diffracted beams for each point of the reciprocal mesh, however half of these (shown as dashed arrows in Figure 2.2.4) are directed into the crystal and are therefore not observed.

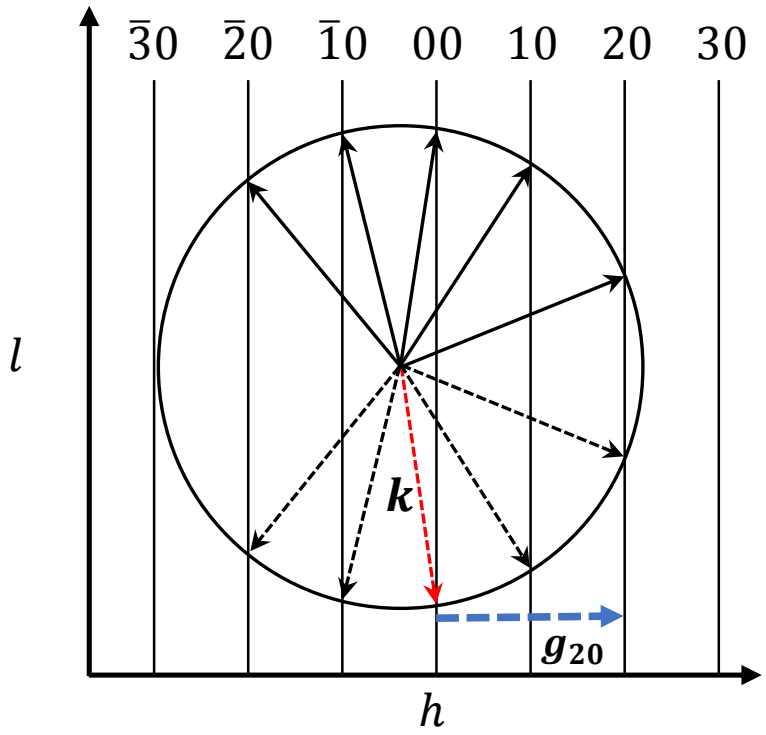

Figure 2.2.4 – Cross-sectional view of the Ewald sphere construction for a periodic surface. The vertical lines represent the infinite reciprocal rods that extend to infinity perpendicular to the surface, passing through the points of the reciprocal mesh. The wavevector k (red arrow) is labelled and the possible scattered wavevectors (k') are shown as black arrows. An example reciprocal mesh vector g_{20} is also shown (blue arrow). The dashed arrows represent wavevectors that propagate into the solid bulk and are not observable by LEED.

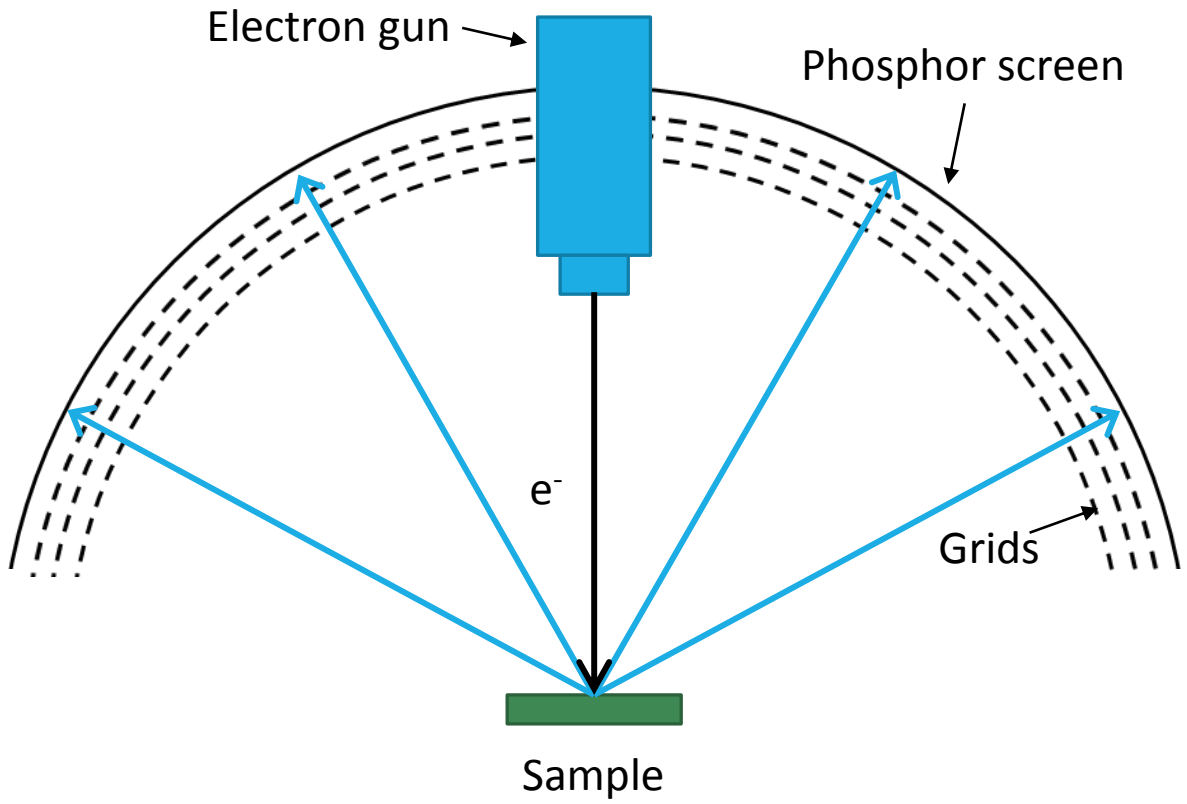

Figure 2.2.5 – Schematic diagram of LEED optics. The various components and their function are described in the main text.

Figure 2.2.5 depicts the various components within a set of rear-view LEED optics. The electron gun produces a monoenergetic beam of electrons of ~1 μA, which is electrostatically focussed onto a nearby sample. The LEED optics also include a series of hemispherical grids which are used to prevent inelastically scattered electrons from reaching the phosphor screen, which, due to their varying wavelengths, would destructively interfere with the diffraction pattern. The first of these grids is held at the same ground potential as the sample and is used to separate the sample from the fields produced by the other grids, allowing the electrons to travel in straight lines in a field-free region. The second grid is held at a negative potential, slightly lower than is used to accelerate the emitted electrons, and thus acts as a high-pass filter that allows only the elastically scattered electrons through. Upon passing through this retarding grid, the elastically scattered electrons are then accelerated, via the application of high voltage, onto the phosphor screen to produce the diffraction pattern image. In some LEED optics, the detector also includes a microchannel plate (MCP), which multiplies the electron signal, allowing diffraction patterns to be observed with electron beams of ~1nA. This low beam current is essential for use on organic adsorbate systems (such as those studied in this work) which are highly susceptible to damage from the electron beam.[79]

An additional concept that is important to consider when conducting LEED experiments is the transfer width of the instrument. The transfer width is effectively the coherence length of the electrons with the angular divergence of the electron beam usually being the limiting factor in determining its size, which for typical LEED instruments, is of the order of hundreds of Angstroms.[77, 80] In order to obtain a diffraction pattern from an ordered structure, its periodicity must be smaller than the transfer width, [77, 80] which considering that typical unit meshes, even for relatively large organic molecules, are of the order of tens of Angstroms,[38] is seldom an issue. However, the average sizes of ordered domains with respect to the transfer width can often have implications on the observed LEED pattern. [77, 80] If the average domains are larger than the transfer width, interference across the domain boundaries will not be important and the resulting LEED pattern will correspond to the sum of the intensities (not the amplitudes) of the individual patterns for each domain. [77, 80] If the domains are on average smaller than the transfer width, then the effects of coherent interference between domains will be significant and will affect the LEED pattern observed. [77, 80]

2.3 Scanning tunnelling microscopy

First demonstrated by G. Binnig and H. Rohrer in 1982,[81] the scanning tunnelling microscope (STM) has made a significant impact on the field of surface science. With the ability to routinely image and manipulate surfaces at the atomic and molecular level, scanning tunnelling microscopy (also abbr. STM) has become a powerful tool for surface characterisation. In this section, the basic theory that describes the operation of STM will be discussed. A more complete overview of the principles can be found in a variety of books[82-85] and review papers[86, 87].

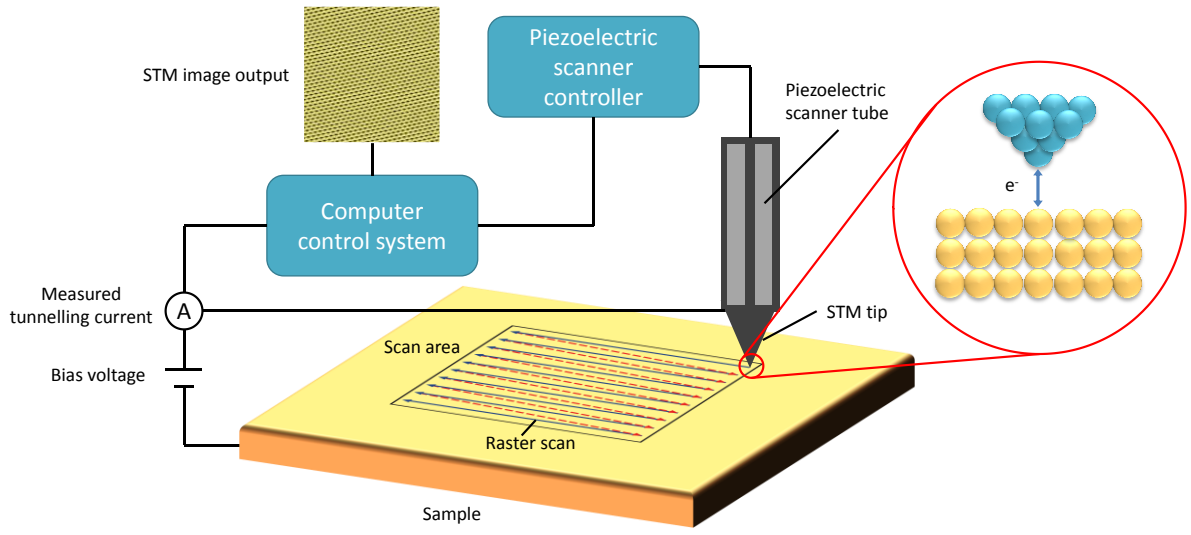

Figure 2.3.1 –Schematic of an STM.

In an STM experiment, an atomically sharp metal tip is brought within a few angstroms of a conductive surface. At this small distance, the respective wavefunctions of the tip and the surface overlap, enabling electrons to be transferred across the gap via quantum tunnelling. In the absence of an applied bias voltage, electrical equilibrium is achieved across the tip-sample junction (Figure 2.3.2a) with the metal tip and sample sharing a common Fermi level. Under these conditions, electrons can tunnel across the gap in either direction with equal probability and no current is observed. If a bias is applied between the tip and sample (Figure 2.3.2 b + c), tunnelling is favoured in one direction and thus a current can be measured.

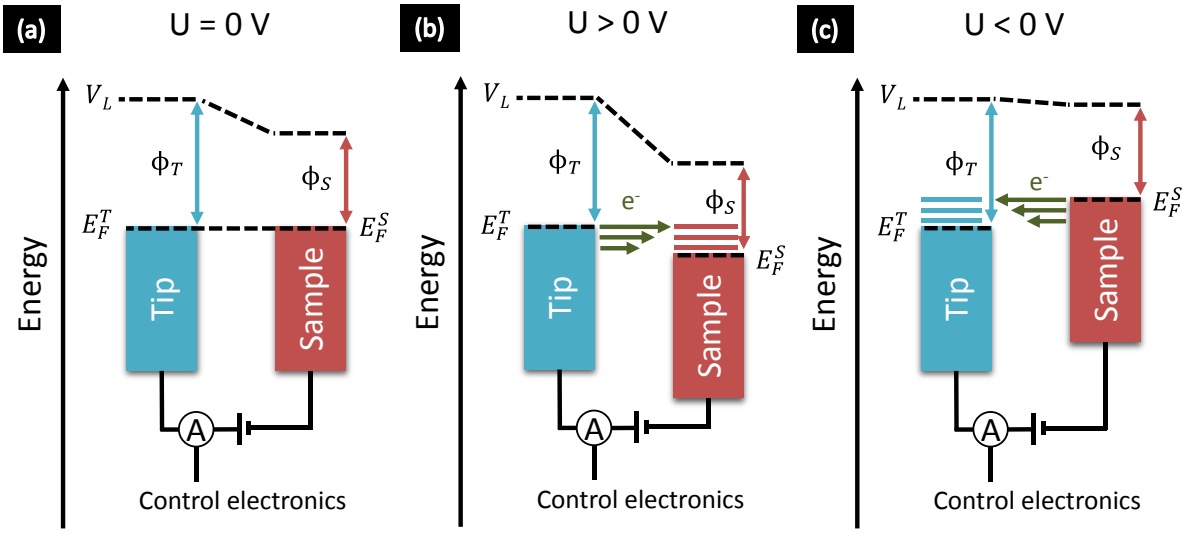

Figure 2.3.2 – Energy level diagrams of a tip-sample junction with different voltage biases (U) applied to the sample. (a) No sample bias: a trapezoidal potential barrier is created as the sample and tip are in electrical equilibrium with no net electron transfer. (b) Positive sample bias: electrons tunnel from filled states of the tip to empty states of the sample. (c) Negative sample bias: electrons tunnel from filled states of the sample to empty states of the tip.

The tunnelling current is defined by the transition probability per unit time, given by Fermi's golden rule, summed over all possible tip and sample states and multiplied by the electronic charge, which can be written as:

$$I = \frac{4\pi e}{\hbar}\int_{-\infty}^{\infty}\left[f_T(E_F^T - eU + \epsilon) - f_S(E_F^S + \epsilon)\right]\cdot \rho_T(E_F^T - eU + \epsilon)\,\rho_S(E_F^S + \epsilon)|\boldsymbol{M}|^2 d\epsilon \qquad [2.3.1]$$

where e is the electronic charge, $\hbar$ is the reduced Planck constant, *f(E)* is the Fermi-Dirac distribution function at energy *E* which accounts for the Pauli exclusion principle and the population of energy states at a given temperature, E_F is the Fermi energy, *U* is the bias voltage applied across the tunnel junction,

$\rho(E)$ is the DOS, $\boldsymbol{M}$ is the tunnelling matrix element which describes the overlap of the tip and sample wavefunctions and the indices T and S correspond to the tip and the sample respectively. Under typical operating conditions the contributions from the Fermi-Dirac distribution are negligible, since $k_B T << eU$, thus the expression for total current reduces to:

$$I \sim \frac{4\pi e}{\hbar} \int_0^{eU} \rho_T(E_F^T - eU + \epsilon)\, \rho_S(E_F^S + \epsilon) |\boldsymbol{M}|^2 d\epsilon \qquad [2.3.2]$$

(Note that this expression is only valid for $U > 0$ whereas for $U < 0$ the integration limits are swapped). From this expression, it can be deduced that only electrons with an energy between E_F - eU and E_F participate in tunnelling, with the tunnelling current corresponding to an integration of electron tunnelling over this energy range. This is illustrated in Figure 2.3.2b which shows that electrons lower in energy than $E_F - eU$ cannot be transferred as there are no unoccupied sample states below this energy and there are no occupied tip states higher in energy than E_F. The main difficulty in solving this expression is with the tunnelling matrix $\boldsymbol{M}$, which requires prior knowledge of the complicated wavefunctions of the tip and the sample. However, at relatively small bias voltages (e.g. in the range of ± 2 V) due to the high sensitivity between tunnelling and the tip-sample separation, only tunnelling between the nearest atoms needs to be considered to give a good approximation of the tunnelling current.[88] In the case of STM, this corresponds to the endmost atom on the ultra-sharp tip and the surface atom directly below it and means that the tunnelling matrix can be approximated with a one-dimensional (1D) tunnelling probability, which is given by:

$$D(\epsilon) = e^{-2ks} \qquad [2.3.3]$$

where s is the tip-sample separation and k is given by:

$$k = \sqrt{\frac{2m}{\hbar^2}(\phi_{eff} - \epsilon)} \qquad [2.3.4]$$

where m is the mass of an electron and φ_{eff} is the effective work function, approximated as the average of the tip and sample work functions. The tunnelling probability here has an inverse exponential relationship with the tip-sample separation. The inverse decay length is given by $2k$, which at typical work function values for the tip and sample equates to a variation in s of 0.1 nm yielding an order of

magnitude change in the tunnelling probability. This illustrates the high spatial sensitivity that allows STM to resolve atomic and sub-molecular features. Incorporating this 1D tunnelling probability simplifies equation 2.3.2 to give an expression for the current for a fixed lateral position of the tip above the sample:

$$I \sim \frac{4\pi e}{\hbar}\int_0^{eU} \rho_T(E_F^T - eU + \epsilon)\,\rho_S(E_F^S + \epsilon)e^{-2ks}d\epsilon \qquad [2.3.5]$$

With the 1D tunnelling approximation, ρ_T and ρ_S now only correspond to densities of states for the endmost atom on the tip and the atom directly below it on the sample respectively. Equation 2.3.5 demonstrates that for a given position of the tip above the surface, the tunnelling current depends on the tip-sample separation, the applied bias voltage and the DOS. This means that for surfaces with a uniform DOS (e.g. a clean metal), the surface topography can easily be extracted from the tunnelling current. However, for more complicated systems where the DOS varies across the surface, any observed tunnelling current, and therefore the apparent height of features, will be a convolution of both electronic and topographic effects.

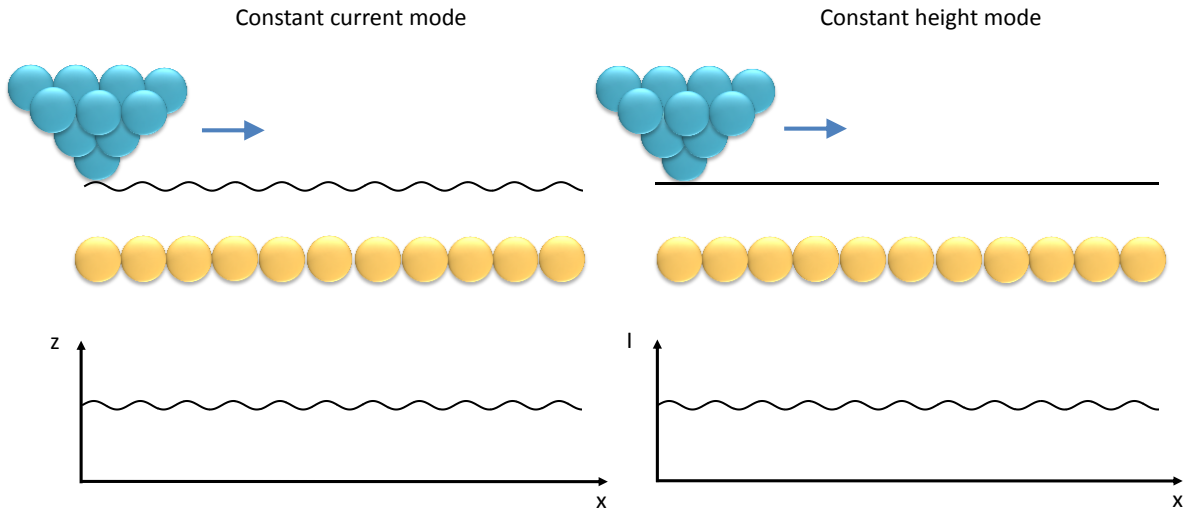

Figure 2.3.3 – The constant current and constant height scanning modes of STM. The trajectories of the tip are depicted for each mode. For constant current mode, the STM contrast is generated by plotting the changes in tip height (z) as a function of position, whereas in constant height mode, the tunnelling current (I) is used.

STM images are typically obtained using one of two imaging modes: constant current mode or constant height mode (see Figure 2.3.3). In both cases, the tip is raster scanned across an area of the surface, using piezoelectric positioners, whilst measuring the tunnelling current. In the constant current mode, a

feedback loop is used to adjust the vertical height of the tip such that the tunnelling current remains constant, causing the tip to track corrugations in the surface DOS. In this scenario, the STM image is generated by recording the tip height at each scanned point on the surface. In constant height mode, the tip height is fixed and does not track the surface, with the measured tunnelling current providing the STM image contrast directly. Since no feedback is required, fast measurements can be made in the constant height mode, however it is limited to very flat samples to avoid the tip coming into contact with the surface. Additionally, due to the exponential relationship of current to tip-sample separation, determining the apparent heights of features in the constant height mode is more difficult and, as a result, the constant current mode is usually favoured.

2.4 X-ray photoelectron spectroscopy

XPS is a key surface science technique that is used to determine the chemical composition and probe the electronic structure of surfaces. The underlying principle of XPS is based on the photoelectric effect, in which a photon is absorbed by a bound electron causing it to be excited to an unbound state above the vacuum level.[89, 90] Considering a simple single-electron model, the kinetic energy of a photoemitted electron is given by:

$$E_k = h\nu - E_b - \Phi \qquad [2.4.1]$$

Where $h\nu$ is the photon energy, E_b is the electron binding energy relative to the Fermi level and Φ is the work function of the material, which corresponds to the minimum photon energy required for photoemission to occur.[91] Since typical work functions are of the order of a few eV,[92] photoemission of electrons close to the Fermi level (valence states) is accessible to light in the ultraviolet (UV) spectrum. Probing these valence states gives useful information on the surface electronic structure and forms the basis of ultraviolet photoelectron spectroscopy (UPS, see section 2.5). In order to liberate the more strongly bound core electrons, with binding energies of hundreds to thousands of eV, X-ray radiation is required.[91]

Considering equation 2.4.1, the photoelectron kinetic energy relates directly to the electron binding energy and thus it transpires that measuring the kinetic energy distribution of photoelectrons emitted using a monochromatic X-ray source will show the distribution of electronic states within the sample. Since core electrons are bound in well-defined electronic states with binding energies that are characteristic of the atom that they are emitted from, the elemental composition of a sample can be identified by XPS.[18, 91] Furthermore, core-electron binding energies are also sensitive to chemistry, with

different oxidation states and bonding environments observable in the XPS spectrum as chemical shifts.[18, 91] However, in order to properly interpret XPS, one must be wary of final-state effects (not considered in the simple approach of equation 2.4.1) in the photoemission process which can lead to additional features and shifts in the apparent electron binding energy.

In a photoemission event, the electron binding energy can be considered as the difference between the (N-1) electron final state and the N-electron initial state:

$$E_b = E_{final}(N-1) - E_{initial}(N) \qquad [2.4.2]$$

Here, the main contributing factor to the initial state is the aforementioned chemical shift, which depends on the formal oxidation state and bonding environment of the emitter atom.[18] As a general rule of thumb, atoms in a higher oxidation state have an increased net positive charge and thus have a stronger coulombic interaction with the surrounding electrons, increasing their binding energy. Similarly, an atom bonded to other more electronegative atoms becomes deshielded as electron density is drawn away from it which leads to an increased binding energy. However, the observed binding energy is also dependent on final state effects and thus cannot be simply attributed to these initial state effects. In some instances, the photoemission process may occur alongside additional electronic excitations resulting in a higher energy final state. This results in so-called 'shake-off' and 'shake-up' features which are often observed at lower kinetic energies than the main photoelectron peak.[91] Similarly, for metal samples, plasmon states may be excited during the photoemission process which results in plasmon loss features.[91] Another possible final state effect results from electronic relaxation of the N-1 state. Equation 2.4.2 applies to situations where the photoelectron is adiabatically removed but if the remaining electrons of the emitter atom are able to respond and screen the core hole on a comparable or faster time-scale than the emission of the photoelectron, then relaxation effects must be considered. This can be expressed as:

$$E_b = E_{final}(N-1) - E_{initial}(N) - E_r \qquad [2.4.3]$$

where, E_r is the energy gained from electronic relaxations in response to the creation of a core hole. These relaxations increase the kinetic energy of the photoelectron and thus lower the apparent binding energy.[91]

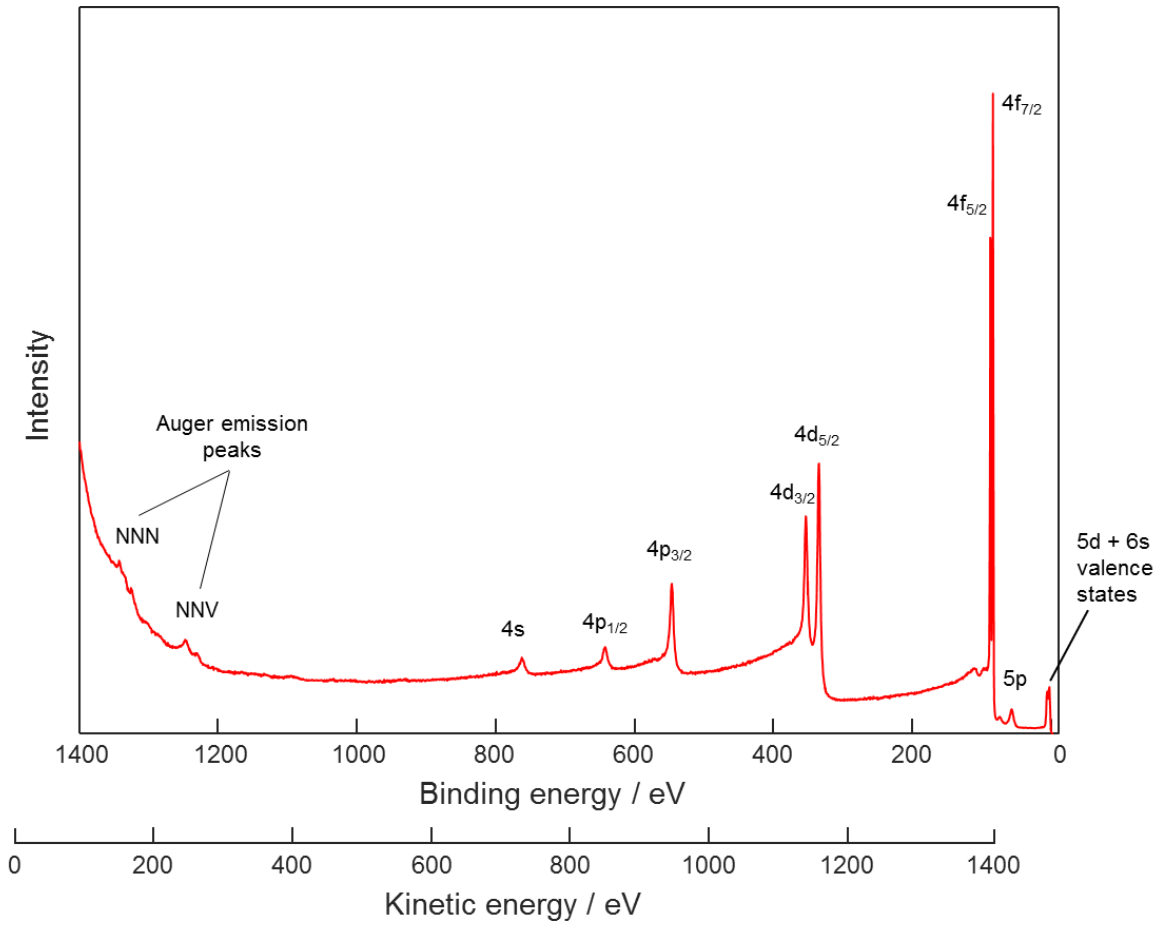

Figure 2.4.1 – XPS spectrum recorded from a clean Au(111) surface using a monochromated Al Kα (hν = 1486.6 eV) X-ray source.

Figure 2.4.1 shows an example photoelectron spectrum of a clean Au(111) surface which demonstrates many of the features typically observed in XPS. The main features are the photoemission peaks that correspond to electrons emitted from core-electron states as described above. Note that for core-levels with an angular momentum quantum number $l > 0$, two peaks are observed due to spin-orbit splitting. In addition to photoemission, peaks caused by Auger electron emission also appear in the spectrum. Auger emission is a secondary process in which a core-hole is refilled by an electron from a higher energy state and the energy gained from this transition is transferred to another electron which is then emitted from the atom.[91] Since Auger emission relies only on the relative energies of states within an atom, the kinetic energy of an Auger electron is independent of the photon energy. As a result, when viewed on a binding energy scale, Auger emission peaks will move relative to the photoemission peaks when the photon energy is changed. Another characteristic feature of XPS is the inelastic background, which is caused by photoelectrons that undergo inelastic collisions before reaching the analyser and electrons emitted in secondary processes. The background intensity reflects the probability distribution

of inelastic electron energies and thus decreases with increasing kinetic energy, with pronounced steps at each photoemission peak and inelastic loss tails observable on the low kinetic energy side.

Figure 2.4.2 depicts a typical setup for an XPS experiment with the two main components being the X-ray source and the electron analyser. An X-ray source capable of producing a single, well-defined, photon energy is needed to probe the occupied electronic states of the surface. The nature and type of X-ray source used in XPS has important implications and limitations on the experiment. Most XPS studies use laboratory X-ray sources which operate by inducing Kα emission of a metal (most commonly Al or Mg) by bombarding it with high energy electrons.[91] For these sources, the Kα emission lines, corresponding to photon energies of 1253.6 eV and 1486.6 eV for Mg and Al Kα emission respectively, are characteristically sharp and dominate the emission spectrum, being significantly more intense than other emission lines and the bremsstrahlung background. The energy resolution of these sources is, however, limited by the intrinsic linewidth of the dominant Kα emission lines (typical full width half maximum of 0.7-0.8 eV).[91] Furthermore, satellite emission lines complicate the XP spectrum by creating additional, low intensity, features. These limitations can, however, be overcome, at the expense of intensity, by introducing a monochromator into the X-ray source.

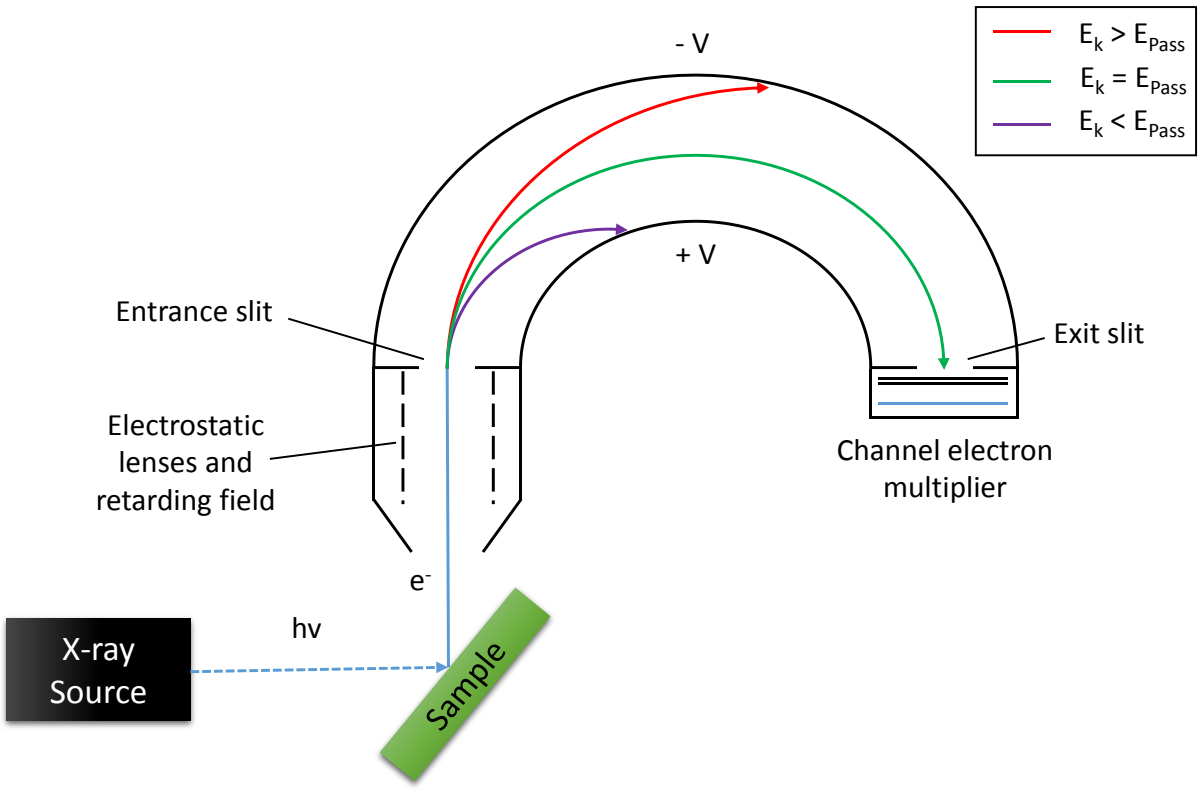

Figure 2.4.2 – Schematic of a typical XPS experimental setup. The components shown are described in the main text.

Whilst most XPS studies are performed using these conventional laboratory X-ray sources, an increasing number of surface science studies are taking advantage of monochromated synchrotron radiation, which offers a large continuous range of photon energies from tens to tens of thousands of eV.[91] Using synchrotron radiation, the principles of XPS remain largely the same, however by using lower photon energies than are accessible with laboratory sources one can achieve higher monochromator spectral resolution.[91] Tuning the photon energy also changes the photoionisation cross-section (i.e. the probability of photoemission occurring), with atoms generally having a greater cross-section at lower photon energies.[93, 94] This effect can be exploited to increase the signal to noise ratio of photoemission peaks, aiding the detection of low intensity features. Tuning the photon energy also changes the photoelectron kinetic energy which in turn affects its IMFP, altering the surface sensitivity of the technique. This can then be exploited to probe different depths into the surface. Synchrotron radiation also offers a higher brilliance of X-rays than can be obtained with conventional laboratory sources, allowing for faster acquisition times, which is ideal for monitoring processes in real-time with XPS. Care must be taken however as at the high X-ray flux densities achieved with synchrotron radiation, samples are more susceptible to radiation damage, particularly for organic adsorbate systems.[95]

Another key component of XPS is the hemispherical electron analyser which measures the photoelectron intensity as a function of kinetic energy. The analyser contains two concentric hemispheres, between which a potential difference is applied to generate an electric field that deflects the path of electrons travelling through the analyser. At a given potential energy, only electrons in a narrow distribution of kinetic energies will be able to pass through the gap between the hemispheres and reach the detector (typically a channel electron multiplier or micro channel plate with a charge coupled device). Here, the mean kinetic energy of electrons passing through the analyser is referred to as the ‘pass energy’ with the distribution of energies around the mean corresponding to the energy resolution of the analyser. To capture an XP spectrum, the analyser can be swept over a range of kinetic energies by changing the potential difference between the two hemispheres, which consequently changes the pass energy.[18] However, the energy resolution is dependent on the pass energy and thus by using this method, the energy resolution will vary across the spectrum.[18] A different approach is to use a retarding field before the entrance slit of the analyser, to reduce the kinetic energy of photoelectrons to a fixed pass energy, which gives consistent energy resolution across the XP spectrum, at the expense of varying angular resolution.[18]

2.5 Ultraviolet photoelectron spectroscopy

UPS is used to study the valence electronic structure of surfaces, offering two distinct advantages over XPS in this energy range: The photoionisation cross-section for valence electrons is orders of magnitude greater for UV photons and laboratory UV sources have superior energy resolution compared to laboratory X-ray sources. In UPS, a He lamp is often used as the photon source, which uses either the He-Iα (hv = 21.22 eV) or the He-IIα (hv = 40.81 eV) emission lines. At these energies, the occupied valence electronic states can be probed and UPS can also be used to determine the surface work function and subsequent work function shifts brought about by the deposition of adsorbates onto the surface.

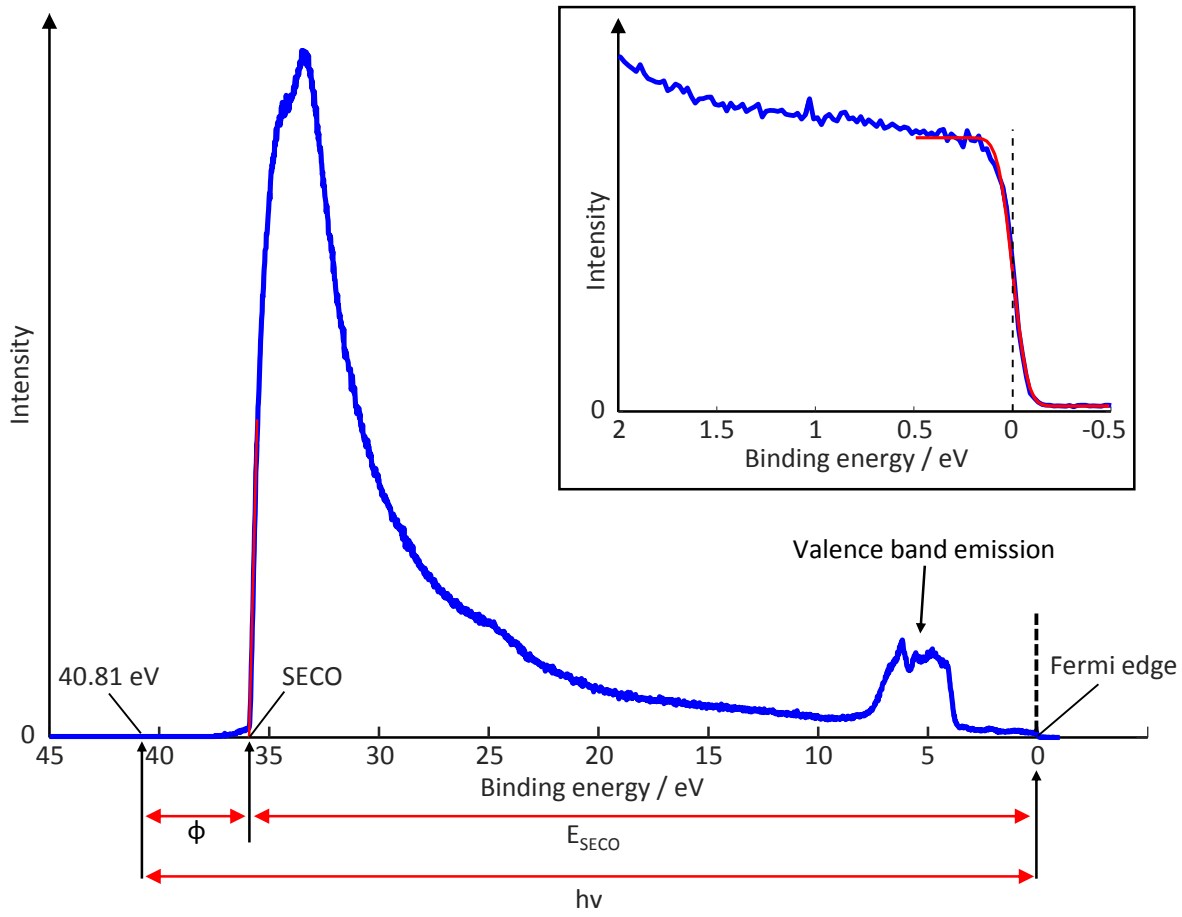

Figure 2.5.1 – UPS survey spectrum of an Ag(100) substrate measured using the He-IIα (hv = 40.81 eV) emission line with the sample held at a bias of -8.00 V. The binding energy scale is displayed relative to the Fermi edge (E_F), with the photon energy and E_{SECO} indicated below the x-axis. E_F (shown magnified in the inset) is determined by fitting a complementary error function (red curve) to the data, which models the Fermi-Dirac statistical nature of the Fermi edge. The position of the SECO is measured by linearly extrapolating the measured steep decline in intensity approaching the SECO to the x-axis intercept (shown as a red line). The work function is then calculated by taking the difference between hv and E_{SECO}.

The surface work function can be obtained by comparing the measured energy of the secondary electron cut-off (SECO) to the photon energy using the following equation:

$$\Phi = hv - E_{SECO} \quad [2.5.1]$$

where E_{SECO} is the energy of the SECO measured relative to the Fermi edge. The process of obtaining the work function from UPS spectra using this equation is illustrated in Figure 2.5.1. As the SECO corresponds to the minimum energy of electrons that can escape the surface, electrons at or around the SECO have a kinetic energy approaching 0. Due to their low kinetic energy, the electrons are very susceptible to influence from any remnant fields within the UHV chamber and will also be affected by the work function of the spectrometer, thus impacting on the accuracy of the measured E_{SECO}. To overcome this, a negative bias can be applied to the sample, which shifts the entire UP spectrum, including the SECO, to higher kinetic energies.

2.6 X-ray standing waves

The X-ray standing wave (XSW) technique is a quantitative structural method, capable of resolving the positions of atoms and molecules within adsorbate systems with high precision (i.e. < 0.05 Å).[21, 91, 96-99] XSW takes advantage of the wavefield formed at a Bragg reflection in a crystal by monitoring the X-ray absorbance of atoms when scanning through the Bragg condition, effectively using the crystal lattice as a ruler to determine the atomic positions. Using the core level photoemission signal (see section 2.4) as a measure of the X-ray absorbance, XSW can provide surface sensitive structural information that is also specific to the different elements and chemically distinct atoms within the adsorbates.[21, 91] Unlike other structural techniques that rely on diffraction (such as quantitative LEED and surface X-ray diffraction), XSW is a local probe technique that can characterise adsorbate systems that do not occupy well-defined adsorption sites or adopt long range ordered structures.[21, 91] Consequently, XSW is apt for studying organic adsorbates (such as those studied in this thesis), which commonly form incommensurate overlayers on surfaces. In particular, XSW is well-suited to determining the height of adsorbate atoms above single-crystal surfaces - a property which gives important insight into the nature of the surface-adsorbate interaction. One advantage of XSW is that it provides this information without the need for the computationally expensive simulations and exhaustive fitting routines needed by other structural techniques[21, 98] such as photoelectron diffraction,[22] quantitative LEED[19] and surface X-ray diffraction.[37] Moreover, as standard DFT codes cannot provide reliable surface structures of organic adsorbate systems due to them not providing a description of long range dispersion interactions,[27] experimental quantitative structural measurement techniques, such as XSW, are therefore useful to

validate the accuracy and benchmark dispersion corrected DFT functionals that are in development.[24, 34] The theory and applications of XSW are the subject of numerous review papers[21, 98, 99] and book chapters;[91, 96, 97] in this section only the fundamental principles will be discussed.

When an X-ray Bragg reflection is established in a crystal, two travelling waves, an incident wave and a reflected wave, combine to form an XSW. The intensity of this standing wavefield has periodicity equal to that of the crystallographic planes and thus has a well-defined phase relationship with the atoms in the crystal. By using a result derived from dynamical diffraction (multiple scattering) theory[100, 101] this effect can be exploited. Typically, when considering Bragg reflections, kinematical (single scattering) theory is used. This considers the incoming X-ray to be a plane wave and sums the scattering events over all atoms at equivalent sites in the crystal, which at the Bragg condition[102] is given by:

$$n\lambda = 2d \sin\theta \qquad [2.6.1]$$

where λ is the X-ray wavelength, d is the scatterer plane spacing and θ is the scattering angle. The result of this is that kinematical theory predicts a delta function, where at the Bragg condition, an infinite scattered intensity is obtained, which drops to zero immediately off the Bragg condition. While kinematic theory is able to successfully show the positions at which interference maxima occur, it is unable to give the intensities or explain the shape of the observed maxima.[103] Describing these effects requires treatment of multiple scattering, which was first demonstrated by Darwin using simple, but valid, geometrical arguments[103] and later by dynamical scattering theory developed by Ewald[104] and von Laue,[105] which is able to reproduce Darwin's results[103] but also provides descriptions of the distribution of X-ray energy inside the crystal and the effect of absorption in a straightforward manner.[101] The result of dynamical scattering theory that is of particular significance to the X-ray standing wave technique is that total reflection is achieved over a finite range of the incident conditions, rather than the delta function predicted by kinematical theory. This effect originates from the length of the wavevector changing over the course of scattering due to the difference in refractive index between the vacuum and the crystal, of which the latter is a medium with a complex dielectric constant.[101, 106] This modifies the construction of the Ewald sphere and, in effect, creates a photonic band gap comprising a region of the incidence conditions where there are no states allowing the wave to propagate and thus corresponds to a region of total reflection. [101, 106] In the case of a non-absorbing crystal, this gives the characteristic top hat shaped Darwin reflectivity curve, with the reflectivity tailing-off rapidly either side of this region.[101, 103, 106] Another key feature is that scanning across this region of total reflectivity shifts the phase the standing wave by π.[21, 98, 100] Here, scanning across the total reflectivity

region is realised by changing the photon energy (and therefore the wavelength) or the incidence angle of the X-ray beam. For low-index reflections of simple, homonuclear, lattices (e.g. fcc and hcp lattices with one atom per unit cell), the low energy (or low angle) edge of the Darwin curve forms an XSW where the nodes coincide with the bulk atomic planes.[21] With a phase shift of π at the high energy (or high angle) edge of the Darwin curve, the nodes move to the interstitial sites with the anti-nodes falling on atomic planes.[100] This effect is illustrated in Figure 2.6.1a.

If the effect of the standing wave on atomic X-ray absorption is considered when traversing the Darwin curve, the atomic positions relative to the bulk scattering planes can be extracted. When scanning across the reflectivity curve, the atomic positions go in and out of phase with the standing wavefield at different points, depending on the distance of the atoms (z) from the bulk scattering planes. Consequently, if one records the X-ray absorption as a function of energy (or angle) across the region of total reflection, the resulting profile is characteristic of z and thus gives information on the atomic positions (see Figure 2.6.1b). Since the XSW extends out beyond the surface, this effect can be exploited to probe atoms adsorbed on the surface as well as those within the crystal.[21, 91, 98]

In an XSW experiment, the X-ray absorption is measured indirectly by recording the photoemission, Auger electron emission or X-ray fluorescence signal.[21, 91] Since the energies of these emission processes are dependent on core level binding energies, this allows absorption profiles for elements to be measured separately. Detecting X-ray fluorescence has the advantage that measurements do not need to be made under UHV conditions, whereas the two electron detection methods offer an intrinsically greater degree of surface specificity due to the short IMFP of low-energy electrons in condensed matter.[78] However, only core-level photoemission is able to resolve different chemical shifts of the same element, and thus measuring the X-ray absorption in this way can provide chemical-state specific structural information.[21, 91, 98] One drawback of this is that in order to obtain the X-ray absorbance from core-level photoemission, the angular resolved photoemission yield must be corrected for non-dipolar effects.[107]

In order to scan through the Bragg scattering condition, one must either change the X-ray wavelength (requiring a tuneable X-ray source) or the angle of incidence with respect to the scattering planes. Indeed, in early experiments which relied on fixed energy laboratory X-ray sources, the Bragg condition was traversed by 'rocking' the crystal substrate to change the angle of incidence.[108, 109] However, this approach has some significant disadvantages, the most prevalent being that at some general angle of incidence, the range of angles over which total reflectivity is achieved (the so-called 'rocking curve') is very narrow, typically spanning only a minute of arc or less.[21, 91] This places very stringent demands on the instrumentation, requiring a very precise sample goniometer and an X-ray beam with an angular

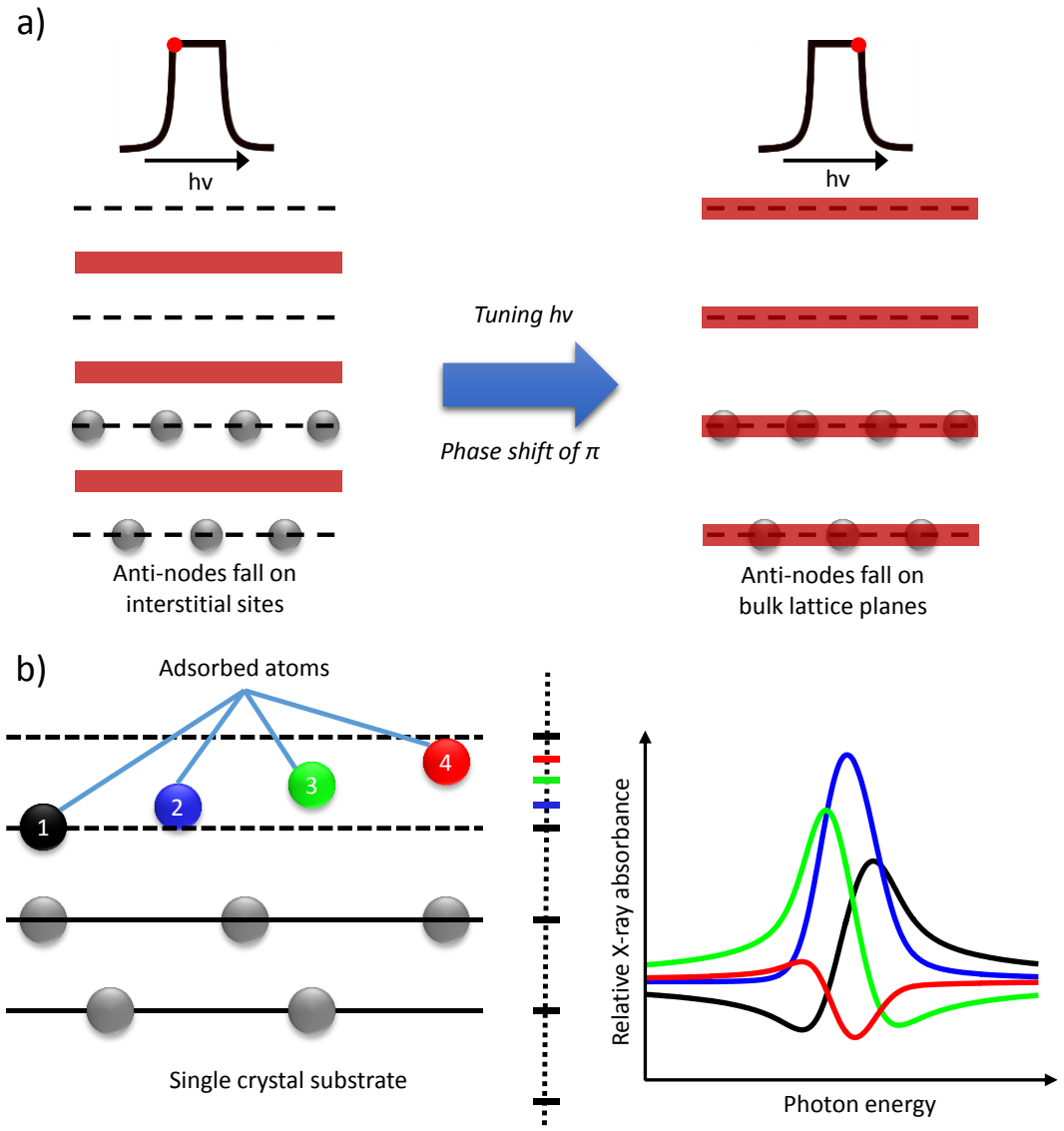

Figure 2.6.1 – An illustration of the fundamental principles of the XSW technique. a) A depiction of the phase relationship between the X-ray standing wave and the scattering crystal at the two extremes of the reflectivity curve. The red lines represent the antinodes of the standing wave and the dotted black lines denote the crystal scattering planes shown both within and projected beyond the crystal surface. Above each panel, a representation of the Darwin reflectivity curve is shown with the red circle indicating the point on the curve that is represented in the diagram below it. The left-hand panel depicts the onset of the reflectivity curve with the XSW the nodes coinciding with the atomic planes. The right-hand panel depicts the other side of the reflectivity curve in which the antinodes fall on the atomic planes. b) An illustration of how the X-ray absorption across the reflectivity curve is characteristic of the position relative to the scatterer planes. The X-ray absorption as a function of photon energy across the reflectivity curve is shown for four adsorbate atoms at different positions relative to the scattering planes.

spread that is much smaller than the width of the rocking curve in order for the standing wave effect to be observed. Furthermore, the crystalline substrate must have a high degree of perfection with a

mosaicity smaller than the rocking curve width. This limits the variety of materials accessible to the XSW technique, with only a few covalently bonded semiconductor materials (such as Si) able to be produced with a sufficient degree of perfection.[21, 91] It transpires, however, that this limitation can be overcome by conducting XSW experiments at normal incidence and by scanning through the Bragg scattering condition by tuning the X-ray wavelength, which is the basis of the NIXSW technique. These effects are best illustrated if one considers the underlying principles of XSW, which are presented below, closely following the discussion included in the cited XSW review papers and book chapters.[21, 91, 97, 98]

Taking the incident X-ray flux amplitude to be unity, the intensity of the standing wavefield at a perpendicular distance (z) from lattice planes spaced by d_H is given by the modulus squared of the sum of the incident and reflected waves such that:

$$I = \left|1 + \left(\frac{E_H}{E_0}\right)\exp\left(\frac{-2\pi i z}{d_H}\right)\right|^2 \qquad [2.6.2]$$

where E_H and E_0 are the amplitudes of the incident and reflected X-rays respectively. The X-ray reflectivity amplitude can be expressed in terms of the geometrical structure factors F_H and $F_{\bar{H}}$ for the respective reflections defined by $\boldsymbol{H}$ and $\boldsymbol{-H}$ as:

$$\frac{E_H}{E_0} = -\left(\frac{F_H}{F_{\bar{H}}}\right)^{\frac{1}{2}}\left[\eta \pm (\eta^2 - 1)^{\frac{1}{2}}\right] \qquad [2.6.3]$$

Here, η is a term that describes how much the scattering conditions differ from the midpoint of the Darwin reflectivity curve. If the Bragg scattering condition is traversed by varying the angle of incidence, the value η relates to the angular deviation ($\Delta\theta$) from the Bragg angle (θ_B) such that:

$$\eta = \frac{-\Delta\theta \sin 2\theta_B + \Gamma F_0}{|P|\Gamma(F_H F_{\bar{H}})^{\frac{1}{2}}} \qquad [2.6.4]$$

where P is the polarisation factor which is equal to unity for σ-polarisation and $\cos(2\theta_B)$ for π-polarisation, F_0 is the structure factor for forward (000) scattering and Γ is given by:

$$\Gamma = \frac{e^2\lambda^2}{4\pi^2\varepsilon_0 mc^2 V} \qquad [2.6.5]$$

where *e* and *m* are the electronic charge and mass respectively, *V* is the volume of the unit cell, *c* is the speed of light in vacuum and ε_0 is the permittivity of free space. Equation 2.6.3 shows that for a non-absorbing crystal, in which the structure factors are all real, unity reflectivity is achieved over a finite region of $\Delta\theta$, which corresponds to values of η in the range of -1 to +1. This defines the width of the Darwin curve and can be written as:

$$\Delta\theta_{range} = \frac{2\left(|P|\Gamma(F_H F_{\bar{H}})^{\frac{1}{2}}\right)}{\sin 2\theta_B} \qquad [2.6.6]$$

Equation 2.6.3 also highlights that the centre of the reflectivity curve does not correspond to the Bragg condition described by kinematical scattering but instead is offset by an amount defined by the forward scattering structure factor F_0:

$$\Delta\theta_{offset} = \frac{\Gamma F_0}{\sin 2\theta_B} \qquad [2.6.7]$$

Equation 2.6.6 also has important implications that can be exploited to circumvent the demanding requirements of crystal perfection and instrumentation needed for XSW experiments. As previously discussed, for an arbitrary angle of incidence, the width of the Darwin curve is very narrow. However, if the experiment is conducted with the incident beam at, or near, normal incidence to the scattering planes, one reaches a turning point in the Bragg equation, where the rate of change to the scattering condition as a function of θ becomes zero and thus the width of the reflectivity curve increases significantly.[109, 110] In fact, equation 2.6.6 suggests for a Bragg angle $\theta_B = 90°$ (and thus $\sin 2\theta_B = 0$) that the width of the rocking curve tends to infinity, though, in reality, the approximations that underpin this equation are not valid under this condition. Nonetheless, at normal incidence the width of the rocking curve becomes comparatively large (of the order of one degree) and thus the NIXSW technique is accessible to less perfect crystal substrates such as metals and metal oxides.

In order to operate at normal incidence, the X-ray wavelength must be tuned and therefore NIXSW experiments are reliant on synchrotron radiation. One advantage of using a tuneable photon source is that one can relinquish the need for a precise sample goniometer by keeping the sample fixed and scanning through the Bragg condition by changing the photon energy (and thus the X-ray wavelength) instead of the angle of incidence. The variation of the X-ray standing wavefield when using this approach can be described by modifying equation 2.6.4 to give η as a function of energy deviation (ΔE):

$$\eta = \frac{-2(\Delta E/E)\sin^2\theta_B + \Gamma F_0}{|P|\Gamma(F_H F_{\bar{H}})^{\frac{1}{2}}} \qquad [2.6.8]$$

for which the energy range of the Darwin reflectivity curve is:

$$\Delta E_{range} = \frac{E|P|\Gamma(F_H F_{\bar{H}})^{\frac{1}{2}}}{\sin^2\theta_B} \qquad [2.6.9]$$

In order to extract structural information from the XSW technique, one must consider how the X-ray absorbance of atoms changes, depending on their position, when scanning through the Bragg condition. In an XSW experiment, the relative X-ray absorbance of an atom is directly related to the local intensity of the standing wavefield, which at a perpendicular distance *z* relative to the Bragg planes is given by:

$$I = 1 + R + 2\sqrt{R}\cos\left(\phi - \left(\frac{2\pi z}{d_H}\right)\right) \qquad [2.6.10]$$

where *R* is the reflectivity, ϕ is the phase angle of the standing wave, which relates to the displacement from the nominal Bragg condition and d_h is the Bragg plane spacing. In theory, one could find the spacing of the adsorbate atoms relative to the lattice planes by finding the value of *z* that gives the best fit to the experimental data. However, in practice the adsorbate atoms are unlikely to adopt a single discrete spacing throughout the structure, even in the most ideal cases, due to thermal vibrations. Furthermore, in more complex systems the adsorbate atoms may occupy two or more sites with distinctly different spacings from the scattering planes. To account for this, a distribution of *z* values must be considered. This can be implemented into equation 2.6.10 to give the expected X-ray absorbance by integrating over all absorbers within the distribution, which gives:

$$I = 1 + R + 2\sqrt{R}\int_0^{d_H} f(z)\cos\left(\phi - \left(\frac{2\pi z}{d_H}\right)\right)dz \qquad [2.6.11]$$

where *f(z)dz* gives the fraction of absorbers at a spacing of *z* within a range of *dz*, defined such that $\int_0^{d_H} f(z)dz = 1$. Alternatively, this can be written as:

$$I = 1 + R + 2f_{co}\sqrt{R}\cos\left(\phi - \left(\frac{2\pi D}{d_H}\right)\right) \qquad [2.6.12]$$

This now gives two structural fitting parameters, which are the coherent fraction (f_{co}) and the coherent position (*D*). In effect, the coherent position is the average distance of the atoms above the nearest scattering plane and the coherent fraction is commonly regarded as a measure of the disorder, although, more exactly, it is a measure of the distribution of atomic positions. In the ideal case of a single adsorption site with no static or dynamic disorder, the coherent fraction is unity and the coherent position is the atomic position relative to the Bragg planes. In practice, thermal vibrations inevitably reduce the coherent fraction to a value less than unity, such that values of 0.8 (or more) still correspond to the occupation of a single site. Lower values commonly arise due to multiple site occupation with interpretation of the coherent position and fraction then requiring model calculations of different possible distributions of the occupied sites. An extreme example of this is that if two equally-occupied sites have heights that differ by exactly half of a lattice spacing the coherent fraction is zero, highlighting that a low coherent fraction does not necessarily imply a high degree of disorder. When interpreting XSW results, it is useful to consider the following:

$$f_{co}\exp\left(\frac{2\pi i D}{d_H}\right) = \int_0^{d_H} f(z)\,exp\left(\frac{2\pi i z}{d_H}\right)dz \qquad [2.6.13]$$

where the coherent fraction and position describe the magnitude and phase of the distribution of absorber position perpendicular to the scattering planes respectively. One convenient way to visualise this is by constructing an Argand diagram. Figure 2.6.2 depicts an Argand diagram for a system in which the absorbing atoms occupy two distinctly different sites. The two red vectors are the components that correspond to each atomic site which each have a phase angle ($2\pi z/d_H$) and an amplitude *f(z)*. Here

the amplitude will relate not only to the static and dynamic disorder of each site but will also represent the relative occupancy of each site. Summing these two component vectors yields a vector (blue arrow) of magnitude f_{co} with a phase angle ($2\pi z/d_H$) corresponding to the overall coherent position.

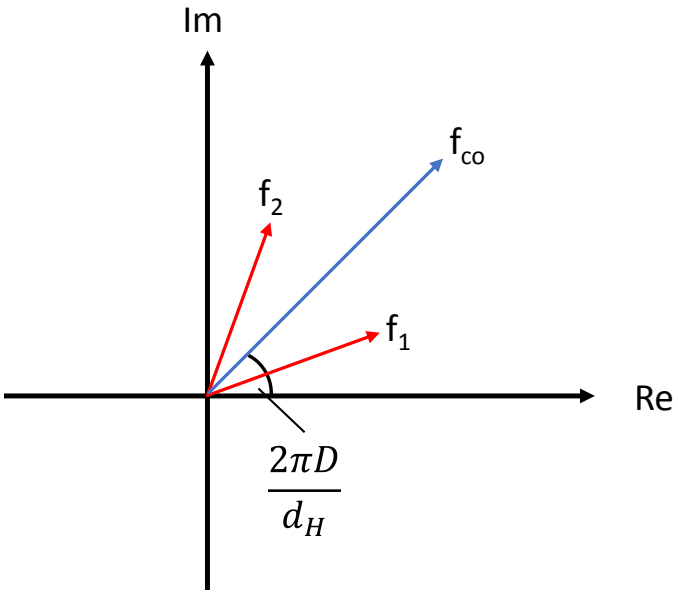

Figure 2.6.2 – Argand diagram illustrating the contributions of two distinctly different sites to the overall coherent fraction and coherent position. The red vectors of magnitude f_n correspond to the two absorber sites. Summing the two red vectors gives the blue vector, for which the magnitude corresponds to the overall coherent fraction (f_{co}) and the phase angle relates to the overall position (D).

As discussed previously, the X-ray absorbance cannot be obtained directly for the different atomic species within the structure and instead it is typically measured indirectly in an element and chemical-state specific fashion by recording the photoemission yield. One complication of this is that the photoemission yield only reflects the intensity of the XSW if the photoemission cross section in the direction of the detector is equal for both the incident and reflected X-ray beams.[21, 111] In general, this is only true in situations where the dipole-approximation can be used to quantitatively describe the photoemission process. The dipole-approximation is only valid if the spatial variation of the electromagnetic wavefield is negligible across the initial state wavefunction (i.e. the orbital from which the electron is emitted). Whilst the dipole approximation holds for sufficiently large wavelengths, at the high energies used for NIXSW measurements, which have corresponding wavelengths of the order of Å, non-dipolar effects cause a significant distortion to the angular photoemission cross-sections, even for core levels.

This issue is demonstrated by considering the angular dependence of the photoemission cross-section $\left(\frac{d\sigma}{d\Omega}\right)$ for excitation from a single X-ray beam, which under the dipole-quadrupole approximation can be written as:[21, 112]

$$\frac{d\sigma}{d\Omega} \propto \left[1 + \left(\frac{\beta}{2}\right)(3cos^2\theta - 1) + (\delta + \gamma cos^2\theta)\sin\theta\cos\phi\right] \qquad [2.6.14]$$

where β is the dipole asymmetry parameter, δ and γ are asymmetry parameters that account for non-dipole effects, θ is the angle between the X-ray polarisation vector and the electron emission direction and φ is the angle between the direction of photon propagation and the projection of the photoelectron in the plane perpendicular to the X-ray polarisation vector. One other key definition is that the sinθ term relates to the angle between the photon propagation direction and the projection of the electron emission direction within the plane containing the photon propagation vector and the X-ray polarisation vector but is more conveniently expressed in this form since this angle can be defined as (90° - θ), for which cos(90° - θ) ≡ sin(θ). One consequence of this is that in an XSW experiment, the sign of the sin(θ) term is different for excitation from the reflected beam compared to the incident beam as the in-plane angle between the photon propagation direction and the photoemission direction becomes (90° + θ), for which cos(90° + θ) ≡ -sin(θ). This means that under the dipole-quadrupole approximation, the photoemission cross-section in the direction of the detector is different for electrons excited by the incident beam compared to the reflected beam, which is known as forward-backward asymmetry (illustrated in Figure 2.6.3a). This causes the photoemission yield to deviate from the XSW intensity at the emitting atom and corrections for these non-dipolar effects must be applied in order to obtain meaningful NIXSW structural fitting parameters.

In order to apply such corrections, it is first useful to define a forward backward asymmetry parameter Q that can be related to the ratio of emission in a given direction from photons propagating in two opposing directions by the following expression:[21, 112]

$$\frac{(1+Q)}{(1-Q)} = \frac{\left[1 + \left(\frac{\beta}{2}\right)(3cos^2\theta - 1) + (\delta + \gamma cos^2\theta)\sin\theta\cos\phi\right]}{\left[1 + \left(\frac{\beta}{2}\right)(3cos^2\theta - 1) - (\delta + \gamma cos^2\theta)\sin\theta\cos\phi\right]} \qquad [2.6.15]$$

It is possible to obtain Q values by using calculated values for the β, δ and γ asymmetry parameters for the orbital being emitted from.[107] It is also possible to measure Q values experimentally by obtaining NIXSW measurements for systems with a known coherent fraction of 0, for which deviations from the photoemission yield will be proportional to the sum of the incident beam and the reflectivity multiplied by the asymmetry ratio described in equation 2.6.15.

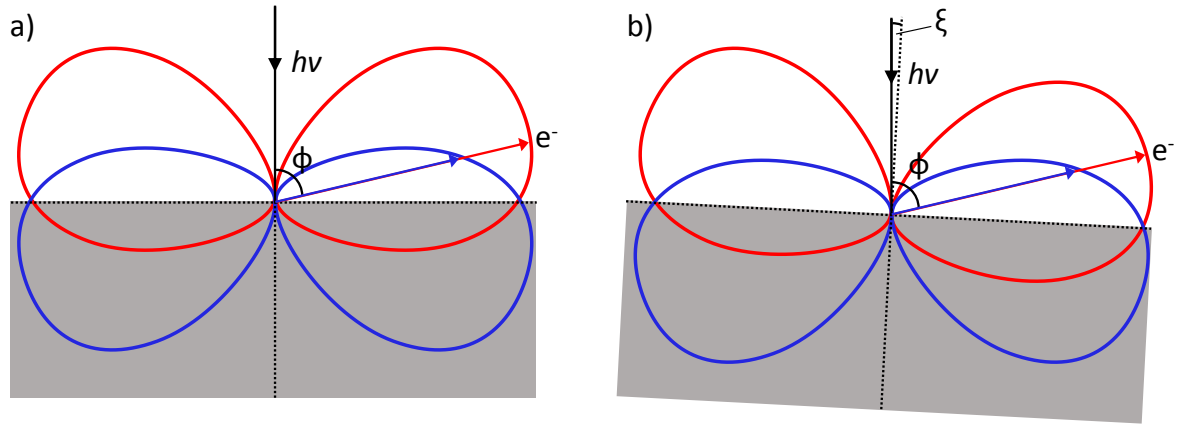

Figure 2.6.3 – Depiction of the angular distribution of photoemitted electrons plotted as a polar diagram for electrons excited by the incident (blue) and reflected (red) beams in a NIXSW experiment for (a) perfect normal incidence and (b) incidence at an angle ξ off normal incidence. Both examples show distributions for a positive forward-backward asymmetry parameter Q and the angle φ represents the angle between the photon propagation vector and emission in the direction of the detector.

A method for correcting for non-dipole effects has been presented by Vartanyants and Zegenhagen,[113] which gives the general result that the photoemission yield (Y) obtained in an XSW experiment should have the form:

$$Y \propto \left\{1 + S_R R + 2|S_I|\sqrt{R} f_{co} \cos\left(\phi + \psi - \left(\frac{2\pi D}{d_H}\right)\right)\right\} \qquad [2.6.16]$$

where S_R, S_I and ψ are parameters dependent on the initial state orbital angular momentum and the relative importance of non-dipole contributions. With no non-dipole effects and σ-polarised X-rays, $S_R = S_I = 1$ and $\psi = 0$, which simply gives the XSW intensity as shown in equation 2.6.12. For more general cases, expressions have not been given for these parameters, however Vartanyants and Zegenhagen[113] have derived a relatively simple expression for emission from an initial s-state which is significantly simpler than the general case as only one outgoing state is possible for both the electric

dipole and electric quadrupole terms. This can be expressed in terms of the forward-backward asymmetry parameter Q and is given by:[112]

$$Y \propto \left\{1 + R\frac{(1+Q)}{(1-Q)} + 2\frac{(1+Q^2 tan^2\Delta)^{1/2}}{(1-Q)}\sqrt{R} f_{co} \cos\left(\phi + \psi - \left(\frac{2\pi D}{d_H}\right)\right)\right\} \quad [2.6.17]$$

where

$$\psi = \tan^{-1}(Q \tan\Delta) \quad [2.6.18]$$

and

$$\Delta = \delta_d - \delta_p \quad [2.6.19]$$

where Δ is the phase difference between the outgoing electrons excited by the electric dipole and electric quadrupole terms, with δ_d and δ_p representing the partial phase shifts of the emitter atom potential for p- and d-waves respectively.[21, 112] While equation 2.6.17 provides a complete basis for describing the non-dipole effects in emission only from an initial s-state, this covers a wide range of useful systems, with the 1s orbital for low atomic number adsorbates such as C, N, O and even the elements in the 2nd row of the periodic table accessible to typical NIXSW photon energies (~ 3 keV). However, expressions for the S_R, S_I and ψ parameters have not yet been derived for emission from core levels other than s-states and thus complete analysis of the photoemission from these states cannot be achieved.[21] Instead, it is common practice to either approximate the core-level as an s-state[114] or to use other approximations to evaluate the non-dipole effects.[21] One other issue with the method of Vartanyants and Zegenhagen[113] is that it assumes perfect normal incidence, which is not possible in an actual NIXSW experiment as one must separate the incident and diffracted beams in order to measure the reflectivity, which can have a significant impact on the values of the non-dipole correction factors (illustrated in Figure 2.6.3b). This issue can be solved by applying additional corrections that account for this slight deviation from perfect normal-incidence.[111]

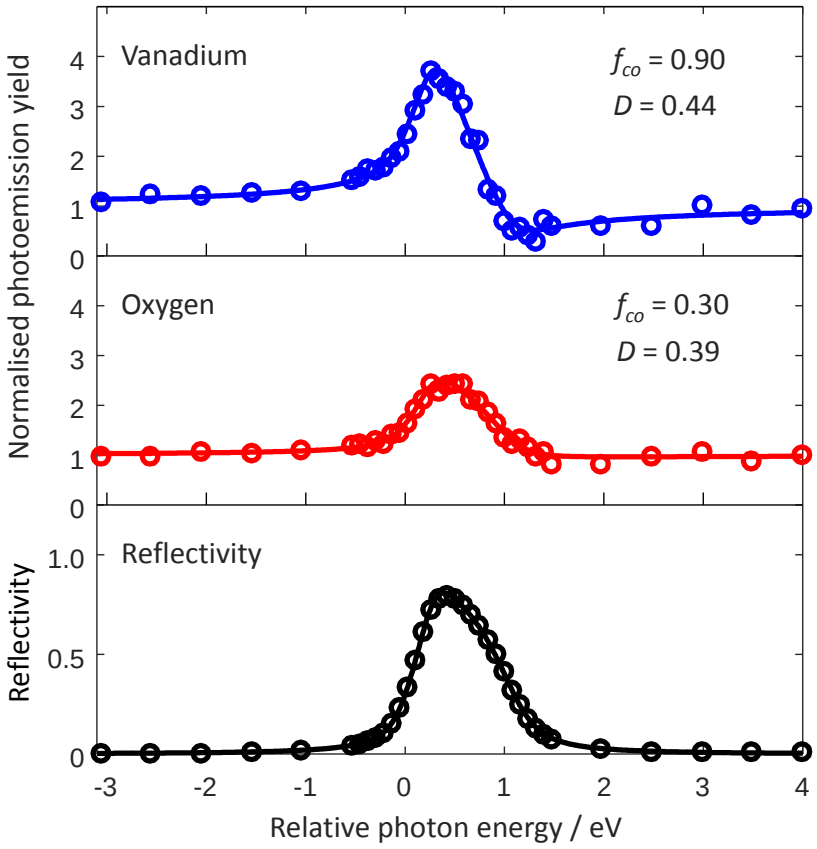

Figure 2.6.4 – Sample set of NIXSW photoemission yield curves and the recorded X-ray reflectivity obtained from VOPc adsorbed on Cu(111) using the (111) Bragg reflection. Photon energies are quoted relative to a Bragg energy of 2972.1 eV. The vanadium and oxygen photoemission yields were recorded from the V $2p_{3/2}$ and O 1s photoemission peaks respectively. Least square fits (solid lines) of the photoemission yield curves (circles) were obtained to extract the coherent fractions and coherent positions.

To demonstrate how structural information is extracted from experimental data, Figure 2.6.4 shows sample NIXSW data obtained from vanadyl phthalocyanine (VOPc) adsorbed on a Cu(111) surface using the (111) reflection of the substrate. The normalised photoemission yield is plotted against the photon energy relative to the Bragg energy to give the NIXSW absorption profile. Here, a clear qualitative difference is observed between the shapes of the NIXSW absorption profiles for the V and O species. These NIXSW profiles are then fitted using equation 2.6.13 to obtain the f_{co} and D parameters. In order to determine the phase and the intensity of the standing wavefield, the X-ray reflectivity is measured simultaneously alongside the absorption profiles. Note that the measured reflectivity curve does not display the top-hat shape of the Darwin curve shown in Figure 2.6.1 but shows an asymmetrical 'Darwin-Prins' profile with reflectivity tailing off at higher photon energies.[101, 106] This deviation from the theoretical Darwin curve shape is caused by X-ray absorption in the

substrate, which at the onset of the Bragg condition is minimal, due to the XSW antinodes falling between atomic sites in the bulk lattice; as the photon energy is increased, the XSW antinodes move towards the atomic sites and the X-ray absorption increases, resulting in a reduced reflection.[21]

The discussion thus far has described how the XSW technique can be used to find the perpendicular distance of absorber atoms relative to the lattice planes of the underlying substrate. Typically, the reflection normal to the surface termination is used, which gives information on the height of the absorber atoms relative to the surface. Of course, XSW will not give the adsorption height directly, instead giving only a height above the nearest bulk lattice plane (including the extended 'virtual' lattice planes beyond the surface). In order to obtain the correct adsorption height, it may be necessary to add an integer number of layer spacings above the surface. Whilst this could introduce some ambiguity into the experiment, typical layer spacings (2-3 Å) are of a similar magnitude to typical adsorption heights and thus it transpires that only one possible number of added layer spacings will give a physically reasonable adsorption height in most cases.[21, 91] In addition to the adsorption height, XSW can also give structural information for the lateral positions of atoms on the surface. This is achieved by taking XSW measurements for two or more reflections of non-parallel scatterer planes and obtaining the atomic positions by triangulation. For example, on a face centred cubic (fcc) (111) surface, the (111) reflection is used to measure the adsorption height and coupled with the $(\bar{1}11)$, the lateral adsorption site can be determined.[21]

Figure 2.6.5 illustrates how XSW triangulation can be used to distinguish between the three high symmetry adsorption sites using the measured coherent positions from the (111) and $(\bar{1}11)$ reflections. From the (111) reflection, the adsorbate height above the substrate $\left(z_{(111)}\right)$ is obtained and from the $(\bar{1}11)$ reflection, the layer spacing relative to the $(\bar{1}11)$ planes is obtained. By using simple trigonometry, it can be seen that for an adsorbed atom in the atop site $z_{(\bar{1}11)} = \frac{z_{(111)}}{3}$ (note that $cos(70.5°) = \frac{1}{3}$), in the hexagonal close packed (hcp) hollow site $z_{(\bar{1}11)} = \frac{z_{(111)} + d_{(111)}}{3}$ and for the fcc hollow site $z_{(\bar{1}11)} = \frac{z_{(111)} + 2d_{(111)}}{3}$ where $d_{(111)}$ is the spacing between the (111) lattice planes.

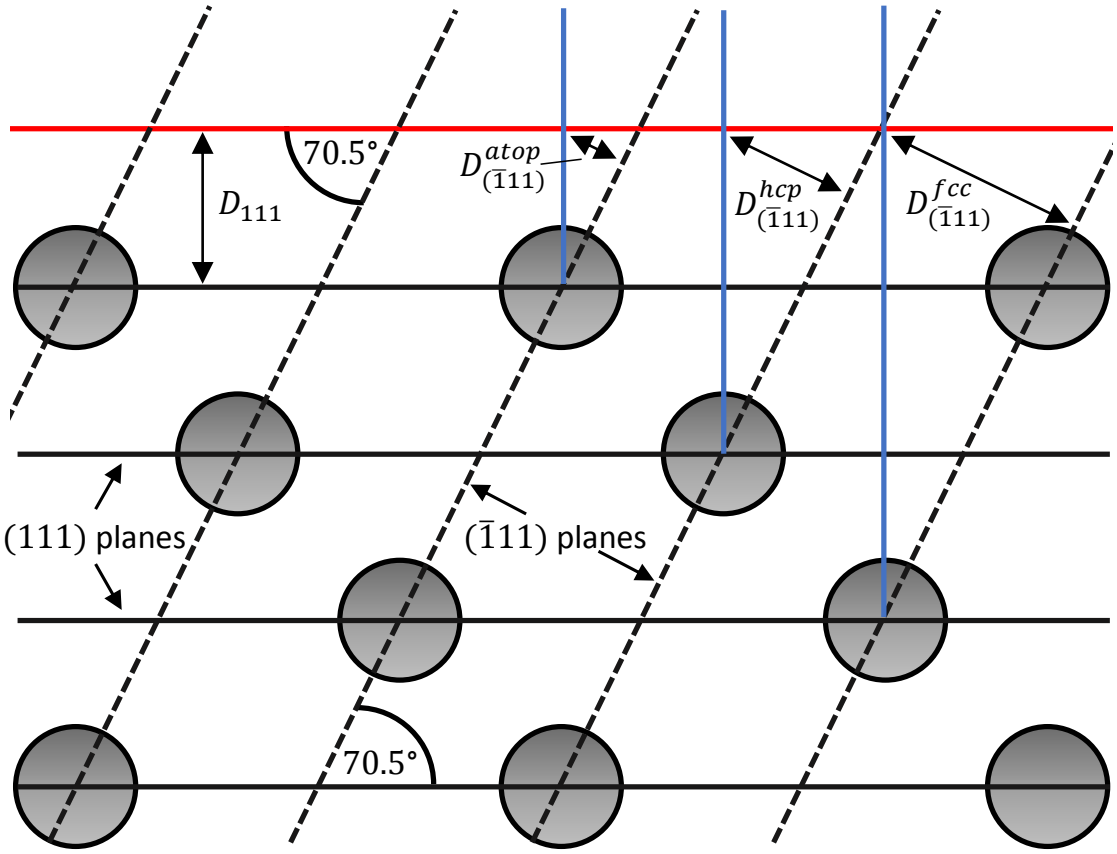

Figure 2.6.5 – Schematic diagram showing how the three high symmetry sites on an fcc (111) substrate can be distinguished by triangulation of the (111) and $(\bar{1}11)$ reflection coherent positions (adapted from the review of Woodruff[21]).

2.7 Density functional theory

DFT is a quantum mechanical technique used to model chemical systems from first principles. With the ability to accurately model the relevant geometries, forces and electronic properties within a variety of chemical systems, DFT has proven to be a very useful tool both for complementing experimental results as well as offering predictive capability for systems that have not or cannot be studied experimentally.[115-117]

In quantum mechanics, the total energy of a chemical system can be determined by solving the time-independent Schrödinger equation (TISE). However, apart from only a few simple systems (e.g. a hydrogen atom), the solution of the TISE contains electron-electron interactions and thus cannot be solved exactly due to the Heisenberg uncertainty principle. Additionally, for many-body systems, the TISE in its pure form is incredibly complex and thus becomes intractable, even to powerful supercomputers.[115, 117] As a result, to accurately calculate the total energy for many-body systems, special methods and approximations must be implemented to allow the TISE to be solved.

The TISE can be simplified by applying the Born-Oppenheimer approximation which asserts that because the atomic nuclei are substantially more massive and thus move significantly slower than electrons, it can be assumed that the electrons instantly equilibrate to any changes in the positions of the nuclei.[118] This allows the TISE to be solved by minimising the electronic energy for a set of fixed nuclear positions. However, the TISE still contains electron-electron interactions and thus has no exact solution. One approximation to make the TISE solvable is to treat the electronic wavefunction as a linear combination of single-electron orbitals, which forms the basis of the Hartee-Fock method.[119, 120] Due to its simplicity, the Hartree-Fock method allows the TISE to be solved at low computational cost but it ignores energy terms from electron exchange and correlation effects and thus calculates inaccurate total-energies. As an alternative, DFT uses a different approach, evaluating the total-energy of the system as a functional of the electron density rather than using the electronic wavefunction.[121, 122] This is possible because under the Born-Oppenheimer approximation, the total energy of the system is a unique functional of the electron density which can be solved self-consistently using the variational principle.[122] This means that the ground-state energy (and thus the ground-state density) can be found by minimising the total-energy functional with respect to the electron density. DFT has the advantage that the evaluation of exchange-correlation effects is inherently included in the technique and thus means that the ground-state energies of chemical systems can in theory be calculated exactly. However, the difficulty is that there is no method to find the exact mathematical form of the total-energy functional and thus approximate methods are required to solve the equations.[121]

One such method is the Kohn-Sham formalism, which considers a fictitious system of non-interacting electrons that is constructed to have the same electron density as its interacting equivalent.[123] This means that the kinetic energy of the electrons can be separated into a non-interacting component and a small correction term to account for the difference in kinetic energy between the interacting and non-interacting systems. Within the Kohn-Sham formalism, most of the energetic terms in the many-electron problem can now be solved exactly, with the nuclear-nuclear, nuclear-electron, and electron-electron interactions being solved classically using coulomb potentials. The non-classical electron-electron interactions of exchange and correlation as well as the kinetic energy correction are combined into a functional of the density, however the exact form of this functional is not known and thus is solved approximately. Initially this meant that early use of Kohn-Sham DFT was not accurate enough for quantum chemistry calculations but over time, this was overcome with improved methods of approximating the exchange-correlation functional such as the local density approximation[123] or the generalised gradient approach.[124] Consequently, Kohn-Sham DFT has been considerably successful and is now widely used to model a variety of chemical systems.

In DFT, a set of functions, known as a basis set, is used to expand the electronic wavefunction to allow for efficient computation.[121] The basis set can either comprise the linear combination of atomic orbitals, often used for molecular systems, or plane waves, which are well suited to large periodic systems and are commonly used for solid-state calculations.[117, 121, 125] For the former, a range of different functions are used to represent atomic orbitals, including Gaussian-type orbitals, Slater-type orbitals or numerical atomic orbitals, which vary in terms of the extent to which computational efficiency is traded for accuracy.[125] Another formalism that is useful in DFT calculations is the pseudopotential approximation, which is used to give a more computationally efficient description of the core electrons and ionic cores of atoms.[121, 126] In the absence of this approximation, the expansion of the electronic wavefunction incurs a high computational cost as a large basis set is needed to describe the tightly bound core orbitals and the rapid oscillations of valence electrons within the core region.[121] Furthermore, as the majority of physical properties are significantly more dependent on the valence electrons than the core electrons, there is less of a need to explicitly model the core orbitals. Consequently, the system can be modelled to a good approximation at a much lower computational cost by replacing the strong ionic potential with a weaker pseudopotential that acts upon a set of pseudo valence wavefunctions within the core region. [121, 126] Outside of the core region, the pseudopotential and the pseudo wavefunctions are identical to the true potentials and wavefunctions such that the valence electrons are still described accurately. [121, 126]

A common feature of DFT codes is the use of periodic boundary conditions, which allows bulk materials to be studied effectively using only a small simulation cell. The periodic boundary conditions take advantage of Bloch's theorem which states that for a particle in a periodically-repeating environment (e.g. electrons in a crystal), the energy eigenstates will have the same periodicity as the repeating lattice.[127] In effect, when modelling a bulk system, this transforms the problem of calculating an infinite (or sufficiently large) number of electronic wavefunctions across an infinite simulation cell, to one of calculating a finite number of electronic wavefunctions at an infinite number of sampling points, known as k-points. Conveniently, due to the wavefunctions at nearby k-points being very similar, it is possible to accurately represent the system by sampling only a few k-points.[121]

When modelling surface structures of adsorbed atoms and molecules, periodic boundary conditions have two important implications. Firstly, as a surface results from the termination of a bulk material in one dimension, the simulation cell must include a vacuum gap to separate the atoms from their periodic projections. This means that the surface is simulated as a slab that is only infinite in the two dimensions within the surface plane and contains only the number of atomic layers explicitly included in the simulation cell perpendicular to the surface. Secondly, the periodic boundary conditions require the

adsorbate structure to be commensurate with respect to the underlying substrate and thus incommensurate adsorption structures cannot be explicitly studied using DFT calculations. Instead, incommensurate structures are often approximated by constraining the model to a similar commensurate unit mesh to make them accessible to DFT.[56, 128, 129]

An important aspect of calculating accurate adsorption structures with DFT is the consideration of dispersion interactions. An issue with many of the standard functionals used in DFT is that they do not describe long-range dispersion interactions, which can result in inaccurate adsorption structures.[27] This problem is particularly pertinent for organic adsorbates, for which dispersion interactions are a key determining factor of the adsorption structure. To combat this, a range of functionals that include dispersion corrections have been developed,[27, 29, 130, 131]however, the efficacy of these dispersion corrections can be highly system-dependent and thus it is difficult to determine *a priori* which correction is most appropriate to use.[31, 33, 34] Consequently, there is currently an ongoing effort to benchmark DFT dispersion corrections using experimental structural measurements.[27, 29, 130, 131]

In section 2.3, it was discussed how, to a reasonable approximation and with relatively small (< 2 V) applied biases, the tunnelling current in an STM experiment depends primarily on the sample DOS. As DFT works with the electron density, the DOS can readily be evaluated from the results of calculations. As a result, DFT can be used to simulate STM images for calculated structures, which is often achieved using the simple formalism of Tersoff and Hamann.[132] In the Tersoff-Hamann approach, the unknown electronic structure of the tip is approximated as an atomic s orbital and in doing so, the expression of the tunnelling current (equation 2.3.5) becomes:

$$I \sim \int_0^{eU} \rho_S(z, \epsilon)\, d\epsilon \qquad [2.7.1]$$

where $\rho_S(z, \epsilon)$ is the sample DOS at the position of the tip apex, z.[133] A simulated STM image can then be constructed by calculating the spatial variance of the sample DOS for a given energy window. Despite the fact that the Tersoff-Hamann approach cannot explain the origin of the atomic-resolution that is achievable with STM, it has been shown to produce reasonably good qualitative predictions of experimental measurements.[77, 133] However, care must be taken as it is well-established that the nature of the tip can have a significant impact on STM image contrast, which, due to the lack of an explicitly defined tip, cannot be analysed within the Tersoff-Hamann approach.

2.8 Instrumentation and methods

2.8.1 Instrumentation

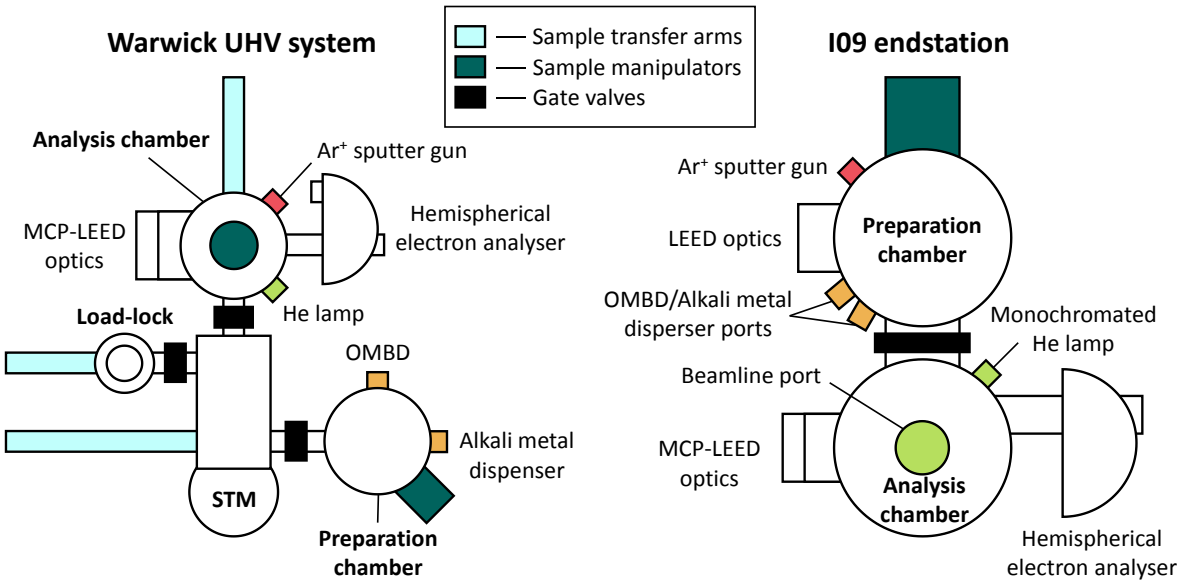

Figure 2.8.1 – Schematic diagrams of the two UHV systems used to conduct the experiments presented in this thesis. Left) – a plan view of the UHV system at the University of Warwick. Right) – a side view of the UHV endstation on beamline I09 at Diamond Light Source.

All characterisation experiments in this thesis were conducted in one of two UHV chambers. STM, LEED and UPS measurements were recorded in an UHV system at the University of Warwick and NIXSW, XPS, UPS and LEED experiments were performed in the UHV endstation installed on beamline I09 of the Diamond Light Source storage ring (schematics of both chambers are shown in Figure 2.8.1). The I09 beamline is equipped with both a double crystal monochromator to provide the 'hard' X-rays (2.1-20.0 keV photon energies) needed to perform the NIXSW experiments and a grazing incidence plane grating monochromator providing soft X-rays (100-2100 eV photon energies) to perform high-resolution soft XPS. Photoelectron spectra for UPS, XPS and NIXSW experiments were collected using a VG Scienta EW4000 HAXPES hemispherical electron analyser (angular acceptance range ± 30°) mounted at 90° to the incident photon beam.

2.8.2 Sample preparation

All experiments used single crystal substrates cut with a precision of 0.1°, which were atomically cleaned *in situ* via cycles of sputtering with Ar^+ ions, followed by annealing to ~500 °C. In the Warwick UHV system, sample temperatures were measured indirectly by a thermocouple in contact with the

sample plate onto which the crystal was mounted. On the I09 endstation, sample temperatures were also measured indirectly but using a thermocouple fitted to the sample plate receptor on the manipulator head. Organic molecules were deposited by sublimation using an OMBD source. All powders were purified by thermal gradient sublimation and were thoroughly degassed before use. Alkali metals were deposited via resistive heating of alkali metal dispensers obtained from SAES.

2.8.3 LEED

LEED was recorded in both UHV systems, providing a cross-reference to ensure that comparable samples were characterised in both places. Low current MCP-LEED optics were used in both UHV systems (Warwick: Omicron SPECTALEED, I09: OCI BDL800IR-MCP LEED) to avoid damaging the molecular overlayer with the electron beam. LEED pattern simulations were used to analyse and identify the symmetry and periodicity of adsorption structures. These simulations were obtained using LEEDpat software.[134]

2.8.4 STM

All STM images were recorded using an ambient-temperature Omicron STM/AFM operated in constant current mode using electrochemically etched polycrystalline tungsten tips. All STM images in this work were analysed, plane corrected and flattened using the Gwyddion open source image-processing software.[135] High frequency noise was removed from images using a low-pass filter within the STM operating software. Unit mesh dimensions obtained from STM were averaged over multiple image and the quoted associated error corresponds to the standard deviation of these measurements. Unit mesh vector lengths were obtained from the inverse distance measured between maxima in fast Fourier transform of the STM images, with the unit mesh included angle and orientation determined from lines drawn through these maxima. The orientation of the unit mesh vectors relative to the substrate surface lattice vectors was determined through comparison of the STM image to the direction of first order substrate beams in the LEED patterns, which were both recorded with the sample in the same orientation.

2.8.5 UPS

UPS measurements conducted at Warwick used a SPECS UVS 10/35 photon source and a SPECS PHOIBOS 100 hemispherical electron analyser. UPS experiments conducted at I09 used a monochromated He lamp fitted on the endstation, which was operated using either the He Iα or He IIα emission lines. Work function measurements were measured as detailed in section 2.5 with the sample held at a negative bias (between -8 V and -10 V) so that the SECO could be detected. Fermi edges were

fitted using a complementary error function and SECO energies were determined by linear extrapolation of the steep intensity gradient on the high kinetic energy side of the SECO to an intensity of 0.

2.8.6 XPS

The high-resolution soft XP spectra and the XP spectra recorded in NIXSW experiments were fitted using the CasaXPS software package. Photoemission peaks were fitted using a Gaussian-Lorentzian product line shape, adjusting the Gaussian/Lorentzian ratio to give the best fit to the experimental peak shapes (determined by eye). Where possible, the background was fitted using a Shirley background to account for the step in intensity either side of the peaks, though for peaks situated on a steeply sloped region of the background, a linear background was used instead due to limitations in the CasaXPS software. The C 1s spectra, which show multiple peaks for TCNQ, were fitted using four components (one for each chemically distinct C environment within the molecule). These four components were fitted allowing ± 0.1 eV variation in the full width half maximum of the peaks with respect to each other and the integrated areas were constrained to be within ± 20% of their relative stoichiometry in the molecule.

2.8.7 NIXSW

For NIXSW experiments, the reflected X-ray intensity was recorded using a fluorescent screen mounted on the port through which the incident photon beam passes. The measured reflectivity curve was used to define the energy scale relative to the Bragg energy, accounting for the energy broadening effects resulting from imperfections in the Si(111) double crystal monochromator and the single crystal substrate. The X-ray absorption profiles were monitored whilst sweeping the photon energy through the Bragg condition by measuring the intensity of the photoemission yield for the elements/chemical species of interest. The coherent fractions and positions were extracted from the X-ray absorption profiles using a dynamical theory fitting programme. A correction for the non-dipole effects in the angular distribution of photoemission using values for the forward-backward asymmetry parameter Q obtained from theory based computations of the relevant β, δ and γ asymmetry parameters[107] (as discussed in section 2.6) was applied in the procedure for fitting the photoemission yield profiles. The specific values for Q used for the different core-levels for the different photon energies and sample orientations used in this thesis are detailed in Appendix E. The initial state wave-function was treated as an s-state, even for the K 2p and Cs 3d orbitals, and perfect normal incidence was assumed in the fitting procedure.

It should be noted that a problem has been identified in the fitting of NIXSW absorption profiles reported both in the work presented in this thesis and by other users of the I09 beamline, returning coherent fractions close to and in excess of unity. A coherent fraction of greater than unity is not possible and due to the thermal vibrations, which cause incoherence in the standing wavefield and create a distribution of the positions of absorber atoms, coherent fractions realistically should not exceed a value of 0.9.[136] The source of this issue has been identified as being due to non-linearity in the detector response of the VG Scienta EW4000 HAXPES hemispherical electron analyser on the I09 beamline at Diamond Light Source, which impacts on the modulation of the photoemission yield when scanning through the rocking curve. This problem has also been observed previously for other similar analysers.[137, 138] The characteristics of the instrument at I09 are currently being investigated but early tests indicate that the response behaviour is complex, requiring further extremely detailed measurements before a reliable correction methodology can be developed. However, conducting a range of tests for highly simplified correction methods show that this non-linearity mostly affects the apparent coherent fraction but only causes negligible changes to the coherent position that are within usual precision estimates of the measurements. Consequently, from this evaluation, the coherent fraction errors in this work were estimated at a value of 0.1 to accommodate the non-linearity issues whereas errors on the coherent position were kept at a typical level of precision for NIXSW measurements (i.e. 0.05 Å).[21, 98]

2.8.8 DFT

DFT calculations performed in collaboration with this work are presented in this thesis and were used to aid in the interpretation of the experimental NIXSW measurements obtained for two of the studied systems. The calculations obtained for TCNQ on Ag(111) (shown in section 4.3) were performed by Simone Velari using the QUANTUM ESPRESSO[139] plane-wave pseudopotential package with ultrasoft pseudopotentials[126] using a kinetic energy cutoff of 408 eV and a GGA-PBE exchange-correlation functional.[140] Dispersion corrected calculations were obtained using the DFT-D method proposed by Grimme[141] as well as the vdW-DF[29] method, which are both implemented in the QUANTUM ESPRESSO package.[142] The adsorption phase was modelled as a periodically repeated cell comprising a single unit mesh of the commensurate TCNQ adsorption phase on Ag(111) described by a $\begin{pmatrix} 2 & 5 \\ -8 & -2 \end{pmatrix}$ matrix of the substrate lattice vectors and containing a total of three TCNQ molecules. The Ag(111) surface was modelled as a slab consisting of three atomic layers and separated from its periodic image by a vacuum gap of 14 Å. The coordinates of the atoms in the bottommost layer of the Ag slab were constrained to values calculated for bulk Ag and the positions of all other atoms in the

simulation cell were relaxed up to forces of 0.026 eV $Å^{-1}$. Due to the very large unit cell, k-point sampling was restricted to the Γ-point alone.

The DFT calculations obtained for the K_2TCNQ adsorption phase on Ag(111) (shown in section 5.1.3) were performed by Reinhard Maurer using the FHI-aims package, which uses a numerical atomic orbitals basis set.[125] The optimised structures were calculated using the 'tight' basis set and numerical settings within FHI-aims. A GGA-PBE functional[140] was used to evaluate exchange-correlation. Dispersion interactions were modelled using both the Tkatchenko-Scheffler vdW^{surf} method (DFT+vdW^{surf})[32] and the many-body dispersion method (DFT-MBD)[31, 33] implemented in the FHI-aims package. The original DFT+vdW^{surf} C_6 and polarisability coefficients[32] (used in both the DFT+vdW^{surf} [32] and DFT-MBD[31, 33] dispersion corrections) were modified for K, using values proposed by Gould and Bucko,[143] to account for its ionic nature in the networks formed with TCNQ. The adsorption structure was modelled as a periodically repeated cell comprising a single unit mesh of the commensurate K_2TCNQ adsorption phase on Ag(111) described by a $\begin{pmatrix} 3 & 0 \\ 1 & 5 \end{pmatrix}$ matrix of the substrate lattice vectors, containing a single TCNQ molecule and two K atoms. The Ag(111) surface was modelled as a slab consisting of four atomic layers and separated from its periodic image by a vacuum gap exceeding 35Å. The coordinates of the atoms in the bottom two layers of the Ag slab were constrained to values calculated for bulk Ag and the positions of all other atoms in the simulation cell were relaxed. The Brillouin zone was sampled with a 4x8x1 Monkhorst-Pack[144] k-grid and the geometries were optimized to below a force threshold of 0.025 eV $Å^{-1}$.

3. TCNQ

3.1 Introduction

7,7,8,8-tetracyanoquinodimethane (TCNQ) is an organic molecule which has been influential in the development of OEDs due to its excellent electron accepting ability.[145, 146] TCNQ first gained interest when it was discovered to form highly conductive charge transfer salts with a range of electron donors.[145] One notable example is the TCNQ salt of the electron donor molecule tetrathiafulvalene, which gave the first example of an organic salt displaying metallic conductivity.[145, 147] This remarkable discovery was instrumental in the field of organic electronics, realising the possibility of high conductivity combined with the highly tuneable properties of organic molecules.[145]

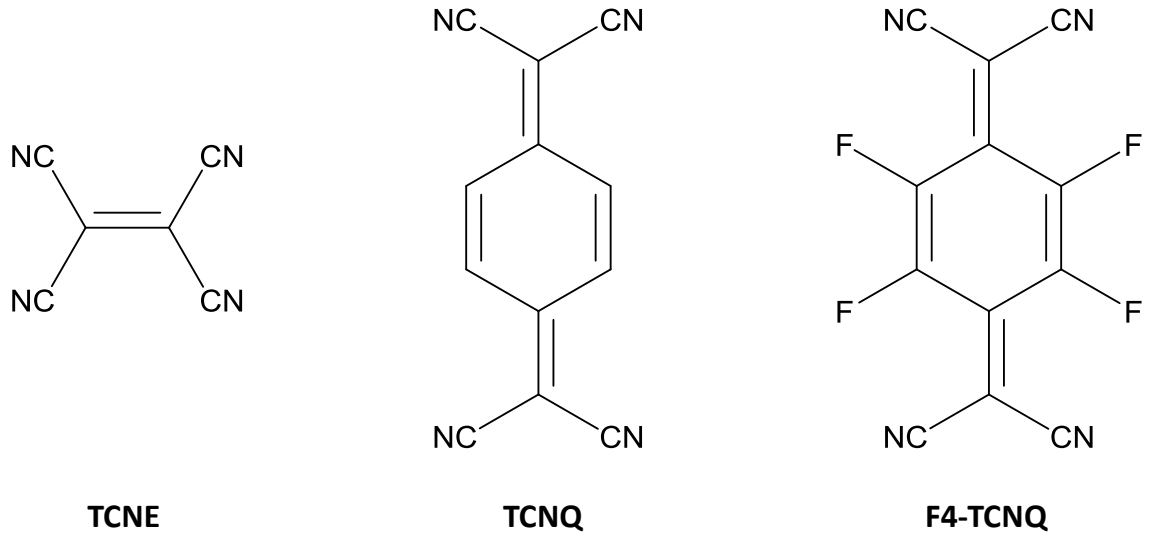

Figure 3.1.1 – The skeletal structure of TCNQ, its parent molecule tetracyanoethylene (TCNE) and its fluorinated derivative 2,3,5,6-tetrafluorotetracyanoquinodimethane (F4-TCNQ).

Following from this initial interest, TCNQ and other related molecules (e.g. F4-TCNQ and TCNE, see Figure 3.1.1) have received a lot of attention and have been incorporated into a variety of OEDs, including OPVs,[148, 149] OLEDs[150, 151] and OFETs[152, 153]. Furthermore, TCNQ has been found to significantly reduce the hole-injection barrier at interfaces with Cu and Ag surfaces and has thus been identified as a candidate for use in HTLs to improve energy level alignment.[154, 155] Because of its numerous potential applications, a substantial research effort has been devoted to understanding the key structural and electronic properties of TCNQ and its impact on device performance. To this effect, a wide range of surface science studies have been conducted, typically investigating TCNQ adsorbed on

coinage metal surfaces. In the following sections, the results of these studies are reviewed along with additional studies of 2D ionic and coordination networks formed between TCNQ and coadsorbed metal atoms on coinage metal surfaces.

3.2 TCNQ on coinage metal surfaces

STM studies show that when adsorbed on the surface of Au(111), TCNQ packs into an incommensurate 'brickwork' structure that promotes the formation of intermolecular N···H hydrogen bonds.[129, 156] This brickwork structure bears striking resemblance to layers of the TCNQ crystal structure when viewed normal to the (020) direction[157] as well as TCNQ adsorbed on an Ir(111)-supported graphene layer, where molecule-substrate interactions are weak.[158] This suggests that the observed structure is largely independent of the underlying substrate resulting from the weak molecule-substrate interactions relative to the intermolecular hydrogen bonds. This conclusion is further supported by the Au(111) surface retaining its herringbone reconstruction upon adsorption of TCNQ,[129, 156] a feature that is usually lifted in the presence of strongly interacting molecules. UPS and XPS measurements indicate that TCNQ adsorbs in a neutral charge state on Au(111), owing to the relatively high work function of the substrate.[57, 159] In contrast, F4-TCNQ, which has a much greater electron affinity than TCNQ, does become negatively charged on Au(111) and subsequently adsorbs in a commensurate structure in which STM shows the lifting of the herringbone reconstruction and also suggests that Au adatoms, abstracted from the underlying substrate, are incorporated into the molecular layer.[54, 160] This implies that charge transfer leads to stronger interactions with the substrate.

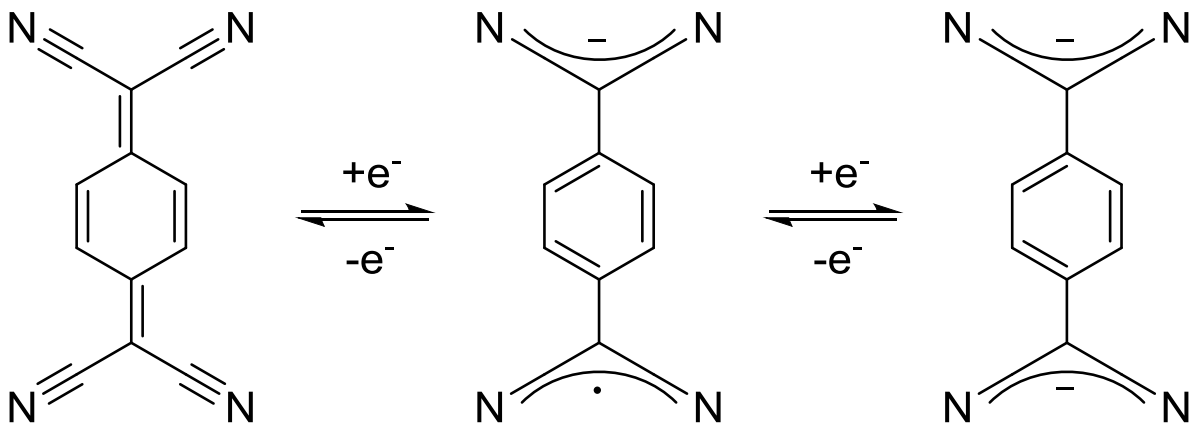

Figure 3.2.1 – Skeletal representation of TCNQ, $TCNQ^-$ and $TCNQ^{2-}$. Upon uptake of electrons, the central quinoid ring of TCNQ aromatises, which disrupts the conjugated π-system that extends through the molecule. The negative charge is largely accommodated by the electronegative cyano groups.[161]

DFT calculations investigating TCNQ on Au(111) suggest that the molecule adsorbs in a bent geometry with the central ring adsorbing at ~3.0 Å above the surface with the peripheral CN groups pointing down to interact with the substrate at a height of ~2.4 Å.[128] This result conflicts with the experimental observations as the calculated adsorption height is indicative of relatively strong TCNQ-Au bonding interactions that have some covalent character. Furthermore, the molecular conformation is not consistent with that expected of a neutral TCNQ molecule as TCNQ has a rigid and planar structure owing to the conjugated π-system that extends throughout the molecule.[17, 161] However, upon uptake of one or more electrons, the central quinoid ring of TCNQ aromatises, with the additional electron(s) being accommodated by the electron-withdrawing cyano groups (Figure 3.2.1).[161] This aromatisation disrupts the π-conjugation, with the peripheral carbons becoming sp^3-hybridised, thus giving the molecule greater flexibility.[161]

It is thus reasonable to expect that the molecule would only deviate from its planar conformation for substrates on which it accepts electrons, though the published DFT models for TCNQ on Au(111) do not reflect this.[128] It should, however, be noted that these calculations do not include corrections for long range dispersion interactions,[128] which are likely to have an effect on the adsorption structure.[24] Additionally, due to the periodic boundary conditions of DFT codes, the exact periodicity of the incommensurate TCNQ Au(111) structure could not be modelled, which may also affect the calculated structure.[128]

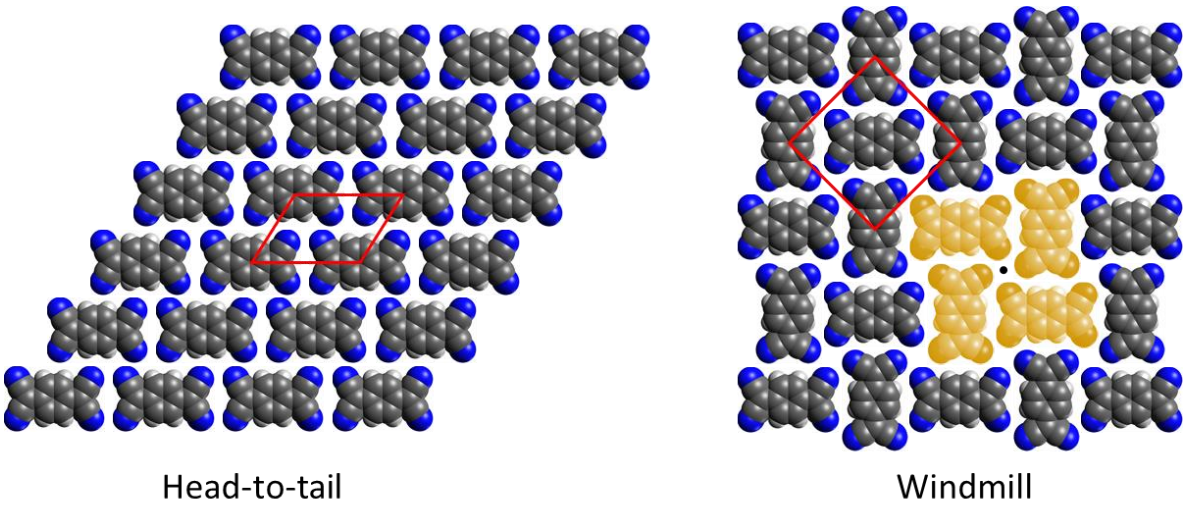

Figure 3.2.2 – Examples of the two common TCNQ packing regimes found on metal surfaces. The unit mesh for each structure is shown in red. A single 'windmill' is highlighted in yellow with a black dot indicating its centre.

In contrast to Au(111), on the low-index surfaces of Ag and Cu, XPS and UPS measurements show that TCNQ becomes negatively charged.[57, 162, 163] On these surfaces, TCNQ forms structures that deviate from the optimal hydrogen-bonding arrangement and are, in some cases, also commensurate with the underlying substrate, indicating stronger molecule-substrate interaction.[17, 57, 58, 164-167] From STM images, these structures can be split into two types of packing regimes (Examples of these are shown in Figure 3.2.2).

The first of these is a 'head-to-tail' arrangement, observed on Cu(100),[17] Ag(100)[58] and Ag(111),[57] in which all of molecules adopt the same orientation, similar to the Au(111) brickwork structure but distorted from the optimal hydrogen-bonding alignment between the rows of molecules. The other type of packing arrangement, which has been reported to form on Cu(111)[164-166] and Ag(111),[167] features units of four TCNQ molecules spiralling around a central point in a windmill-like structure. From this windmill unit, a diverse range of structures can form depending on their relative spacing and the sharing of TCNQ molecules between windmill units. An example of this is on Cu(111), which, depending on the substrate temperature, forms two distinctly different structures that include windmill motifs.[164, 165] This also emphasises how the deposition conditions can influence the resulting structure and is further highlighted by TCNQ on Ag(111), which adopts a windmill-type structure at lower coverages but switches to a head-to-tail structure when the coverage is increased.[57, 167] This therefore shows that the phase space of TCNQ on Cu and Ag surfaces is complex and most lkely results from the fine balance of molecule-substrate, intermolecular hydrogen bonding and electrostatic repulsion interactions between the molecules.[38, 39]

In both packing regimes identified above, negatively charged TCNQ molecules pack together with the cyano groups of adjacent molecules close to each other. This observation is rather unusual as the negative charge is typically localised on the cyano groups[161, 168] and thus would seemingly cause unfavourable electrostatic repulsions between molecules. DFT calculations performed for TCNQ on Cu(100)[17] and Cu(111)[164, 165] offer some possible insight into this. On both substrates, the calculations predict that TCNQ becomes negatively charged and adsorbs in a significantly bent conformation, with the peripheral cyano N atoms more than 1 Å below the central ring of the molecules,[17, 164, 165] a conclusion that is qualitatively supported on Cu(100) by the results of near edge X-ray absorption fine structure (NEXAFS) measurements[17]. This bending enables the molecule to bond with the underlying substrate, which, according to the DFT models, causes the substrate atoms to be lifted out of the surface plane by ~0.3 Å. [17, 164, 165] It is then predicted that a stress field generated around the lifted substrate atoms overcome the electrostatic repulsions between molecules and make it energetically favourable for the negatively charged cyano groups to be in close proximity. [17, 164, 165] However, one other possible

explanation, which has not currently been explored by DFT is the incorporation of adatoms from the underlying substrate into the molecular layer to which could act as counterions. This hypothesis is supported by the similar TCNQ head-to-tail and windmill assemblies observed when it is codeposited with metal atoms (see section 3.3).[54, 57-59, 164] Furthermore, the related molecules TCNE and F4-TCNQ, are both reported to form networks with adatoms from the underlying substrate on coinage metal surfaces. Specifically, low temperature STM images show that Ag adatoms are etched away from the step-edges near to TCNE molecular islands, suggesting that Ag atoms are incorporated into the TCNE adsorption layer.[60] Additionally, STM of the ordered overlayer formed by F4-TCNQ on Au(111) features bright protrusions between molecules that are attributed to adatoms.[54] Similar bright protrusions have also been observed in STM images for TCNQ on Ag(111), which may also be caused by the presence of adatoms.[57, 167] However, as STM images show a convolution of structural and electronic effects,[85] it is not possible to confirm the origin of these bright protrusions from STM alone.

DFT calculations may be able to offer some insight into this by comparing the adsorption energies of STM measured assemblies of TCNQ both with and without adatoms, though a suitable dispersion correction for this system would need to be identified. Experimentally obtained quantitative structural measurements may also be able to shed light on whether adatoms are present in TCNQ adsorption structures and furthermore could also provide a reference point to compare to DFT models. Despite this, there are currently no quantitative structural measurements available for TCNQ or its derivatives adsorbed on metal surfaces with the exception of one NIXSW investigation of F4-TCNQ on Cu(111).[169] In this NIXSW study, the molecule is reported to bend down towards the surface, though the coherent fractions reported (0.43, 0.28, 0.15 for F, N and C respectively) are so low that attributing the associated coherent positions of F and N atoms to single heights, as reported in this paper,[169] is certainly questionable. Also, the lack of information regarding the coverage or molecular ordering for the measured surface[169] makes it difficult to identify other possible causes of these low coherent fractions.

3.3 Coadsorption of TCNQ with metal atoms on coinage metal surfaces

The codeposition of TCNQ with metal atoms has been found to form 2D networks on coinage metal surfaces. This approach has been implemented for a variety of metals, including transition metals such as Fe, Mn and Ni[54, 58, 164, 170, 171] as well as alkali metals such as Li, Na, and Cs.[57, 59, 168, 172] One feature common to all of these networks is that the metal atoms link the TCNQ molecules together through bonds to the cyano groups. Aside from this, the resulting structure can vary significantly depending on the usual competition of molecule-substrate and intermolecular interactions and can also be dictated by the nature of bonding between the molecule and metal atoms,[59] as well as their stoichiometry.[58, 171]

Overall, the same head-to-tail and windmill packing motifs described earlier (see section 3.2) are the most prevalent in these networks.

The structural effects of the bonding between TCNQ and the coadsorbed metal atoms were investigated by Abdurakhmanova *et al.* studying analogous $MnTCNQ_4$* and $CsTCNQ_4$ networks on Ag(100) with STM and DFT.[59] Here, it was found that the highly directional coordinative bonding of the TCNQ to the Mn metal centres directed the structure, restricting the C-N-Mn bond angle to 180°. Conversely, the ionic bonding between the negatively charged TCNQ and positively charged Cs ions, which does not require specific bond angles, allows greater flexibility in the structure with the molecules able to orient in a geometry that promotes hydrogen bonding.[59]

Further DFT analysis performed for the aforementioned $CsTCNQ_4$/Ag(100) system also suggests that the alkali metal can have a significant impact on the electronic properties of the surface.[59, 168] As previously discussed TCNQ molecules become negatively charged on many metallic substrates, which combined with the image charges in the metal creates relatively strong dipole moments perpendicular to the surface, increasing the surface work function. The addition of alkali adatoms, which become positively charged and produce strong dipoles of opposite polarity due to their low ionisation potential, stabilise the metal-organic networks and also reduce the work function increase caused by TCNQ molecules alone. [57, 59, 172] Floris *et al*. investigated the influence of the alkali metal on the structural and electronic properties of the system by performing DFT calculations for the $CsTCNQ_4$/Ag(100) structure observed by STM. [168] Specifically, this was achieved by studying the effect that changing the alkali metal had on the system.[168] One surprising feature of the structure predicted by DFT calculations is that despite the alkali ions occupying 'pores' or 'holes' in the molecular assembly that are large enough to comfortably accommodate them in a coplanar bonding arrangement, they instead rest above the molecular plane.[168] This effect has been rationalised as being due to the larger positive dipole moment that arises from the increased height of the alkali metal ion above the surface, which counteracts the negative molecular dipoles more effectively.[168] The DFT calculations therefore predict an interesting result, indicating a close relationship between the height of the alkali metal ion above the substrate and the surface work function. DFT calculations performed using other alkali metals (K, Na, Li), assumed to occupy the same sites in an identical TCNQ assembly (the formation of this structure for these other alkali metals has not yet been demonstrated experimentally), conclude that the smaller alkali metals

*The notation here of M_xTCNQ_y, where M is a metal and x and y are integers, is used throughout this thesis to denote the stoichiometry of the adsorbed structures. The integers x and y are not explicitly included in the notation if their value is equal to 1.

adsorb closer to the surface, producing a smaller positive dipole.[168] As a result, the negative molecular dipoles are screened less, thus reducing the overall work function shift.[168] The DFT calculations therefore predict that by using different alkali metals, the surface work function can be tuned and that this effect could be exploited to optimise the energy level alignment in OEDs. Consequently, these TCNQ-alkali metal networks have been identified as a possible basis for tuneable hole-extraction layers bridging the metal-organic interfaces in practical devices.[59, 168]

4. TCNQ on Ag(111)

The conventional wisdom, based largely on DFT calculations, is that TCNQ adsorbs on coinage metal surfaces in a bent conformation with the peripheral cyano groups pointing down towards the surface.[17, 128, 164, 165] Upon accepting electrons, the conjugated π-system that extends across the entire TCNQ molecule is disrupted, increasing its flexibility.[161] Consequently, when adsorbed on surfaces in which TCNQ accepts electrons, a more prominent bend is expected. TCNQ is known to accept electrons from the Ag(111) surface[57] and thus is expected to adsorb on it in a significantly bent geometry. In this chapter, an investigation of the charge-transfer and adsorption structure of TCNQ on Ag(111) using a range of surface techniques is presented, with a particular focus on resolving the molecular conformation from quantitative structural measurements obtained using the NIXSW technique.

4.1 STM and LEED

Table 4.1.1 – Summary of the TCNQ adsorption phases characterised by STM and LEED on Ag(111) along with the preparation conditions used to form them. The STM measured unit mesh dimensions are given where b_1 and b_2 are the vector lengths, γ is the included angle and Θ is the angle between vector b_1 and the substrate <110> directions. Associated errors for the unit mesh dimensions are shown in parentheses and give the uncertainty on the last significant figure of the quoted value. Matrices consistent with the STM measured unit mesh dimensions are also shown for each phase. Unit mesh values are not quoted for the mixed phase as it is a combination of phases 1 and 2 along with some disordered regions between domains.

Phase	b_1 / Å	b_2 / Å	γ / °	θ / °	Matrix	Preparation conditions
Mixed	-	-	-	-	-	Deposition of TCNQ to an apparent saturated monolayer.
1	11.2(2)	7.3(1)	106(1)	48(3)	$\begin{pmatrix} 0.93 & 4.26 \\ -2.91 & -1.63 \end{pmatrix}$	Annealing the mixed phase to 210 °C
2	20.4(7)	12.3(3)	97(2)	24(2)	$\begin{pmatrix} 2 & 5 \\ -8 & -2 \end{pmatrix}$	Annealing the mixed phase/ phase 1 to 270 °C or depositing a submonolayer coverage of TCNQ.

TCNQ was sublimed at 130 °C from an OMBD source onto an Ag(111) single crystal held at room temperature to an apparent saturated monolayer (ML) coverage.† STM images of the resulting surface (Figure 4.1.1a-c) show the TCNQ molecules as oblong protrusions packed into a mixture of ordered domains on the surface, with some small regions of disorder in between. The ordered regions comprise TCNQ molecules arranged in one of two coexisting assemblies. The first of these is a head-to-tail type

† Note that throughout this thesis, monolayer coverage refers to a single layer of the adsorbate that completely covers the surface and does not represent the absolute coverage (i.e. one TCNQ molecule per surface atom).

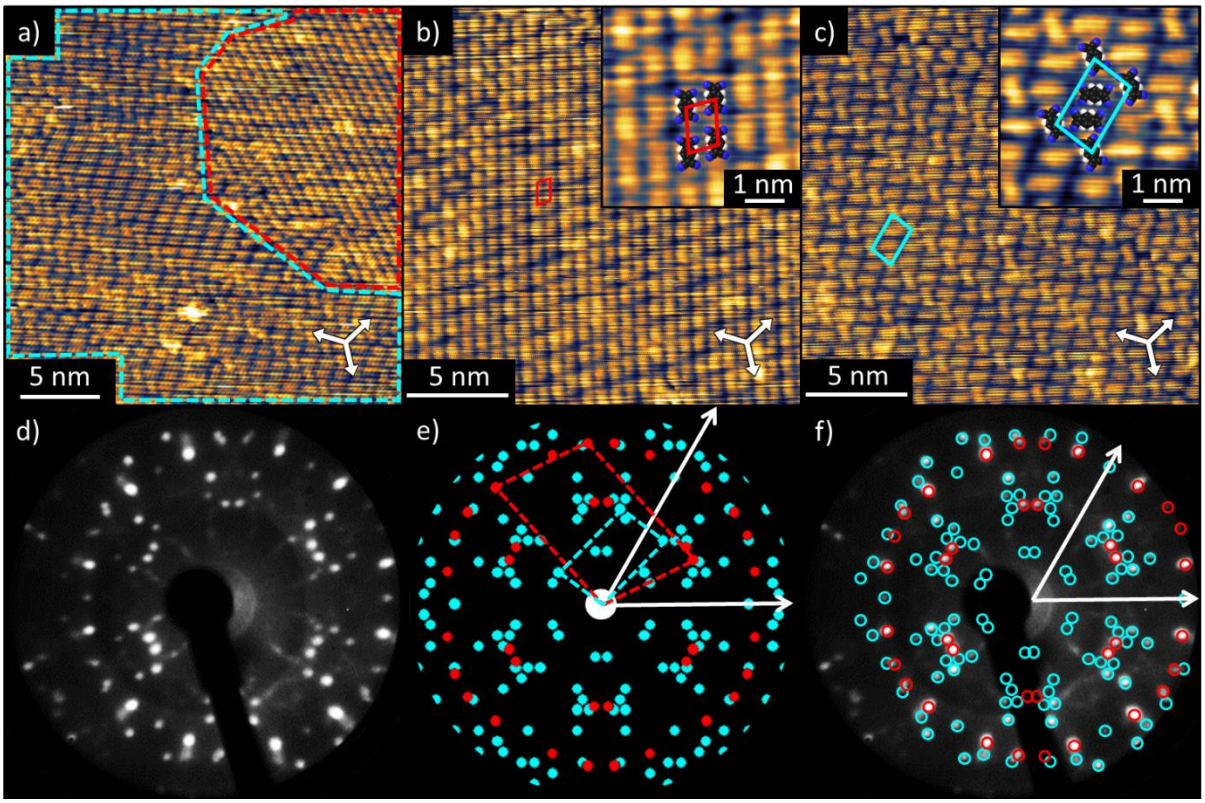

Figure 4.1.1 – STM and LEED from TCNQ deposited at ~1 ML on Ag(111). (a) STM image showing two coexisting phases with phase I outlined in red and phase II outlined in blue (V_{samp} = 0.25 V, I = 85 pA). (b) Selected area STM image of phase I with the unit mesh indicated by the red parallelogram (V_{samp} = 0.25 V, I = 85 pA). Inset: Expanded portion of the image with superimposed scaled models of TCNQ molecules. (c) Selected area STM image of phase II with the unit mesh indicated by a blue parallelogram (V_{samp} = 0.30 V, I = 65 pA,). Inset: Expanded portion of the image with superimposed scaled models of TCNQ molecules. In all of the STM images, the substrate <110> directions are indicated by the three white arrows. (d) Experimental LEED pattern recorded at an electron kinetic energy of 14.5 eV. (e) The combined simulated LEED patterns obtained from the STM measured unit mesh dimensions for phase I (red) and phase II (blue). The two parallelograms indicate the reciprocal unit meshes of a single domain from each phase and the white arrows represent two of the substrate <211> directions. (f) Experimental LEED pattern with an overlaid assignment of the beams corresponding to phase I (red) and phase II (blue). The white arrows represent two of the substrate <211> directions.

assembly (referred to here as phase I, shown in Figure 4.1.1b), which has been reported previously by Wackerlin *et al.*.[57] The STM measurements indicate that phase I is described by an incommensurate rhombic unit mesh containing a single TCNQ molecule with vector lengths b_1 = (11.2 ± 0.2) Å and b_2 = (7.3 ± 0.1) Å, an included angle γ = (106 ± 1)° and with vector $\mathbf{b_1}$ oriented at an angle θ = (48 ± 3)° relative to the substrate <110> directions. The second molecular assembly (referred to here as phase II, shown in Figure 4.1.1c) comprises rows of TCNQ 'windmill' units in which four molecules spiral around a central point. Phase II is described by a three-molecule unit mesh with dimensions, measured

by STM, of $b_1 = (20.4 \pm 0.7)$ Å, $b_2 = (12.3 \pm 0.3)$ Å, $\gamma = (97 \pm 2)°$ and $\theta = (24 \pm 2)°$, which are consistent with a commensurate $\begin{pmatrix} 2 & 5 \\ -8 & -2 \end{pmatrix}$ matrix of the substrate lattice vectors (b_1 = 20.8 Å, b_2 = 12.6 Å, γ = 97.3°, θ = 23.4°).

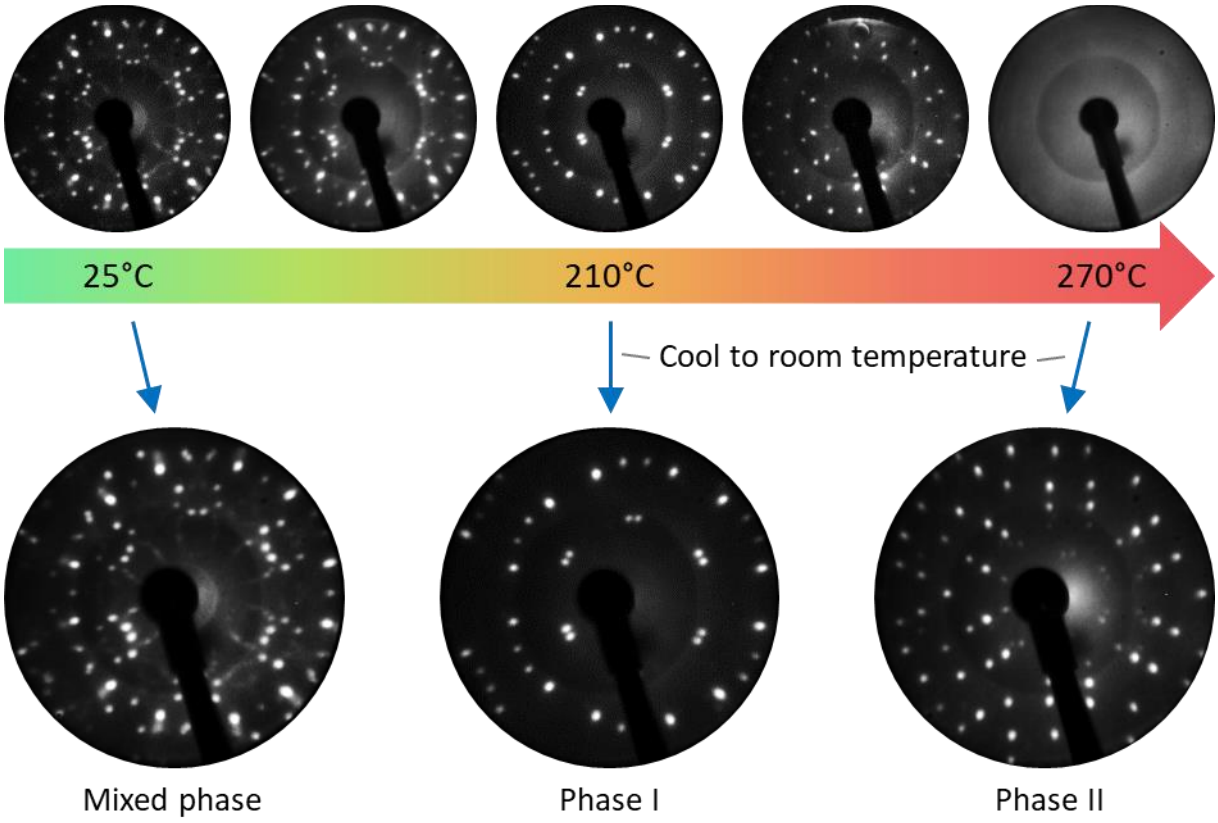

Figure 4.1.2 –LEED recorded from a sample of ~1 ML TCNQ on Ag(111) as it is heated. Top row: LEED patterns captured whilst heating the sample. Bottom row: LEED patterns captured at room temperature after heating the sample to the temperature indicated. All LEED patterns were recorded using an electron kinetic energy of 14.5 eV.

LEED captured from this mixed phase surface (Figure 4.1.1d) produces a complex diffraction pattern displaying multiple beams from the TCNQ overlayer along with some streaking. The experimental LEED pattern is closely reproduced by combining the simulated LEED patterns obtained from the STM measured unit meshes for phase I (red) and phase II (blue) (Figure 4.1.1e), which confirms the accuracy of the STM-measured unit mesh dimensions. Furthermore, since LEED probes the surface using an electron beam with a diameter approaching 1 mm (in contrast to the nm scale of STM images),[173] the good agreement between the experimental and simulated LEED patterns confirms that the two phases observed by STM are both prominent across macroscopic regions of the surface. The streaks in the experimental LEED pattern are characteristic of molecules adsorbing in well-defined orientations but

with varying intermolecular separations and are consistent with the disordered regions observed between the ordered molecular domains.

Annealing the mixed phase sample results in a series of phase changes on the surface, which were monitored in real-time by LEED (Figure 4.1.2). Initial heating of the sample causes the phase II diffraction pattern and the streaks to fade until, at a sample temperature of 210 °C, only a sharp and intense LEED pattern corresponding to phase I remains. Upon returning to room temperature (~25 °C, RT) from 210 °C, the phase I LEED pattern remains and does not revert to the initial mixed phase LEED pattern. This suggests that the change to the adsorption structure is irreversible with phase I now dominating on the surface. STM of the resulting surface (Figure 4.1.3) supports this, showing large ordered domains of the phase I assembly. The STM images also appear to show a completely saturated TCNQ monolayer, with no spaces observed between the ordered domains. The STM and LEED results therefore suggest that the TCNQ molecules initially adsorb in a metastable mixed phase but upon annealing, the TCNQ molecules become sufficiently mobile, enabling them to reorganise into the more favourable phase I adsorption structure.

Further annealing of the sample to temperatures beyond 210 °C results in the phase I LEED pattern fading and the phase II LEED pattern returning then fading again to leave no observable TCNQ diffraction beams at a sample temperature of 270 °C. Upon cooling from 270 °C to RT, a sharp LEED pattern that includes only the phase II diffraction beams returns. STM of the surface after annealing to 270 °C (Figure 4.1.4a), shows ordered, phase II domains, which are separated by regions that do not show any observable features that can be attributed to the TCNQ molecules. These regions were interpreted as either areas of bare substrate or highly mobile TCNQ molecules that cannot be resolved. In either case, this suggests that a TCNQ coverage of less than one monolayer is present on the surface, implying that a significant proportion of the TCNQ molecules have desorbed from the surface. This also suggests that the observed phase change is driven by the reduction in TCNQ coverage and that phase II is the more favourable packing regime at coverages below one monolayer. To test this conclusion, separate preparations at lower initial coverages were pursued. At submonolayer coverages, prepared without annealing the sample after TCNQ deposition, the surface also exhibited only phase II domains. This supports the conclusion that phase II is the favoured assembly at submonolayer coverages. A different TCNQ adsorption phase has also been reported previously on Ag(111), with STM showing that TCNQ forms molecular chains when deposited at coverages lower than those reported here.[167, 174] This suggests that there is a lower limit on the coverage at which phase II is the favourable molecular assembly. Heating the sample to temperatures in excess of 270 °C eventually

results in the irreversible loss of the TCNQ LEED pattern, which is consistent with the molecules desorbing from the surface.

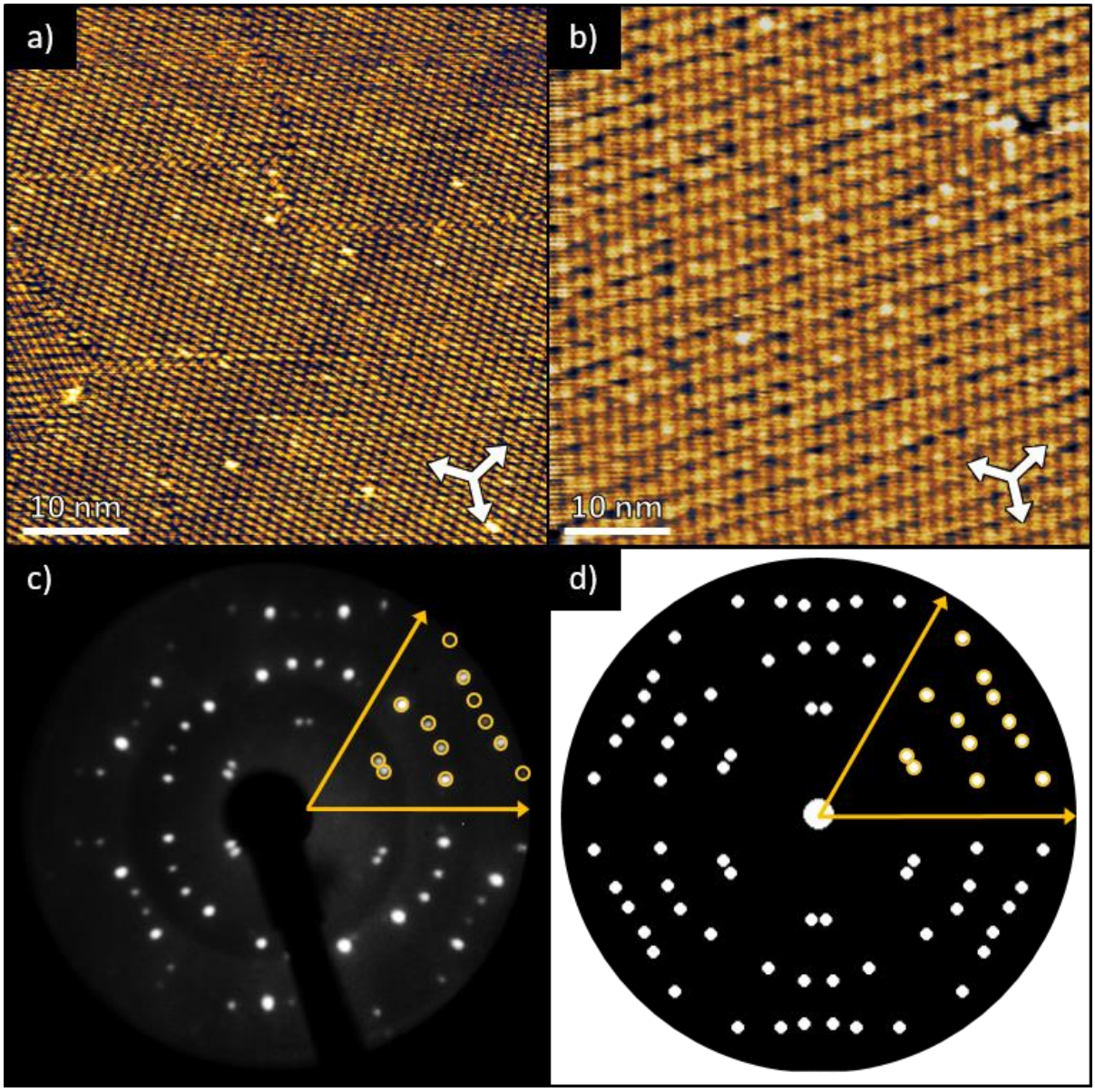

Figure 4.1.3 – STM and LEED of 1 ML TCNQ on Ag(111) annealed to 210 °C. (a) Representative STM image showing large ordered phase I domains (V_{samp} = 0.5 V, I = 65 pA). (b) Selected area STM image of a single domain (V_{samp} = -2.25 V, I = 75 pA). In both STM images, the white arrows indicate the substrate <110> directions. (c) Experimental LEED pattern captured using an electron kinetic energy of 24.5 eV. (d) Simulated LEED pattern derived from the STM measured unit mesh for phase I. In both the experimental and simulated LEED patterns, two of the substrate <211> directions are shown by the yellow arrows. To aid in the comparison of the two patterns, the diffraction beams are highlighted by yellow circles in one sector. Note that at the electron kinetic energy used, some diffraction beams are only faintly visible.

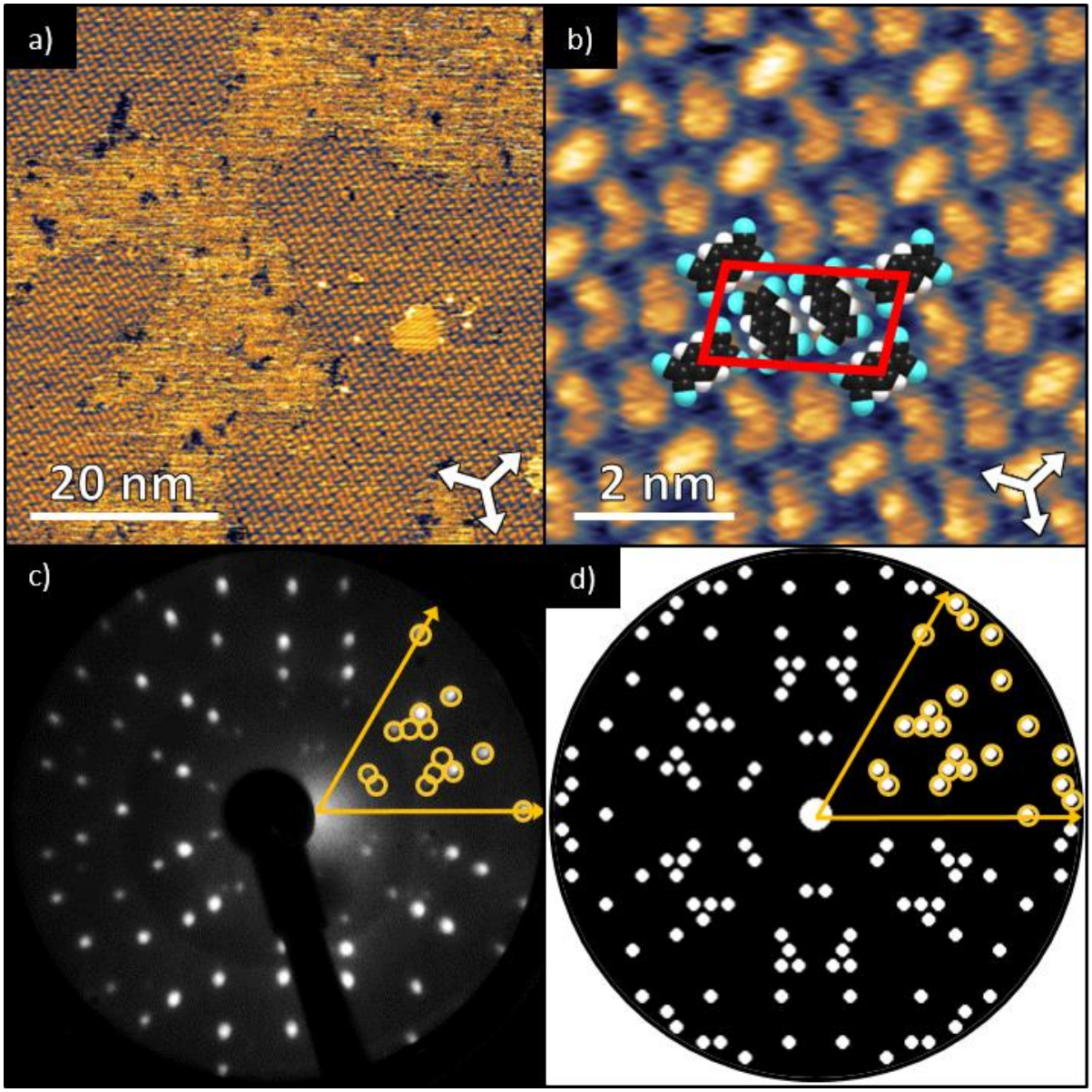

Figure 4.1.4 – STM and LEED obtained from submonolayer coverages of TCNQ on Ag(111) obtained by annealing ~1 ML to 270 °C. (a) STM overview showing three phase II domains (V_{samp} = -0.15 V, I = 100 pA). (b) Selected area STM image from a single phase II domain (V_{samp} = -1.0 V, I = 55 pA). In both STM images, the white arrows indicate the substrate <110> directions. (c) The experimental LEED pattern captured using an electron kinetic energy of 14.5 eV. (d) Simulated LEED pattern derived from a $\begin{pmatrix} 2 & 5 \\ -8 & -2 \end{pmatrix}$ commensurate matrix. In both the experimental and simulated LEED patterns, two of the substrate <211> directions are shown by the yellow arrows. To aid in the comparison of the two patterns, the diffraction beams are highlighted by yellow circles in one sector. Note that at the electron kinetic energy used, some diffraction beams are only faintly visible.

With the ability to form samples containing single adsorption phases via annealing, a more detailed analysis could be performed on the respective LEED patterns to assess the accuracy of the STM measured unit meshes and the commensurability of each phase. In Figure 4.1.3d, a simulated LEED pattern derived from the STM measured phase I unit mesh dimensions is shown. Since phase I does not share the three-fold rotational symmetry or the <211> mirror planes of the underlying substrate, there are six unique but equivalent domains. The simulated LEED pattern is in excellent agreement with the experimental LEED pattern (Figure 4.1.3c), thus confirming, by a technique not susceptible to instrumental drift or calibration errors, the accuracy of the STM-derived unit mesh. Moreover, this also confirms that phase I (for which the unit mesh can be described by a non-integer $\begin{pmatrix} 0.93 & 4.26 \\ -2.91 & -1.63 \end{pmatrix}$ matrix) is incommensurate with respect to the underlying substrate. Figure 4.1.4d shows the simulated LEED pattern corresponding to a $\begin{pmatrix} 2 & 5 \\ -8 & -2 \end{pmatrix}$ commensurate matrix, which is consistent with the STM measured phase II unit mesh dimensions. As this unit mesh also does not share the three-fold rotational symmetry or <211> mirror planes of the substrate, six distinct domains are observed for phase II. Comparing the simulated LEED pattern to the experimental LEED pattern shows excellent agreement (Figure 4.1.4c), which again confirms the accuracy of the STM measured unit mesh and indicates that phase II is commensurate with the underlying Ag(111) substrate.

4.2 XPS and UPS

Figure 4.2.1 shows high-resolution soft XPS recorded for the mixed TCNQ phase, with the binding energies of the main fitted components for these spectra, as well as for spectra recorded for the two single-phase samples, shown in Table 4.2.1. The C 1s spectrum clearly shows at least three distinct peaks, which were fitted with four components corresponding to the four chemically inequivalent C species in TCNQ (see the inset of the C 1s spectrum), with peak intensities constrained (± 5%) to their

expected stoichiometry. In previous reports, the C 1s spectrum has been used to infer the charge state of TCNQ, with the relative binding energies and overall line shape of the spectrum showing characteristic differences when TCNQ is negatively charged compared to when it is neutral.[57, 175] Based on this interpretation, the C 1s spectrum presented here is consistent with previous XPS measurements of negatively charged TCNQ, indicating that TCNQ accepts electrons from the Ag(111) substrate.[57] The value of the N 1s binding energy is also in good agreement with other systems in which TCNQ is believed to be negatively charged.[57, 175, 176] As there were no significant differences between the XPS

recorded for the various preparations of TCNQ on Ag(111), as can be seen from the binding energies in Table 4.2.1, it is suggested that TCNQ is negatively charged in both phase I and phase II.

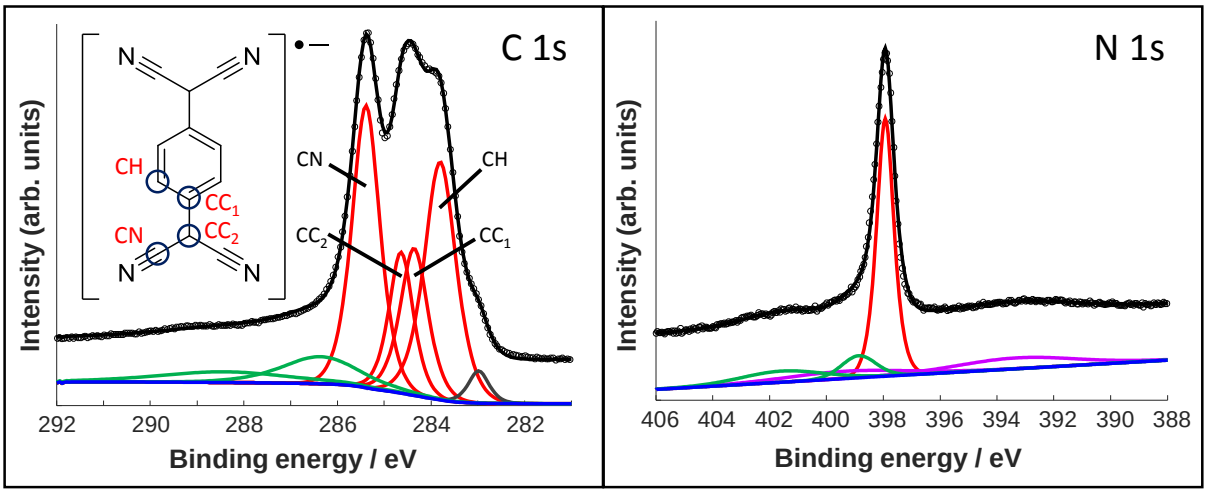

Figure 4.2.1 – High resolution soft XPS spectra obtained from the TCNQ on Ag(111) mixed adsorption phase. The C 1s spectrum was recorded using a photon energy of 435 eV, with measured intensity (black circles) and the sum of fitted components (black line) comprising a Shirley background (blue),[177] four main C 1s components (red), shakeup features (green) and, a beam damage feature (grey). The inset shows a schematic of the TCNQ molecule in a $TCNQ^-$ charge state, with the four chemically inequivalent carbon environments indicated. The N 1s spectrum was recorded using a photon energy of 550 eV, with measured intensity (black circles), and the sum of fitted components (black line) comprising a linear background (blue), one main N component (red), two N shakeup features (green) and two Ag 3d plasmon features (purple).

Table 4.2.1 – XPS measured binding energies of the main C 1s and N 1s peaks for three different preparations of TCNQ on Ag(111).

Component	Mixed phase / eV	Phase I / eV	Phase II / eV
CH	283.8	283.9	283.8
CC_1	284.4	284.4	284.3
CC_2	284.6	284.7	284.7
CN	285.4	285.4	285.4
N	397.9	398.0	398.0

The conclusion that TCNQ becomes negatively charged on the Ag(111) surface is also reinforced by UPS work function measurements, reported both here (Figure 4.2.2) and in a previous study,[57] that show an increase of 0.4 eV when TCNQ is deposited on clean Ag(111). This is consistent with TCNQ accepting electrons from the substrate as neutral molecules would be expected to decrease the work function via the 'push-back' effect.[11] Moreover, the UPS spectrum of TCNQ on Ag(111) (Figure 4.2.2) shows three peaks corresponding to TCNQ valence states, which is in excellent agreement with UPS reported previously for alkali intercalated TCNQ films in which the molecules become negatively

charged.[175, 176] Using the same assignment as Precht *et al.*[175, 176], the peak at 0.83 eV was attributed to the former TCNQ LUMO, which is shifted below the Fermi level and accepts electrons from the substrate; the peaks at 2.05 eV and 3.31 eV correspond to the original TCNQ HOMO and a lower energy occupied state respectively.

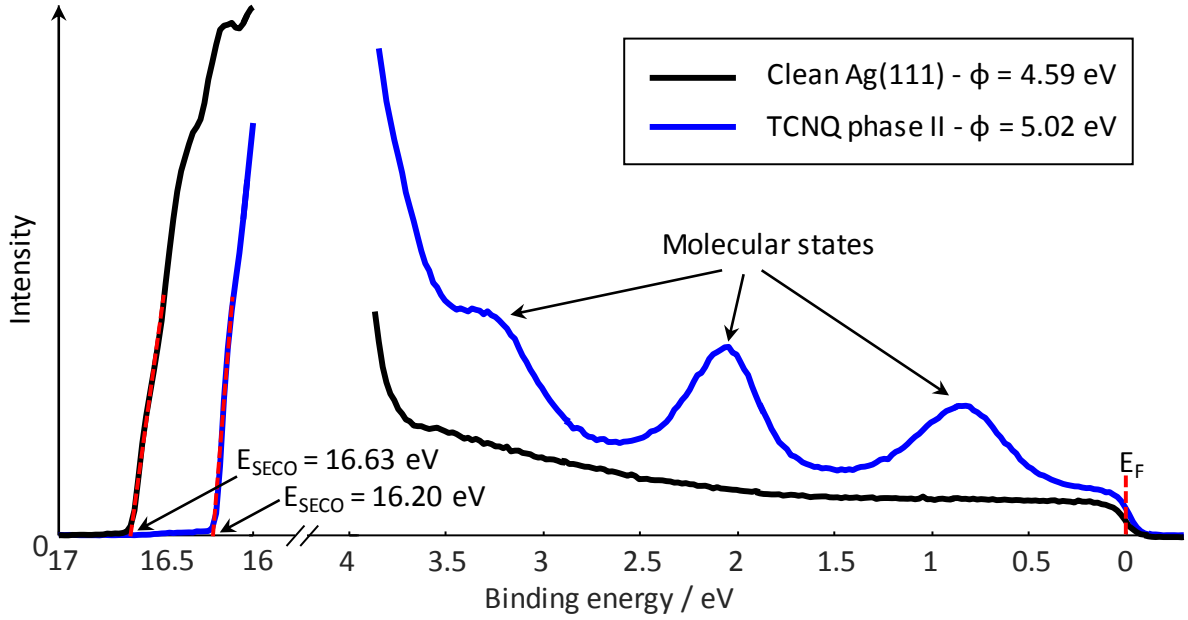

Figure 4.2.2 – UPS obtained from clean Ag(111) and the phase II TCNQ structure on Ag(111). The spectra were recorded using monochromated He-Iα emission (hv = 21.22 eV) with the sample held at a bias of -8.00 V to allow the SECO to be measured. The red dashed-lines indicate the fitting of the SECO and Fermi edge, which were used to determine the surface work functions.

The STM results suggest that the change from phase I to phase II, achieved by annealing the sample to 270 °C, is driven by a reduction in the TCNQ coverage. To further investigate this, C 1s XPS was recorded before and after the annealing steps used to prepare each of the TCNQ phases and the corresponding spectra are shown in Figure 4.2.3. After annealing to 210 °C, which results in a transition from a mixed adsorption phase to a surface of only phase I, the C 1s spectrum remains essentially identical to the 'as deposited' mixed phase sample. This indicates that the coverage does not change in this initial annealing step and that the phase change is a result of the molecules rearranging on the surface. This is consistent with the STM results, which appeared to show a saturated monolayer both before and after annealing to 210 °C. The C 1s spectrum recorded after annealing to 270 °C, which results in a transition to the phase II structure, shows a similar spectral shape but a significantly reduced intensity compared to the previous two samples. This indicates that the anneal to 270 °C causes a reduction in the TCNQ coverage, most likely caused by the molecules desorbing from the surface.

Comparison of the integrated intensity of the C 1s spectra indicates that this annealing step causes a ~20% reduction in the TCNQ coverage. This result is consistent with the STM results, which appear to show regions of either bare surface or high mobility after annealing to 270 °C. The XPS measurements thus support the conclusion that the transition from phase I to phase II is caused by a reduction in the TCNQ coverage.

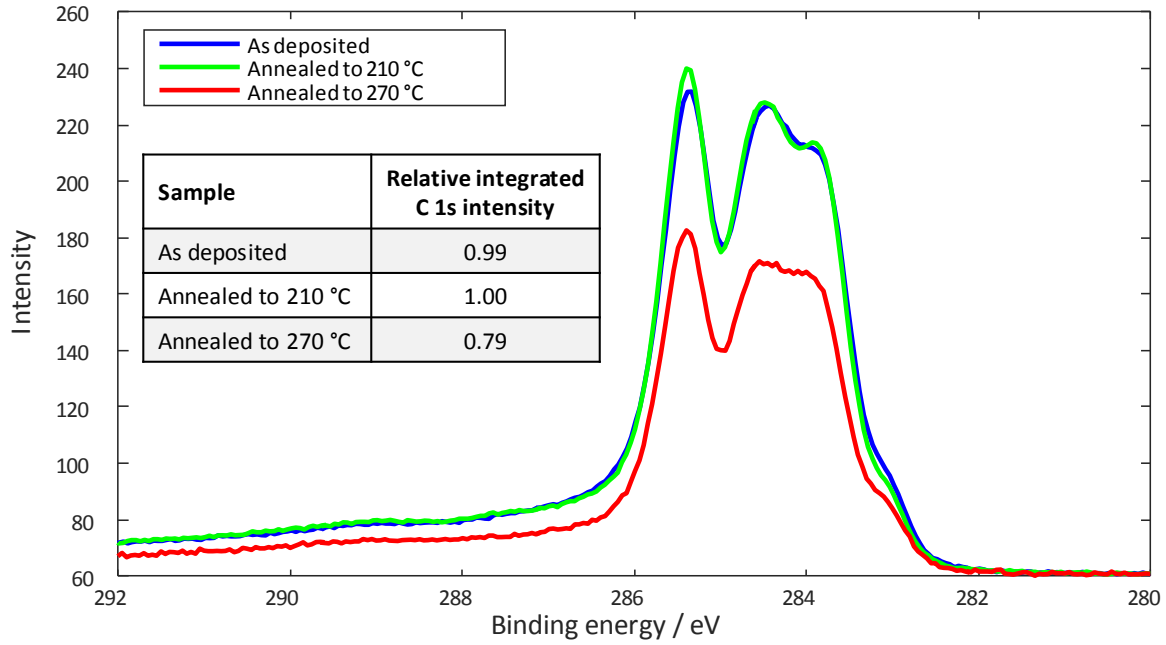

Sample	Relative integrated C 1s intensity
As deposited	0.99
Annealed to 210 °C	1.00
Annealed to 270 °C	0.79

Figure 4.2.3 – C 1s XPS recorded from a saturated monolayer of TCNQ on Ag(111) before and after the anneal steps used to prepare the different adsorption phases. Spectra were recorded at room temperature using a photon energy of 435 eV and are normalised relative to the background intensity measured on the high kinetic energy side of the spectrum. The inset table shows the relative integrated intensities of the C 1s spectra.

4.3 NIXSW and structural models

NIXSW measurements were recorded to obtain detailed quantitative structural information from the TCNQ Ag(111) adsorption phases. Specifically, NIXSW was performed using the (111) Bragg reflection of the Ag substrate to determine the adsorption height of the molecules relative to the surface, exploiting the chemical sensitivity of the NIXSW technique to resolve the differences in height between the constituent atoms of TCNQ and thus determine the molecular conformation. Figure 4.3.1 shows a sample set of C and N photoemission yield curves obtained from the respective 1s photoelectron spectra. Separate NIXSW profiles were obtained from the different C 1s photoemission components shown in Figure 4.2.1, though due to the lower energy resolution obtained when using the hard X-rays required for NIXSW, the CC_1 and CC_2 components could not be distinguished and were fitted as a single

component instead. Table 4.3.1 shows the coherent fractions (f_{co}) and coherent positions ($D_{(111)}$) measured for each of the TCNQ Ag(111) adsorption phases. As NIXSW only measures the atomic spacing relative to the nearest scattering plane, the $D_{(111)}$ values quoted include the addition of an Ag(111) bulk layer spacing ($d_{(111)} = 2.359$ Å) to give a physically reasonable adsorption height. Additionally, since the coherent position is measured relative to the projection of the bulk lattice planes, the effects of surface relaxations must be considered when determining the adsorption height from NIXSW. However, for the (111) surfaces of fcc metals, relaxations are generally negligible (e.g. < 0.02 Å)[178] and are often passivated by the presence of adsorbates,[179] so the measured $D_{(111)}$ values are considered as adsorption heights.

Table 4.3.1 – Coherent fractions (f_{co}) and coherent positions ($D_{(111)}$) obtained from the three preparations of TCNQ on Ag(111) using the (111) reflection of the substrate. Error values are shown in parentheses in units of 0.01. Separate fitting parameters were obtained for the different C 1s photoemission components as defined in Figure 4.2.1 (due to lower resolution at the photon energies required for NIXSW, components CC_1 and CC_2 were fitted together in a single component here). The coherent position $D_{(111)}$ is given as $D_{(111)} = (P+1)d_{111}$ where P is the fractional coherent position and d_{111} is the spacing of the (111) lattice planes (2.359 Å).

Component	f_{co}			$D_{(111)}$ / Å		
	Mixed phase	**Phase I**	**Phase II**	**Mixed phase**	**Phase I**	**Phase II**
CH	0.94(10)	1.04(10)	0.95(10)	2.85(5)	2.83(5)	2.86(5)
CC	0.97(10)	1.02(10)	0.99(10)	2.77(5)	2.77(5)	2.78(5)
CN	0.87(10)	0.94(10)	0.89(10)	2.71(5)	2.74(5)	2.76(5)
N	0.38(10)	0.41(10)	0.39(10)	2.57(5)	2.67(5)	2.75(5)

For all three adsorption phases, the NIXSW results are very similar, yielding high C coherent fractions (> 0.8), low N coherent fractions (~0.4) and a slight downward trend in the adsorption heights going from the central ring of the molecule to the peripheral nitrile groups. The high C coherent fractions suggest that the molecules occupy a single, well-defined height above the surface. However, the low N coherent fraction, which is lower than can be typically be attributed to thermal vibrations alone, indicates that the N atoms must occupy at least two distinctly different heights above the surface. The heights of the various C components differ by (0.14 ± 0.10) Å showing that the core of the molecule is not significantly bent. However, the fact that the N atoms must occupy two significantly different heights is consistent with the idea that the negatively-charged adsorbed TCNQ is flexible, and is no longer rigidly planar. One possible explanation of the low N coherent fraction is that some CN groups point up and others point down towards the surface. If equal numbers of CN groups pointed up and down, the N heights would need to differ by up to (0.86 ± 0.10) Å to reduce the coherent fraction to the measured value of (0.4 ± 0.1). In this scenario, a small reduction to the coherent fraction of the CN carbon atoms would also be expected. The NIXSW measurements are qualitatively consistent with this,

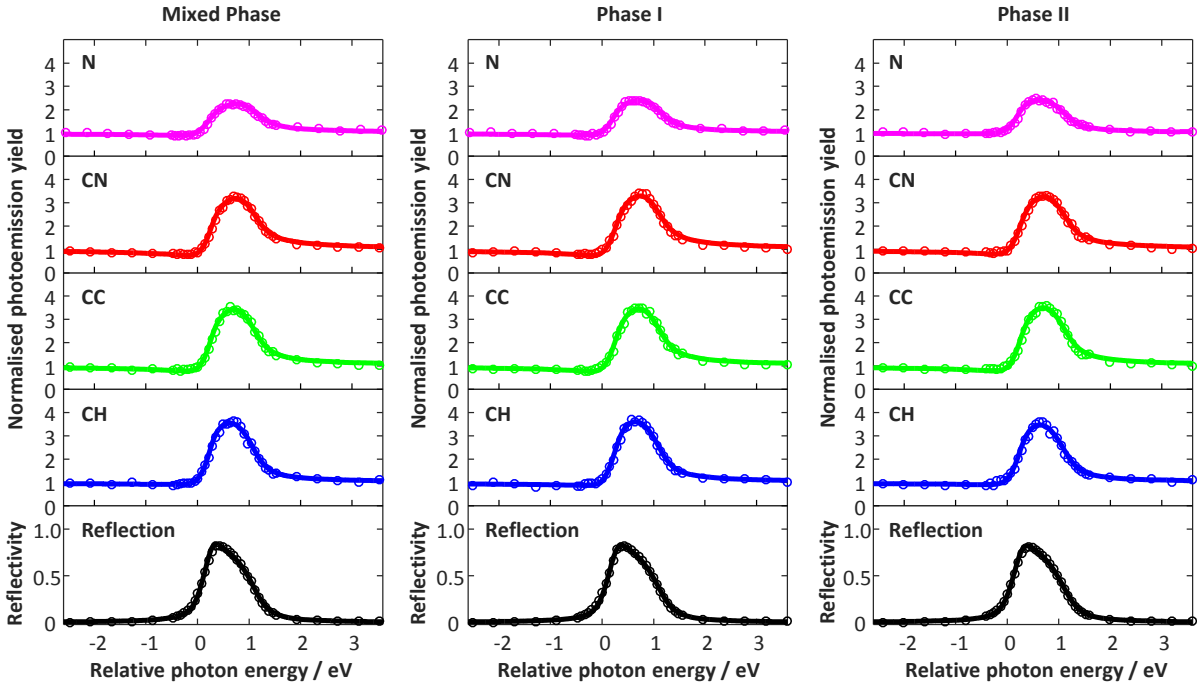

Figure 4.3.1 – Sample set of NIXSW photoemission yield curves obtained from the three different preparations of TCNQ on Ag(111) using the (111) reflection of the substrate. Photoemission yields were obtained from fitted peaks in the C 1s and N 1s XPS spectra, which also allowed the chemically inequivalent C species to be analysed separately (see Figure 4.2.1). Photon energies are quoted relative to the Bragg energy (2.630 keV). Least square fits (solid lines) to the photoemission yields (circles) were obtained to extract the coherent fractions and coherent positions.

showing a lower coherent fraction for CN than for both the CH and CC components. The N coherent position, which must represent a weighted average of the different contributing atomic heights, is the only value that varies significantly between the different adsorption phases, increasing as the sample is annealed. Rather surprisingly, the N coherent position for the mixed phase is not an intermediate value of the two single-phase adsorption structures. However, STM and LEED of the mixed phase did suggest the presence of disordered regions on the surface which may account for the lower coherent position measured for N.

The NIXSW results therefore suggest that TCNQ adsorbs on Ag(111) with the core of the molecule relatively parallel to the surface but with some of the peripheral CN groups pointing up and others pointing down. This result is difficult to rationalise with a pure TCNQ monolayer as the cyano groups would all be expected to point down to interact with the substrate. However, if the TCNQ adsorption layer included Ag adatoms obtained from the substrate, it could be possible that some cyano groups point up to bond to the adatoms, whilst other point down to bond to the surface. Although no obvious features that could be attributed to adatoms were visible in the STM images, in both the phase I and

phase II packing regimes on Ag(111) the molecules arrange with negatively charged cyano groups in close proximity, which would be expected to create unfavourable electrostatic repulsions. Similar, seemingly unfavourable, assemblies have also been observed on Cu(111) and Cu(100), with the results of DFT calculations suggesting that the substrate atoms are lifted out of the surface plane by ~0.3 Å, generating a stress field that overcomes these electrostatic repulsions.[17, 164, 165] However, in contrast to the NIXSW measurements for the present system, these stress field models suggest that the TCNQ molecules adsorb in a considerably bent conformation. If Ag adatoms were incorporated into the molecular assembly, they could potentially act as counterions to the negatively charged TCNQ molecules.

The presence of substrate adatoms in structures formed by TCNQ and similar molecules on metal surfaces has also been suggested based on the interpretation of STM images. Within the ordered structures formed by F4-TCNQ on the Au(111) surface, STM images show bright protrusions between molecules which are interpreted to be Au adatoms.[54] It has also been previously suggested, based on similar STM evidence, that Ag adatoms may be present in the phase I structure formed by TCNQ on Ag(111).[57, 167] Furthermore, step-edge etching has been reported in low temperature STM images of F4-TCNQ on Cu(100)[180] and for TCNE on Ag(111),[60] which implies that substrate adatoms are abstracted from the substrate and are incorporated into the molecular networks. Additionally, there are numerous examples of adsorption structures formed between TCNQ and codeposited metal atoms (such as Mn, Fe and Ni),[54, 58, 59, 164, 170] showing similar structures to those observed here. In one particular example Shi *et al.*[171] report DFT simulations of Mn-TCNQ networks formed on Cu(100), in which the N atoms occupy two distinctly different heights above the surface, differing by 0.90 Å, with N atoms bonded to the substrate occupying a lower adsorption height than those bonded to the Mn adatoms. This system, albeit with different metal adatoms, displays structural features that match those identified here by NIXSW for TCNQ on Ag(111). The results from the literature therefore suggest that the inclusion of adatoms in the TCNQ adsorption phases on Ag(111) is not only plausible but could result in a TCNQ adsorption conformation that is consistent with the measured NIXSW results.

To further investigate the possibility of Ag adatoms being incorporated into the TCNQ adsorption phases on Ag(111), DFT calculations (performed by Simone Velari, as detailed in section 2.8) were employed to generate structural models that could be compared with the NIXSW results. Due to the constraint of periodic boundary conditions, DFT calculations were only accessible to the commensurate phase II adsorption structure. Within phase II, three possible adatom sites were identified, referred to here as the α site and the two symmetrically equivalent β sites (as shown in Figure 4.3.2). Optimised structures were then calculated for all possible occupancies of these sites and the resulting models were

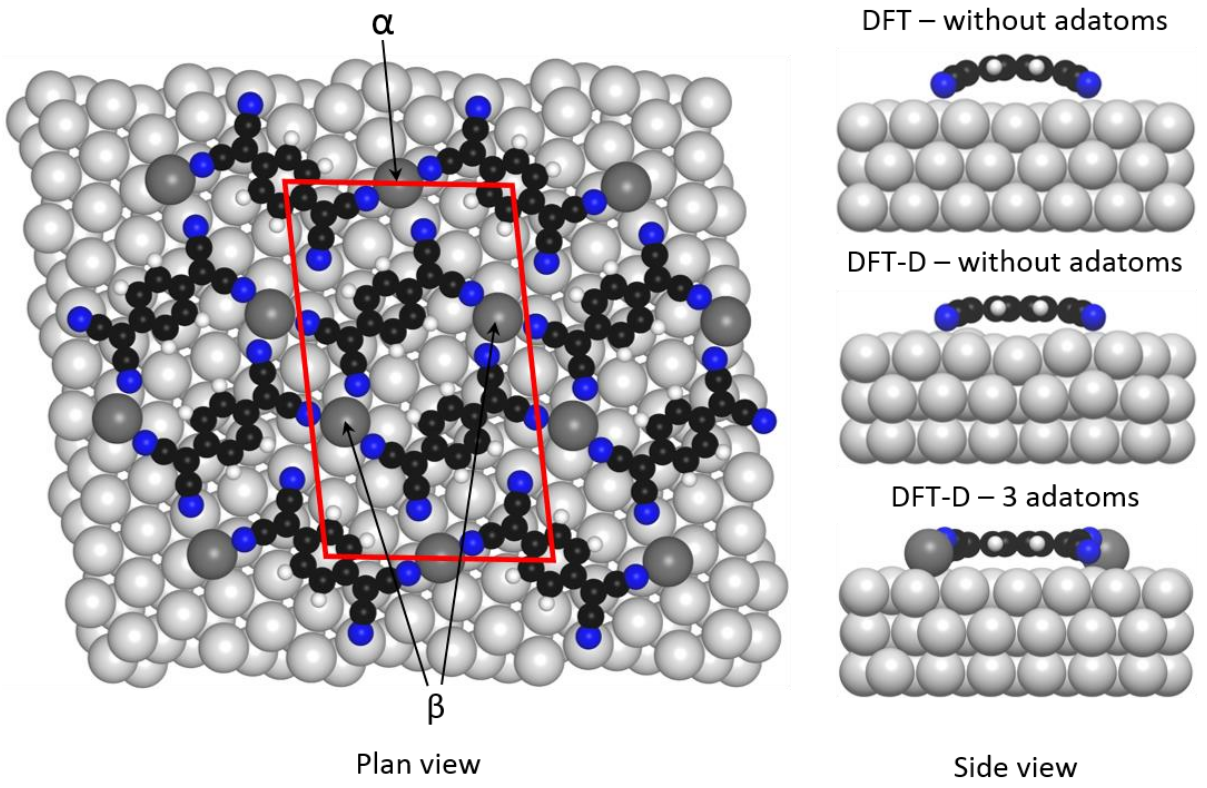

Figure 4.3.2 – DFT models calculated for the phase II structure of TCNQ on Ag(111). Left: Plan view of the DFT-D optimised model of phase II with three Ag adatoms included per unit mesh (shown by the red parallelogram). This model includes two different types of Ag adatom sites, which are labelled α and β. Alternative models, with 1, 2 or all 3 adatoms removed from the structure shown were also explored. Right: Side views of a single TCNQ molecule within the DFT and DFT-D optimised models without adatoms and the DFT-D optimised model with all three adatom sites occupied. Ag atoms are coloured grey, with adatoms shaded darker than the substrate atoms, C atoms are coloured black, N atoms are coloured blue and H atoms are coloured white. Visualisations were produced using the open-access software package VESTA.[181]

then calculated for all possible occupancies of these sites and the resulting models were compared to the experimental NIXSW results. One key factor for modelling the adsorption structure of organic molecules on metal surfaces is the consideration of dispersion interactions, which are not accounted for in standard DFT functionals. A variety of dispersion corrections are available for DFT codes; however, their performance is highly system-dependent and, consequently, it is difficult to determine which correction is most appropriate to use. Because of this, DFT calculations were performed using two different dispersion corrections, as well as without dispersion corrections. The structures calculated using these dispersion corrections were compared to the NIXSW measurements to identify the functional that best reproduces the experimentally measured adsorption heights. For this system, the DFT-D correction proposed by Grimme[27] closely reproduces the experimental adsorption heights, with

dispersionless DFT calculations yielding adsorption heights that were ~0.5 Å too large and the vdW-DF method of Dion *et al.*[29] yielding even larger adsorption heights, ~0.2 Å above those predicted without dispersion corrections (results of the vdW-DF and pure DFT calculations are shown in Appendix C). This result clearly indicates the impact that dispersion interactions can have on the molecular adsorption structure and the highlights importance of having an experimental reference to determine the dispersion correction that best describes the system.

Table 4.3.2 – Expected NIXSW fitting parameters obtained from the atomic coordinates of the DFT-D models. The experimental NIXSW results for the phase II TCNQ Ag(111) sample are shown in the top row for comparison. Adatom models are listed in the left-hand column stating the number of adatoms and the sites occupied. For the DFT-D models, the $D_{(111)}$ values are taken relative to the average height of the outermost Ag layer. Expected NIXSW fitting parameters from a weighted model derived from a Boltzmann distributed occupancy of the calculated models at 300 K is shown at the bottom.

	f_{co}				$D_{(111)}$ / Å			
	CH	CC	CN	N	CH	CC	CN	N
Experiment	0.95(10)	0.99(10)	0.89(10)	0.39(10)	2.86(5)	2.78(5)	2.76(5)	2.75(5)
DFT-D								
Model								
0	0.98	0.98	1.00	0.99	2.82	2.79	2.60	2.38
1 α	0.99	0.99	0.93	0.77	2.80	2.79	2.67	2.48
1 β	0.98	0.99	0.91	0.69	2.80	2.80	2.67	2.44
2 αβ	0.99	0.99	0.87	0.56	2.78	2.79	2.75	2.64
2 ββ	0.95	0.98	0.90	0.57	2.75	2.78	2.77	2.70
3	0.98	0.99	0.92	0.66	2.74	2.78	2.84	2.88
Weighted average at 300 K	0.99	0.99	0.88	0.60	2.78	2.79	2.73	2.59

To compare the DFT-D calculations with the experimental data, expected NIXSW fitting parameters were obtained from the atomic coordinates of the structural models (shown in Table 4.3.2). In the absence of adatoms, the DFT-D calculations predict that the molecule bends down towards the surface with the cyano C atoms 0.22 Å below those in the central ring and the N atoms an additional 0.22 Å below that. This degree of bending is significantly less than observed in previous DFT calculations of TCNQ on coinage metal surfaces that do not account for dispersion interactions[17, 128, 164] and indeed the dispersionless calculations performed without adatoms presented here (both DFT and DFT-D models are shown in Figure 4.3.2) also show an exaggerated bend of 0.58 Å. Without adatoms, the DFT-D calculations also predict that all the CN groups point down towards the surface, with the N atoms essentially coplanar with each other, yielding a very high coherent fraction, in clear contrast to the experimental results. Models containing adatoms give much better agreement with the experimental results, showing a flattening of the molecular backbone and distinctly different N heights, caused by

the cyano groups either pointing up towards nearby Ag adatoms or pointing down towards substrate when no adatoms are nearby. This reduces the N coherent fraction and better reflects the experimental results. In addition to the changes in molecular conformation, the inclusion of adatoms in the adsorption structure also has a pronounced effect on the structure of the outermost substrate layer in the DFT-D models. In the absence of adatoms, the top Ag layer is predicted to buckle significantly, with atoms spanning a vertical range of 0.62 Å, showing similarity to the DFT structures calculated for TCNQ on other coinage metal surfaces.[17, 164, 165] With the addition of an increasing number of adatoms into the adsorption structure, the buckling is reduced significantly, with the top Ag layer spanning only a 0.25 Å range for the model with three adatoms per unit mesh (see Figure 4.3.2).

The relative energies of the DFT-D models (included in Table 4.3.3, calculated using the bulk cohesive energy per atom as the reference level for adatom formation)[182] also suggest that the inclusion of Ag adatoms in the adsorption layer is favourable. In particular, the 1 adatom α site model and 2 adatom model, with the α site and β site occupied, stand out as the lowest energy models. However, because the energy differences between some models are only a few tens of meV it is expected that several of the models would coexist at RT. It is therefore more appropriate to compare the experimental results with a distribution of the various adatom occupancies for the TCNQ adsorption phase rather than to a single model. To achieve this, the relative occupancy of each model was estimated using a Boltzmann distribution of the relative adsorption energies (shown in Table 4.3.3, see Appendix B). This analysis reveals that the two lowest energy models are dominant and corresponds to an estimated overall 58% average occupancy of the available adatom sites at 300 K.

Table 4.3.3 – Estimated occupancy of the DFT-D calculated structures at 300 K obtained using the relative adsorption energies of each model to calculate a Boltzmann distribution. The degeneracy gives the number of unique but symmetrically equivalent adatom configurations possible for each model.

Model	Relative energy / eV	Degeneracy	Occupancy / %
0	-0.004	1	0.45
1 α	-0.105	1	22.26
1 β	-0.050	2	5.22
2 αβ	-0.116	2	67.87
2 ββ	0.000	1	0.38
3	-0.059	1	3.81

Using these relative occupancies, NIXSW parameter values (shown in Table 4.3.2) were obtained for an appropriately weighted average of the DFT-D models, which shows good overall agreement with

the experimental results. Discrepancies between the predicted and measured $D_{(111)}$ values are mostly less than 0.1 Å and although the predicted N f_{co} is considerably higher than the experimentally measured value, the predicted value does not include the effects of vibrational disorder which can typically reduce the coherent fraction by up to 20%.[21, 98]

In summary, the experimental NIXSW results show that in phase II the TCNQ molecules do not adsorb in a bent geometry on Ag(111) but instead the core of the molecule remains relatively flat with the peripheral cyano groups pointing either up or down, generating a distribution of N heights. Upon comparison with DFT-D models, it was found that these structural features are best reconciled by an adsorption structure that includes Ag adatoms. Similar structural features are shown by the NIXSW for phase I and the mixed phase, which could suggest that Ag adatoms are also involved in these adsorption structures. Coincidentally, STM images reported by Wackerlin *et al.*[57] of the phase I structure show small protrusions and depressions between the molecules that were tentatively assigned to Ag adatoms and vacancies respectively. The distribution of these features appeared to be dynamic at room temperature, with some of the protrusions and vacancies changing sites between consecutively recorded STM images of the same sample area, with the protrusions retaining an overall 71 % occupancy of the available sites.[57] If these features do indeed correspond to Ag adatoms, these observations suggest a similar adatom occupancy to that estimated by DFT-D and NIXSW for phase II. If the TCNQ cyano groups behave similarly to phase II, (i.e. pointing up to bond to nearby adatoms and down towards the substrate in the absence of adatoms) this 71% occupancy would be consistent with the NIXSW results.

One additional issue to address is that despite the NIXSW and DFT showing clear evidence for adatom involvement in the phase II structure, the STM did not show any evidence of features that could be attributed to the location of Ag adatoms. Figure 4.3.3 shows comparisons of simulated STM images, obtained using the Tersoff-Hamann approach[132] for the no-adatom (a) and 3-adatom (c) DFT-D models (simulations performed by Simone Velari) compared with the experimental image (b) shown on the same scale. Whilst the simulations from the two models are rather different in detail, there are no visible features attributable to the Ag adatom locations. Figure 4.3.3(d) further illustrates this, showing the simulated STM image for the 3-adatom model with the structural model overlaid to highlight the locations of the Ag adatoms. One other point of note is that the experimental STM images contain a significant amount of noise that could potentially mask details corresponding to Ag adatoms. To further investigate this, a unit mesh average of the experimental image was obtained (Figure 4.3.3e) to reduce the noise of the experimental image and despite this, only features attributable to the TCNQ molecule were visible. This analysis therefore shows that features corresponding to Ag adatoms were not present in the STM images for phase II but also that this is nonetheless consistent with adatoms being present

in the adsorbed TCNQ layer. This phenomenon of adatoms being invisible by STM has been reported previously for other similar systems and thus its occurrence for TCNQ on Ag(111) is unsurprising.[183, 184]

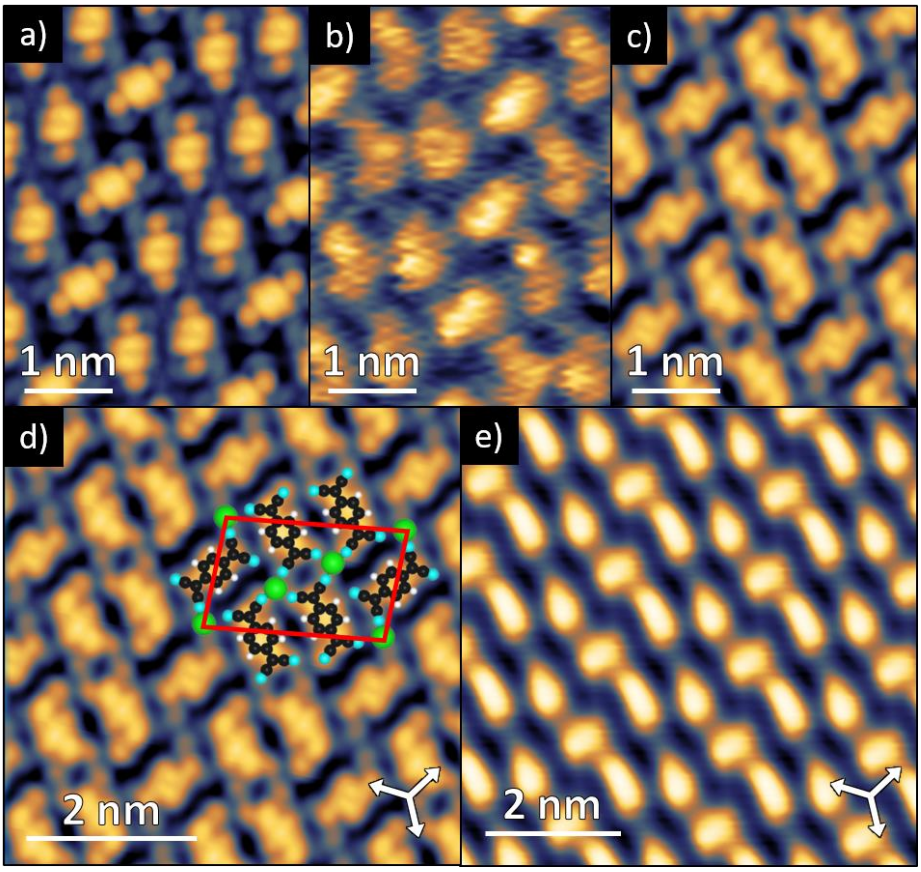

Figure 4.3.3 – Comparison of the experimental STM with the DFT-D models. (a) and (c) show Tersoff-Hamann[132] simulated STM images from the no-adatom and 3-adatom DFT-D models. which are compared alongside a similar area experimental image (b). (d) shows the simulated STM image for the 3-adatom DFT-D model with the structural model overlaid. (e) shows a unit-mesh-averaged experimental image, produced using the WSxM software package.[185]

4.4 General discussion and conclusions

STM and LEED showed that TCNQ forms two distinctly different ordered phases on the Ag(111) surface that are initially present as a mixture when deposited at a saturated monolayer, with each phase able to be isolated by heating the sample to different temperatures. Using XPS to estimate the coverages of the annealed samples and by depositing TCNQ at lower coverages, it was found that the incommensurate phase I head-to-tail structure is favoured at a saturated monolayer coverage, whereas the commensurate phase II windmill assembly is favoured at submonolayer coverages. XPS and UPS of the adsorption phases revealed that TCNQ becomes negatively charged on Ag(111), increasing the

surface work function by 0.4 eV. NIXSW measurements show that in the mixed adsorption phase and in both isolated adsorption structures, TCNQ adopts a relatively flat geometry, although low coherent fractions were measured for the N atoms, clearly indicating that the N atoms occupy two or more distinctly different heights above the surface. Comparing with DFT-D optimised models of the phase II adsorption structure (performed in collaboration with this work by Simone Velari, as detailed in section 2.8.8), it was found that the structural features identified by NIXSW are best reconciled by the participation of Ag adatoms in the phase II TCNQ assembly. Since NIXSW for all measured phases yielded similar results, it was concluded that Ag adatoms are also present in the mixed phase and phase I structures.

It has been previously suggested (but not definitively proven) based on STM evidence that substrate adatoms could be involved in the phase I structure formed by TCNQ on Ag(111)[57, 167] as well as for TCNQ[129] and F4-TCNQ[54] on Au(111). The results here clearly demonstrate that substrate adatoms are incorporated into the TCNQ layer on Ag(111). As TCNQ accepts electrons from the substrate, it becomes negatively charged and therefore, with its associated image charge, forms strong dipoles that are expected to create unfavourable repulsion interactions. The presence of positively charged Ag adatoms could provide a way to stabilise the observed TCNQ assemblies by acting as counterions in a similar fashion to the structures reported when transition metal[58, 59, 164, 170, 171] or alkali metal[57, 59, 172] atoms are co-deposited with TCNQ.

The results presented in this chapter, contrast considerably with essentially all published adsorption structures for TCNQ and its fluorinated analogue F4-TCNQ on coinage metal surfaces, which suggest that the molecule adsorbs in a considerably bent conformation with all four cyano groups pointing down towards the substrate.[17, 128, 164, 165] These studies typically consist of using DFT calculations to optimise the geometry of a structural model interpreted from STM image contrast[128, 129, 164, 165] and, in some cases, Tersoff-Hamann[132] simulations are used to judge the agreement between the calculated structures and the experimental STM images.[54, 61] For the present system, quantitative experimental structural measurements, obtained using the NIXSW technique, were instrumental in determining the correct adsorption structure and highlight some potential pitfalls of relying only on STM and DFT.[17, 128, 164, 165] Due to the nature of STM, which maps information on the surface electronic structure, there is no reliable one-to-one correspondence of image protrusions with surface atoms, which could lead to incorrectly interpreted adsorption structures. For example, the STM shown in this chapter did not display any features to indicate the presence of Ag adatoms within the structure and consequently it would not have been obvious from this evidence alone that adatoms should be included in subsequent DFT calculations. It is therefore conceivable that this aspect of the adsorption structure could easily

have been missed without the accompanying experimental structural measurements. One additional factor was that the NIXSW measurements were used to identify the dispersion correction that best replicates the measured substrate-molecule spacing. The significant impact of these dispersion corrections on the predicted adsorption structure were highlighted by the calculations for TCNQ on Ag(111), with the molecular adsorption height varying by up to 0.7 Å depending on the dispersion correction that was used. Whilst a considerable research effort has been undertaken to develop corrections to give an accurate description of vdW forces within adsorption structures[27] it can be difficult to determine *a priori* which correction is most appropriate to use for a given system. Measuring quantitative structural information thus provides a useful way to identify the optimal dispersion correction and calculate more reliable structures.

For the adsorption of TCNQ on coinage metal surfaces, the possible inclusion of substrate adatoms has been previously unexplored by DFT and most of the calculations in the current literature also do not include dispersion corrections. [17, 128, 164, 165] For note, the DFT-D calculations presented here that did not include adatoms predicted a bent conformation for TCNQ on Ag(111), similar to the previously calculated structures on other coinage metal surfaces. [17, 128, 164, 165] Moreover, this molecular bend was further exaggerated when the dispersion correction was not applied. It may therefore be possible that adatoms are present in the adsorption layers reported for TCNQ on other coinage metal surfaces. As molecule-substrate interactions are typically stronger on Cu surfaces than on Ag or Au, it would be reasonable to expect that adatoms could also be present in the previously studied systems of TCNQ on Cu(100)[17] and also TCNQ[164, 165] or F4-TCNQ on Cu(111).[169] A NIXSW investigation of the latter system has been published although the reported coherent fractions (0.43, 0.28, 0.15 for F, N and C respectively) are so low that attributing the corresponding coherent positions of the F and N atoms to single heights, as this paper reports,[169] is certainly questionable. The lack of information given regarding the surface ordering or coverage of the sample studied makes it difficult to identify possible causes of these low coherent fractions. For TCNQ on Cu(100), the bent conformation obtained from DFT calculations was also qualitatively supported by NEXAFS measurements which indicate that the C-N bonds are tilted by ~10° from the surface parallel. However, the NEXAFS measurements cannot distinguish between the CN groups tilting towards or away from the surface and thus would also be reasonably consistent with the conformation measured in this chapter (~11° pointing down to the surface and ~7° pointing up out of the surface). Consequently, these systems require a more thorough investigation.

5. Coadsorption of TCNQ with alkali metals on Ag(111)

In this chapter, an experimental characterisation of charge transfer networks formed between TCNQ and alkali metals on the Ag(111) surface, is presented. The primary aim of this work was to use experimental techniques to investigate the predictions of DFT calculations reported for similar TCNQ/alkali metal networks on Ag(100), which suggest that varying the alkali metal has a significant impact on the electronic and structural properties of the surface and could provide a useful way to tune the surface work function.[168] To achieve this, STM and LEED were used to identify the range of ordered adsorption phases accessible to TCNQ codeposited with each alkali metal. XPS and UPS were then combined with precise quantitative structural measurements obtained with the NIXSW technique to probe the electronic and structural properties of the interface.

5.1 Coadsorption of TCNQ and K on Ag(111)

5.1.1 STM and LEED

K/TCNQ networks were prepared by sequentially depositing K onto a sample of the phase II TCNQ adsorption structure characterised in chapter 4. After each K deposition, the sample was annealed to 200 °C to promote the formation of large ordered domains on the surface. Figure 5.1.1 shows the progression of the surface structure monitored by LEED as the K deposition time was increased. Initial deposition of K begins to produce a new set of diffraction beams alongside the pure TCNQ pattern up until six minutes of K deposition, when the pure TCNQ beams fade completely and only the new K/TCNQ LEED pattern remains. Further deposition of K causes this K/TCNQ pattern to fade while a different set of diffraction beams appears, which then becomes dominant on the surface after sixteen minutes of K deposition. The LEED therefore suggests that the TCNQ adsorption structure changes upon deposition of K, with at least two possible adsorption phases forming at different K coverages.

Figure 5.1.2 shows STM and LEED obtained from the K/TCNQ adsorption phase formed at low K exposure (corresponding to the LEED pattern shown from six minutes of K deposition in Figure 5.1.1). STM of this phase (Figure 5.1.2a) shows large ordered domains of rounded oblong protrusions, interpreted as TCNQ molecules, packed into a windmill assembly. STM images taken at large negative biases (i.e. -1.5 V, Figure 5.1.2b) show bright circular protrusions at the centres of these TCNQ windmills, which were interpreted as the locations of K atoms. The resulting structure suggests a nominal 1:1 stoichiometry with each TCNQ cyano group bonding to a different K atom to form an interlinked network. This type of arrangement is common for TCNQ coadsorbed on surfaces with metal

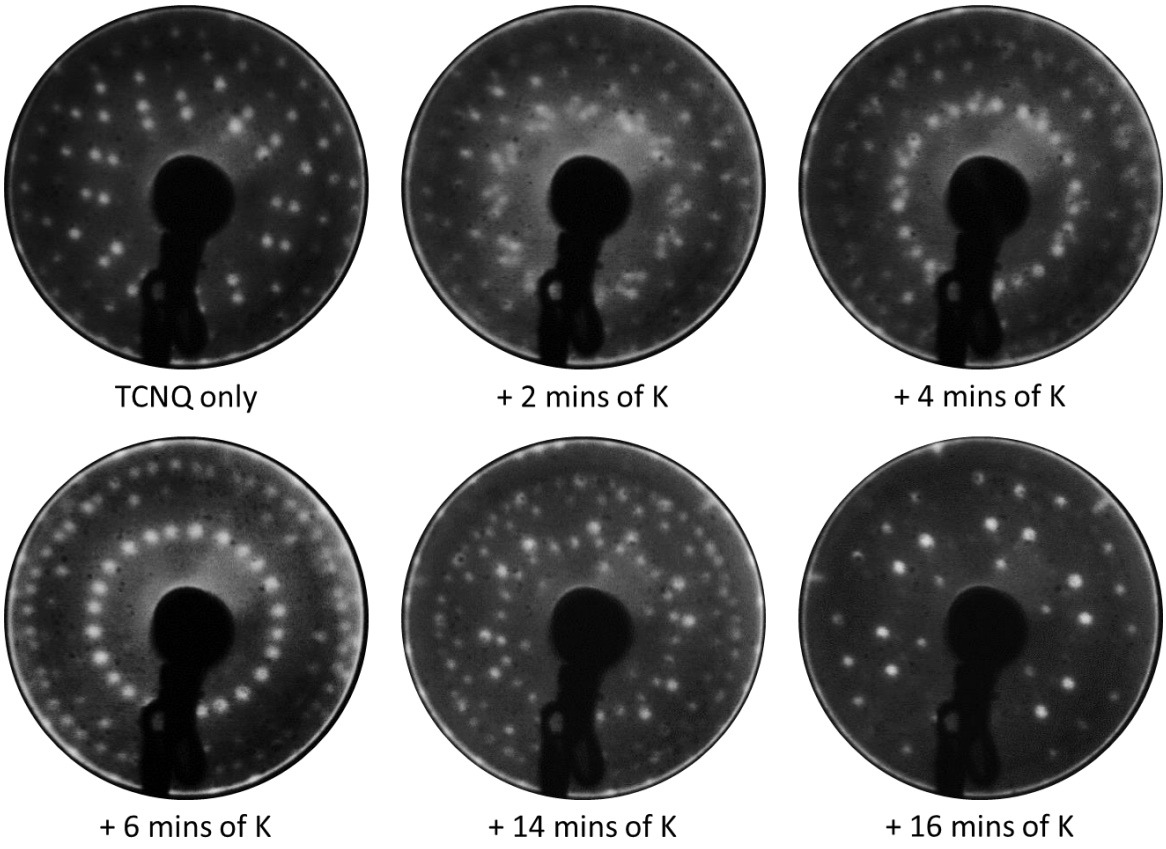

Figure 5.1.1 – LEED patterns of TCNQ on Ag(111) recorded after sequential depositions of K. Each pattern was recorded after annealing the sample to 200 °C with an electron kinetic energy of 14.5 eV.

atoms[57-59, 164, 172] and also bears a strong resemblance to the structure of bulk crystalline KTCNQ, in which layers of TCNQ molecules arrange in layers of similar windmill structures that lie between layers of K^+ ions.[186] The surface unit mesh contains two TCNQ molecules and two K atoms, and has dimensions, averaged from measurements obtained from thirteen different STM images, of $b_1 = (13.0 \pm 0.4)$ Å and $b_2 = (13.7 \pm 0.4)$ Å with an included angle of $(92 \pm 2)°$ and the vector $\mathbf{b_1}$ oriented at $(9 \pm 2)°$ to the substrate <110> directions. Figure 5.1.2e shows a simulated LEED pattern derived from a unit mesh described by a $\begin{pmatrix} 4.28 & 4.93 \\ -3.22 & 2.09 \end{pmatrix}$ matrix of the substrate lattice vectors, which is consistent with the STM measured unit mesh and shows excellent agreement with the experimental LEED pattern. This confirms the accuracy of the STM-derived unit mesh and, as the matrix elements are non-integer, indicates that the adsorption structure is incommensurate with respect to the Ag(111) substrate. As the overlayer mesh does not share the three-fold rotational and <211> mirror symmetries of the substrate, there are six symmetrically equivalent domains of the overlayer, the beams of which are coloured differently in the simulated LEED pattern.

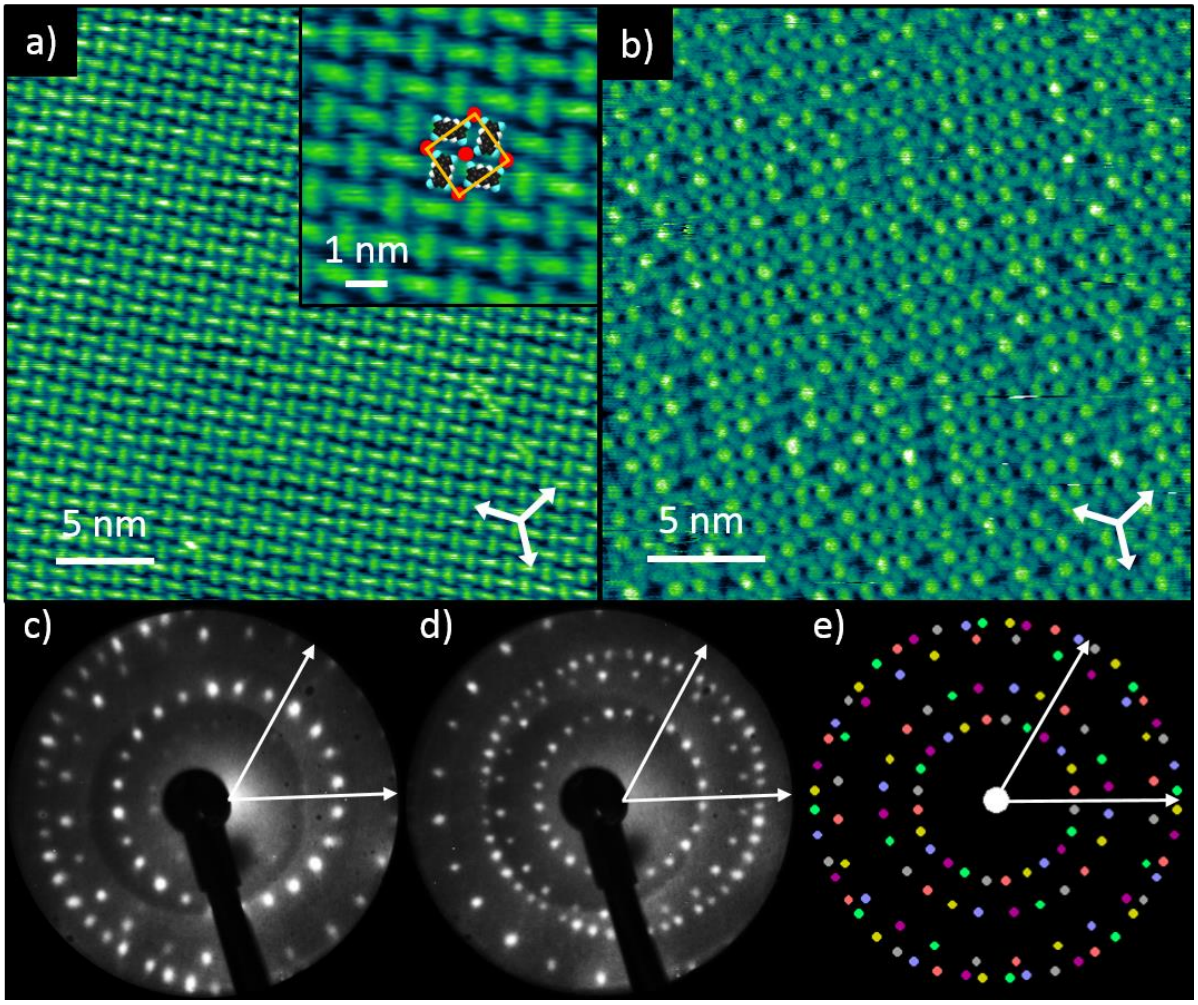

Figure 5.1.2 – STM and LEED of the K/TCNQ windmill phase. (a) Representative STM image showing an ordered domain of TCNQ molecules arranged into windmill-like structures (V_{samp} = 0.1 V, I = 175 pA). Inset: Expanded region of the image with superimposed scaled molecular models, K atoms and the overlayer unit-mesh indicated. (b) STM image showing alternative contrast with bright protrusions, interpreted to be K atoms, visible between TCNQ molecules (V_{samp} = –1.5 V, I = 300 pA) In both STM images, the white arrows indicate the substrate <110> directions. (c) LEED pattern recorded at an electron kinetic energy of 14.5 eV with two of the substrate. (d) LEED pattern recorded at an electron kinetic energy of 23.5 eV. (e) Simulated LEED pattern derived from the STM measured unit mesh, with beams originating from the six distinct domains coloured differently. In all of the LEED patterns, two of the substrate <211> directions are indicated by the white arrows.

While the STM images indicate that the ordered phase can accommodate one K atom per TCNQ molecule, the images recorded at larger negative bias voltages appear to show a significant concentration of K atom vacancies (~80 % of sites occupied). STM images obtained when the surface was prepared using a lower K exposure (while still displaying a similar LEED pattern) also show the same windmill assembly but show an apparent decrease in the K site occupation (~60 % of K sites occupied, Figure 5.1.3). This suggests that the windmill structure, which has enough sites to

accommodate one K atom per TCNQ molecule, is favourable for a range of K/TCNQ stoichiometry. Similar structures with a nominal 1:1 stoichiometry have been reported for Na/TCNQ and Li/TCNQ networks on Au(111)[57, 172] and on the Ag(100) surface, Cs/TCNQ networks with a smaller stoichiometric ratio of 1:4, are found to form.[59] The LEED in Figure 5.1.1 indicates that the nominal 1:1 K/TCNQ windmill structure forms alongside pure TCNQ domains, suggesting that structures with a lower K:TCNQ ratio are not accessible on the Ag(111) surface.

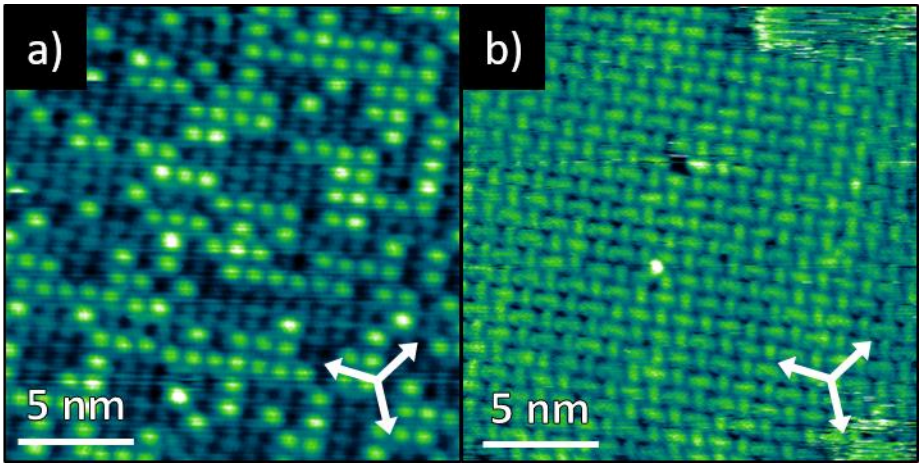

Figure 5.1.3 – STM images from the K/TCNQ windmill phase prepared at low K exposures. (a) STM image showing bright protrusions interpreted as K atoms, (V_{samp} = -1.5 V, I = 300 pA), (b) STM image recorded with alternate contrast showing TCNQ molecules arranged in the same windmill arrangement as shown in Figure 5.1.2 (V_{samp} = -1.4 V, I = 60 pA). In both STM images, the white arrows indicate the substrate <110> directions.

As shown in Figure 5.1.1, further deposition of K onto the sample produces a second K/TCNQ phase which initially coexists alongside the windmill structure before becoming dominant on the surface. STM of this second K/TCNQ phase (Figure 5.1.4a) shows ordered domains of TCNQ arranged in a 'head-to-tail' packing regime where all of the molecules have the same orientation. The unit mesh of this head-to-tail phase contains a single TCNQ molecule and has dimensions, averaged from measurements obtained from fifteen different STM images, of b_1 = (8.7 ± 0.3) Å and b_2 = (12.5 ± 0.4) Å, with an included angle of (109 ± 2)° and vector $\mathbf{b_1}$ oriented at an angle of (2 ± 2)° to the substrate <110> directions. The experimental LEED pattern shows diffraction beams from three unique domains, indicating that the molecular overlayer does not share the threefold rotational symmetry but does include the <211> mirror planes of the underlying Ag(111) substrate. For this to occur, one of the unit

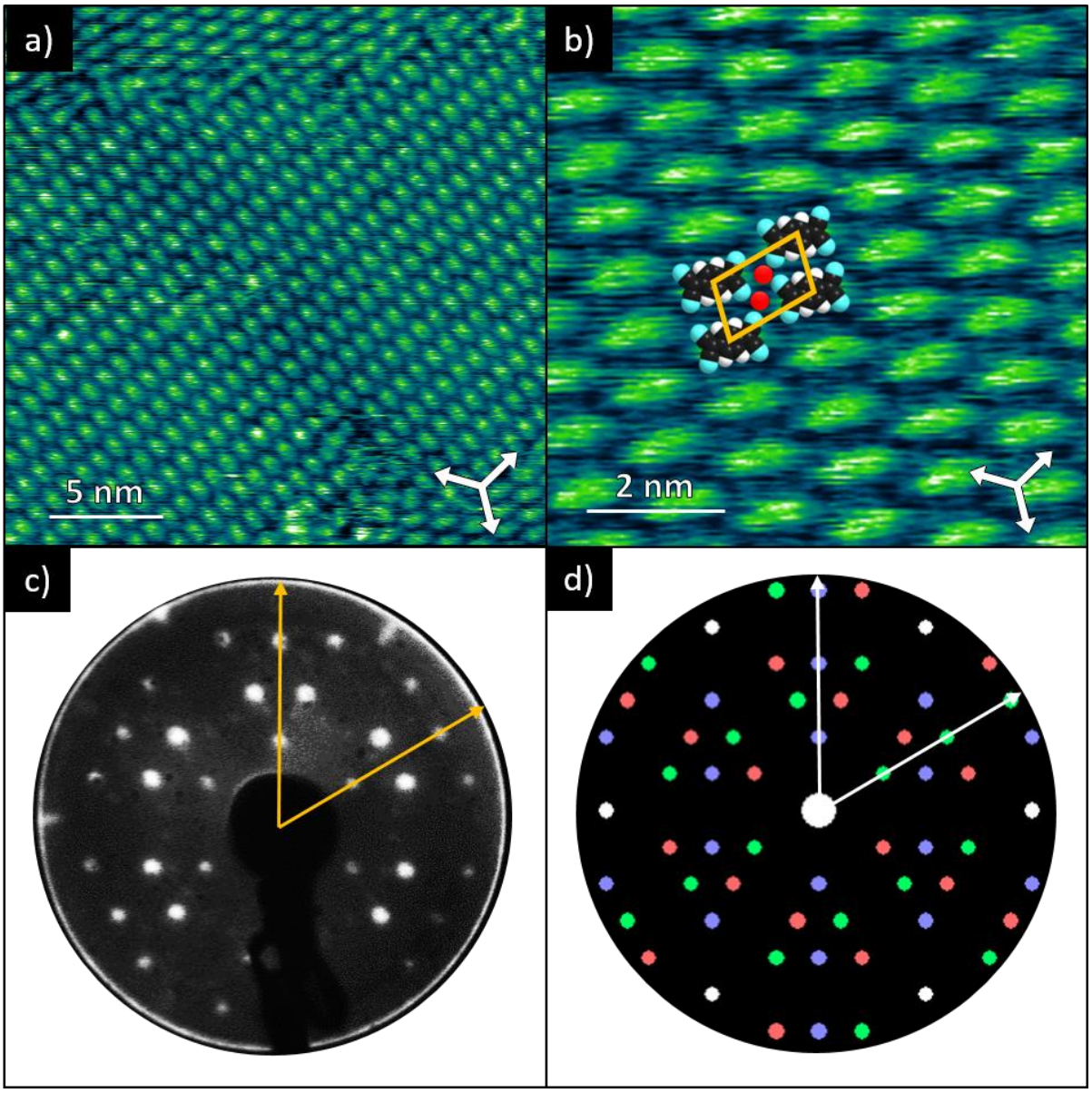

Figure 5.1.4 – STM and LEED of the K/TCNQ head-to-tail phase. (a) STM image showing ordered domains of TCNQ molecules (V_{samp} = 0.6 V, I = 100 pA). (b) Expanded region of the same STM image with scaled TCNQ molecular models and K^+ ions superimposed. The yellow parallelogram represents the overlayer unit-mesh. In both STM images, the white arrows indicate the substrate <110> directions. (c) LEED pattern recorded at an electron kinetic energy of 24.5 eV with two of the substrate <211> directions indicated by the yellow arrows. (d) Simulated LEED pattern derived from an $\begin{pmatrix} 3 & 0 \\ 1 & 5 \end{pmatrix}$ commensurate matrix, with beams from each unique but symmetrically equivalent domains coloured differently and white arrows indicating two of the substrate <211> directions.

mesh vectors must align with the substrate <110> directions and thus it was concluded that unit mesh vector $\mathbf{b_1}$ is aligned with the substrate <110> directions. This agrees, within the associated error range, with the (2 ± 2)° offset angle measured by STM. These unit mesh dimensions are in good agreement

with a $\begin{pmatrix} 3 & 0 \\ 1 & 5 \end{pmatrix}$ commensurate matrix of the substrate lattice vectors, which is further supported by the simulated LEED pattern derived from this commensurate mesh (shown in Figure 5.1.4c) showing excellent agreement with the experimental LEED pattern (Figure 5.1.4b).

For this adsorption phase, STM images recorded from the head-to-tail phase at larger negative voltage biases did not show the same circular protrusions between the molecules, corresponding to K atoms, as observed for the windmill phase. Consequently, it was not possible to ascertain the K/TCNQ stoichiometry from the STM images. However, since the unit mesh contains only a single TCNQ molecule, the structure must be able to accommodate an integer number of K atoms per TCNQ molecule and as the head-to-tail phase was formed by further deposition of K, a K:TCNQ stoichiometric ratio of greater than one is expected. In Figure 5.1.4 a structure for this adsorption phase was proposed by superimposing scaled TCNQ molecular models over the protrusions in the STM contrast and placing K atoms (using the K^+ ionic radius of 1.37 Å)[187] in sites between the molecules. The spaces between the molecules appear to be large enough to accommodate two K atoms per unit mesh and, consequently, this adsorption phase was tentatively assigned to a K_2TCNQ stoichiometry.

5.1.2 XPS and UPS

Figure 5.1.5 shows high-resolution soft XPS recorded from the KTCNQ windmill adsorption phase. The C 1s spectrum shows three distinct features, which were fitted with four components that correspond to the four chemically inequivalent C species in TCNQ (see the inset of the K 2p and C 1s spectrum). The relative intensities of these components are in reasonably good agreement with the expected stoichiometry of each C environment. As discussed in section 4.2 the line shape of the TCNQ C 1s spectrum is known to be characteristic of its charge state. [57, 175, 176] It was also shown, that in the absence of K, TCNQ accepts electrons from the Ag(111) substrate, becoming negatively charged. Here, in the KTCNQ windmill adsorption phase, the overall line shape of the C 1s spectrum remains the same, albeit with a small shift of ~0.2 eV in the binding energies (Table 5.1.1) compared to TCNQ adsorbed on Ag(111) alone (Table 4.2.1), indicating that the TCNQ molecules retain their negative charge. The N 1s spectrum shows a single peak at a binding energy of 398.1 eV, which is also in good agreement with other systems in which TCNQ is negatively charged[57, 175, 176] and is shifted by 0.2 eV from the value observed for TCNQ on Ag(111). The K 2p spectrum gives binding energies of 293.3 eV and 296.1 eV for the K $2p_{3/2}$ and K $2p_{1/2}$ components respectively, which are consistent with typical values for K^+ in ionic systems.[188] For comparison, XPS of K deposited by itself on Ag(111) gave binding energies of 294.5 eV and 297.3 eV for the respective K $2p_{3/2}$ and K $2p_{1/2}$ components. Overall, the XPS

results are consistent with the TCNQ molecules adsorbing in a negatively charged state and combining with K^+ counterions to form an ionic network.

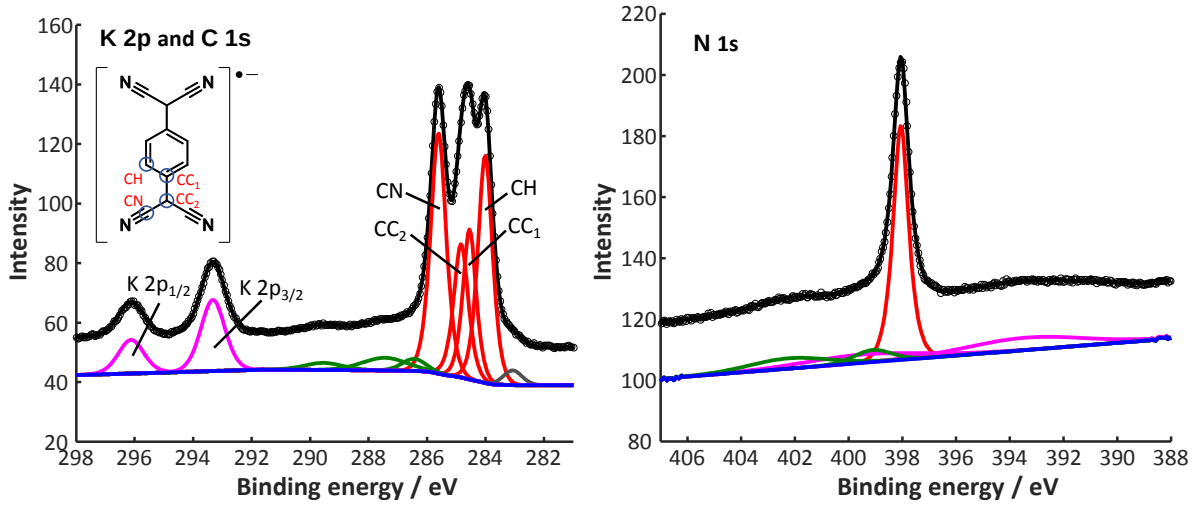

Figure 5.1.5 - Soft XPS recorded from the KTCNQ windmill phase on Ag(111). The K 2p/ C 1s spectrum was recorded using a photon energy of 435 eV, with measured intensity (black circles) and the sum of fitted components (black line) comprising a Shirley background (blue),[177] four main C 1s components (red), shakeup features (green), a beam damage feature (grey) and a K2p doublet component (purple). The N 1s spectrum was recorded with a photon energy of 550 eV, with measured intensity (black circles), and the sum of fitted components (black line) comprising a linear background (blue), one main component (red), two N shakeup features (green) and two Ag 3d plasmon features (purple).

Table 5.1.1 – XPS measured binding energies of the main C 1s, N 1s and K 2p components from the KTCNQ windmill phase. The relative intensities (peak areas) of the C 1s and K 2p components are also shown.

Component	**CH**	**CC_1**	**CC_2**	**CN**	**K $2p_{3/2}$**	**K $2p_{1/2}$**	**N**
Binding energy / eV	284.0	284.5	284.8	285.6	293.3	296.1	398.1
Relative intensity	1.68	1.01	1.00	1.89	0.83	0.43	-

The C 1s and K 2p XP spectrum was used to estimate the K/TCNQ stoichiometry within the windmill phase by comparing the relative peak intensities after correcting for the relevant photoionisation cross-sections (see Appendix D). From this, a K:TCNQ ratio of between 0.8-0.9 was obtained, which is in good agreement with the ~80 % occupancy of K sites suggested by the STM images in Figure 5.1.2 (it should be noted that the STM and XPS were not measured on the same sample, however similar preparation conditions were used in both cases). The XPS is therefore consistent with the interpretation that this K/TCNQ windmill phase has a nominal 1:1 stoichiometry but can feature a significant density of vacancies. Figure 5.1.6 shows high-resolution soft XPS recorded from the K/TCNQ head-to-tail adsorption phase, with the associated binding energies shown in Table 5.2.2. The C 1s spectrum shows four distinct peaks, which have each been fitted with a separate component, consistent with the four

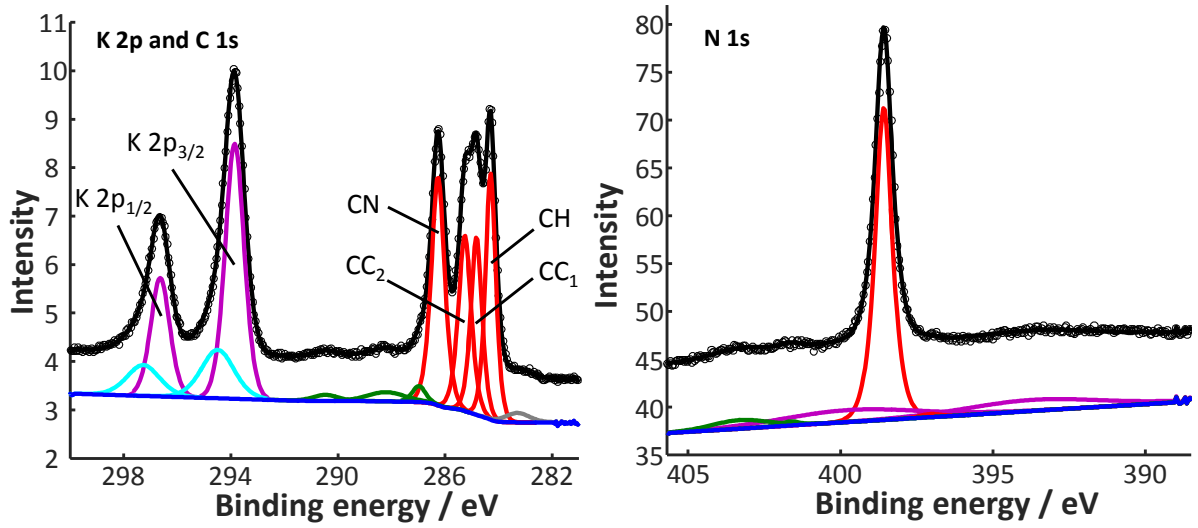

Figure 5.1.6 - Soft XPS recorded from the K/TCNQ head-to-tail phase on Ag(111). The K 2p/ C 1s spectrum was recorded at a photon energy of 435 eV, with measured intensity (black circles) and the sum of fitted components (black line) comprising a Shirley background (blue),[177] four main C 1s components (red), shakeup features (green), a beam damage feature (grey) and two asymmetrical K 2p peaks, each fitted with two components (purple main component and cyan minor component). The N 1s spectrum was recorded using a photon energy of 550 eV, with measured intensity (black circles), and the sum of fitted components (black line) comprising a linear background (blue), one main component (red), two N shakeup features (green) and two Ag 3d plasmon features (purple).

Table 5.1.2 – XPS measured binding energies of the main C 1s, N 1s and K 2p components from the K/TCNQ head-to-tail phase. The relative intensities (peak areas) of the C 1s and K 2p components are also shown.

Component	**CH**	**CC_1**	**CC_2**	**CN**	**K $2p_{3/2}$**	**K $2p_{1/2}$**	**N**
Binding energy / eV	284.3	284.8	285.3	286.3	293.9	296.7	398.6
Relative intensity	1.29	1.00	1.13	1.54	2.35	1.09	-

chemically inequivalent C environments within the TCNQ molecule. For this phase, the C 1s line shape differs from the windmill phase in two ways: showing increased intensity in the middle two components with respect to the two outer components and showing larger energy separations between the C components. Compared to the windmill phase, the head-to-tail phase CH and CC_1 components are shifted up in binding energy by 0.3 eV and the CC_2 and CN peaks are shifted by a further 0.2 eV and 0.4 eV respectively. The relative intensities of the C components deviate from the expected stoichiometry of the C environments within TCNQ, with the intensity of the two CC environments increasing relative to the CH and CN environments. Similar shifts in binding energy and changes to the apparent stoichiometry of components in the C 1s spectrum were reported by Precht *et al.* during intercalation of Na atoms into TCNQ thin films and were attributed to the formation of a $TCNQ^{2-}$ species.[176] It is unclear why a change to the TCNQ charge state would affect the apparent

stoichiometry measured by XPS and the authors do not provide an explanation as to why the charge state might change the C 1s spectrum in this way.[176] One possibility could be that the main C 1s components lie on top of shake-up components that have not been included when fitting the spectrum and the change in charge state shifts the main peaks relative to these shake-up features and/or changes the intensity of the shake-up features, causing an apparent change in the relative intensity of each component. Nonetheless, as the XPS measured for the K/TCNQ head-to-tail phase shows good agreement with XPS reported for a different system that includes a $TCNQ^{2-}$ charge state and because this charge state is consistent with the stoichiometry of the networks inferred from the STM images, it was concluded that the K/TCNQ head-to-tail phase also includes a $TCNQ^{2-}$ charge state. The N 1s spectrum shows only a single N peak, at a binding energy of 398.6 eV, which is 0.5 eV higher than in the windmill phase and is also consistent with previously reported XPS attributed to $TCNQ^{2-}$.[176] The K 2p spectrum features two asymmetrical peaks separated by the typical K 2p spin orbit splitting of 2.8 eV.[189] The asymmetric peaks were fitted as two components, with the main components at binding energies of 293.9 eV and 296.7 eV for K $2p_{3/2}$ and K $2p_{1/2}$ respectively, showing a 0.6 eV increase compared to the KTCNQ windmill phase. The minor components were observed at binding energies of 294.5 eV and 297.3 eV and thus have the same binding energy as K adsorbed alone on Ag(111), possibly suggesting that some portion of the K on the surface does not interact with TCNQ.

Analysis of the relative XPS peak intensities, correcting for the relative photoionisation cross-sections of each orbital, suggests a surface composition of ~3 K atoms per TCNQ molecule, though including only the intensity from the main K components gives an estimated ratio of ~2.4 K atoms per TCNQ (see Appendix D). Assuming that the minor components correspond to excess K atoms that are not interacting with TCNQ, this is reasonably consistent with the head-to-tail structure having a K_2TCNQ stoichiometry. This result is also consistent with the assembly inferred from the STM images in Figure 5.1.4 and agrees with proposed $TCNQ^{2-}$ charge state, for which two K^+ counterions would be needed to neutralise. The XPS also suggests that a significant excess of K atoms was present alongside the head-to-tail adsorption phase in the samples studied by XPS, from which the NIXSW measurements (shown in the following section) were also obtained. It was not determined whether this nominal 2:1 head-to-tail adsorption phase could be obtained without an excess of K atoms present on the surface.

Figure 5.1.7 shows UPS obtained from the K/TCNQ adsorption phases on Ag(111). As the STM measurements, presented earlier, indicate that the windmill phase forms at a range of K/TCNQ stoichiometry, measurements were obtained from two samples of this adsorption phase prepared at different K coverages. The low K coverage windmill phase sample corresponds to the minimum K coverage required to form the windmill phase without coexistence of the pure TCNQ adsorption phase.

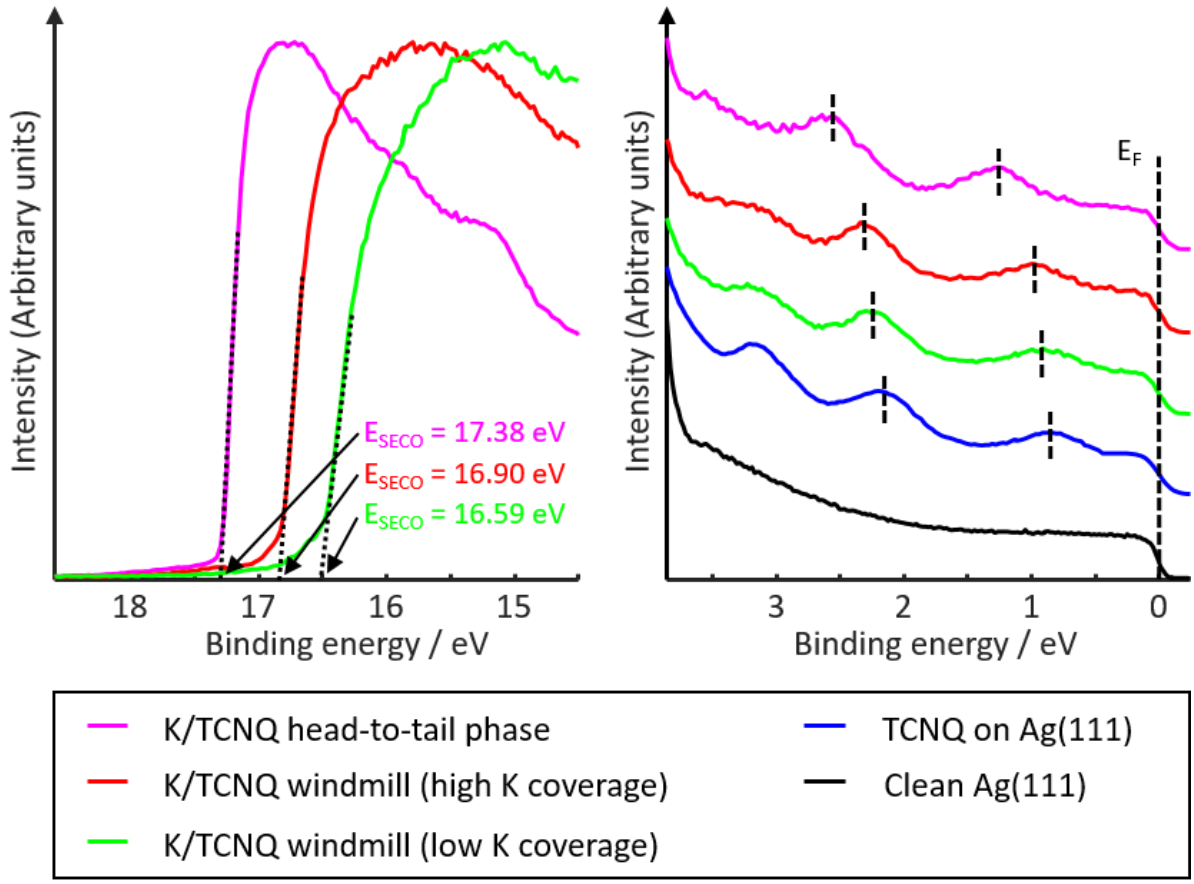

Figure 5.1.7 – UPS obtained from the K/TCNQ adsorption phases on Ag(111). The left panel shows measurements of the SECO, measured with a -10.0 V bias applied to the sample. The right panel shows the energy region close to the Fermi edge (E_F). For comparison, spectra obtained from the clean Ag(111) substrate and from pure TCNQ on Ag(111) are also shown. Black dashed lines mark the centre of two TCNQ valence states in each spectrum to aid in the comparison of the binding energy shifts. The intensity shown on the y-axis is arbitrary and the spectra are scaled and offset relative to each other for clarity. All binding energies are quoted relative to E_F. Measurements were obtained using the He-Iα (hv = 21.22 eV) emission line.

The high K coverage windmill phase was prepared by doubling the K deposition time used to prepare the low K coverage sample. The UPS obtained from the K/TCNQ adsorption phases on Ag(111) show the same peaks exhibited by the pure TCNQ adsorption phase, which were attributed to valence TCNQ states based on a similar assignment reported by Precht *et al*. for alkali metal intercalated thin films of TCNQ in which the molecule becomes negatively charged. [175, 176] As the K coverage is increased, the TCNQ valence states corresponding to the former TCNQ HOMO and LUMO (marked by the dashed black lines in the right-hand panel of Figure 5.1.7) shift to higher binding energy, with an overall shift of ~0.5 eV observed between the K/TCNQ head-to-tail phase and the pure TCNQ phase. A third feature,

observed at 3.31 eV in the spectrum for the pure TCNQ phase does not shift significantly but does appear to be suppressed as the K coverage is increased.

Table 5.1.3 – UPS measured work functions (Φ) measured for the K/TCNQ adsorption phases on the Ag(111) substrate. Measurements were obtained by subtracting the SECO energy (E_{SECO}, as shown in Figure 5.1.7) from the photon energy (hv = 21.22 eV).

Sample	Φ / eV
K/TCNQ windmill (low K coverage)	4.71 ± 0.05
K/TCNQ windmill (high K coverage)	4.38 ± 0.05
K/TCNQ head-to-tail phase	3.92 ± 0.05

Table 5.1.3 shows work function measurements obtained from the UPS. As discussed in section 4.2, the adsorption of TCNQ on Ag(111) is accompanied by a work function increase from (4.59 ± 0.05) eV to (5.02 ± 0.05) eV, caused by the TCNQ molecules accepting electrons from the substrate. The UPS measurements of the K/TCNQ adsorption phases show that the surface work function decreases as the K coverage increases, which is consistent with the K atoms donating electrons to the surface.[11] The measurements of the K/TCNQ windmill phases obtained at different K coverages, with values of (4.71 ± 0.05) eV and (4.38 ± 0.05) eV measured for the low and high K coverage samples respectively, show that a range of work functions spanning at least (0.33 ± 0.10) eV is accessible to this adsorption phase. For the head-to-tail phase, which has a nominal stoichiometry of K_2TCNQ, an even lower work function of (3.92 ± 0.05) eV was measured, suggesting that further electrons are donated to the surface.

5.1.3 NIXSW and structural models

Table 5.1.4 shows NIXSW measurements recorded from the KTCNQ windmill phase as well as K adsorbed alone on Ag(111) obtained using the (111) reflection of the substrate. High coherent fractions (>0.8) were obtained for all three chemically distinct C environments present within TCNQ, indicating that the molecules occupy a well-defined and uniform height above the surface. The corresponding coherent positions show that the molecules adopt a relatively flat conformation ~2.8 Å above the surface, with the peripheral nitrile C atoms only very slightly lower (<0.1 Å) than the central C ring. In contrast, a low coherent fraction of (0.41 ± 0.10) was measured for N, which is lower than can typically be attributed to thermal vibrations alone and suggests that the N atoms must occupy two or more distinctly different heights above the surface. The N coherent position of (2.79 ± 0.05) Å, which is a weighted average of these different contributing heights, is almost identical to the height of the C atoms, indicating that the two or more different N atoms heights must be distributed relatively evenly about the central ring of the molecule. The coherent fractions for K, both alone and coadsorbed with TCNQ

in the windmill phase, are high and are thus consistent with a single well-defined adsorption height. Without TCNQ, the coherent position of the K atoms corresponds to a height of (2.81 ± 0.05) Å above the surface, in excellent agreement with the results of a previous quantitative LEED structure determination of K on Ag(111).[190] In the KTCNQ windmill phase, the K ions adsorb at a height of (3.56 ± 0.05) Å, some (0.77 ± 0.10) Å above the TCNQ molecules. This result is qualitatively consistent with DFT calculated structures for similar TCNQ/alkali networks on the Ag(100) surface, which predict that the alkali metal ions occupy elevated heights above the TCNQ molecules.[168] One other remarkable result predicted by these calculations is that even in situations where the sites occupied by the alkali metal ions were sufficiently large to allow them to adsorb in contact with the substrate, they occupy sites above the TCNQ molecules instead due to the larger dipole moment that this generates.[168] In this respect, it is interesting to establish if the height of the K ions is reconcilable with simple considerations of the expected N-K interaction distance for the present KTCNQ system on Ag(111).

Table 5.1.4 – NIXSW fitting parameters from the KTCNQ windmill phase and K adsorbed alone on Ag(111) obtained using the (111) reflection of the substrate. Separate fitting parameters were obtained for the different C 1s photoemission components as defined in Figure 5.1.5 (due to lower resolution at the photon energies required for NIXSW, components CC_1 and CC_2 were fitted together in a single component here). The coherent position D(111) is given as $D(111) = (P+1)d_{111}$ where P is the fractional coherent position and d_{111} is the spacing of the (111) lattice planes (2.359 Å). Values for the K/TCNQ windmill phase are averaged from measurements of two separately prepared samples, with three repeat measurements recorded for each sample. For K adsorbed by itself on Ag(111), the values are averaged over five repeat measurements for a single sample preparation. Error estimates are shown in parentheses in units of 0.01.

Component	KTCNQ windmill phase		K only	
	f_{co}	$D_{(111)}$ / Å	f_{co}	$D_{(111)}$ / Å
K	0.79(10)	3.56(5)	0.82(10)	2.81(5)
CH	1.00(10)	2.85(5)	-	-
CC	1.00(10)	2.79(5)	-	-
CN	0.91(10)	2.79(5)	-	-
N	0.41(10)	2.79(5)	-	-

The C and N NIXSW measurements from the KTCNQ windmill phase are essentially identical to the values obtained from TCNQ alone on Ag(111) (see section 4.3), which could indicate that a similar adsorption conformation is adopted by TCNQ in both structures. For pure TCNQ on Ag(111), the combined DFT-D and NIXSW results show that the low N coherent fraction can be rationalised by the inclusion of Ag adatoms within the molecular adsorption structure. This results in some cyano groups

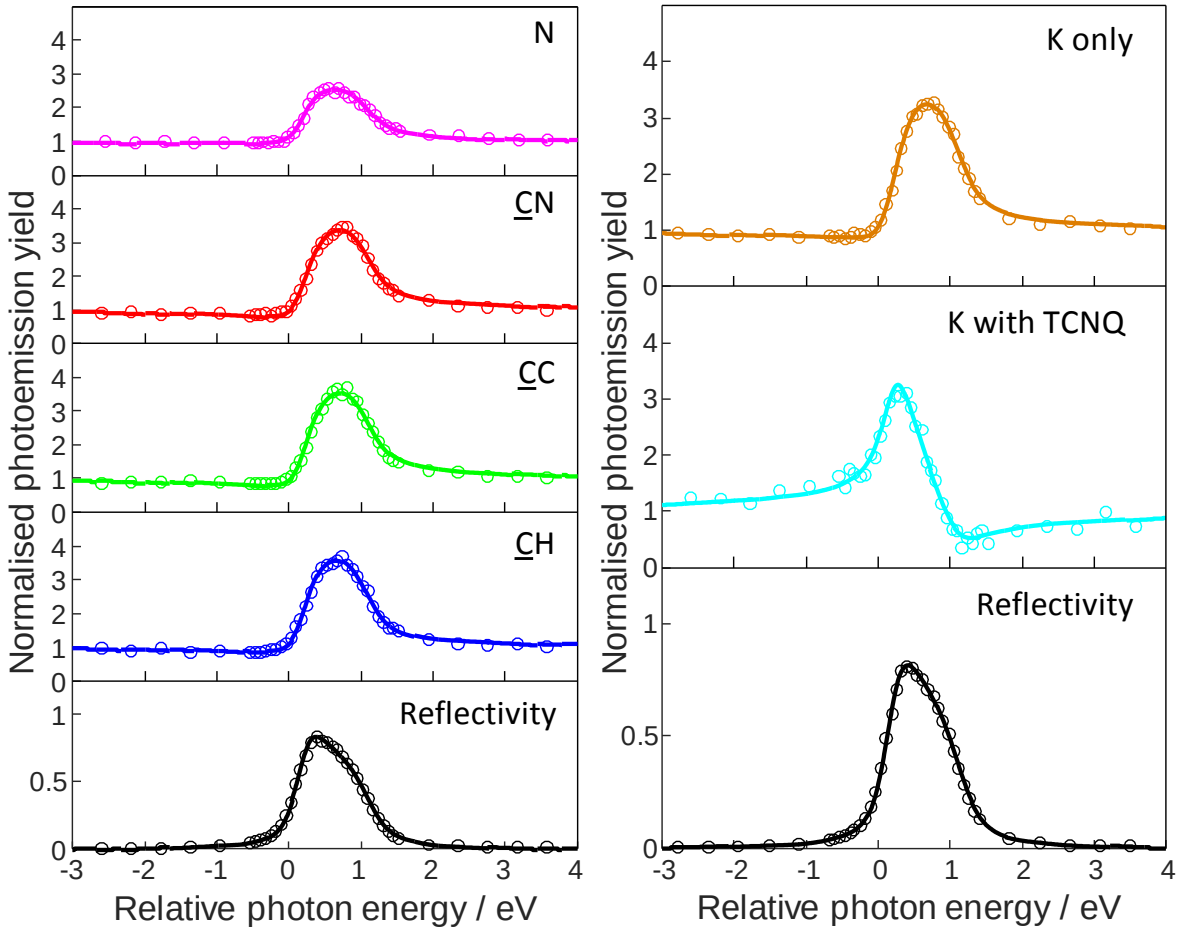

Figure 5.1.8 – Sample set of NIXSW photoemission yield curves obtained from the KTCNQ windmill phase, in addition to K adsorbed by itself on Ag(111), using the (111) reflection of the substrate. Photon energies are quoted relative to the Bragg energy of 2.630 keV. Least square fits (solid lines) to the photoemission yields (circles) were obtained to extract the coherent fractions and coherent positions.

bonding to nearby adatoms and pointing away from the surface whereas the other cyano groups, located further from the Ag adatoms, point down towards the surface. For the KTCNQ windmill phase, the near-identical NIXSW parameters cannot be reconciled in a similar fashion. While the windmill structure shares similarities with the structure formed by TCNQ with the Ag adatoms, the nominal 1:1 stoichiometry of the KTCNQ windmill phase means that *every* CN group is near to a K ion. Using the same reasoning as the pure TCNQ structure, it would be expected that all N atoms would bond to K ions in a consistent fashion throughout the structure, which would result in all N atoms occupying the same height above the surface. One possible solution to this may lie in the fact that STM images (Figure 5.1.2b) and XPS stoichiometry estimations indicate that there is a significant proportion of vacant K sites, for which the surrounding cyano groups could adopt a significantly different geometry compared to the occupied sites. However, the estimated vacancy concentration of ~20 % could at most only reduce

the coherent fraction to 0.6, assuming that the height difference between N atoms at the vacancies and N atoms at the occupied sites was exactly half the spacing of the Ag(111) planes (i.e. a height difference of 1.18 Å). A smaller or larger height difference would lead to an even higher coherent fraction. The presence of these vacancies is thus insufficient to account for the much lower measured N coherent fraction alone.

To investigate the possible structural causes of the low N coherent fraction, as well as to establish whether the K adsorption height is consistent with expected N-K interaction distances, a model of the windmill phase was constructed based on the interpretation of STM images (shown in Figure 5.1.9a). The molecules in this model are assumed to lie flat and coplanar, consistent with the NIXSW measurements for the C atoms. The K ions occupy sites between four cyano groups for which a circle 5.23 Å in diameter can be drawn through the centres of the four N atoms (red circle in Figure 5.1.9a). In the bulk crystal structure of KTCNQ, N-K interatomic distances of 2.93 Å are observed,[186] which corresponds to the sum of the K^+ ionic radius (1.37 Å)[187] and the N van der Waals radius (1.55 Å).[41] To satisfy these same interatomic distances in the constructed model, the K^+ ions would need to adsorb 1.30 Å above the N atoms, which is significantly greater than the (0.77 ± 0.10) Å height difference suggested by the measured coherent positions. Moreover, the NIXSW measurements also suggest that the N atoms are not coplanar and instead occupy a distribution of heights. If the coherent fraction of (0.41 ± 0.10) measured for N is attributed to the influence of two equally occupied N sites at different heights (the simplest multi-site model), a height difference of up to (0.84 ± 0.09) Å‡ is required to reduce the coherent fraction to the measured value. In this scenario, the measured N coherent position of (2.79 ± 0.05 Å) represents the average of the two heights and so, in the limiting case, half of the N atoms would have a height of 2.36 Å with the other half 3.23 Å above the surface. The high K coherent fraction indicates that there is no significant distribution of K adsorption heights, which excludes the possibility of having two distinctly different sites, one with all cyano groups pointing up and the other with all cyano groups pointing down. Instead, both N heights must be present in the cyano groups surrounding each K site. In this situation, there are two possibilities; either the cyano groups alternate between pointing up and down, or one adjacent pair of cyano groups point up and the other pair points down. In the former, the upward pointing cyano groups determine the height of the K^+ ions which, in

‡ This value accounts for reductions in the coherent fraction caused by incoherence in the standing wavefield resulting from vibrations of the Ag atoms within the crystal by using appropriate Debye-Waller factors. This value does not include any considerations of coherent fraction reductions caused by vibrations of the absorbing atoms themselves and thus corresponds to a limiting case of the maximum possible separation for the measured coherent fraction.

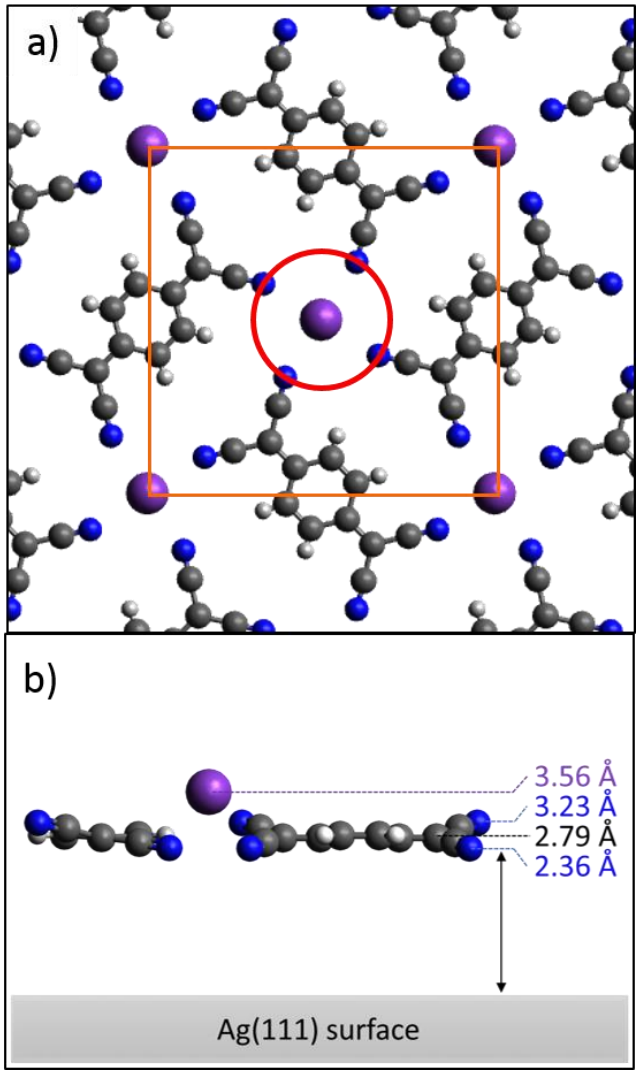

Figure 5.1.9 – Models constructed from the experimental measurements obtained from the KTCNQ windmill phase. (a) Plan view of the KTCNQ windmill phase. The orange square depicts the unit mesh with sides 13.4 Å in length. The red circle cuts through the centre of the four N atoms surrounding a K^+ ion and has a diameter of 5.23 Å. (b) Side view of the proposed 'twist' model with the heights of the K^+ ion, N atoms and the centre of the molecule highlighted.

the limiting case, would be forced up to 4.53 Å, significantly higher than the experimentally measured value. By contrast, the latter scenario (with matching adjacent pairs) allows the K ions to adsorb much closer to the surface. While not strictly necessary, this 'adjacent pairs' model would be satisfied if the TCNQ molecules were tilted with respect to the surface by rotation about the long molecular axis. Interestingly, in the bulk crystal structure of KTCNQ (in which TCNQ arranges into similar windmill structures around out of plane K^+ ions), the molecules are tilted about the long molecular axis in just this fashion, with a tilt angle of between 8.9-15.8° depending on the structural phase.[186] For comparison, the limiting case, corresponding to two N heights separated by (0.84 ± 0.09) Å, would be achieved with

a tilt of (11 ± 1)°. This tilt also lowers the coherent fractions expected for the C atoms in the molecule but to a lesser extent, with expected values of 0.76, 0.95 and 0.76 for the CH, CC and CN coherent fractions respectively. The experimental values for CC and CN are consistent with this model, but the measured coherent fraction for CH is significantly higher than suggested by this tilted model and instead suggests that the central carbon ring lies parallel the surface. A solution to this inconsistency is provided if the peripheral CN groups are twisted with respect to the central ring, rather than the full planar molecule being tilted (this twist model is depicted in Figure 5.1.9b). It should be noted, however that whilst the twist model can satisfy all of the experimental results, other factors such as the influence of K vacancies (described above) and thermal vibrations, will also contribute to the low coherent fraction, so the actual N height separation will of course be lower than the limiting case of (0.84 ± 0.09) Å, thereby reducing the required twist or tilt angle.

Table 5.1.5 - NIXSW fitting parameters obtained from the K_2TCNQ head-to-tail phase. Separate fitting parameters were obtained for the different C 1s photoemission components identified in Figure 5.1.6 (due to lower resolution at the photon energies used for NIXSW, components CC_1 and CC_2 were fitted together in a single component here). Separate fitting parameters were also obtained for the different K 2p photoemission components identified in Figure 5.1.6. The coherent position D(111) is given as $D(111) = (P+1)d_{111}$ where P is the fractional coherent position and d_{111} is the spacing of the (111) lattice planes (2.359 Å). Values are averaged from measurements of two separately prepared samples, with five repeat measurements recorded for each sample. Error estimates are shown in parentheses in units of 0.01.

Component	K_2TCNQ head-to-tail phase	
	f_{co}	$D_{(111)}$ / Å
K main	0.81(10)	3.29(7)
K minor	0.47(10)	3.65(16)
CH	0.86(10)	2.97(5)
CC	0.66(10)	2.99(5)
CN	0.56(10)	3.22(5)
N	0.55(12)	3.30(5)

NIXSW measurements recorded from the K_2TCNQ head-to-tail phase using the (111) reflection of the Ag(111) substrate are shown in Table 5.1.5. For K, separate NIXSW parameters were obtained for the two components identified by high-resolution XPS in Figure 5.1.6. The main component, which is assigned to the K atoms within the molecular networks, shows a high coherent fraction of (0.81 ± 0.10), consistent with values typically attributed to a single adsorption height. The corresponding coherent position indicates that K adsorbs at a height of (3.29 ± 0.07) Å, which is lower than the K atoms in the

windmill phase but is significantly higher than K adsorbed alone on Ag(111). This result is also qualitatively consistent with the DFT calculated structures for similar TCNQ/alkali networks on the Ag(100) surface, which predict that the alkali metal ions occupy elevated heights above the surface due to interactions of dipole moments.[168] The minor K component, which was assigned to excess K that is not bound to the TCNQ, shows a much lower coherent fraction, indicating that this K species occupies a larger distribution of adsorption heights. Additionally, this minor K component gives a significantly larger coherent position than the main K component, possibly suggesting that these excess K atoms are adsorbed above the K/TCNQ networks.

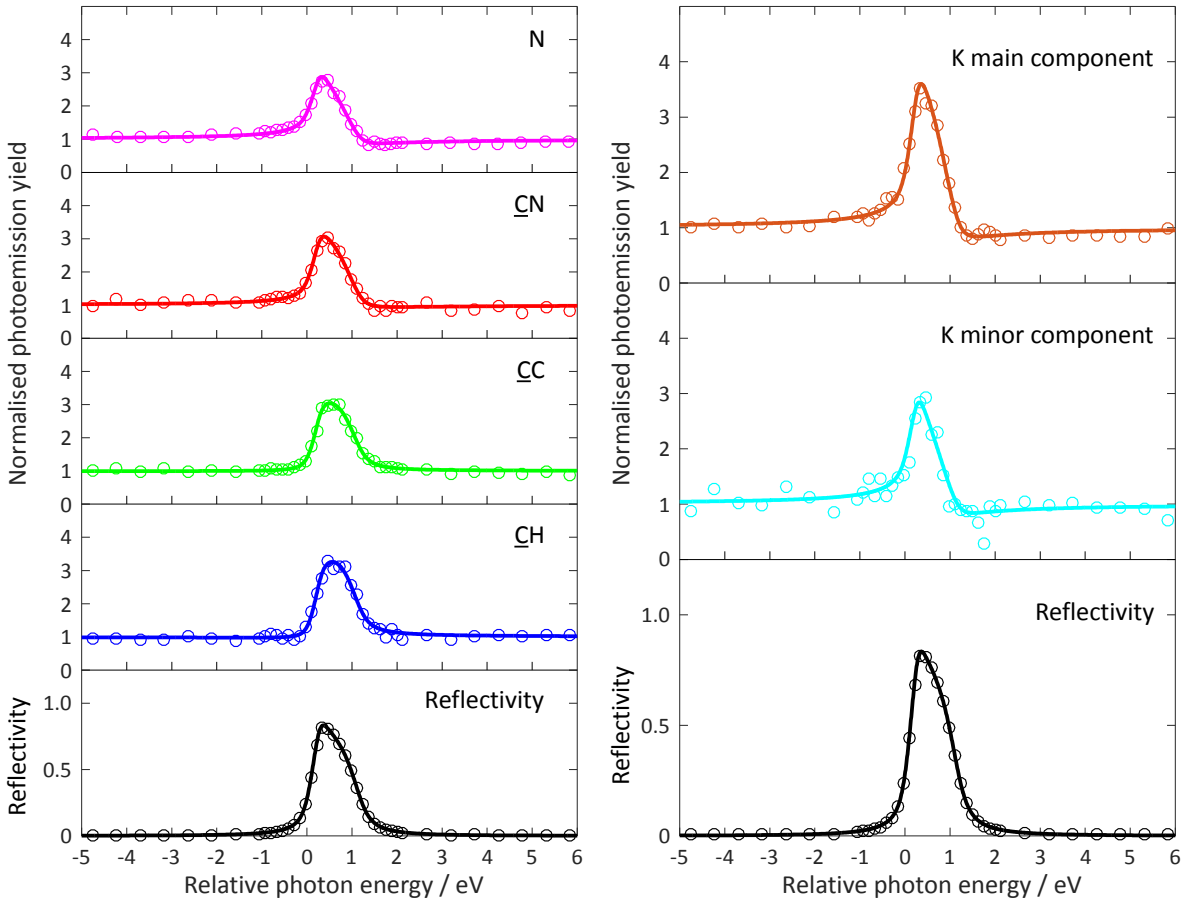

Figure 5.1.10 – Sample set of NIXSW photoemission yield curves obtained from the K_2TCNQ head-to-tail phase using the (111) reflection of the substrate. Photon energies are quoted relative to the Bragg energy of 2.630 keV. Least square fits (solid lines) to the photoemission yields (circles) were obtained to extract the coherent fractions and coherent positions.

The C and N NIXSW measurements show a trend in the coherent fractions, with a high value of (0.86 ± 0.10) measured for the CH component and decreasing values measured for components moving towards the extremities of the molecule, with N giving a coherent fraction of (0.55 ± 0.12).

This indicates that the central quinoid ring of TCNQ adsorbs at a well-defined height, whereas the peripheral groups occupy a significant distribution of heights. The CH coherent position indicates that the central quinoid ring of the molecule adsorbs at a height of (2.97 ± 0.05) Å. Moving toward the extremities of the molecule, the coherent positions increase with the N atoms adsorbing, on average, (0.33 ± 0.10) Å above the centre of the molecule, suggesting that TCNQ adopts a conformation in which the cyano groups bend away from the substrate. The adsorption height of (3.30 ± 0.05) Å suggested by the N coherent position is significantly higher than in either the KTCNQ windmill phase or TCNQ adsorbed alone on Ag(111) but is comparable to the K adsorption height measured in the present phase. This implies that the upward bending conformation is caused by the K ions, which occupy an elevated height, lifting the cyano groups away from the surface.

While the measured coherent positions suggest that, on average, the TCNQ molecules adopt an upward bending geometry, the coherent fractions indicate that the peripheral 'arms' of the molecule containing the cyano groups occupy a significant distribution of heights. As the K_2TCNQ head-to-tail phase is commensurate with the underlying Ag(111) substrate, it was possible to obtain geometry-optimised structural models from dispersion corrected DFT calculations to compare to the NIXSW measurements and identify possible causes of the low coherent fractions. These calculations were performed by Reinhard Maurer as detailed in section 2.8.8. As there are numerous dispersion corrections available for DFT codes, which have highly system-dependent performance, it is difficult to determine *a priori* which correction is most appropriate to use. As a result of this, structures were calculated using two different dispersion corrections (DFT+vdW^{surf} [32] and DFT-MBD[31, 33] as detailed in section 2.8.8) and were compared to the NIXSW measured adsorption heights to initially determine whether the functionals gave a good representation of the experimental results. The initial models were constructed using the commensurate $\begin{pmatrix} 3 & 0 \\ 1 & 5 \end{pmatrix}$ unit mesh containing one TCNQ molecule and two K atoms, with the orientation of the molecules based on the contrast observed in the STM images. Although the STM contrast did not show any features that could be assigned to the location of K atoms, the NIXSW measurements suggest that the TCNQ molecules interact with the alkali metals through the cyano groups and thus the K atoms were positioned within the spaces between cyano groups. From this starting point, the structure was allowed to relax, yielding similar structural models for both dispersion corrections.

Figure 5.1.11 shows the structure obtained using the DFT+vdW^{surf} dispersion correction, which are also qualitatively representative of the models calculated using the DFT-MBD correction. The calculations predict that both K atoms in the unit mesh occupy symmetrically equivalent sites located between cyano groups from four different TCNQ molecules. The side view shows that the molecules adopt a

conformation in which the peripheral cyano groups are bent away from the substrate towards the K atoms, consistent with the measured coherent positions. However, the calculated models predict that both ends of the molecule bend away from the surface at a similar angle and thus do not show the distribution of heights expected for the low measured coherent fractions.

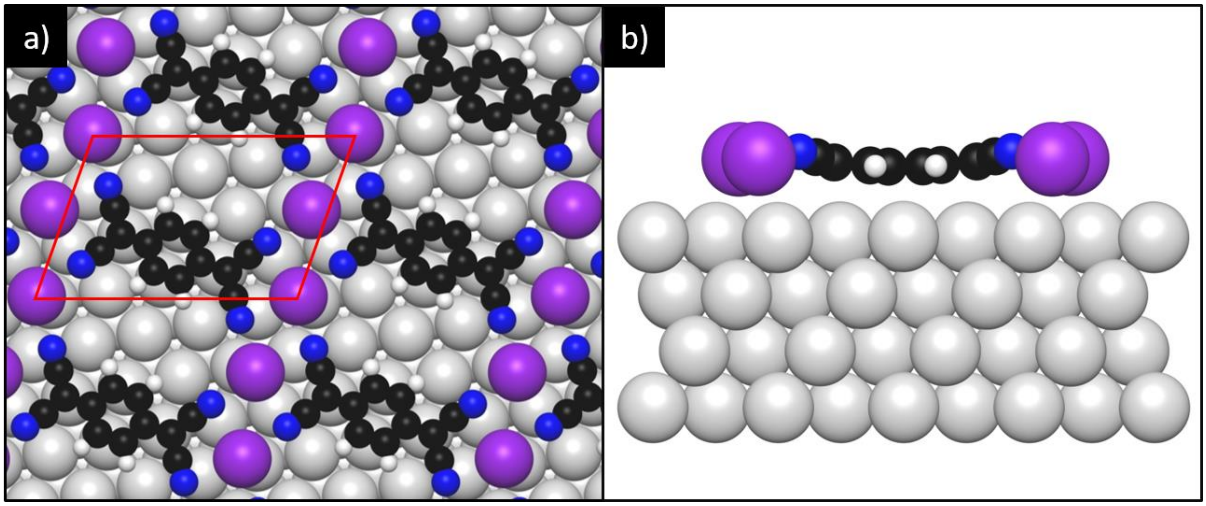

Figure 5.1.11 – Geometry optimised structural models obtained for the K_2TCNQ head-to-tail phase on Ag(111) using DFT+vdW^{surf} calculations. a) – Plan view of the structure showing the molecular orientation and positions of the K atoms with the unit mesh indicated by the red parallelogram. b) – Side view of the structure showing the relative heights and adsorption conformation. Visualisations were produced using the open-access software package VESTA.[181]

Table 5.1.6 - Expected NIXSW fitting parameters obtained from the atomic coordinates of the geometry-optimised DFT models calculated using the two dispersion corrections alongside the experimental NIXSW results for the K_2TCNQ head-to-tail phase. For the DFT models, the $D_{(111)}$ values are taken as the vertical distance relative to the average height of the outermost Ag layer. Calculated f_{co} values do not account for vibrational motion of the absorbed atoms but do account for incoherence in the XSW caused by vibrations in the Ag crystal giving a maximum possible coherent fraction of 0.95.

	f_{co}					$D_{(111)}$ / Å				
	CH	CC	CN	N	K	CH	CC	CN	N	K
Experiment	0.86	0.66	0.56	0.55	0.81	2.97	2.99	3.22	3.30	3.29
Model										
DFT-MBD	0.94	0.93	0.94	0.94	0.95	2.87	2.98	3.26	3.47	3.17
DFT+vdW^{surf}	0.94	0.94	0.94	0.94	0.95	2.93	2.99	3.17	3.31	3.26

To quantitatively compare the DFT calculations with the experimental data, expected NIXSW fitting parameters were calculated using the atomic coordinates from the DFT models (shown in Table 5.1.6). The DFT models predict coherent positions that are in excellent agreement with the experimental

NIXSW measurements, particularly for the DFT+vdW^{surf} model, which gives values within the associated experimental error ranges. However, both models also predict high coherent fractions that are not consistent with the experimentally measured values. The DFT calculations therefore suggest that the lowest energy structure does not include any features that can even partially explain the low measured coherent fractions. It should be noted that the values calculated in Table 5.1.6 do not account for reductions to the coherent fractions caused by vibrational motion of the absorber atoms. As the experimental measurements were recorded at ambient temperature (~300 K), it could be possible for the molecules to vibrate with relatively high amplitudes if the adsorption potential of the structure is shallow. Currently there are no measurements, or calculations available to suggest how large the vibrational amplitudes for TCNQ adsorbed on metal surfaces might be. It is therefore difficult to assess the impact that such vibrational motion would have on the coherent fraction. The vibrational amplitudes of bulk crystalline TCNQ have, however, been measured by X-ray diffraction[157] and ^{14}N nuclear quadrupole resonance,[191] which may give some indication of the possible vibrational amplitudes that could occur within the adsorption structure. The ^{14}N nuclear quadrupole resonance measurements by Murgich[191] investigated the thermal rotational modes of the TCNQ within its bulk crystal lattice by modelling the molecule as a rigid rotor, which yielded root mean square (rms) angular amplitudes between 1.5° and 4.2° about the various molecular axes that are consistent with values measured by X-ray diffraction.[157]

Table 5.1.7 – Calculated rms rotational amplitudes required to produce the experimentally observed coherent fractions. Values were calculated by considering the distribution of adsorption heights generated by rotation about the short in-plane molecular axis of TCNQ as indicated in Figure 5.1.12, using the molecular geometry adopted by TCNQ in the DFT+vdW^{surf} model. Incoherence in the XSW caused by vibrations in the Ag crystal are accounted for using appropriate Debye-Waller factors resulting in a maximum possible coherent fraction of 0.95.

Component	Measured f_{co}	Required rms rotational amplitude / °
CH	0.86 ± 0.10	5 ± 5
CC	0.66 ± 0.10	4.4 ± 1.0
CN	0.56 ± 0.10	3.1 ± 0.5
N	0.55 ± 0.12	2.7 ± 0.6

For the present system, the coherent fraction is high for the central quinoid ring of TCNQ but gradually decreases towards the extremities of the molecule, indicating that the peripheral groups occupy a significant distribution of heights. This trend in the coherent fractions is qualitatively consistent with the molecule rotating about its short in-plane axis, or with the peripheral ‘arms’ of the molecule moving up and down in a wagging motion, which, due to the structure of the molecule, will create a larger distribution of heights for the atoms closer to the extremities of the molecule. To assess whether such

motion could produce the low coherent fractions observed by NIXSW, the rotational amplitudes required to reduce the coherent fraction to the measured values were calculated and are shown in Table 5.1.7. The calculated values are relatively consistent between the different components of the molecule and indicate that rotations of similar amplitudes to those observed in bulk crystalline TCNQ[157, 191] are sufficient to reproduce the experimentally observed coherent fractions. It was therefore concluded that thermal rotations or wagging of the peripheral groups are a plausible explanation of the observed low coherent fractions.

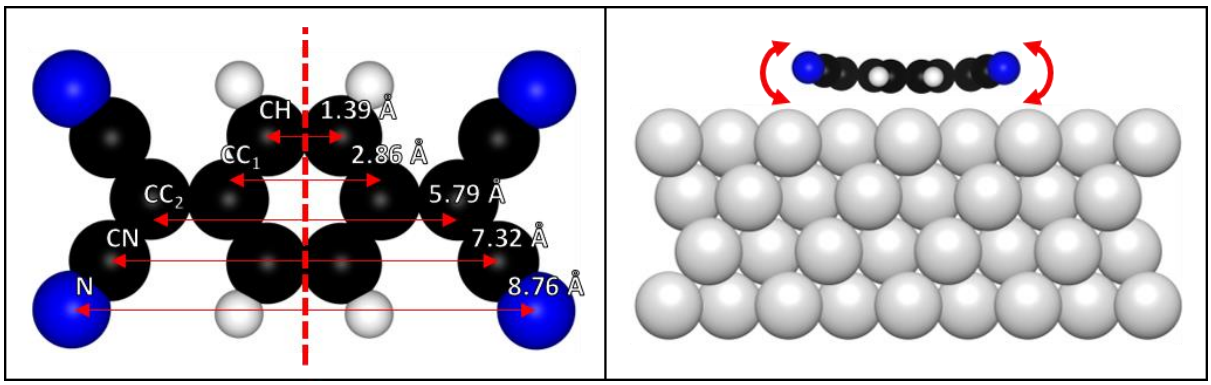

Figure 5.1.12 – Illustration of the impact of vibration/rotation on the distribution of heights occupied by the constituent atoms of TCNQ. Left) – Plan view of TCNQ with lateral spacings between equivalent atoms indicated by the red arrows. Values were obtained from the DFT+vdW^{surf} calculated structure of K_2TCNQ. Right) – Side view of TCNQ in the geometry calculated using DFT+vdW^{surf} for K_2TCNQ with red arrows indicating the direction of the proposed wagging/rotational motion. Visualisations were produced using the open-access software package VESTA.[181]

5.2 Coadsorption of TCNQ and Cs on Ag(111)

5.2.1 STM and LEED

Using the same method as for the K/TCNQ networks, Cs/TCNQ networks were prepared by sequentially depositing Cs atoms onto a sample of the phase II TCNQ adsorption structure on Ag(111), characterised in chapter 4. After each Cs deposition, the sample was annealed to 200 °C to promote the formation of large ordered domains on the surface. The changes to the adsorption structure were monitored by LEED after each Cs deposition and during each anneal step.

At relatively low Cs exposures, the resulting surface produces a complicated LEED pattern with a high density of diffraction beams (Figure 5.2.1c). STM from this surface (Figure 5.2.1 a+b) shows ordered domains of rounded oblong protrusions, interpreted as TCNQ molecules, arranged in a complicated assembly defined by a large unit mesh. Averaging measurements from six STM images gives unit mesh vectors lengths of b_1 = (36.8 ± 0.4) Å and b_2 = (39.0 ± 0.3) Å, which have an included angle of (97 ± 1)°

and vector $\mathbf{b_1}$ rotated by (49 ± 2)° relative to the substrate <110> directions. From the STM images, it is difficult to resolve the exact orientations and positions of all TCNQ molecules in the cell. However, based on the unit mesh size and by overlaying scaled models, it was estimated that the unit mesh contains sixteen TCNQ molecules. Small circular protrusions are also visible in the STM contrast at the centres of some TCNQ clusters, which were tentatively interpreted to be Cs atoms. However, due to the complex nature of this adsorption phase, it was not possible to reliably infer any information about the Cs/TCNQ stoichiometry. However, as further Cs deposition was found to produce a different phase with a 1:1 stoichiometry (discussed in the following paragraph), this phase must have a Cs/TCNQ ratio of less than one. The STM also shows circular depressions, which appear to be caused by holes or pores in the molecular overlayer.

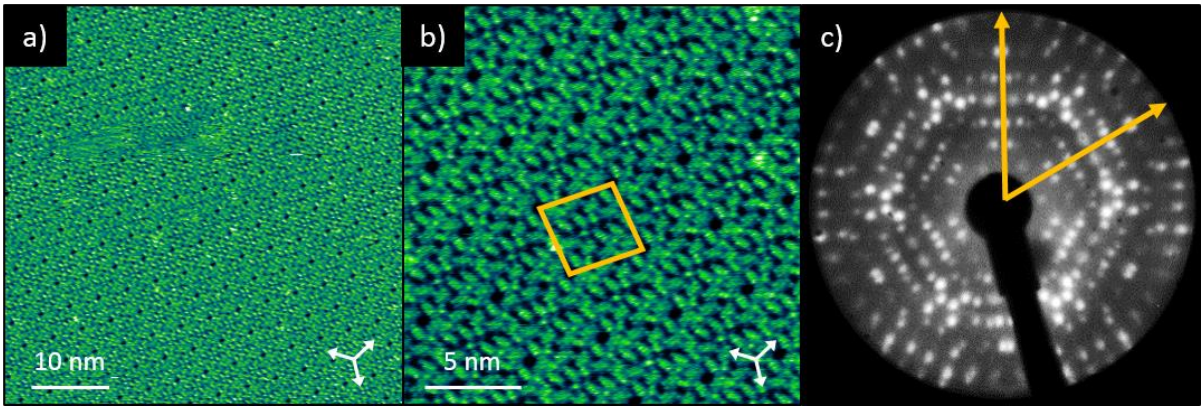

Figure 5.2.1 – STM and LEED from the Cs/TCNQ coadsorption phase formed at low Cs exposures. (a) – Large area STM image showing a single domain of the ordered structure formed on the surface (V_{samp} = -0.4 V, I = 300 pA). (b) – Expanded image of an ordered domain showing TCNQ molecules as rounded oblong protrusions packed into a complicated arrangement (V_{samp} = -0.4 V, I = 250 pA). In both STM images, the white arrows indicate the substrate <110> directions. The yellow rhombus indicates the surface unit mesh. (c) LEED pattern captured at an electron kinetic energy of 14.5 eV with two of the substrate <211> directions indicated by the yellow arrows.

Further deposition of Cs onto the sample produces a different LEED pattern, indicating a phase transition. The new LEED pattern (Figure 5.2.2 c+d) shows some similarities to that of the K/TCNQ windmill phase (see Figure 5.1.2) suggesting that a similar phase is formed with Cs. STM of this new adsorption phase (Figure 5.2.2) confirms this, showing TCNQ molecules as rounded oblong protrusions arranged in a windmill assembly. The STM contrast here also shows small circular protrusions at the centre of each windmill unit, which were interpreted as Cs atoms. From this interpretation, the STM suggests a 1:1 Cs/TCNQ stoichiometry.

Averaging measurements from six STM images of the CsTCNQ windmill phase gives unit mesh vectors of length b_1 = (13.9 ± 0.1) Å and b_2 = (13.6 ± 0.3) Å with an included angle of (94 ± 2)° and vector $\mathbf{b_1}$

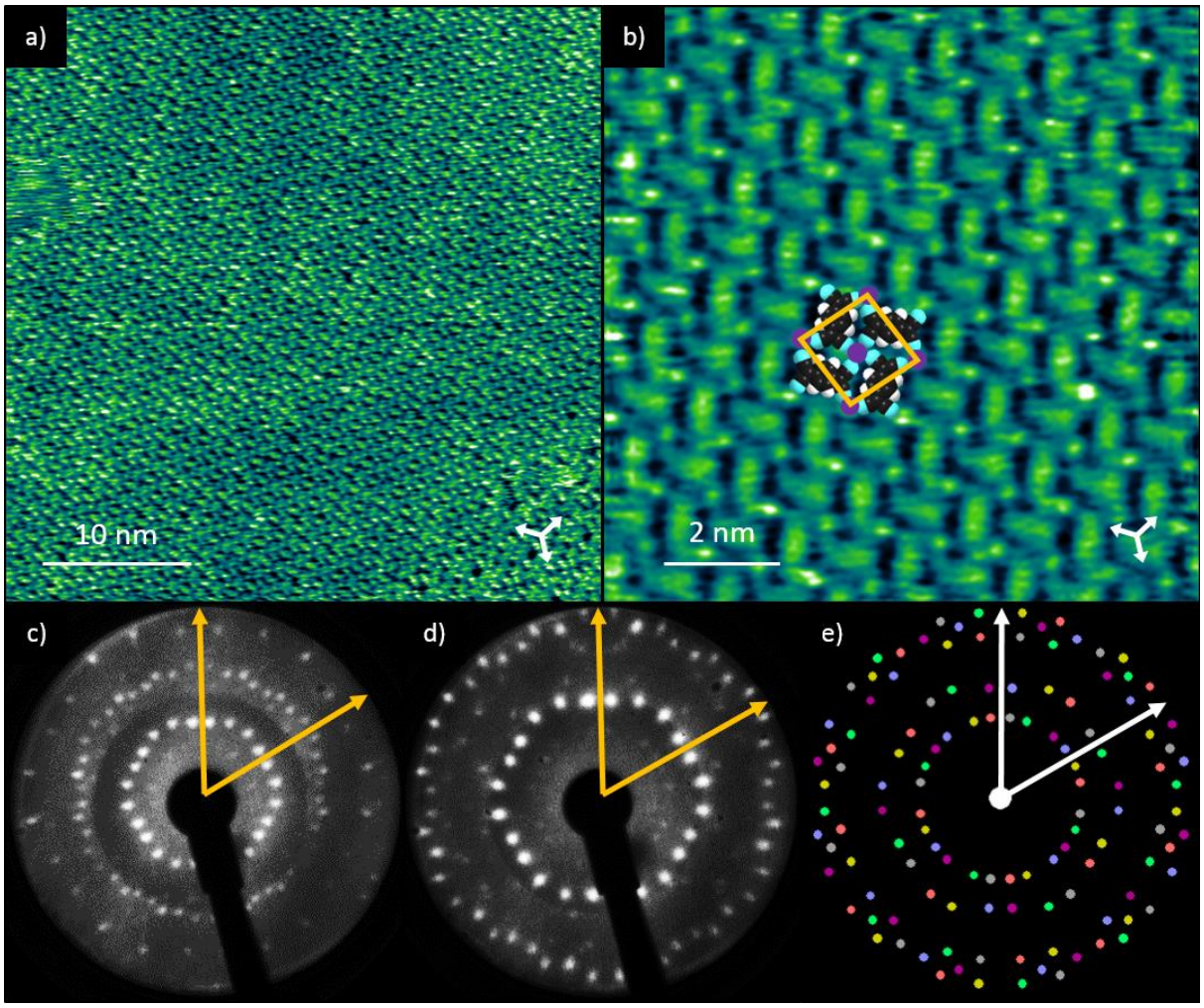

Figure 5.2.2 – STM and LEED of the Cs/TCNQ windmill phase formed after further Cs deposition onto the structure shown in Figure 5.2.1. (a) – Large area STM image showing an ordered domain of TCNQ molecules arranged into windmill-like structures (V_{samp} = -0.4 V, I = 250 pA). (b) – Expanded area STM image, with scaled molecular models, Cs atoms and the overlayer unit-mesh superimposed (V_{samp} = -0.9 V, I = 300 pA). In both STM images, the white arrows indicate the substrate <110> directions. (c) – LEED pattern recorded at an electron kinetic energy of 23.5 eV with two of the substrate <211> directions indicated by yellow arrows. (d) LEED pattern recorded at an electron kinetic energy of 14.5 eV with two of the substrate <211> directions indicated by yellow arrows. (e) Simulated LEED pattern derived from the STM measured unit mesh with beams originating from the six distinct domains coloured differently and two of the substrate <211> directions indicated by white arrows.

rotated by (7 ± 2)° to the substrate <110> directions. Figure 5.2.2e shows a simulated LEED pattern expected for a unit mesh described by a matrix of $\begin{pmatrix} 4.51 & 5.07 \\ -3.44 & 1.83 \end{pmatrix}$, which is consistent with the STM measurements and is in excellent agreement with the experimental LEED pattern (Figure 5.2.2 c+d). This confirms the accuracy of the STM measured unit mesh and indicates that this adsorption structure is incommensurate with respect to the underlying Ag(111) substrate. As the unit mesh does not share

the 3m symmetry of the substrate, six unique but symmetrically equivalent domains are observed, the diffraction beams from which are coloured differently in the simulated LEED pattern.

Comparison of the respective K and Cs TCNQ windmill phases show that the two structures are closely related, with the STM-measured unit mesh dimensions of the two phases agreeing within error and both unit meshes oriented similarly to the underlying Ag(111) substrate. A small, but clear difference between the two structures is however observable by LEED, with the Cs/TCNQ phase showing prominent diffraction beams arranged in a hexagon around the specular beam, whereas the equivalent diffraction beams of the K/TCNQ adsorption phase are arranged in a ring. This is indicative of the included angles in the unit mesh differing for the two phases and suggests that the included angle of the K/TCNQ windmill phase is closer to 90° than that of the Cs/TCNQ windmill phase.

Even further deposition of Cs onto the sample brings about another change to the adsorption structure, producing a LEED pattern (Figure 5.2.3 c+d) that shows some similarities with the K/TCNQ head-to-tail phase. STM of this surface (Figure 5.2.3 a+b) reflects this, showing TCNQ molecules as oblong protrusions packed in a head-to-tail type assembly, with further small circular protrusions, interpreted to be Cs atoms, arranged in rows between the molecules in a 2:1 ratio. Unlike the K head-to-tail phase, this Cs phase also shows large depressions in the STM contrast of a comparable size to the molecules, which appear to correspond to holes or pores in the molecular overlayer. Averaging measurements from ten STM images gives unit mesh vector lengths of $b_1 = (9.3 \pm 0.2)$ Å and $b_2 = (12.6 \pm 0.2)$ Å with an included angle of $(110 \pm 2)°$ and vector $\mathbf{b_1}$ oriented at an angle of $(3 \pm 1)°$ to the substrate <110> directions. The observed experimental LEED pattern shows diffraction beams from three unique domains, indicating that the molecular overlayer does not share the threefold rotational symmetry but does include the <211> mirror planes of the underlying Ag(111) substrate. For this to occur, one of the unit mesh vectors must align with the substrate <110> directions and thus it was concluded that unit mesh vector $\mathbf{b_1}$ is actually aligned with the substrate <110> directions and does not have a small offset of $(3 \pm 1)°$ as suggested by the STM measurements. Figure 5.2.3e shows a simulated LEED pattern obtained from a unit mesh described by a matrix of $\begin{pmatrix} 3.22 & 0.00 \\ 0.73 & 4.68 \end{pmatrix}$, which is consistent with the STM measured unit mesh dimensions, assuming that vector $\mathbf{b_1}$ is in alignment with the substrate <110> directions. The simulated pattern for this unit mesh is in excellent agreement with the experimental pattern, confirming that this matrix gives an accurate description of the surface periodicity and, consequently, that this structure is incommensurate with respect to the underlying Ag(111) substrate.

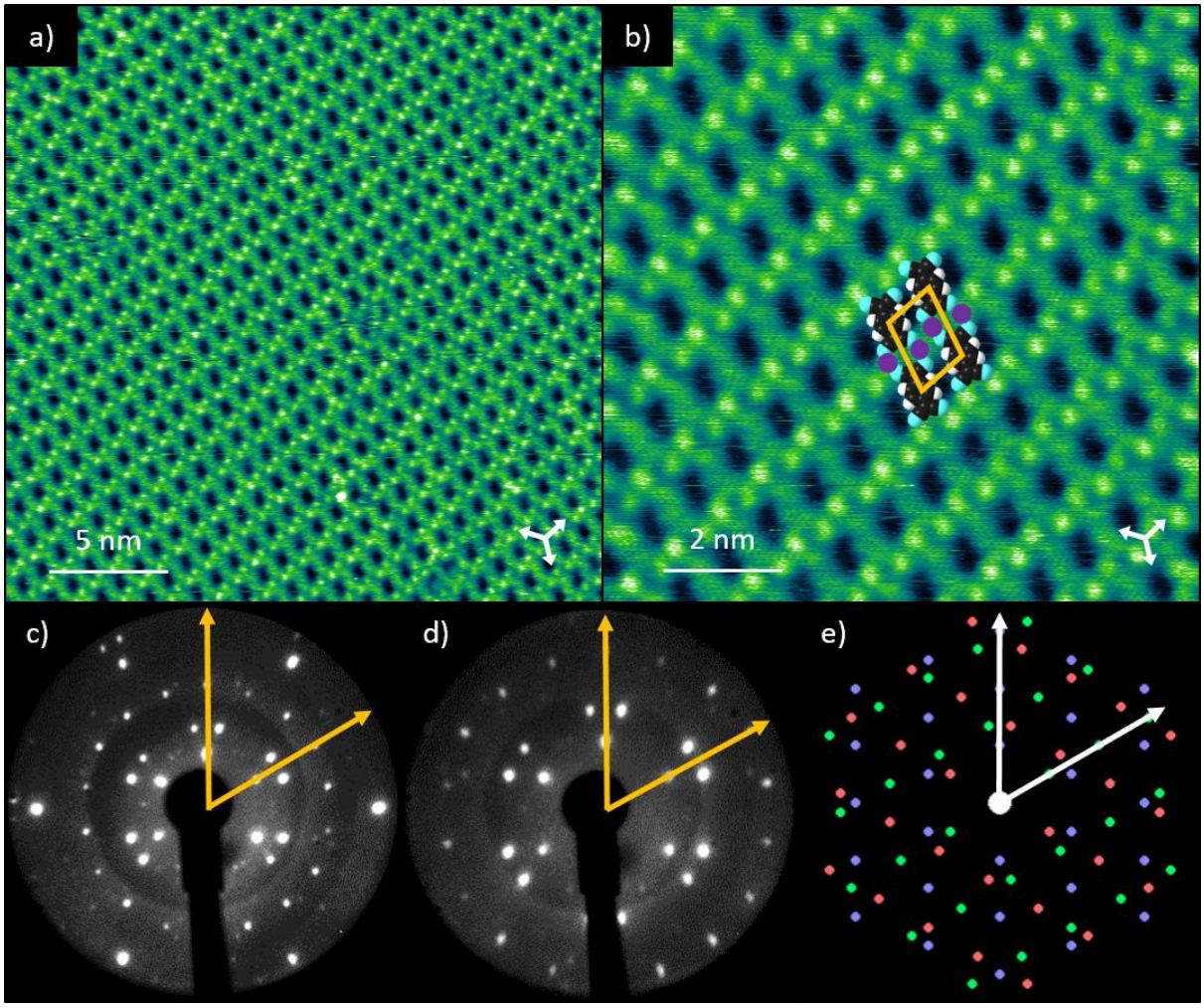

Figure 5.2.3 – STM and LEED from the Cs/TCNQ head-to-tail phase formed after further Cs deposition onto the Cs/TCNQ windmill phase. (a) – Large area STM image showing an ordered domain of TCNQ molecules arranged into a head-to-tail structure (V_{samp} = -0.9 V, I = 300 pA). (b) – Expanded area STM image with scaled molecular models, Cs atoms and the overlayer unit-mesh superimposed (V_{samp} = -0.9 V, I = 300 pA). In both STM images, the white arrows indicate the substrate <110> directions. (c) – LEED pattern recorded at an electron kinetic energy of 23.5 eV (d) LEED pattern recorded at an electron kinetic energy of 14.5 eV. (e) Simulated LEED pattern derived from the STM measured unit mesh with beams originating from the six distinct domains coloured differently. In all of the LEED patterns, two of the substrate <211> directions are indicated by yellow/white arrows.

5.2.2 XPS and UPS

Estimates of the surface composition were obtained from the Cs/TCNQ windmill and head-to-tail phases by comparing the photoionisation cross-section corrected peak areas from survey XP spectra

recorded at a photon energy of 850 eV (see Appendix D).[§] From this, Cs:TCNQ ratios of ~1.5 and ~2.0 were obtained for the windmill and head-to-tail phases respectively. The value obtained for the head-to-tail phase is in good agreement with the stoichiometry suggested by STM, whereas the value obtained for the windmill phase is moderately larger than the suggested 1:1 ratio. This could indicate that the windmill phase adopts a Cs_3TCNQ_2 stoichiometry or that excess Cs is present on the surface, though the Cs 3d spectrum (Figure 5.2.4) did not show any significant secondary component, which would be expected if excess Cs was present on the surface. It should be noted, that due to the relatively low energy resolution and low peak intensities obtained in the survey spectra, the associated error on the measured Cs:TCNQ ratio could be quite large. Surface composition estimates of the related K/TCNQ windmill phase suggested a K:TCNQ ratio of ~0.8, attributed to a nominal 1:1 stoichiometry with a significant density of vacant K sites. Due to the close similarity between the KTCNQ and CsTCNQ windmill phases, it is difficult to suggest reasons why they might have a different alkali metal/TCNQ stoichiometry. Since the stoichiometry estimates obtained for the K/TCNQ phase were obtained from high-resolution XP spectra they were considered more reliable than the values measured for Cs/TCNQ from the survey spectra. Considering all of these factors, it was concluded that a nominal 1:1 stoichiometry is most likely for the Cs/TCNQ windmill phase, despite the survey spectra suggesting a higher Cs:TCNQ ratio of ~1.5.

Figure 5.2.4 shows high-resolution soft XPS recorded from the CsTCNQ windmill phase. The C 1s spectrum shows at least three distinct peaks, which have been fitted with four components corresponding to the four chemically inequivalent C environments within the TCNQ molecule. The relative intensities of these components (shown in Table 5.2.1) are in reasonable agreement with the expected stoichiometry of each environment. The overall line shape of the C 1s spectrum and the relative binding energies of the fitted C 1s components are closely similar to those measured from the KTCNQ windmill phase and TCNQ adsorbed alone on Ag(111), which were both attributed to $TCNQ^-$ species. This indicates that TCNQ is also negatively charged with a $TCNQ^-$ charge state in the CsTCNQ windmill phase. The N 1s spectrum also reflects this, showing a single feature at a binding energy of 398.2 eV which is in good agreement with other systems (both in this thesis and elsewhere in the literature) in which TCNQ is negatively charged.[57, 175, 176] The Cs 3d spectrum shows peaks at binding energies of 724.8 eV and 738.8 eV for the Cs $3d_{5/2}$ and Cs $3d_{3/2}$ components respectively, which

[§] The high-resolution Cs 3d XP spectrum was measured using a different pass energy to the C 1s and N 1s spectra meaning that this data is not comparable and, consequently, could not be used to provide an estimate of the surface composition; the lower resolution survey spectra were used instead.

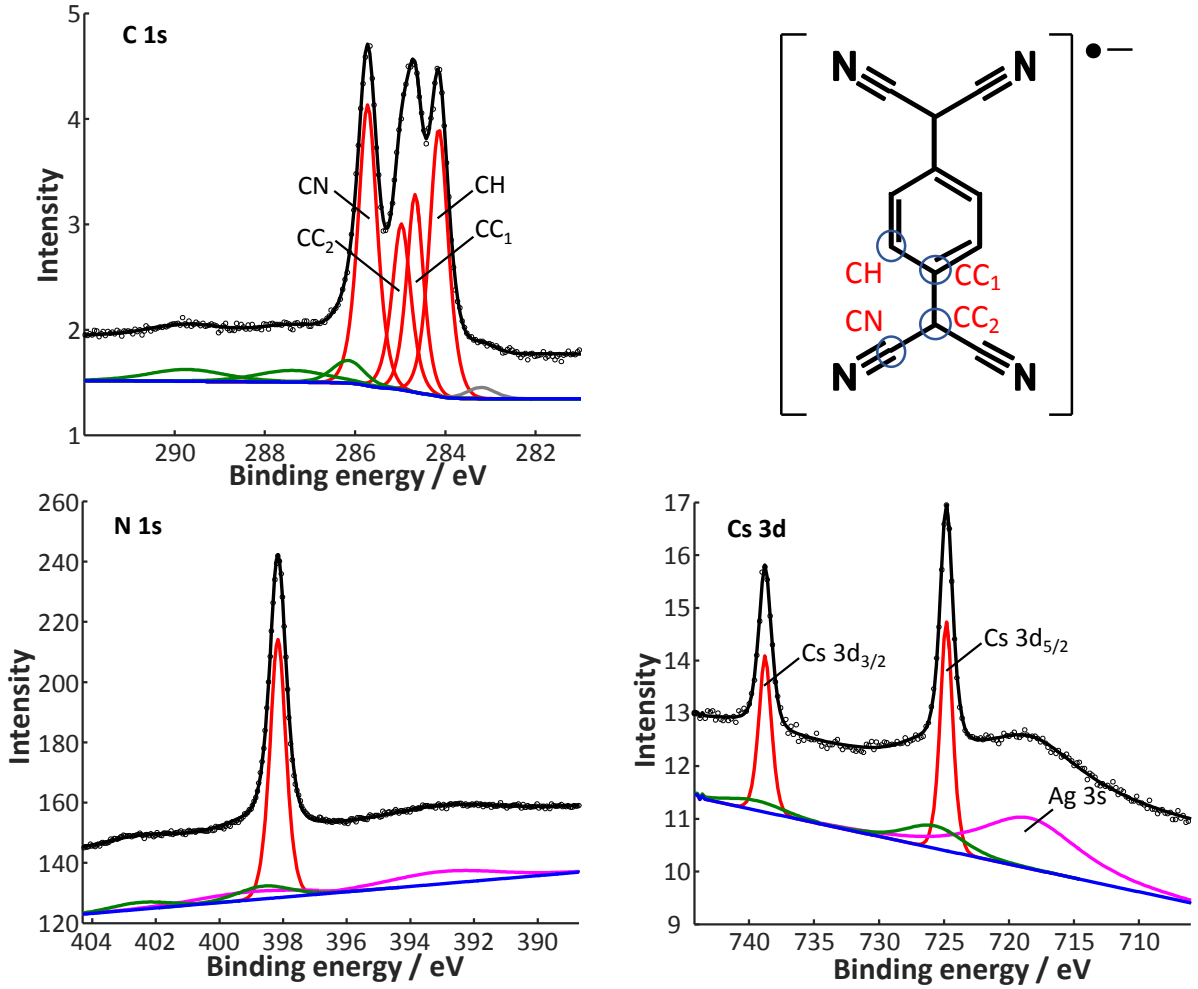

Figure 5.2.4 - Soft XPS recorded from the CsTCNQ windmill phase on Ag(111). The C 1s spectrum was recorded using a photon energy of 435 eV, showing measured intensity (black circles) and the sum of fitted components (black line) comprising a Shirley background (blue),[163] four main C 1s components (red), shakeup features (green) and a beam damage feature (grey). The schematic of the TCNQ molecule highlights the four different C environments to which the C 1s peaks are assigned. The N 1s spectrum was recorded using a photon energy of 550 eV, showing measured intensity (black circles), and the sum of fitted components (black line) comprising a linear background (blue), one main component (red), two N shakeup features (green) and two Ag 3d plasmon features (purple). The Cs 3d spectrum was recorded using a photon energy of 850 eV, showing measured intensity (black circles) and the sum of fitted components (black line) comprising a linear background (blue), a single split Cs 3d component (red), two shakeup features (green) and the Ag 3s emission peak (purple).

are in good agreement with values reported for ionic Cs^+.[192] For Cs adsorbed by itself on Ag(111), the Cs $3d_{5/2}$ and Cs $3d_{3/2}$ components were measured at binding energies of 725.6 eV and 739.6 eV. The Cs 3d binding energy thus shifts by 0.8 eV when incorporated into the TCNQ networks.

Table 5.2.1 – XPS measured binding energies of the main C 1s, N 1s and Cs 3d components from the CsTCNQ windmill phase. The relative intensities (peak areas) of the C 1s components are also shown.

Component	**CH**	**CC_1**	**CC_2**	**CN**	**Cs $3d_{3/2}$**	**Cs $3d_{1/2}$**	**N**
Binding energy / eV	284.1	284.7	285.0	285.7	724.8	738.8	398.2
Relative intensity	1.62	1.07	1.00	1.70	-	-	-

High-resolution soft XPS from the Cs_2TCNQ head-to-tail phase are shown in Figure 5.2.5. Like the windmill phase, the C 1s spectrum shows three distinct features that were fitted with four main components corresponding to the four chemically inequivalent C environments within the TCNQ molecule. Comparing the relative intensities of these fitted components (Table 5.2.2) shows reasonably good agreement with the expected stoichiometric ratio of the four C environments. For the related K_2TCNQ head-to-tail phase, XPS showed a significant deviation of the relative C 1s peak intensities from their expected stoichiometry, which was also observed in a related system which was believed to contain $TCNQ^{2-}$ species.[176] The absence of this for the Cs head-to-tail phase could indicate that a $TCNQ^{2-}$ species has not formed. This result would be surprising though as both the K and Cs head-to-tail TCNQ phases contain two alkali metal atoms per TCNQ molecule and Cs has an even lower ionisation energy than K so a $TCNQ^{2-}$ charge state would also be expected to form more easily in the Cs phase. The C 1s spectrum for the Cs_2TCNQ head-to-tail phase does show similar binding energies to those measured for the K_2TCNQ head-to-tail phase and also shows an increase of 0.2 eV to the energy separation between the CH and CN peaks compared to the CsTCNQ windmill phase. The binding energy shifts are therefore consistent with the formation of the $TCNQ^{2-}$ species that is expected from the Cs_2TCNQ stoichiometry. The reason for the peak intensities not deviating from the expected stoichiometric ratio, as was observed in this thesis for the K_2TCNQ head-to-tail phase and in the literature for thin films with intercalated Na atoms,[176] in which TCNQ is believed to adopt a $TCNQ^{2-}$ charge state, was not determined. The possibility of the main C 1s peaks overlapping shake-up features that are not included when fitting the XPS was suggested as one potential cause for the changes in the apparent stoichiometry. It could be possible that any such satellites features are present at different energies relative to the main C 1s peaks in the Cs_2TCNQ phase giving rise to the different relative peak intensities. Regardless, this result indicates that the deviation of the relative intensities from the expected stoichiometry is not characteristic of the $TCNQ^{2-}$ species.

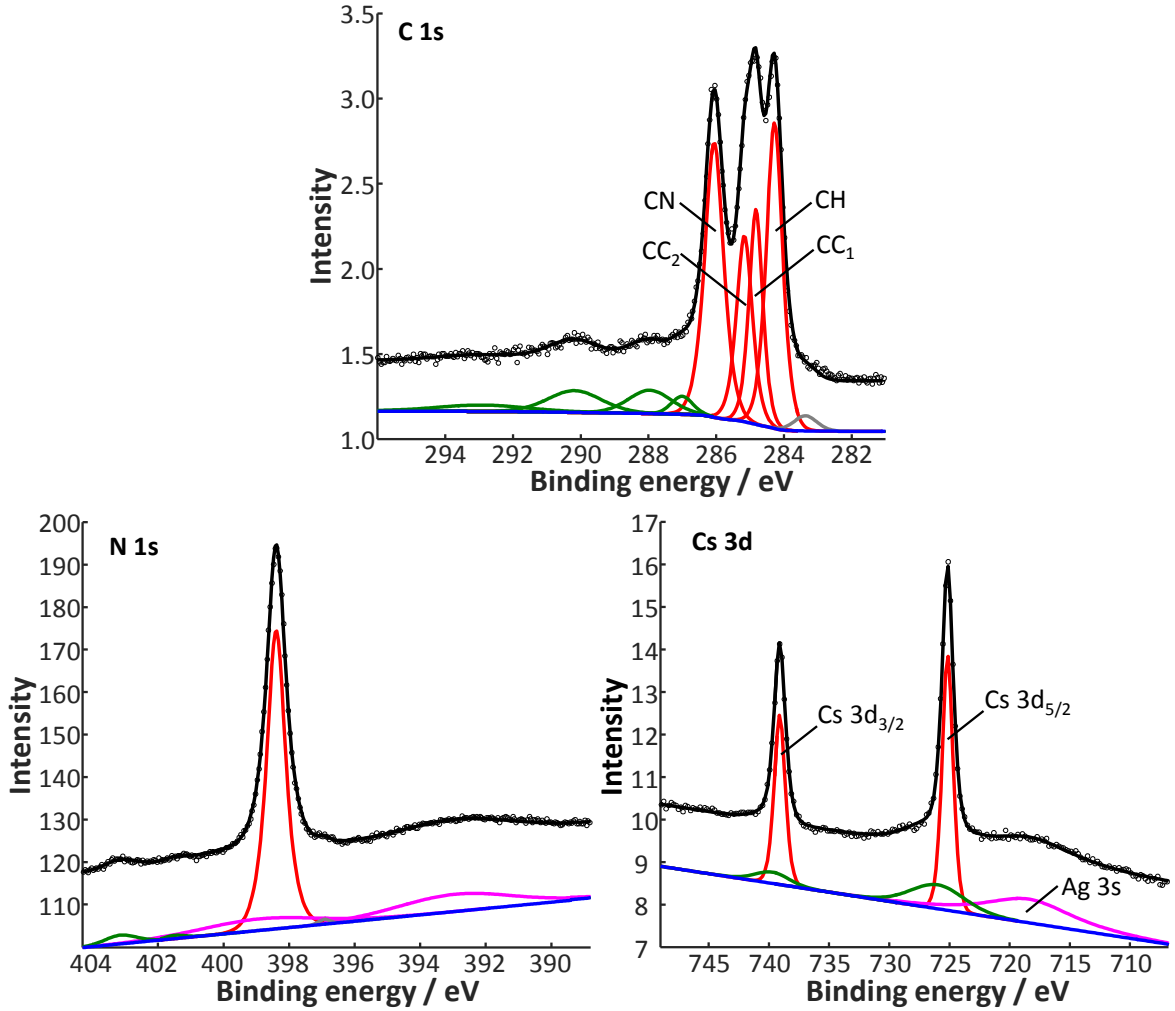

Figure 5.2.5 - Soft XPS from the Cs_2TCNQ head-to-tail phase. The C 1s spectrum was recorded using a photon energy of 435 eV, showing measured intensity (black circles) and the sum of fitted components (black line) comprising a Shirley background (blue),[163] four main C 1s components (red), shakeup features (green) and a beam damage feature (grey). The N 1s spectrum was recorded using a photon energy of 550 eV, showing measured intensity (black circles), and the sum of fitted components (black line) comprising a linear background (blue), one main component (red), two N shakeup features (green) and two Ag 3d plasmon features (purple). The Cs 3d spectrum was recorded using a photon energy of 850 eV, showing measured intensity (black circles) and the sum of fitted components (black line) comprising a linear background (blue), a single split Cs 3d component (red), two shakeup features (green) and the Ag 3s emission peak (purple).

The N 1s spectrum shows a single N peak at 398.4 eV, displaying a 0.2 eV increase in binding energy compared to the CsTCNQ windmill phase. This is also in reasonable agreement with previously studied systems in which a $TCNQ^{2-}$ species is believed to form.[176] For the analogous K/TCNQ phases, a larger binding energy shift of 0.5 eV was observed in the N 1s spectrum, which could indicate some differences in the TCNQ charge states for the different alkali metals. The Cs 3d spectrum for the

Cs_2TCNQ head-to-tail phase shows two Cs peaks at binding energies of 725.1 eV and 739.1 eV corresponding to the respective Cs $3d_{5/2}$ and Cs $3d_{3/2}$ components of a single Cs chemical shift. The head-to-tail phase Cs 3d peaks are therefore shifted to higher binding energy by 0.3 eV from the windmill phase, which is also qualitatively consistent with the formation of $TCNQ^{2-}$.

Table 5.2.2 – XPS measured binding energies of the main C 1s, N 1s and Cs 3d components for the head-to-tail phase. The relative intensities (peak areas) of the C 1s components are also shown.

Component	**CH**	**CC_1**	**CC_2**	**CN**	**Cs $3d_{3/2}$**	**Cs $3d_{1/2}$**	**N**
Binding energy / eV	284.3	284.8	285.2	286.1	725.1	739.1	398.4
Relative intensity	1.69	1.01	1.00	1.78	-	-	-

Figure 5.2.6 shows UPS recorded from the Cs/TCNQ windmill and head-to-tail phases formed on the Ag(111) surface, which show the same peaks exhibited by the pure TCNQ and K/TCNQ adsorption phases. These were attributed to valence TCNQ states, using the same assignment used by Precht *et al.*[175, 176] for alkali metal intercalated TCNQ thin films. The observation of these valence molecular states has previously been shown to be a characteristic of negatively charged TCNQ[57, 175, 176] and thus their presence here further supports that the molecules are negatively charged within the Cs/TCNQ adsorption phases. As the Cs coverage is increased, the TCNQ valence states corresponding to the former TCNQ HOMO and LUMO (marked by the dashed black lines in the right-hand panel of Figure 5.2.6) shift to higher binding energy, with an overall shift of ~0.4 eV observed between the Cs/TCNQ head-to-tail phase and the pure TCNQ phase. A similar effect and comparable shift was observed for the K/TCNQ adsorption phases as the K coverage was increased.

Table 5.2.3 shows work functions, measured by UPS, for the two Cs/TCNQ adsorption phases. These measurements show that the addition of Cs to the pure TCNQ adsorption phase, for which $\Phi = (5.02 \pm 0.05)$ eV, is accompanied by a significant decrease in the work function, with $\Phi = (4.00 \pm 0.05)$ eV measured from the Cs/TCNQ windmill phase. Subsequent deposition of Cs, resulting in the transition from the windmill to the head-to-tail phase, causes a further decrease in the work function to $\Phi = (3.58 \pm 0.05)$ eV. This considerable work function shift, to a value well below the $\Phi = (4.59 \pm 0.05)$ eV measured for clean Ag(111), is an indication that the Cs atoms are donating electrons to the surface and become positively charged. This result is consistent with the Cs/TCNQ networks being ionic in nature. Compared to their analogous K/TCNQ adsorption phases, the Cs/TCNQ adsorption phases exhibit a larger shift to the surface work function, which can be attributed to the lower ionisation energy of Cs.

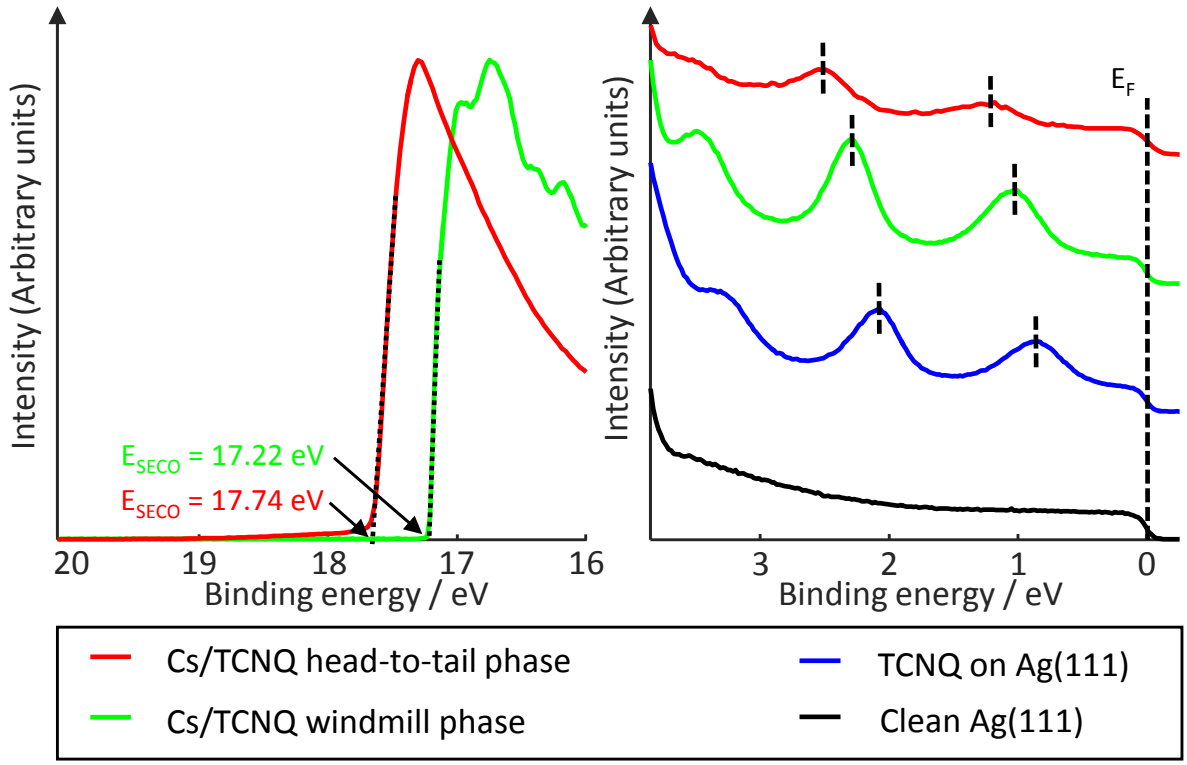

Figure 5.2.6 - UPS obtained from the Cs/TCNQ adsorption phases on Ag(111). The left panel shows measurements of the SECO, measured with a -10.0 V bias applied to the sample. The right panel shows the energy region close to the Fermi edge (E_F). For comparison, spectra obtained from the clean Ag(111) substrate and from a sample of TCNQ alone on Ag(111) are shown. Black dashed lines mark the centre of two molecular states in each spectrum to highlight the binding energy shifts. The intensity shown on the y-axis is arbitrary with the spectra scaled and offset relative to each other for clarity. The UPS obtained for the Cs/TCNQ head-to-tail phase was measured at Warwick using a different experimental geometry to the other spectra, which were recorded at the I09 beamline of Diamond Light Source (see section 2.8.5). Consequently, the relative intensities of features are not comparable. All binding energies are quoted relative to E_F. Measurements were obtained using the He-Iα (hv = 21.22 eV) emission line.

Table 5.2.3 – UPS measured work functions (Φ) measured from the Cs/TCNQ adsorption phases on Ag(111). Work functions were obtained by subtracting the SECO energy (E_{SECO}, as shown in Figure 5.2.6) from the photon energy (hv = 21.22 eV).

Sample	**Φ / eV**
CsTCNQ windmill phase	4.00 ± 0.05
Cs_2TCNQ head-to-tail phase	3.58 ± 0.05

5.2.3 NIXSW and structural models

Table 5.2.4 shows NIXSW measurements obtained from the CsTCNQ windmill phase and Cs adsorbed by itself on Ag(111) using the (111) reflection of the substrate. It should be noted that for this phase, coherent fractions close to and greater than unity were measured for the C components, which should not be possible. The cause of this issue is discussed in section 2.8.7 and consequently the error estimates on the measured coherent fractions throughout this thesis have been increased to accommodate this. Nonetheless, the NIXSW shows high coherent fractions (> 0.9) for all three C components, indicating that the molecule adopts a well-defined uniform height above the surface. There is also little variation between the coherent positions measured from the three C components, suggesting that the molecule adopts a relatively flat geometry at a height of ~2.8 Å above the surface. The N NIXSW also yields a relatively high coherent fraction of (0.79 ± 0.10), which, despite being lower than the observed C coherent fractions, is still reasonably consistent with a single adsorption height. The coherent position of N is slightly lower (~0.1 Å) than the C atoms, suggesting that the peripheral groups of the molecule bend slightly towards the surface.

Table 5.2.4 – NIXSW fitting parameters from the CsTCNQ windmill phase and Cs adsorbed by itself on Ag(111) using the (111) reflection of the substrate. Separate fitting parameters were obtained from the different C 1s photoemission components as defined in Figure 5.2.4 (due to lower resolution at the photon energies used for NIXSW, components CC_1 and CC_2 were fitted together in a single component here). The coherent position $D_{(111)}$ is given as $D_{(111)} = (P+1)d_{111}$ where P is the fractional coherent position and d_{111} is the spacing of the (111) lattice planes (2.359 Å). Values are averaged from measurements of two separate sample preparations with five repeat measurements recorded for each sample. Error estimates are shown in parentheses in units of 0.01.

Component	CsTCNQ windmill phase		Cs only	
	f_{co}	$D_{(111)}$ / Å	f_{co}	$D_{(111)}$ / Å
Cs	0.52(10)	3.64(5)	0.90(10)	2.91(5)
CH	1.01(10)	2.87(5)	-	-
CC	1.06(10)	2.83(5)	-	-
CN	0.96(10)	2.82(5)	-	-
N	0.79(10)	2.71(5)	-	-

NIXSW of Cs adsorbed by itself yielded a high coherent fraction of (0.90 ± 0.10) indicating that Cs adsorbs at a uniform height above the surface, given by the coherent position, of (2.91 ± 0.05)Å, which is in excellent agreement with the results of a quantitative LEED structural determination for Cs on Ag(111).[193] In contrast, the Cs NIXSW from the CsTCNQ windmill phase shows a significantly lower

coherent fraction of (0.52 ± 0.10). This value is lower than can be typically be attributed to thermal vibrations alone and this suggests that Cs occupies two or more heights above the surface. The corresponding coherent position gives an adsorption height of (3.64 ± 0.05) Å, indicating that, on average, the Cs atoms adsorb above the TCNQ molecules in the windmill structure.

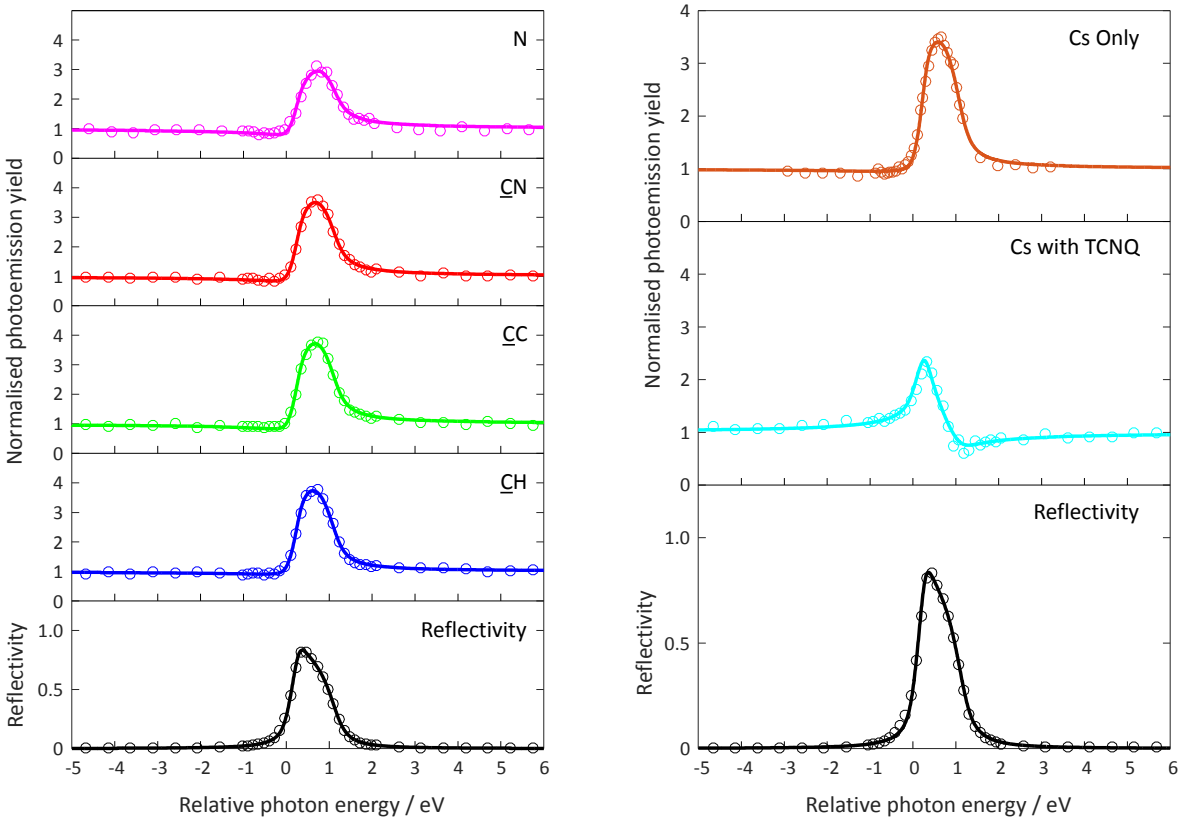

Figure 5.2.7 - Sample set of NIXSW photoemission yield curves obtained from the CsTCNQ windmill phase, in addition to Cs adsorbed by itself on Ag(111), using the (111) reflection of the substrate. Photon energies are quoted relative to the Bragg energy of 2.630 keV. Least square fits (solid lines) to the photoemission yields (circles) were obtained to extract the coherent fractions and coherent positions.

Due to the similarities observed between the KTCNQ and CsTCNQ windmill phases in LEED, STM and XPS, the NIXSW results for the two phases were also expected to be closely related. Indeed, the C NIXSW for the two phases shows that the molecule adsorbs in a relatively flat geometry at a height of ~2.8 Å. However, the NIXSW measurements from the N, K and Cs components highlight some clear differences between the two phases. One such difference is that a significantly greater coherent fraction was measured for N in the CsTCNQ windmill phase than in its K analogue. In the KTCNQ phase, the low N coherent fraction of (0.41 ± 0.10) was attributed to the N atoms adopting two distinctly different heights above the surface caused by some CN groups pointing up whilst others point down. For the CsTCNQ phase, the measured N coherent fraction of (0.79 ± 0.10) is more consistent with the N atoms

occupying a uniform height above the surface. It is worth noting that, within the quoted error range, it is still possible for the N coherent fraction to correspond to two equally occupied adsorption heights separated by a vertical distance of up to (0.41 ± 0.16) Å, though this is a limiting case that does not account for reduction to the coherent fraction caused by absorber atom vibrations. Indeed, for a single adsorption height, a rms vibrational amplitude of (0.22 ± 0.09) Å would reduce the coherent fraction to the measured value. Whilst this vibrational amplitude is seemingly large, as discussed previously, this only corresponds to a relatively small rotational amplitude (i.e. < 2°) due to the structure of the molecule.

The behaviour of the alkali metals is also different between the K and Cs TCNQ windmill phases. In the KTCNQ windmill phase, the NIXSW suggests that the K atoms occupy a uniform height of (3.56 ± 0.05) Å above the substrate. In contrast, NIXSW measurements of the Cs windmill phase give a low Cs coherent fraction, suggesting that the Cs atoms occupy a larger distribution of heights above the surface, with an average height of (3.64 ± 0.05) Å given by the measured coherent position. If the Cs atoms occupy a single adsorption height, a substantial rms vibrational amplitude of (0.41 ± 0.07) Å would be required to reduce the coherent fraction to the measured value. A more reasonable explanation of the low coherent fraction is that the Cs atoms occupy two or more heights above the surface. As the Cs windmill phase contains two Cs atoms per unit cell, it is possible that Cs atoms could adsorb at distinctly different heights in each of these sites. In this scenario, two Cs heights differing by up to (0.74 ± 0.10) Å would be needed to reduce the coherent fraction to the measured value, though because thermal vibrations will cause some reduction of the coherent fraction, the actual separation is expected to be lower than this value. Comparison of the K and Cs coherent positions indicates that on average the Cs adsorbs ~0.1 Å higher above the surface than K in their respective windmill phases. This result qualitatively agrees with DFT calculations of similar TCNQ alkali metal structures formed on the surface of Ag(100) for which the larger alkali metals were found to adsorb further above the TCNQ molecules.[168]

To try and rationalise the structural features identified by NIXSW, particularly those corresponding to low coherent fractions, a structural model of the CsTCNQ windmill phase was constructed (Figure 5.2.8) based on the molecular assembly observed by STM (as shown in Figure 5.2.2). Due to the relatively diffuse nature of the features observed in the STM images, there is some ambiguity in the molecular orientations and exact positions of the TCNQ and Cs atoms within the mesh so the model was constructed by using simple geometric arguments, assuming that the Cs atoms and TCNQ molecules are equally spaced from one another. The vertices of the unit mesh were placed on one set of the Cs atoms and it was assumed that the other Cs atom is located at the centre of the unit mesh. The

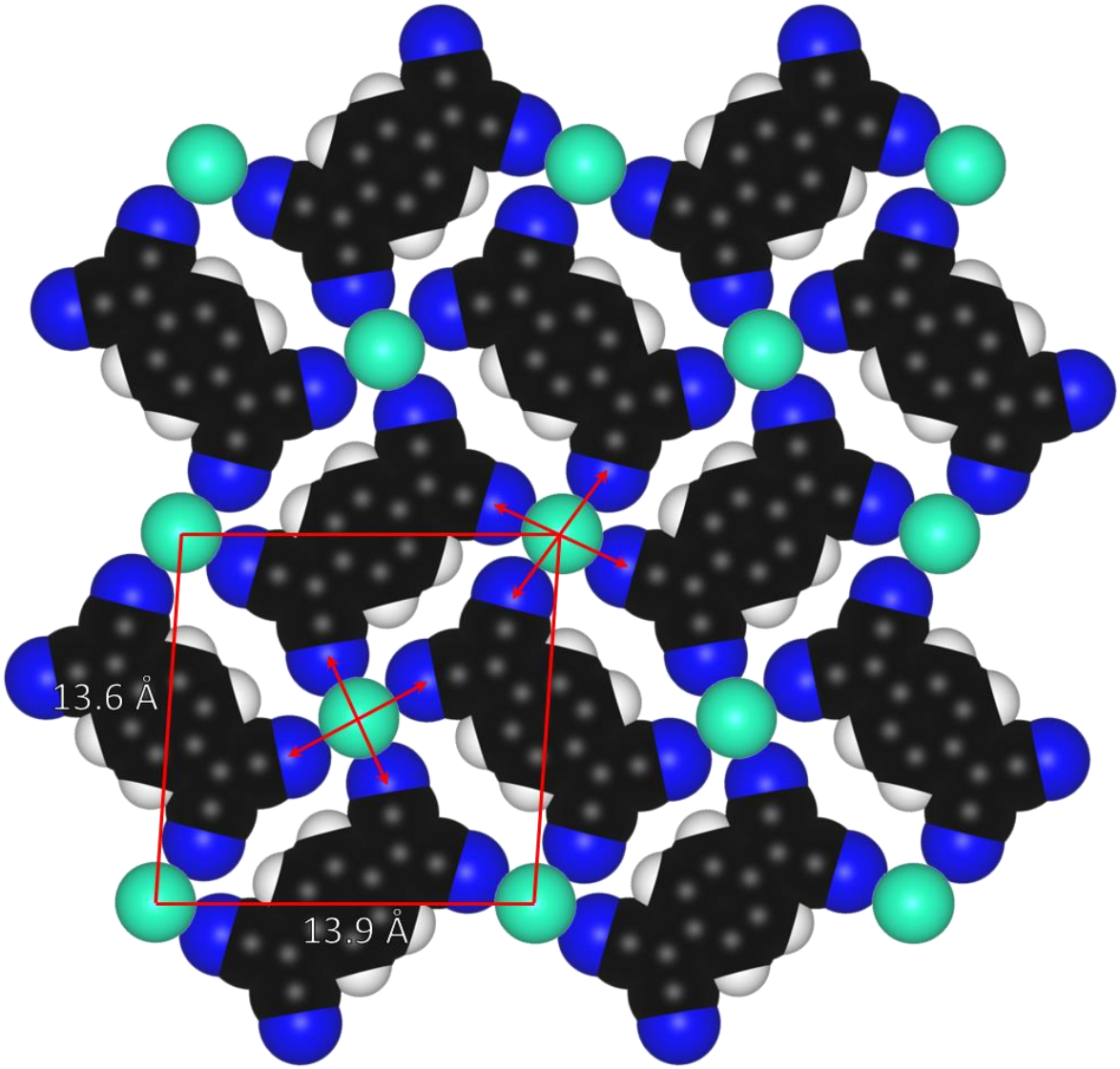

Figure 5.2.8 – Plan view of a scaled structural model constructed for the CsTCNQ windmill phase derived from STM measurements. The surface unit mesh is indicated by the red rhombus. H atoms are coloured white, N atoms blue, C atoms black and Cs atoms green. The TCNQ molecules are shown as space-filled models with the atom sizes scaled to their corresponding van der Waals radii.[41] The Cs atoms are scaled to the Cs^+ ionic radius.[187] The red arrows indicate the spacings between opposite N atoms at each Cs adsorption site. Visualisations were produced using the open-access software package VESTA.[181]

TCNQ molecules were then oriented along the rows of Cs atoms and were positioned in the centre of the rhombuses made by the Cs atoms to yield a model that shows good qualitative agreement with the STM image contrast. In the model shown in Figure 5.2.8, the atoms are represented by spheres corresponding to the van der Waals radii (1.70 Å, 1.55 Å and 1.20 Å for C, N and H respectively)[41] for the TCNQ molecules and to the ionic radius (1.67 Å)[187] for Cs^+. As the model should therefore give a

good representation of the size of the atoms, it is clear that the centres of the TCNQ windmills are not large enough to accommodate Cs in a coplanar geometry. The larger average adsorption height measured for Cs compared to the TCNQ molecules is qualitatively consistent with the Cs atoms resting on top of the N atoms at the centres of the windmills.

The NIXSW measurements suggest that on average, the Cs atoms occupy a height of (0.9 ± 0.1) Å above the N atoms. Using the minimum Cs-N separation of 3.07 Å obtained from the Cs_2TCNQ_3 bulk crystal structure[194] and assuming that the N atoms all occupy the same height, a diagonal N-N separation of at least 5.8 Å is required for the Cs atoms to occupy the height of (3.64 ± 0.05) Å measured by NIXSW. In the proposed model, the N-N diagonal distances (indicated by the red arrows in Figure 5.2.8) are 5.5 Å and 5.9 Å for the Cs site at the corners of the unit mesh and 5.8 Å and 5.3 Å for the Cs site at the centre of the unit mesh. As the Cs height is determined by the shortest N-N diagonal distance, the model suggests that the Cs atoms should occupy a height greater than that measured by NIXSW. This is further complicated by the low coherent fraction measured for Cs, which indicates that a significant proportion of the Cs atoms adsorb even closer to the surface than this average value. It should be noted that measured N coherent fraction of (0.79 ± 0.10) could correspond to two distinct N heights separated by up to (0.41 ± 0.16) Å to create an asymmetrical adsorption site, similar to the structure proposed for the KTCNQ windmill phase and this could allow Cs to adsorb closer to the surface. Furthermore, the exact orientations of the TCNQ molecules and positions of the Cs atoms could not be determined from the STM and so it is possible that the pores in the molecular adsorption structure are larger than those in the proposed model. However, even if this were the case, the model does not suggest any obvious reasons for Cs to occupy two or more distinctly different heights above the surface, as indicated by the NIXSW measurements. This may highlight that there are some significant differences between the two Cs sites in the structure that have not been accounted for in the model. Despite the high-resolution Cs 3d XPS only appearing to show a single significant component, it could also be possible that excess Cs atoms are present on the surface without showing a detectable chemical shift. Consequently, one possible cause of the low Cs coherent fraction could be the presence of excess Cs on the surface adsorbed at a distinctly different height to the Cs atoms within the networks.

Table 5.2.5 shows NIXSW measurements from the Cs_2TCNQ head-to-tail phase, obtained using the (111) reflection of the Ag(111) substrate. High coherent fractions were measured from the CH and CC components, suggesting that the core of the molecule adsorbs relatively parallel to the surface at a height, given by the corresponding coherent positions, of (2.89 ± 0.05) Å. Moving towards the extremities of the molecule, the coherent fraction decreases, with the CN and N components giving

Table 5.2.5 - Averaged NIXSW fitting parameters obtained from the Cs_2TCNQ head-to-tail phase using the (111) reflection of the Ag(111) substrate. Separate fitting parameters were obtained for the different C 1s photoemission components identified in Figure 5.2.5 (due to lower energy resolution at the photon energies required for NIXSW, components CC_1 and CC_2 were fitted together in a single component here). The coherent position $D_{(111)}$ is given as $D_{(111)} = (P+1)d_{111}$ where P is the fractional coherent position and d_{111} is the spacing of the (111) lattice planes (2.359 Å). Values are averaged from measurements of two separately prepared samples, with a total of eight repeat measurements. Error estimates are shown in parentheses in units of 0.01.

Component	Cs_2TCNQ head to tail phase	
	f_{co}	$D_{(111)}$ / Å
Cs	0.79(10)	3.40(5)
CH	0.90(10)	2.89(5)
CC	0.80(10)	2.89(5)
CN	0.67(10)	3.09(5)
N	0.41(10)	3.05(5)

values of (0.67 ± 0.10) and (0.41 ± 0.10) respectively. This indicates that, in contrast to the core of the molecule, the peripheral groups occupy a broad distribution of heights above the surface. The corresponding coherent positions of (3.09 ± 0.05) Å and (3.05 ± 0.05) Å show that, on average, the peripheral groups are bent away from the surface. A high coherent fraction of (0.79 ± 0.10) was measured for Cs, which is consistent with a single adsorption height throughout the structure given by the corresponding coherent position of (3.40 ± 0.05) Å. This shows that in the head-to-tail phase, the Cs atoms adsorb significantly further from the surface than for Cs adsorbed by itself on Ag(111) but adsorb closer to the surface than in the CsTCNQ windmill phase. The alkali metal adsorption heights therefore follow the same trend observed for K in the analogous adsorption structures.

As the STM, LEED and XPS highlighted numerous similarities between the Cs and K head-to-tail phases, it was expected that the NIXSW measurements for the two phases would also be closely related. This was reflected in the coherent positions measured for the C and N components for both phases, which indicate that the peripheral cyano groups of the TCNQ molecule are, on average, tilted away from the surface. This contrasts with the corresponding windmill phases, for which the peripheral groups, on average, tilt slightly towards the surface. The trend in coherent fractions is also qualitatively similar for both head-to-tail phases, with the central CH component of the molecule affording the highest value, with progressively lower coherent fractions measured for each component moving towards the cyano groups at the extremities of the molecule. As was the case with the K_2TCNQ

head-to-tail phase, this indicates that the constituent atoms of TCNQ occupy a larger distribution of adsorption heights the further they are from the centre of the molecule. The cause of this increasing height distribution could not be precisely determined for the K_2TCNQ head-to-tail phase, though thermal vibrations causing the peripheral groups to tilt up and down was found to be a plausible explanation. Similar thermal vibrations could therefore be a possible cause of the trend in coherent fractions observed for the Cs_2TCNQ head-to-tail phase.

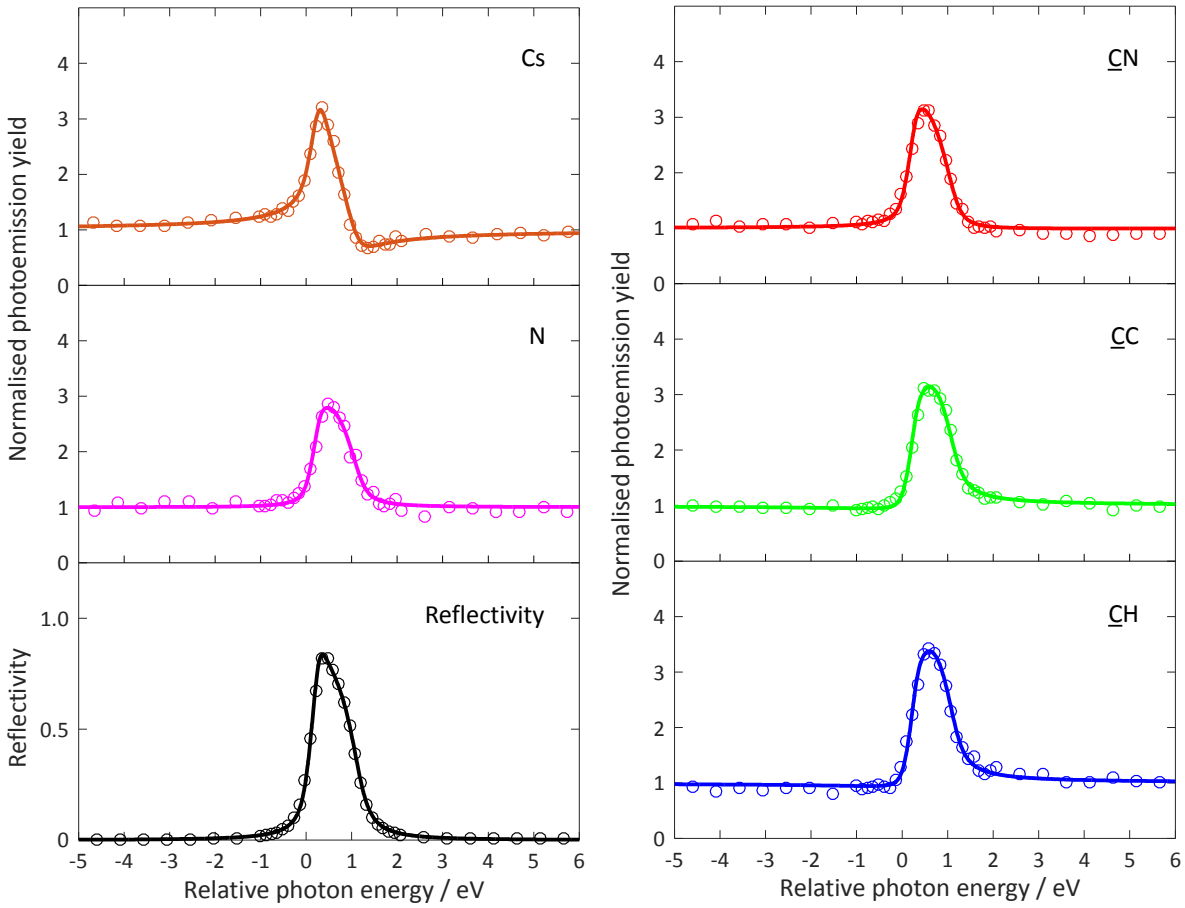

Figure 5.2.9 - Sample set of NIXSW photoemission yield curves obtained from the Cs_2TCNQ head-to-tail phase using the (111) reflection of the Ag(111) substrate. Photon energies are quoted relative to the Bragg energy of 2.630 keV. Least square fits (solid lines) to the photoemission yields (circles) were obtained to extract the coherent fractions and coherent positions.

Some differences were also observed in the NIXSW results for the K and Cs head-to-tail-phases. In the Cs head-to-tail structure, TCNQ adsorbs with the N atoms considerably closer (on average by (0.21 ± 0.10) Å) to the surface than in the analogous K structure, indicating that the tilting of the cyano groups away from the surface occurs to a lesser extent in the Cs head-to-tail phase. Furthermore, Cs adsorbs higher above the surface than K in the respective head-to-tail adsorption phases, which is

qualitatively consistent with DFT calculations reported for similar TCNQ/alkali metal networks.[168] These calculations suggest that larger alkali metal atoms, due to their lower ionisation potential, are more effective at counteracting the dipoles produced by the negatively charged TCNQ molecules and achieve this by adsorbing at an elevated height to generate a larger dipole moment of opposite polarity.[168] The difference in adsorption height could also simply correspond to the fact that Cs has a larger ionic radius than K.

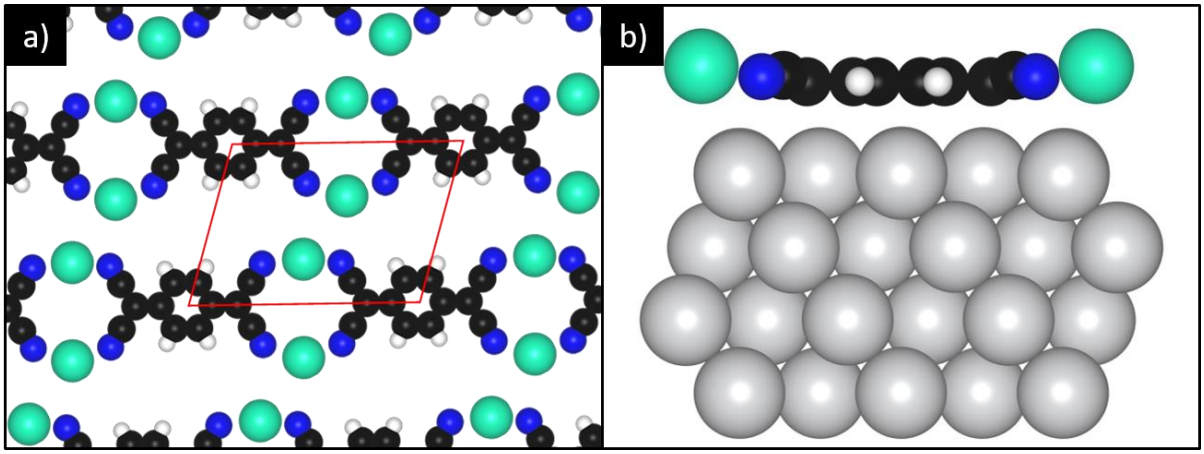

Figure 5.2.10 – Proposed structural model for the Cs_2TCNQ head-to-tail phase based on the interpretation of STM images (see Figure 5.2.3). a) Top view of the proposed structural model (substrate atoms not shown), with the surface unit mesh indicated by the red parallelogram. The internal bond angles and bond lengths are taken from the bulk crystal structure of TCNQ. The radii of the atoms/ions shown are not to scale. b) Side view of the proposed structural model with adsorption heights taken from the NIXSW coherent positions. Radii of atoms/ions shown are not to scale. Visualisations were produced using the open-access software package VESTA.[181]

To further analyse the NIXSW results, a structural model for the Cs_2TCNQ head-to-tail phase was constructed (Figure 5.2.10), based on the contrast observed in STM images. Due to the relatively diffuse nature of the features observed in the STM images, there is some ambiguity in the molecular orientations and exact positions of the TCNQ and Cs atoms within the cell, however some useful insight into the adsorption structure can still be extracted from this model. In this model the Cs atoms occupy twofold sites between the cyano groups. This differs from the K head-to-tail phase and the K and Cs windmill phases, which all feature the alkali metal in a site surrounded by four TCNQ cyano groups. This could give a possible explanation as to why in the Cs head-to-tail phase, the cyano groups are not lifted as far from the as in the corresponding K phase, as each N atom interacts with fewer alkali metal atoms. Figure 5.2.10b shows a side view of the proposed Cs_2TCNQ head-to-tail phase structural model which was constructed using the adsorption heights suggested by the NIXSW coherent positions. However, while the NIXSW for the Cs, CH and CC components were all consistent with a single uniform adsorption height, the CN and N components yielded relatively low coherent fractions suggestive of a

distribution of adsorption heights. In the K_2TCNQ head-to-tail phase, a similar trend in coherent fraction was best reconciled by thermal vibrations causing the peripheral groups to tilt up and down, which is also compatible with the NIXSW results here. As this Cs head-to-tail phase is incommensurate with respect to the underlying Ag(111) substrate, it is not possible to explicitly model its structure using dispersion corrected DFT calculations and gain further insight into the structural features highlighted by NIXSW. Consequently, it is difficult to assess whether the molecule does, adopt the conformation shown in Figure 5.2.10b with the reductions in the coherent fractions caused by thermal motion, or whether the low coherent fractions occur due to the molecule adsorbing in a twisted or tilted geometry on the surface. As dispersion corrected DFT calculations of the closely similar K_2TCNQ head-to-tail phase indicated that the lowest energy structure did not feature the molecule in a tilted or twisted geometry, it was concluded that the low coherent fractions in the Cs_2TCNQ head-to-tail phase are most likely to be caused by thermal vibrations.

5.3 General discussion and conclusions

Codeposition of TCNQ and alkali metals on Ag(111) results in the formation of charge-transfer networks. Different structures could be accessed by varying the TCNQ/alkali metal stoichiometry, with both K and Cs producing windmill and head-to-tail assemblies for nominal alkali metal/TCNQ ratios of 1:1 and 2:1 respectively. For Cs, an additional ordered phase with a large unit mesh was formed at a Cs:TCNQ ratio of < 1, for which no equivalent K/TCNQ phase was observed. Instead, relatively low K coverages resulted in the formation of the windmill phase with an apparently large density of vacant K sites. In all of the measured phases, XPS and UPS measurements suggested that the TCNQ molecules are negatively charged and the alkali metals adsorb as positively charged ions. The XPS also suggested that in the windmill phases, TCNQ adopts a $TCNQ^-$ charge state whereas a $TCNQ^{2-}$ charge state is adopted in the head-to-tail phase. In all phases, the alkali metal/TCNQ stoichiometry reflects the number of positive counterions required to stabilise the TCNQ charge state.

UPS work function measurements showed that the surface work function decreased significantly with increasing alkali metal coverage, further demonstrating that the alkali metals donate electrons to the surface to form K^+/Cs^+ species. In the respective windmill and head-to-tail phases for the different alkali metals, Cs lowered the work function more than K. This result was attributed to Cs having a lower ionisation potential than K and is consistent with the results of DFT calculations reported for similar TCNQ/alkali metal networks on Ag(100).[168] These DFT calculations reported by Floris *et al.* also predict that the charge-transfer responsible for these work function shifts have implications on the surface structure,[168] the conclusions of which will be discussed here. On the surface of Ag, TCNQ molecules accept electrons from the substrate, becoming negatively charged[57] and this, along with the

corresponding image charge in the metal surface, forms a negative dipole.[168] Coadsorbed alkali metal atoms become positively charged and thus act as local positive dipoles that screen the surrounding negative dipoles associated with the TCNQ molecules.[168] One consequence of this is that the alkali metal ions occupy elevated heights above the surface as this creates a larger positive dipole moment to better compensate the negative dipoles.[168] Moreover, the extent of this compensation of dipoles is dependent on the alkali metal used, as larger alkali metals have lower ionisation energies and are able to screen the negative dipoles more effectively, resulting in a larger work function shift.[168] This is realised by the larger alkali metals adsorbing further above the surface thus generating a greater positive dipole moment.[168]

The NIXSW measurements presented in this chapter show that in all of the measured phases, the alkali metal ions occupy an elevated height above the surface that is significantly greater than when the alkali metal is adsorbed alone on Ag(111). Furthermore, Cs was found to adsorb further from the surface than K in their respective windmill and head-to-tail structures. Both of these observations are consistent with the dipole moment effects predicted by the DFT calculations.[168] An alternate explanation for the elevated heights adopted by the alkali metals could simply be that they are resting on top of the molecular layer and in this scenario, Cs adsorbing higher above the surface than K in comparable structures could be due to its larger ionic radius.[187] Indeed, for the studied phases, the alkali metal height was consistent with the alkali metals lying in close contact with the N atoms. However, the measurements obtained for the head-to-tail phases in particular indicate that the TCNQ cyano groups are actively lifted away from the surface compared to the pure TCNQ structure on Ag(111), which suggests that the alkali metals preferentially adopt an elevated height above the surface.

Another interesting observation is that the alkali metal adsorption heights are lower in the head-to-tail phases compared to the windmill phases, which could indicate that the alkali metal height decreases as its coverage increases. This possible trend can also be rationalised with similar dipole moment arguments to those described earlier,[168] as with an increased number of alkali metal ions, a smaller positive dipole moment is required per ion to screen the negative dipoles associated with TCNQ accepting electrons from the substrate. Consequently, the alkali metal ions wouldn't need to occupy such an elevated height above the surface, which is consistent with the lower adsorption heights measured by NIXSW at higher alkali metal coverages.

The NIXSW measurements indicated that the TCNQ conformation varies between the different TCNQ/alkali metal networks. One feature common to all of the measured structures is that the central quinoid ring of the molecule adsorbs relatively parallel to the surface at a height of ~2.9 Å. In both windmill phases, the coherent positions indicate that, on average, the cyano groups are angled slightly

towards the substrate, whereas in the head-to-tail phases, the cyano groups are bent up away from the substrate. This difference was attributed to the increased alkali metal coverage in the head-to-tail phases resulting in more interactions between the cyano groups and the alkali metals located above the molecules causing the cyano groups to be lifted further from the substrate.

For the KTCNQ windmill phase, high coherent fractions and comparable coherent positions were measured for all C components suggesting that the molecule adsorbs in a relatively flat geometry. However, the low coherent fraction measured for N clearly shows that the N atoms occupy two or more different heights above the surface. The simplest model for the windmill assembly that is compatible with the NIXSW measurements has the central TCNQ ring essentially parallel to the surface, with the peripheral moieties twisted such that out of the four CN groups surrounding each K ion, one adjacent pair point up and the other pair point down. This proposed model bears a close resemblance to the bulk crystal structure of KTCNQ which includes layers of TCNQ arranged in similar windmills around out-of-plane K^+ ions, with the molecules tilted so that some CN groups point up while others point down.[186]

While the CsTCNQ windmill phase is similar to its K counterpart, the NIXSW measurements highlight some key structural differences between the two phases other than the previously discussed differences in alkali metal adsorption height. Most notably, the CsTCNQ phase has a high coherent fraction for N but a low coherent fraction for the alkali metal whereas the opposite was true for the KTCNQ phase. The high N coherent fraction indicates that the out-of-plane twisting of the CN groups, identified to be a key feature of the KTCNQ phase, is significantly less pronounced or does not occur in the CsTCNQ phase. The low Cs coherent fraction is lower than can typically be attributed to thermal vibrations and suggests the occupation of two or more distinctly different adsorption heights. As there are two Cs sites within the surface mesh, one possibility could be that the Cs atoms in these two sites occupy distinctly different heights above the surface. However, the substantial height difference required to reduce the coherent fraction to the measured value is not consistent with the relatively uniform height of the cyano groups suggested by the high coherent fractions measured for the CN and N components. This suggests that some other factors may contribute significantly to the low Cs coherent fraction or that the proposed model does not provide a good description of the adsorption phase. It should be noted that XPS estimates of the surface composition did suggest that an excess of Cs was present on the surface in this phase.

In the head-to-tail phases for both K and Cs, the measured coherent fractions decrease towards the extremities of the TCNQ molecule, indicating that the central quinoid ring occupies a single well-defined height but moving towards the peripheral cyano groups, the distribution of heights

occupied increases. As the K_2TCNQ head-to-tail phase is commensurate with respect to the underlying Ag(111) substrate, dispersion corrected DFT calculations (performed by Reinhard Maurer) were obtained to provide further insight into the low coherent fractions. The calculated structures showed excellent agreement with the measured coherent positions but did not show any structural features that could account for the low measured coherent fractions. However, it was determined that, due to the structure of TCNQ, the trend in coherent fractions could be reconciled if thermal vibrations could cause the peripheral 'arms' of the molecule to tilt up and down by relatively small angles (i.e. < 4°), comparable to vibrations observed in the bulk crystal structure of TCNQ.[157, 191]

6. TCNQ on Ag(100)

In the literature, it is generally accepted, based on the results of DFT calculations, that TCNQ adopts a bent conformation when adsorbed on coinage metal surfaces, with the peripheral cyano groups of the molecule pointing down to bond with the substrate.[17, 128, 129, 164, 165] However, experimental structural measurements presented earlier in this thesis (chapter 4) found that on the Ag(111) surface, TCNQ adopts a much flatter geometry that results from the incorporation of Ag adatoms from the substrate into the adsorption layer. The possible inclusion of substrate adatoms in adsorption structures formed by TCNQ on other substrates has generally not been explored (with one notable exception)[129] and since there are also no published quantitative experimental structural measurements for these TCNQ adsorption phases, it is difficult to establish how widespread this phenomenon might be. The measurements presented in this chapter expand upon this by characterising the adsorption structures formed by TCNQ on Ag(100). Moreover, these measurements also provide a useful reference for the results presented in chapter 7 in which networks formed by co-deposition of TCNQ and alkali metals on Ag(100) were studied.

6.1 STM and LEED

On the Ag(100) surface, TCNQ was found to form five distinct ordered phases under different preparation conditions. To aid in later discussion, Table 6.1.1 gives a summary of these adsorption phases, detailing their unit mesh dimensions and the preparation conditions used to form them. Each phase has also been assigned a number along with a descriptor, which will both be used to refer to them in this section (e.g. High-density phase 2, Windmill phase 4, etc.).

Deposition of TCNQ onto a clean Ag(100) substrate was monitored by LEED (Figure 6.1.1), which displays two distinctly different diffraction patterns depending on the coverage deposited. These LEED patterns correspond to low-density phase 1 and high-density phase 2 respectively. The same LEED patterns have been reported previously for TCNQ on Ag(100) by Feyer *et al.* and were attributed to adsorption structures with unit meshes described by a commensurate $\begin{pmatrix} 1 & 4 \\ -3 & -1 \end{pmatrix}$ matrix at lower coverages and an incommensurate $\begin{pmatrix} 0.58 & -2.92 \\ 3.02 & 0.92 \end{pmatrix}$ matrix at higher coverages.[163] Feyer *et al.* also report that annealing high-density phase 2 to a temperature of 310 °C results in a transition to low-density phase 1, possibly suggesting that this low-density phase is favoured thermodynamically.[163]

Table 6.1.1 – Summary of the TCNQ adsorption phases characterised by STM and LEED on Ag(100) and the preparation conditions used to form them. The STM measured unit mesh dimensions are given where b_1 and b_2 are the vector lengths, γ is the included angle and Θ is the angle between vector b_1 and the substrate <110> directions. Associated errors for the unit mesh dimensions are shown in parentheses and give the uncertainty on the last significant figure of the quoted value. Matrices consistent with the STM measured unit mesh dimensions are also shown for each phase.

Phase	Descriptor	b_1 / Å	b_2 / Å	γ / °	θ / °	Matrix	Preparation conditions
1	Low-density	11.8(3)	9.1(3)	123(4)	77(2)	$\begin{pmatrix} 1 & 4 \\ -3 & -1 \end{pmatrix}$	Deposition of TCNQ at a coverage lower than a saturated monolayer (pure phase) or annealing high-density phase 2 to 310 °C (forms in a mixture of phases).
2	High-density	9.1(3)	9.0(1)	97(2)	8(2)	$\begin{pmatrix} 0.43 & -3.05 \\ 3.06 & 0.76 \end{pmatrix}$	Deposition of TCNQ at a coverage beyond a saturated monolayer of low-density phase 1.
3	High-density	20.3(4)	12.0(1)	98(2)	22(2)	$\begin{pmatrix} 6.51 & 2.63 \\ -2.08 & 3.60 \end{pmatrix}$	Annealing high-density phase 2 to temperatures between 280-310 °C.
4	Windmill	27(1)	25(1)	101(2)	33(2)	$\begin{pmatrix} 7.84 & 5.09 \\ -6.01 & 6.22 \end{pmatrix}$	Annealing low-density phase 1 to temperatures between 260-340 °C (forms in a mixture of phases).
5	Windmill	26(1)	27(1)	94(2)	18(2)	$\begin{pmatrix} 8.56 & 2.78 \\ -3.50 & 8.66 \end{pmatrix}$	Annealing low-density phase 1 to 340 °C (forms in a mixture of phases).

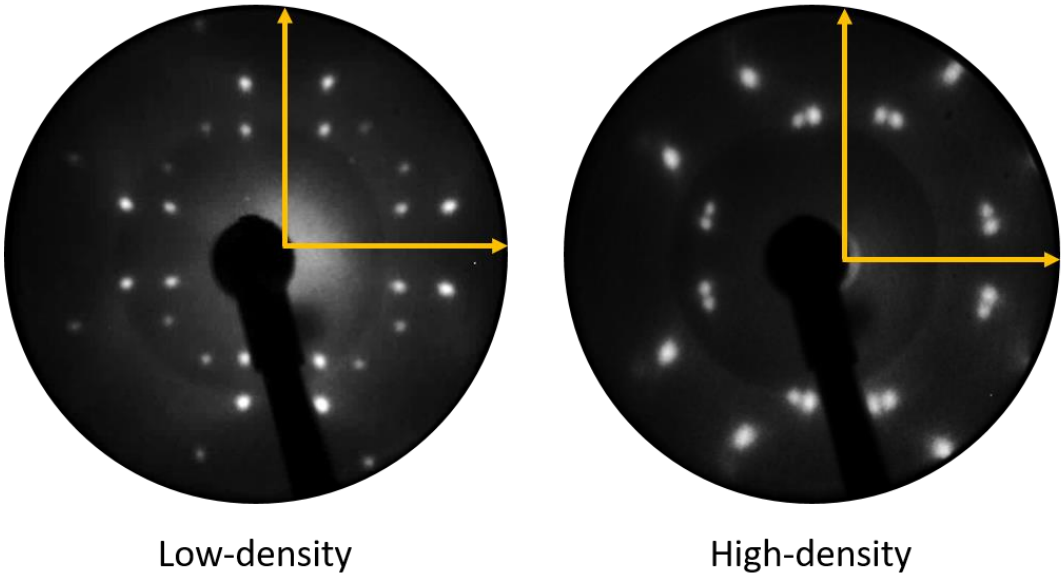

Figure 6.1.1 – LEED patterns recorded from two different coverages of TCNQ deposited onto a clean Ag(100) substrate. The low coverage phase is assigned to a low-density structure, which transitions to a high-density structure when the TCNQ coverage is increased.[163] Both LEED patterns were recorded with an electron kinetic energy of 14.5 eV. The substrate <110> directions are indicated by the yellow arrows.

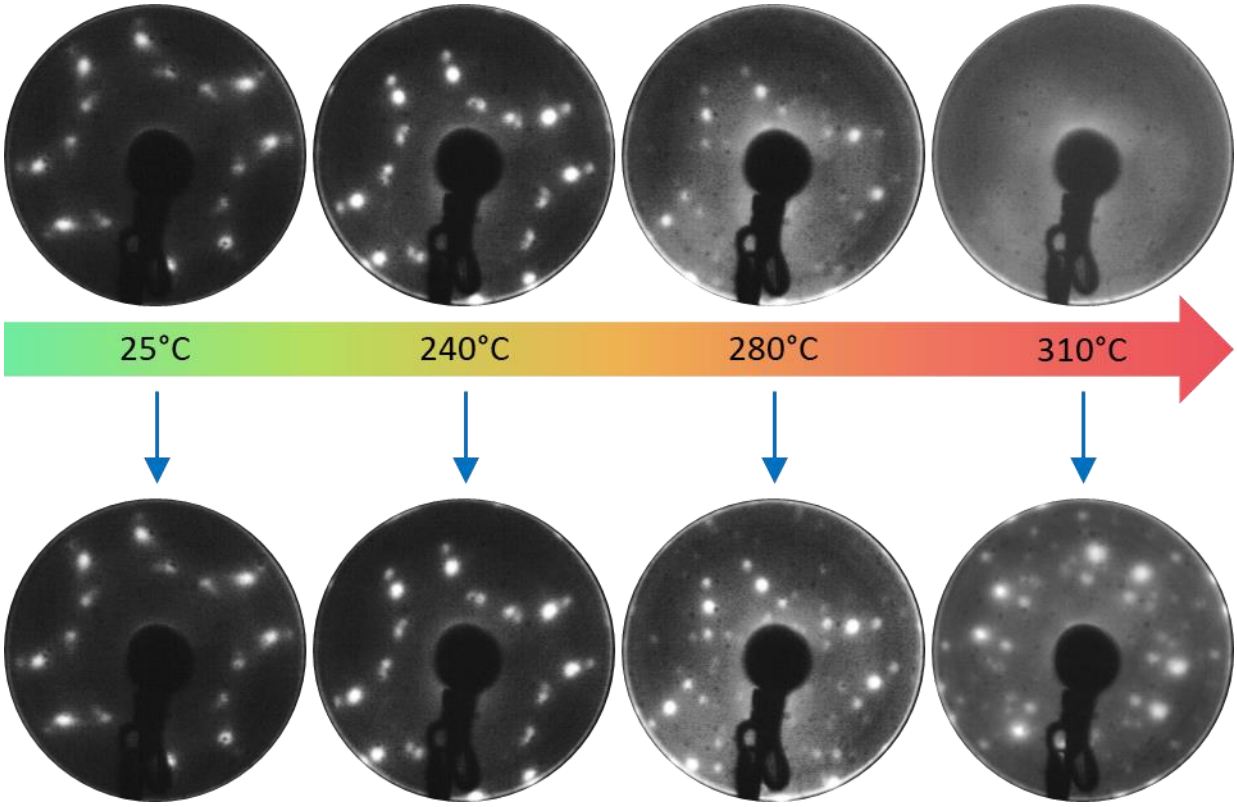

Figure 6.1.2 – LEED patterns recorded whilst annealing a sample of high-density phase 2 up to a temperature of 310 °C. The LEED patterns at the bottom were recorded after allowing the sample to cool to ambient temperature after annealing to the temperature indicated. All LEED patterns were recorded using an electron kinetic energy of 14.5 eV.

Figure 6.1.2 shows LEED patterns recorded whilst annealing a sample of high-density phase 2. Initial annealing of the sample up to 240 °C sharpens the diffraction beams from the incommensurate phase. Further annealing beyond this triggers a phase transition, forming a new, previously unreported, LEED pattern corresponding to high-density phase 3 (discussed later). This new LEED pattern persists until 310 °C when all diffraction beams fade leaving no observable LEED pattern. Upon cooling to ambient temperature, diffraction beams corresponding to low-density phase 1 appear along with another coexisting LEED pattern corresponding to windmill phase 4 (discussed later). The transition from low-density phase 1 to high-density phase 2 at 310 °C identified by Feyer *et al.*[163] was thus reproduced here, though the additional coexisting phase observed here has not been reported previously.

A similar experiment was also performed, in which LEED was used to monitor the adsorption structure whilst annealing a sample consisting of low-density phase 1. Figure 6.1.3 shows that upon annealing, diffraction beams corresponding to windmill phase 4 gradually appear alongside the low-density phase 1 LEED pattern, until at an annealing temperature of 340 °C, only a diffuse LEED pattern remains. STM of the surface after annealing to 340 °C (Figure 6.1.6, discussed later) reveals that this

diffuse LEED pattern corresponds to the coexistence of three phases: low-density phase 1, windmill phase 4 and windmill phase 5.

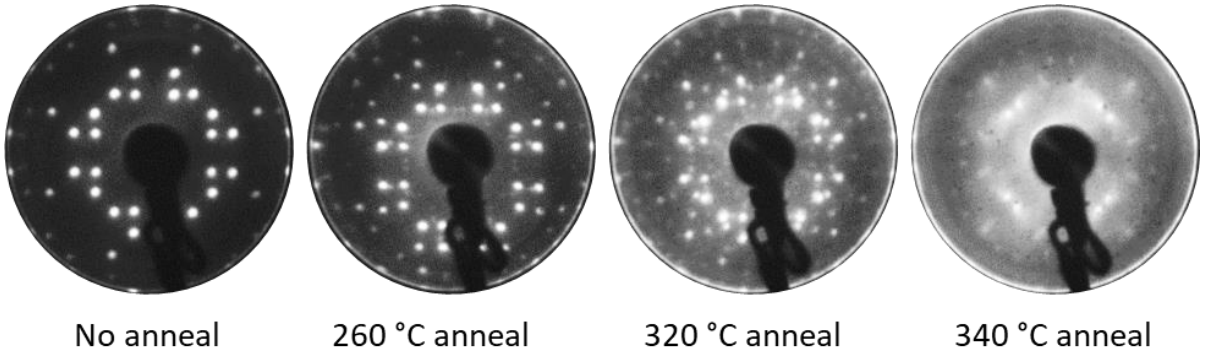

Figure 6.1.3 – LEED patterns recorded after annealing a sample comprising of low-density phase 1 to the indicated temperatures. All of the LEED patterns were recorded after the sample had cooled back to ambient temperature (~25 °C) using an electron kinetic energy of 18.0 eV.

STM was used to characterise the molecular assembly in all the adsorption phases identified by LEED. For all phases, STM images show rounded oblong protrusions that will be interpreted as the locations of the TCNQ molecules in the following discussion. STM recorded from low-density phase 1 (Figure 6.1.4) shows ordered domains of TCNQ molecules packed in a head-to-tail type arrangement, described by a unit mesh containing only one molecule. Averaging over values obtained from eight STM images, the unit mesh vector lengths were measured at $b_1 = (11.8 \pm 0.3)$ Å and $b_2 = (9.1 \pm 0.3)$ Å, with an included angle $\gamma = (123 \pm 4)°$ and vector $\mathbf{b_1}$ oriented at an angle $\theta = (77 \pm 2)°$ to the Ag(100) substrate <110> directions. These values are consistent with the previously reported $\begin{pmatrix} 1 & 4 \\ -3 & -1 \end{pmatrix}$ commensurate matrix (for which vector lengths of $b_1 = 11.92$ Å and $b_2 = 9.14$ Å are expected, with an included angle of $\gamma = 122.5°$ and vector $\mathbf{b_1}$ oriented at $\theta = 76.0°$ to the substrate <110> directions), indicating that the adsorption phase observed in the STM images corresponds to the phase identified by LEED. STM of this phase has been reported previously by Tseng *et al.* for which the same the unit mesh dimensions and suggested molecular orientations were obtained.[58] Figure 6.1.4 also shows a LEED pattern simulated for a $\begin{pmatrix} 1 & 4 \\ -3 & -1 \end{pmatrix}$ commensurate adsorption phase, which is in excellent agreement with the measured LEED pattern. This further confirms, that the adsorption structure is defined by the suggested commensurate matrix.

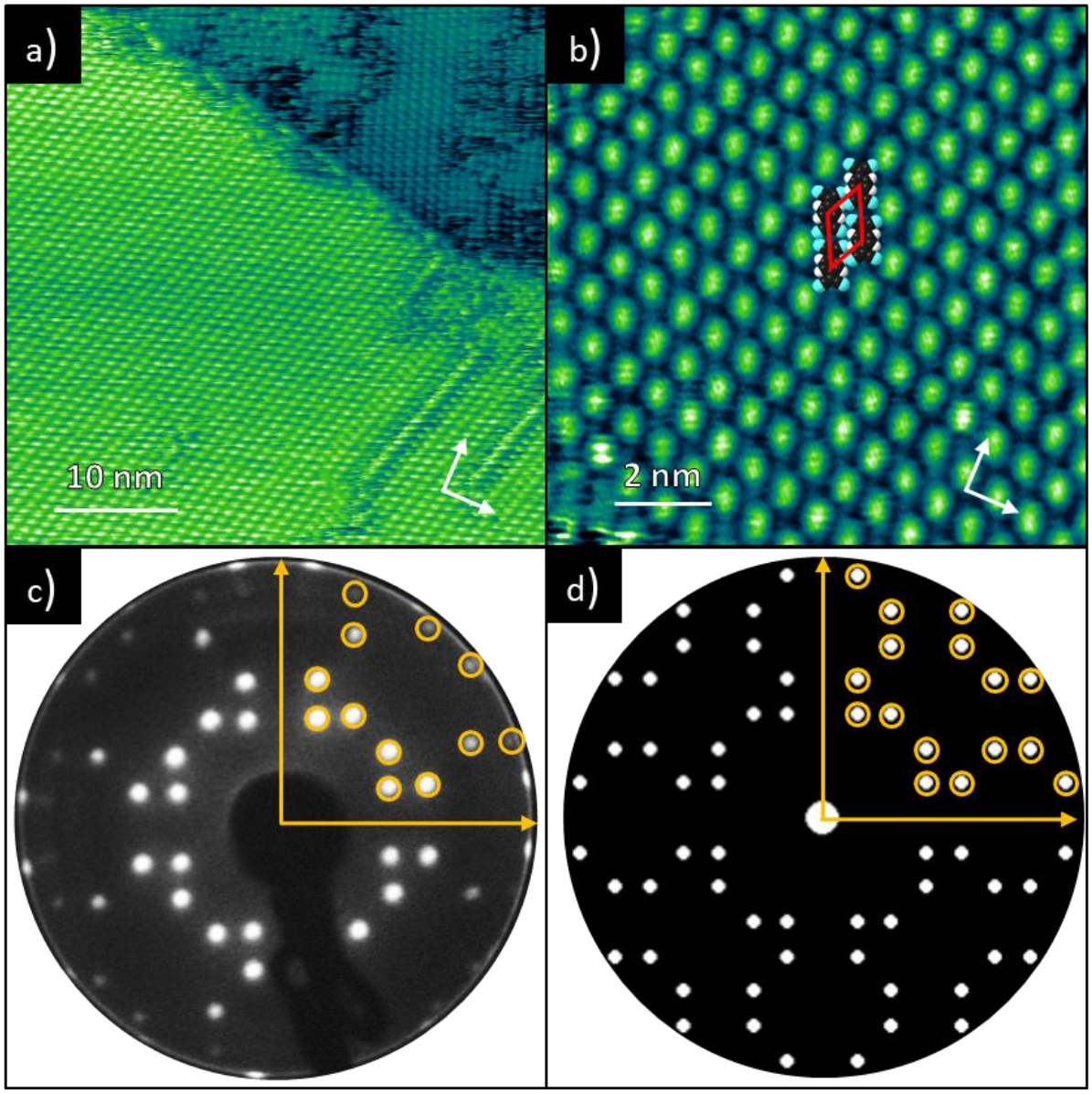

Figure 6.1.4 – STM images and LEED patterns recorded from low-density phase 1. a) – Large area STM image showing ordered TCNQ domains (V_{samp} = -0.2 V, I = 75 pA). b) – STM image of a single TCNQ domain, with scaled TCNQ molecular models and the surface unit mesh (red parallelogram) superimposed (V_{samp} = 0.25 V, I = 150 pA). In both STM images, the white arrows indicate the substrate <110> directions. c) – Experimental LEED pattern recorded using an electron kinetic energy of 18.0 eV. d) – Simulated LEED pattern obtained for a $\begin{pmatrix} 1 & 4 \\ -3 & -1 \end{pmatrix}$ commensurate adsorption phase. In both the experimental and simulated LEED patterns, the substrate <110> directions are indicated by the yellow arrows. To aid in the comparison of the two LEED patterns, the diffraction beams in one quadrant of the pattern are highlighted by yellow circles.

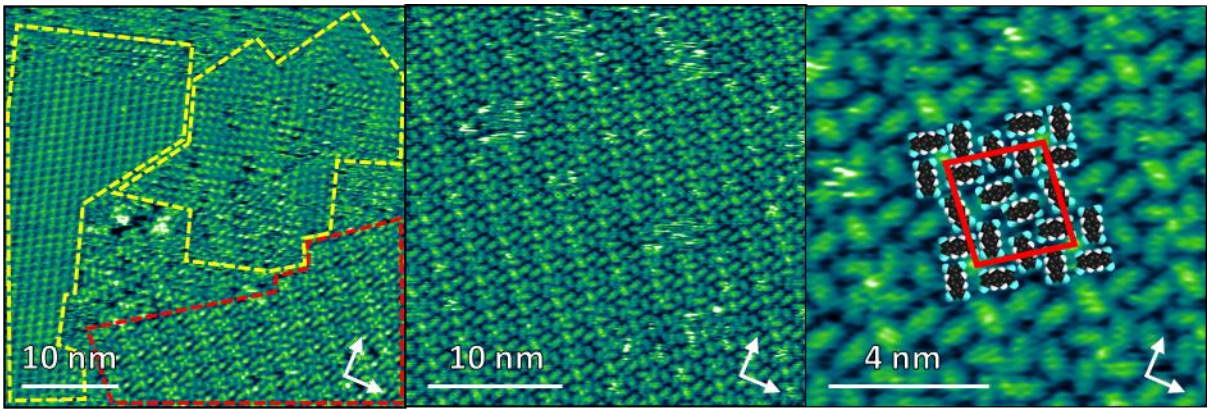

Figure 6.1.5 – STM images recorded after annealing a low-density phase 1 sample to 320 °C. Left) – Large area STM image showing ordered domains of two distinctly different phases. The regions outlined in yellow correspond to low-density phase 1 and the region outlined in red is a domain of windmill phase 4. (V_{samp} = -0.35 V, I = 100 pA) Middle) – Large area STM image showing single ordered domain of windmill phase 4 (V_{samp} = -0.05 V, I = 150 pA). Right) – Selected area image of windmill phase 4 with the unit mesh (red parallelogram) and scaled molecular models of TCNQ overlaid. (V_{samp} = -0.05 V, I = 150 pA). In all three STM images, the white arrows indicate the substrate <110> directions.

Figure 6.1.5 shows STM images recorded after annealing a low-density phase 1 sample to 320 °C. The images show that low-density phase 1 is still present on the surface, along with domains of a new molecular assembly (windmill phase 4) and some disordered regions. This reflects the formation of new diffraction beams alongside those from low-density phase 1 observed by LEED when the sample was annealed to 320 °C (Figure 6.1.3). STM of this phase shows TCNQ arranged in a complex structure that is described by a large unit mesh containing eight molecules, four of which are arranged into windmill units and the remaining four occupying sites in between. Unit mesh dimensions for windmill phase 4 were obtained by averaging measurements from six STM images, yielding vector lengths of b_1 = (27 ± 1) Å and b_2 = (25 ± 1) Å, with an included angle γ = (101 ± 2)° and vector $\mathbf{b_1}$ oriented at an angle θ = (33 ± 2)° to the substrate <110> directions. The STM contrast also appears to show small bright protrusions at the centres of the windmill units, which could indicate that Ag adatoms from the substrate participate in the adsorbate assembly. In chapter 4, it was shown that Ag adatoms are incorporated into TCNQ adsorption structures formed on the Ag(111) surface and, consequently, similar involvement of adatoms in the TCNQ windmill units observed on Ag(100) is certainly plausible.

Figure 6.1.6 shows STM images recorded after annealing a low-density phase 1 sample to 340 °C, which show a mixture of phases on the surface, along with small clusters of TCNQ molecules and large areas with no resolvable features. As the edges of the ordered domains appear diffuse in the STM images

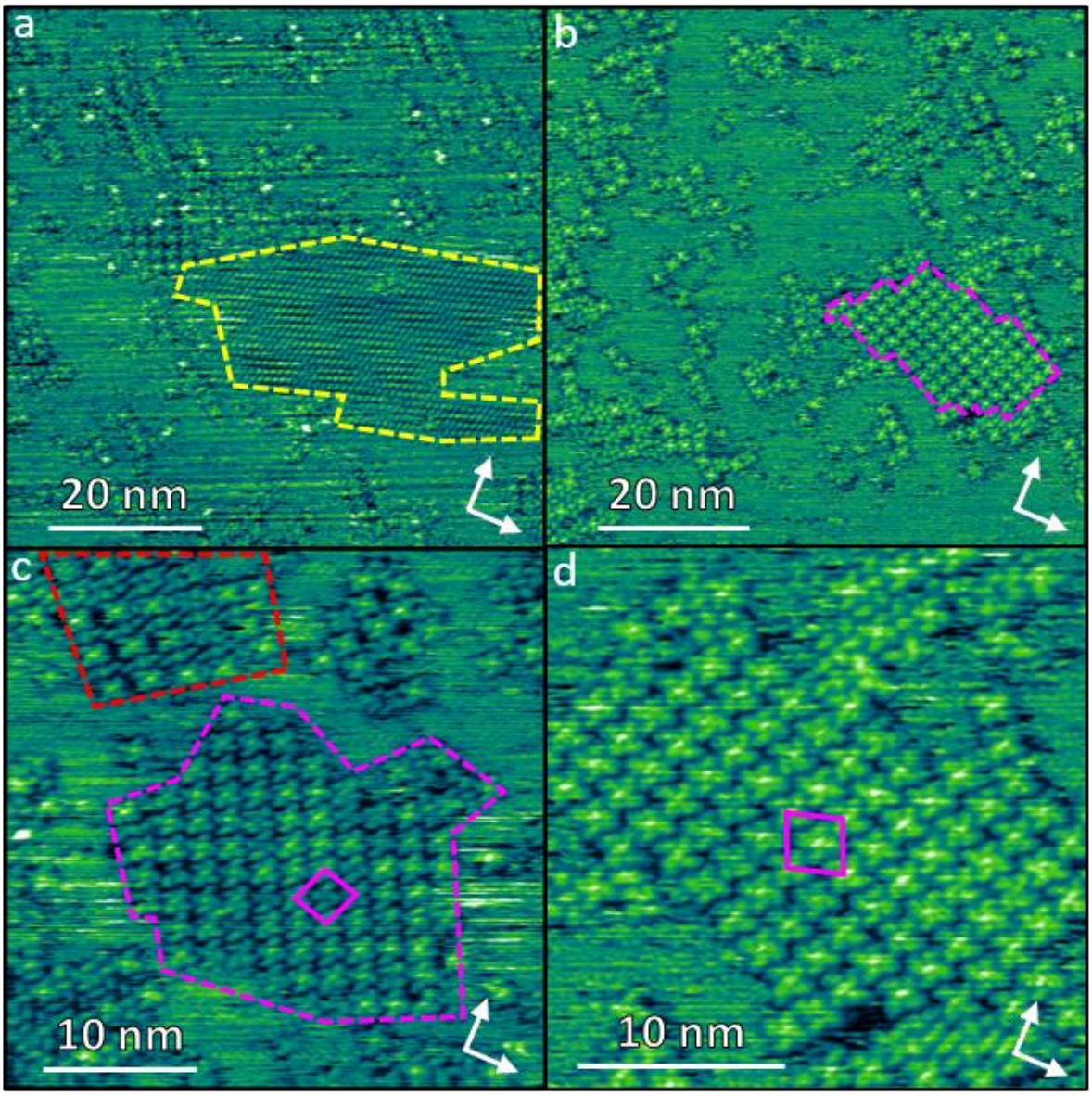

Figure 6.1.6 – STM images recorded after annealing a sample of low-density phase 1 to 340 °C. a) – Large area STM image, with a domain corresponding to low-density phase 1 outlined in yellow (V_{samp} = -1.25 V, 75 pA). b) – Large area STM image, with a domain of windmill phase 5 outlined in purple (V_{samp} = 1.25 V, 75 pA). c) – STM image centred on a single domain of windmill phase 5 (outlined in purple) with the unit mesh indicated by the purple rhombus. A small domain of windmill phase 4 is also present in this image and is outlined in red (V_{samp} = 1.25 V, 75 pA). d) – Selected area STM image showing an expanded region of windmill phase 5 (V_{samp} = 1.25 V, 75 pA). In all of the STM images, the substrate <110> directions are indicated by the white arrows.

and the shape and size of domains were observed to change between consecutive images, the featureless regions most likely correspond to areas containing highly mobile TCNQ molecules that diffuse rapidly across the surface. The presence of these regions indicates that the TCNQ coverage has decreased as a result of the annealing and suggests that a significant proportion of the molecules have desorbed from

the surface. LEED recorded during the annealing process (Figure 6.1.3) indicate that low-density phase 1 is no longer dominant on the surface after annealing to 340 °C as only a diffuse set of diffraction beams remain. Despite this, some regions containing low-density phase 1 were still infrequently observed in STM images of the surface. Small domains of windmill phase 4 were also still present (outlined in red) as well as a new adsorption phase (windmill phase 5, outlined in purple), which consists of TCNQ windmill units packed together in a near square arrangement. Unit mesh dimensions were obtained for windmill phase 5 by averaging measurements from seven STM images, yielding vector lengths of $b_1 = (26 \pm 1)$ Å and $b_2 = (27 \pm 1)$ Å, an included angle $\gamma = (94 \pm 2)°$ and with vector $\mathbf{b_1}$ oriented at an angle $\theta = (18 \pm 2)°$ to the substrate <110> directions. The unit mesh for windmill phase 5 (shown by the purple rhombus in Figure 6.1.6) contains two windmill units, totalling eight TCNQ molecules. Close inspection of the STM reveals that the two windmill units in the mesh are of opposing chirality, forming an assembly similar to those reported for TCNQ codeposited in a 1:4 ratio on Ag(100) with either Ni[58] or Mn.[59] In these TCNQ/transition metal assemblies, the alternating chirality of the windmill units was attributed to the high directionality of coordinative bonds formed between the TCNQ cyano groups and the metal atoms, which impose a C-N-M bond angle of ~180 °.[59] This could suggest that the windmill units observed here for TCNQ adsorbed on Ag(100) contain Ag adatoms from the substrate, which, as a transition metal, would also be expected to bond to the molecules through similar coordinative interactions with the TCNQ cyano groups. The STM contrast is consistent with this suggestion, showing small circular protrusions at the centre of the windmill units that could correspond to Ag adatoms. The reported $NiTCNQ_4$ and $MnTCNQ_4$ assemblies are both described by a commensurate $\begin{pmatrix} 9 & 3 \\ -3 & 9 \end{pmatrix}$ unit mesh,[58] which corresponds to dimensions of $b_1 = b_2 = 27.4$ Å with an included angle $\gamma = 90$ ° and with vector $\mathbf{b_1}$ oriented at an angle $\theta = 18.4$ ° to the substrate <110> directions. The unit mesh dimensions measured here for windmill phase 5 formed by TCNQ on Ag(100) are in relatively good agreement with this commensurate matrix, showing further similarities to the reported TCNQ/transition metal structures.[58]

In addition to the ordered domains formed after annealing to 340 °C, the STM shows TCNQ windmills in small clusters, chains and even isolated units on the surface. The fact that the TCNQ windmills can be resolved in isolated units by STM at ambient temperature suggests that they are very stable. In the windmills, the TCNQ molecules, which become negatively charged on the surface of Ag,[57] arrange with one cyano group from each of four molecules pointing towards a central point. As negative charge localises on the TCNQ cyano groups,[161] this arrangement would be expected to be highly unfavourable due to electrostatic repulsions, unless a counterion is present at the centre of the windmill unit. Furthermore, this arrangement does not promote favourable intermolecular interactions between the molecules within the same windmill unit and would therefore be unfavourable without the incorporation

of Ag adatoms. The STM measurements therefore provide indirect evidence of the involvement of Ag adatoms within the windmill units formed by annealing the sample. As these windmill structures were only observed after annealing the sample, it is suggested that the incorporation of adatoms into the TCNQ layer is thermally activated.

Figure 6.1.7 shows STM and LEED recorded from a sample of high-density phase 2. To promote the formation of larger ordered domains, the sample was annealed to 200 °C, as at this temperature the LEED pattern sharpens without causing a phase transition. STM recorded from the resulting surface shows large ordered domains of TCNQ molecules arranged in a head-to-tail type structure that is described by a single molecule unit mesh. Averaging over values obtained from eight different STM images, the unit mesh vector lengths were measured at $b_1 = (9.1 \pm 0.3)$Å and $b_2 = (9.0 \pm 0.1)$Å, with an included angle $\gamma = (97 \pm 2)°$ and vector $\mathbf{b_1}$ oriented at an angle $\theta = (8 \pm 2)°$ from the substrate <110> directions. Figure 6.1.7d shows the LEED pattern expected for a unit mesh defined by a matrix of $\begin{pmatrix} 0.43 & -3.05 \\ 3.06 & 0.76 \end{pmatrix}$ which agrees, within the associated error ranges, with the unit mesh dimensions measured by STM. Comparing this simulated LEED pattern with the experimentally measured LEED pattern shows excellent agreement and thus confirms the accuracy of the unit mesh measurements. As discussed before, LEED of high-density phase 2 has been reported previously, for which a unit mesh described by a $\begin{pmatrix} 0.58 & -2.92 \\ 3.02 & 0.92 \end{pmatrix}$ matrix ($b_1 = 8.6$ Å, $b_2 = 9.1$ Å, $\gamma = 96°$, $\theta = 11°$) was proposed.[163] There are some small discrepancies between this unit mesh and the values measured here by STM, with one of the vector lengths and the orientation relative to the substrate falling just beyond the error ranges associated with the STM measurements. Furthermore, the matrix obtained here by STM (for which the simulated LEED pattern is shown in Figure 6.1.7d) shows better agreement with the experimental LEED pattern and thus it was concluded that this unit mesh gives a better description of high-density phase 2 than the previously proposed matrix.[163]

High-density phase 2 displays a similar assembly to low-density phase 1, with both structures comprising a head-to-tail packing arrangement of TCNQ molecules. However, the former has a significantly higher density of TCNQ molecules per unit area than the latter (1.23×10^{14} cm^{-2} and 1.06×10^{14} cm^{-2} respectively). This difference is consistent with the higher coverage needed to form high-density phase 2. These results suggest that low-density phase 1 is more favourable at lower coverages but further TCNQ adsorption causes the structure to compress, resulting in high-density phase 2. Similar behaviour has been reported previously for other adsorption systems and can be explained by considerations of the molecule-substrate and molecule-molecule interactions as the surface coverage is increased.[195-197] An increased density of molecules on the surface results in more

molecule-substrate interactions thus increasing the overall adsorption energy at the cost of a lower adsorption energy for each individual molecule. This is caused by the molecules being forced away from favourable adsorption sites (as indicated here by the transition from a commensurate structure to

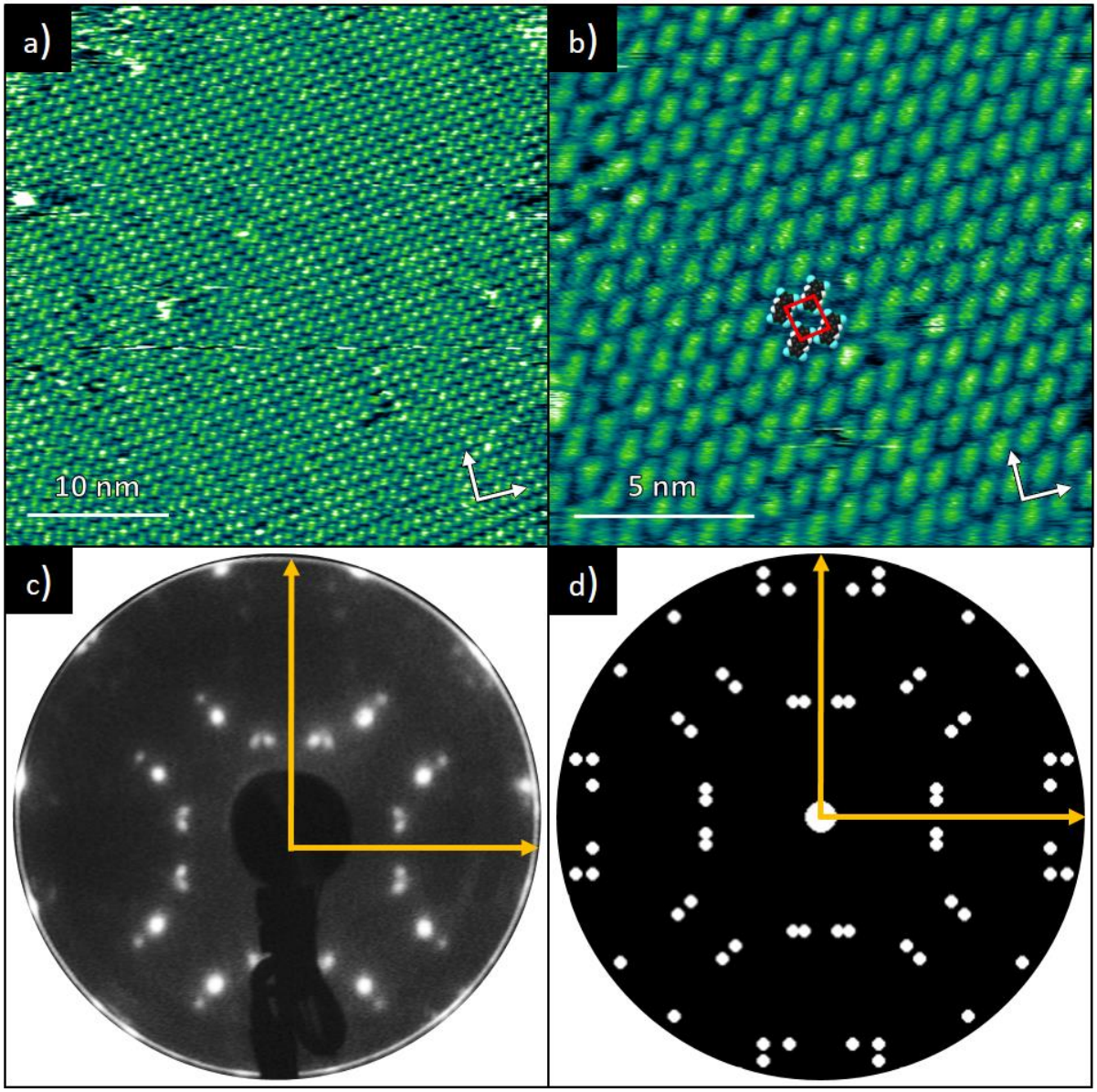

Figure 6.1.7 – STM and LEED recorded from high-density phase 2. The sample was annealed to 200 °C prior to the STM measurements to promote the formation of ordered domains. a) –STM image showing a large domain of the ordered adsorption phase (V_{samp} = -0.1 V, 100 pA). b) – Selected area STM image of high-density phase 2 with the unit mesh indicated by the red parallelogram and scaled molecular models superimposed over the STM contrast (V_{samp} = -0.1 V, 100 pA). In both STM images, the white arrows indicate the substrate <110> directions. c) – Experimentally measured LEED pattern obtained using an electron kinetic energy of 23.5 eV. d) – LEED pattern simulated from the unit mesh dimensions obtained from the STM images. In both the experimental and simulated LEED patterns, the yellow arrows indicate the substrate <110> directions.

an incommensurate structure) as well as increased Pauli repulsions as the molecules are forced closer together. [195-197] If the balance of these effects results in an increase to the total adsorption energy of the system, more molecules will adsorb on the surface to form a more compressed structure.[195-197]

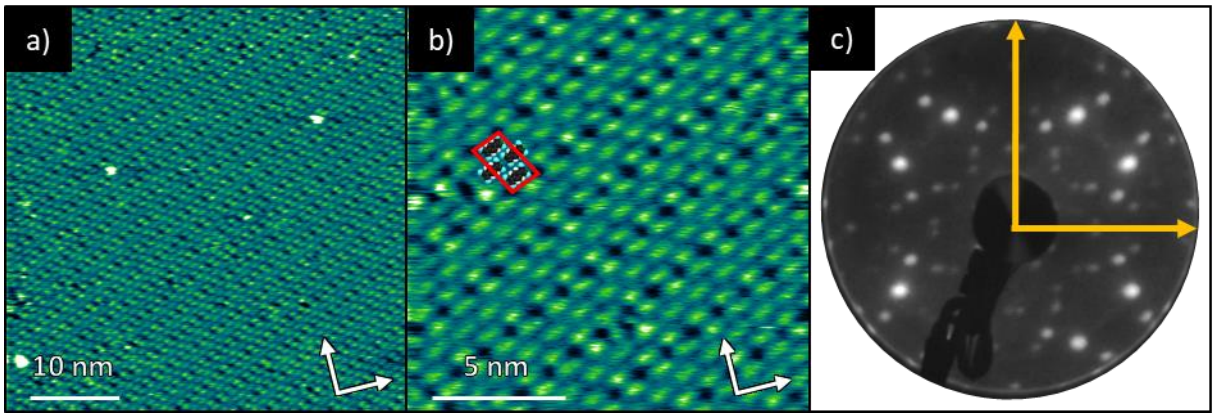

Figure 6.1.8 – STM and LEED recorded from high-density phase 3. a) – Large area STM image showing a single ordered domain (V_{samp} = 0.9 V, 75 pA). b) – Selected area STM image showing an expanded view of an ordered domain. The unit mesh is indicated by the red parallelogram and scaled molecular models are superimposed over the STM contrast (V_{samp} = 1.0 V, 150 pA). In both STM images, the white arrows indicate the substrate <110> directions. c) - LEED pattern recorded from the sample using an electron kinetic energy of 16.0 eV. The yellow arrows indicate the substrate <110> directions.

Figure 6.1.8 shows STM and LEED recorded from the intermediate adsorption phase (high-density phase 3) formed by annealing high-density phase 2 to temperatures between 280-310 °C as shown in Figure 6.1.2. STM of this phase also shows TCNQ molecules packed into a head-to-tail structure. However, unlike high-density phase 2 or low-density phase 1, high-density phase 3 includes pores between the rows of molecules. This adsorption structure is described by a three molecule unit mesh, which from averaging values obtained from eleven different STM images was measured to have vector lengths of b_1 = (20.3 ± 0.4) Å and b_2 = (12.0 ± 0.1) Å with an included angle γ = (98 ± 2)° with vector $\mathbf{b_1}$ oriented at an angle θ = (22 ± 2)° to the substrate <110> directions. These unit mesh dimensions suggest that the TCNQ molecules pack with a density of 1.24 x 10^{14} cm^{-2}, which, despite the observable pores in the structure, is comparable to high-density phase 2 and is significantly denser than low-density phase 1. This indicates that the phase transition is not driven by a change in coverage. Instead, this implies that the increased thermal energy supplied to the system during the annealing step enables the structure to rearrange and could indicate that high-density phase 3 is thermodynamically favoured over high-density phase 2.

6.2 XPS and UPS

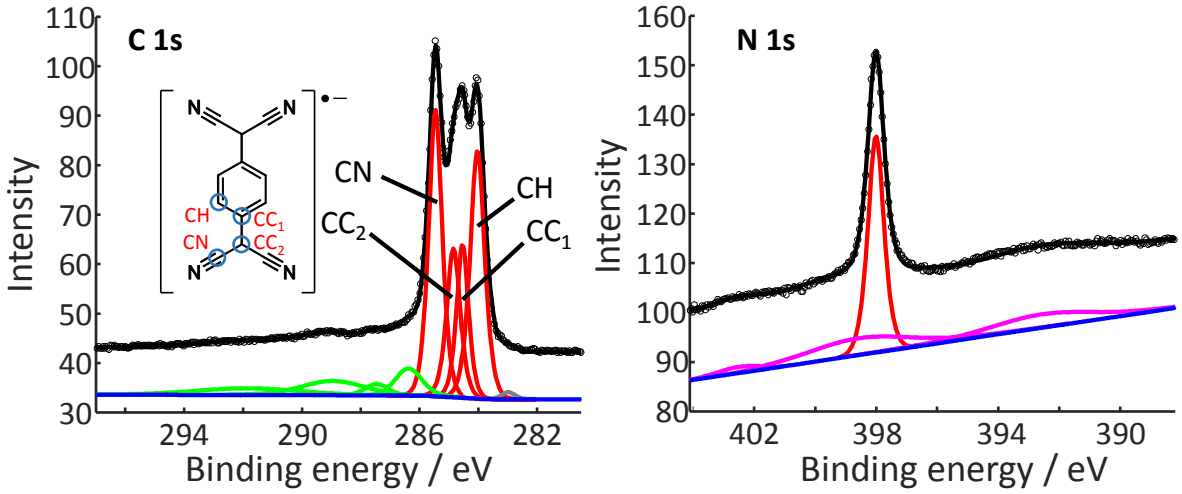

Figure 6.2.1 – High resolution C 1s and N 1s XPS spectra obtained from low-density phase 1. The C 1s spectrum was recorded at a photon energy of 435 eV, with measured intensity (black circles), and the sum of fitted components (black line) comprising a Shirley background (blue),[177] four main C 1s components (red), shakeup/satellite features (green) and a beam damage feature (grey). The inset shows a schematic of the singly negatively charged TCNQ molecule, highlighting the four chemically inequivalent carbon environments which are assigned to the four main peaks. The N 1s spectrum was recorded at a photon energy of 550 eV, with measured intensity (black circles), and the sum of fitted components (black line), comprising a linear background (blue), one main N component (red) and Ag 3d plasmon features (purple).

Table 6.2.1 – XPS measured binding energies of the main C 1s, and N 1s components from low-density phase 1.

Component	**CH**	**CC_1**	**CC_2**	**CN**	**N**
Binding energy / eV	284.0	284.5	284.9	285.5	398.0

Figure 6.1.1 shows high-resolution soft XPS recorded from low-density phase 1, with binding energies of the main fitted components shown in Table 5.1.1. The C 1s spectrum clearly shows at least three distinct peaks, which were fitted with four components corresponding to the four chemically inequivalent C species in TCNQ, with the relative peak intensities constrained (± 5%) to their expected stoichiometry. The spectral line shapes and the corresponding binding energies measured here from the C 1s and N 1s spectra are in excellent agreement with the XPS measured from the TCNQ adsorption phases on Ag(111) (see Figure 4.2.1 and Table 4.2.1). As the XPS recorded from TCNQ on Ag(111) was determined to be characteristic of $TCNQ^-$ from comparisons with XPS for other systems in which TCNQ is believed to be negatively charged,[57, 175, 176] it was concluded that TCNQ also becomes negatively charged when adsorbed on Ag(100).

The work function was measured by UPS from a sample of low-density phase 1 at (4.95 ± 0.05) eV, showing that the adsorption of TCNQ on Ag(100) increases the surface work function by ~0.5 eV from typical values measured for clean Ag(100) (4.3-4.6 eV).[198-200] This result is also consistent with TCNQ becoming negatively charged on the surface as a neutral adsorbate would decrease the work function via the 'push back' effect and an electron donating adsorbate would decrease the work function further still. [11]

6.3 NIXSW and structural models

Table 6.3.1 – NIXSW fitting parameters obtained from high-density phase 2 and low-density phase 1 using the (200) reflection of the Ag(100) substrate. Separate fitting parameters were obtained for the different C 1s photoemission components as identified in Figure 6.2.1 (due to lower resolution at the photon energies used for NIXSW, components CC_1 and CC_2 were fitted together in a single component here). The coherent position $D_{(200)}$ is given as $D_{(200)} = (P+1)d_{200}$ where P is the fractional coherent position and d_{200} is the spacing of the (200) lattice planes (2.043 Å). For each phase, values are averaged over a total of eight repeat measurements from two separate sample preparations. Error estimates are shown in parentheses in units of 0.01.

Component	High-density phase 2		Low-density phase 1	
	f_{co}	$D_{(200)}$ / Å	f_{co}	$D_{(200)}$ / Å
CH	0.67(10)	2.69(5)	0.68(10)	2.70(5)
CC	0.76(10)	2.56(5)	0.79(10)	2.65(5)
CN	0.69(10)	2.45(5)	0.70(10)	2.51(5)
N	0.63(10)	2.28(5)	0.81(10)	2.36(5)

NIXSW measurements were recorded from both high-density phase 2 and low-density phase 1. Using the Bragg reflection from the (200) planes, which lie parallel to the surface, the adsorption heights of TCNQ and its constituent atoms were determined. The coherent positions measured by NIXSW correspond to the layer spacing above the nearest scattering plane so the $D_{(200)}$ values quoted in Table 6.3.1 include the addition of the spacing between (200) planes in bulk Ag ($d_{(200)}$ = 2.043 Å) to give physically reasonable adsorption heights. As the coherent position is measured relative to the projection of the bulk lattice planes, the effects of surface relaxations must be considered when determining the adsorption height from NIXSW. For clean Ag(100), these relaxations are negligible (i.e. (0.00 ± 0.03) Å in the first two surface layers)[201] and are often passivated by the presence of adsorbates, so the $D_{(200)}$ values quoted here were considered to be adsorption heights.

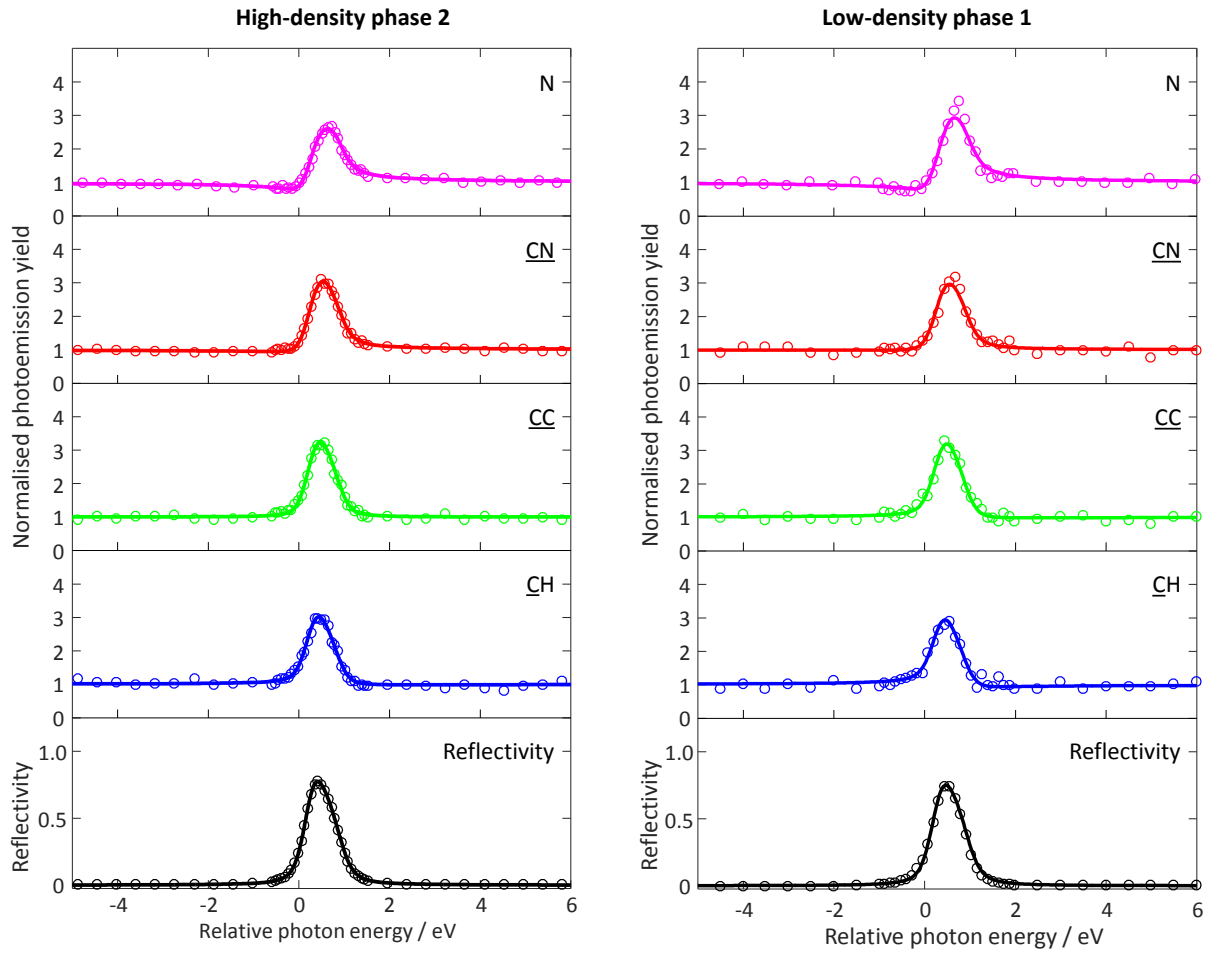

Figure 6.3.1 – Sample set of NIXSW photoemission yield curves obtained from samples of high-density phase 2 and low-density phase 1 using the (200) reflection of the Ag(100) substrate. Photon energies are quoted relative to the Bragg energy of 3036.0 eV. Least square fits (solid lines) to the photoemission yields (circles) were obtained to extract the coherent fractions and coherent positions.

The (200) reflection NIXSW measurements for both adsorption phases agree within the associated error ranges, suggesting that the molecule adopts similar adsorption conformations in both assemblies. For all of the C and N components, moderate coherent fractions (0.6-0.8) were obtained, suggesting that the molecule occupies a small distribution of adsorption heights. The coherent positions indicate that TCNQ adsorbs with the central ring at a height of ~2.7 Å above the surface with the N atoms on the peripheral cyano groups lying ~0.4 Å closer to the surface. This contrasts significantly with the NIXSW obtained for TCNQ on Ag(111) (see section 4.3), which, on average, adopted a flatter geometry, owing to the incorporation of Ag adatoms within the structure. The NIXSW for TCNQ on Ag(100) shows good qualitative agreement with DFT calculated structures reported for TCNQ on various coinage metal surfaces, which predict that the molecule adsorbs with all four cyano groups bent towards the substrate.[17, 128, 164, 165] Indeed, the DFT-D model calculated for TCNQ adsorbed on the Ag(111) surface

without adatoms (see Table 4.3.2) shows strong similarities to the coherent positions measured for TCNQ on Ag(100), with the N atoms also lying ~0.4 Å below the central quinoid ring. The NIXSW results therefore could suggest that Ag adatoms are not incorporated into either of the two measured adsorption phases of TCNQ on Ag(100).

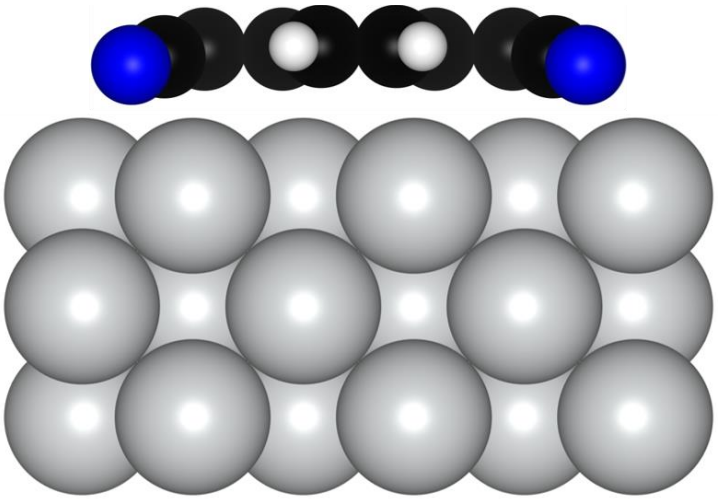

Figure 6.3.2 – Side view model of the bent TCNQ adsorption conformation suggested by the measured coherent positions for low-density phase 1. This visualisation was produced using the open-access software package VESTA.[181]

As the coherent fractions measured for all components agree within the relatively large associated error ranges, it was not possible to identify any trends in the distribution of adsorption heights across the molecule. The measured coherent fractions, which span a range of 0.5-0.9 (including error ranges), are mostly lower than values typically attributed to a single layer spacing,[21, 98] suggesting that each of the separate components occupy some distribution of adsorption heights. This distribution of heights must be contained within the unit mesh, which for both adsorption phases requires the distribution to be achievable, whether by thermal motion or occupancy of multiple heights, within a single TCNQ molecule. The lack of an observable trend in the coherent fractions rules out the possibility of adsorption conformations in which the molecule adopts a significantly tilted or twisted geometry as this would cause the atoms near the centre of the molecule show a much smaller height distribution to those at the extremities. Instead, the measured values suggest a relatively similar distribution of heights across the molecule, which cannot be reconciled by any simple adsorption conformation and could indicate that the low coherent fractions are caused by thermal vibrational modes of the TCNQ molecule.

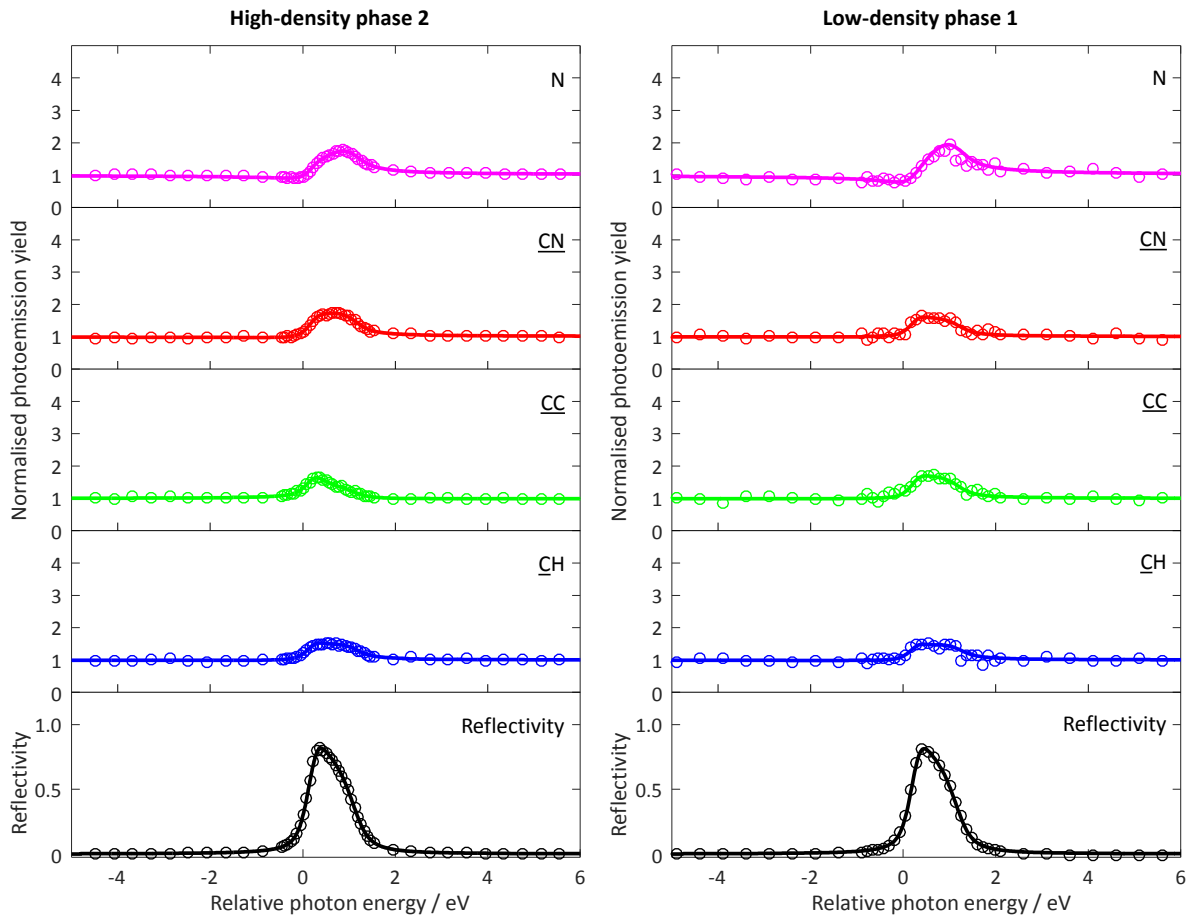

Figure 6.3.3 - Sample set of NIXSW photoemission yield curves obtained from samples of high-density phase 2 and low-density phase 1 using the (111) reflection of the Ag(100) substrate. Photon energies are quoted relative to the Bragg energy of 3036.0 eV. Least square fits (solid lines) to the photoemission yields (circles) were obtained to extract the coherent fractions and coherent positions.

NIXSW measurements were also recorded using the (111) Bragg reflection of the Ag(100) substrate to provide information on the lateral registry of the adsorbate structures, particularly for the commensurate structure of low-density phase 1 which should have a well-defined relationship with the underlying substrate. For a given height of the absorber atoms ($z_{(200)}$ i.e. the adsorption height measured by the (200) reflection NIXSW), the coherent position ($P_{(111)}$) expected for different adsorption sites on the Ag(100) surface can be predicted by simple triangulation. Specifically, for the two full-symmetry sites of the Ag(100) surface (the sites that retain the full point group symmetry of the underlying substrate) these are given by:

$$P_{(111)atop} = \frac{z_{(200)}}{\sqrt{3}d_{111}} \qquad [6.3.1]$$

$$P_{(111)hollow} = 0.5 + \frac{z_{(200)}}{\sqrt{3}d_{111}} \quad [6.3.2]$$

for the atop and hollow sites, where $z_{(200)}$ is the adsorption height measured by the (200) reflection NIXSW and d_{111} is the layer spacing between Ag(111) lattice planes (2.359 Å).[202] Due to the symmetry of the substrate, these two values of P_{111} are the only possibilities for atoms at a given adsorption height, as averaging over the four unique but symmetrically equivalent (and thus equally occupied) domains on the surface will give a position corresponding to the nearest of the two high-symmetry sites overall.[202] Moving further from each high-symmetry site results in a smooth decrease in the coherent fraction until, at points equidistant between the atop and hollow sites, a coherent fraction of 0 is obtained and the coherent position switches between the two discrete values.

Table 6.3.2 - NIXSW fitting parameters obtained from samples of high-density phase 2 and low-density phase 1 using the (111) reflection of the Ag(100) substrate. Separate fitting parameters were obtained from the different C 1s photoemission components as defined in Figure 6.2.1 (due to lower resolution at the photon energies required for NIXSW, components CC_1 and CC_2 were fitted together in a single component here). The coherent positions expected for atoms occupying the two high-symmetry sites ($P_{(111)\text{ - atop}}$ and $P_{(111)\text{ - hollow}}$ for the atop and hollow sites respectively) on the Ag(100) surface are also shown in the table and are shown in fractional units as values between 0 and 1. Error estimates are shown in parentheses in units of 0.01.

Component	High-density phase 2			
	f_{co}	$P_{(111)}$	$P_{(111)\text{ - atop}}$	$P_{(111)\text{ - hollow}}$
CH	0.17(10)	0.84(4)	0.66(3)	0.16(3)
CC	0.19(10)	0.72(4)	0.63(3)	0.13(3)
CN	0.15(10)	0.01(4)	0.60(3)	0.10(3)
N	0.32(10)	0.99(4)	0.56(3)	0.06(3)
Component	**Low-density phase 1**			
	f_{co}	$P_{(111)}$	$P_{(111)\text{ - atop}}$	$P_{(111)\text{ - hollow}}$
CH	0.21(10)	0.84(3)	0.66(3)	0.16(3)
CC	0.15(10)	0.87(4)	0.63(3)	0.13(3)
CN	0.15(10)	0.95(6)	0.60(3)	0.10(3)
N	0.51(10)	0.02(4)	0.56(3)	0.06(3)

Table 6.3.2 shows NIXSW fitting parameters obtained using the (111) reflection from samples of high-density phase 2 and low-density phase 1. For both phases, the C components show low coherent fractions (i.e. < 0.2) which indicates that the C atoms do not occupy sites close to a specific high symmetry site. The corresponding coherent positions are not consistent with either of the high symmetry

sites and consequently are physically meaningless. These erroneous coherent positions were attributed to the fact that at low coherent fractions, the modulations in the NIXSW photoemission yield profile are dominated by the reflectivity and thus it is difficult to distinguish between different coherent positions. As a result, the coherent positions measured from species with low coherent fractions are unreliable. Larger coherent fractions were measured for the N component in both phases with values of (0.32 ± 0.10) and (0.51 ± 0.10) for high-density phase 2 and low-density phase 1 respectively. The measured coherent fractions are sufficiently large to imply that there is a well-defined lateral registry but are lower than would be expected for the N atoms being centred on a high-symmetry site. For both phases, the measured coherent position is consistent with the fourfold hollow. Coupled with the low coherent fractions, this indicates that the N atoms either occupy sites that are closer to the hollow site than atop but are laterally offset from the centre of the site, or the N atoms occupy a mixture of sites above the substrate but show a preference for adsorbing closer to the hollow site. The former is consistent with the registry suggested by Tseng *et al*. from STM of low-density phase 1, although no evidence was given to support this assignment.[58] Nonetheless, the NIXSW measurements obtained using the (111) reflection show that the N atoms have a well-defined registry with the Ag(100) substrate and preferentially adsorb towards the fourfold hollow site, whereas the C atoms do not exhibit any preference for lateral adsorption sites. This is consistent with the general expectation that TCNQ interacts with the substrate through the cyano groups and thus the registry is determined by the formation of N-Ag bonds.[17, 128, 164, 165] This is also consistent with the NIXSW measured using the (200) reflection, which showed that the cyano groups bend down towards the substrate in a conformation that could facilitate such bonding.

6.4 General discussion and conclusions

Using STM and LEED, five different ordered adsorption phases were identified for TCNQ on Ag(100). When TCNQ is deposited on Ag(100), the molecules arrange into a commensurate head-to-tail type packing arrangement (low-density phase 1), which compresses into a higher density incommensurate head-to-tail structure (high-density phase 2) as the coverage is increased. Annealing this incommensurate phase to temperatures between 280-310 °C results in a phase transition to a different incommensurate head-to-tail structure (high-density phase 3). This transition occurs with no apparent change to the TCNQ coverage and could suggest that high-density phase 3 is thermodynamically favoured over high-density phase 2. Annealing to temperatures greater than 310 °C causes a phase transition to the commensurate low-density phase 1 structure, which occurs with an apparent reduction in the TCNQ coverage, attributed to molecules desorbing from the substrate. Annealing to these temperatures also results in the formation of two coexisting phases that include TCNQ molecules

arranged into windmill units (windmill phase 4 and windmill phase 5). Higher temperature annealing further reduces the TCNQ coverage and increases the proportion of the TCNQ molecules arranged in windmill type structures on the surface. The STM of these windmill units showed small circular protrusions at the centre, which suggests possible involvement of Ag adatoms in the adsorption structure. This was further supported by the packing of these windmill units showing close similarity to adsorption phases formed between TCNQ and coadsorbed transition metal atoms on Ag(100).[58, 59] Furthermore, isolated windmill units were sufficiently stable to be observed by STM and, considering that the windmill arrangement does not promote intermolecular bonding, this also supports the suggested involvement of Ag adatoms in these structures. These windmill structures were only observed after annealing the sample, which could imply that the suggested incorporation of adatoms into the TCNQ layer requires some thermal activation.

XPS and UPS measurements showed that TCNQ accepts electrons from the Ag(100) substrate, increasing the surface work function by ~0.5 eV. This result was expected as TCNQ has already been shown, both in this thesis and elsewhere,[57] to accept electrons from the Ag(111) surface, which has a larger work function than Ag(100).[92, 199] The UPS and XPS measurements were only obtained from low-density phase 1, however it is expected that TCNQ would be negatively charged in all of the identified adsorption phases and would exhibit similar results.

NIXSW measurements recorded from samples of high-density phase 2 and low-density phase 1 showed that TCNQ adopts a bent conformation on Ag(100), with the central ring of the molecule adsorbing 2.7 Å above the surface and the N atoms of the cyano groups ~0.4 Å below this, pointing down towards the substrate. This conformation could suggest that Ag adatoms are not incorporated into either of these phases as adatom participation on Ag(111) resulted in a flatter average geometry, with some CN groups pointing up and others pointing down. Moreover, this bent geometry measured on Ag(100) is consistent with DFT calculated structures for TCNQ adsorbed on other coinage metal surfaces, that do not include substrate adatoms,[17, 128, 164, 165] including those presented in section 4.3 for TCNQ on Ag(111). However, it is not certain that participation of Ag adatoms on the Ag(100) surface would affect the adsorption conformation in the same manner as observed on Ag(111) and any effects would likely also be dependent on the molecule-adatom stoichiometry.

The NIXSW measurements recorded using the (200) reflection yielded moderate coherent fractions for all of the C and N components, with values lower than can typically be attributed to a single adsorption height. As the unit meshes for both phases measured by NIXSW contain only a single molecule, each molecule must contain the complete distribution of heights inferred from the coherent fractions. As the measured coherent fractions are relatively similar for all of the separate photoemission components

within the TCNQ molecule, they cannot be reconciled by any simple twisted or tilted adsorption conformation. This could indicate that the reduced coherent fractions are instead caused by thermal vibrations.

NIXSW measurements obtained using the (111) reflection of the Ag(100) substrate indicate that, in both high-density phase 2 and low-density phase 1, the N atoms show a preference towards adsorbing in, or close to, the fourfold hollow sites of the Ag(100) substrate. The corresponding coherent fractions measured for N were sufficiently large to suggest a well-defined lateral registry but were lower than would be expected for the N atoms being centred on the hollow site. This was attributed to a mismatch between the molecular footprint and the underlying substrate lattice causing the four N atoms within the TCNQ to occupy inequivalent sites above the surface. The C atoms did not show any specific preference for either site, as was indicated by the very low coherent fractions measured for each C component using the (111) reflection. This is consistent with the general expectation that TCNQ interacts with the substrate via the cyano groups and thus the N atoms would have a more defined registry to the substrate than the C atoms. The bond angles and bond lengths of the molecules C backbone are highly constrained and do not match the footprint of the underlying substrate so it is unsurprising that the C atoms occupy a variety of different low symmetry sites. In contrast, the cyano groups are located at the ends of more flexible ‘arms’ of the molecule so are better able to adapt to the geometry of the substrate.

7. Coadsorption of TCNQ with alkali metals on Ag(100)

In this chapter, an experimental characterisation of charge transfer networks formed between TCNQ and alkali metals on the Ag(100) surface is presented. Initially, an STM and LEED study was conducted to reproduce the previously reported $CsTCNQ_4$ assembly[59, 168] and to identify new phases formed by TCNQ and other alkali metals (K and Na). From this, two closely related phases formed by K and Cs coadsorbed with TCNQ were identified and were subsequently studied using XPS, UPS and NIXSW to investigate the impact of varying the alkali metal on the electronic and structural properties of the interface.

7.1 STM and LEED

Table 7.1.1 – Summary of the TCNQ/alkali metal structural phases characterised by STM and LEED on Ag(100). The nominal stoichiometry inferred from the STM and LEED measurements are shown for each phase. Due to the complex nature of Na phase 1 and the ambiguity of its STM image contrast, a reliable stoichiometry could not be determined. All phases except for Na phase 1 were confirmed to be commensurate with the underlying Ag(100) substrate. For these commensurate phases, matrices of the substrate lattice vectors that describe the unit mesh are shown and the unit mesh dimensions corresponding to these matrices are given, where b_1 and b_2 are the vector lengths, γ is the included angle and Θ is the angle between vector b_1 and the substrate <110> directions. For Na phase 1, which was not confirmed to be commensurate with the Ag(100) substrate, the unit mesh dimensions were obtained from STM measurements with errors for the unit mesh dimensions shown in parentheses, giving the uncertainty on the last significant figure of the quoted value.

Phase	Nominal stoichiometry	b_1 / Å	b_2 / Å	γ / °	θ / °	Matrix
Cs phase 1	$CsTCNQ_4$	19.4	19.4	90.0	26.6	$\begin{pmatrix} 6 & 3 \\ -3 & 6 \end{pmatrix}$
K phase 1	$KTCNQ_4$	19.4	19.4	90.0	26.6	$\begin{pmatrix} 6 & 3 \\ -3 & 6 \end{pmatrix}$
K phase 2	$KTCNQ_2$	14.5	14.5	90.0	36.9	$\begin{pmatrix} 4 & 3 \\ -3 & 4 \end{pmatrix}$
K phase 3	KTCNQ	12.9	12.9	90.0	26.6	$\begin{pmatrix} 4 & 2 \\ -2 & 4 \end{pmatrix}$
Na phase 1	Unconfirmed	45(6)	34.6(5)	92(3)	0(3)	-
Na phase 2	$NaTCNQ_2$	18.5	18.5	90.0	38.7	$\begin{pmatrix} 5 & 4 \\ -4 & 5 \end{pmatrix}$
Na phase 3	NaTCNQ	12.9	12.9	90.0	26.6	$\begin{pmatrix} 4 & 2 \\ -2 & 4 \end{pmatrix}$

TCNQ/alkali metal networks were formed by depositing alkali metal atoms onto a sub monolayer coverage of the commensurate $\begin{pmatrix} 1 & 4 \\ -3 & -1 \end{pmatrix}$ TCNQ adsorption phase formed on Ag(100) (low-density phase 1, characterised in chapter 6). STM and LEED were used to characterise the molecular assembly and periodicity of the resulting adsorption structures. To aid in later discussion, the phases that were

formed are summarised in Table 7.1.1 and are each assigned an identifier (e.g. K phase 2), which will be used to refer to them throughout this section.

7.1.1 Cs/TCNQ coadsorption

Figure 7.1.1 shows STM and LEED measured from ordered networks (Cs phase 1) formed by codepositing Cs and TCNQ on Ag(100). The STM images show ordered domains of oblong protrusions, interpreted as TCNQ molecules, arranged into a windmill assembly. Bright circular protrusions are also present at the centre of each windmill and were interpreted as the locations of Cs atoms. The observed molecular assembly is consistent with the $CsTCNQ_4$ networks formed on Ag(100) previously reported by Abdurakhmanova et al.[59] for which a commensurate $\begin{pmatrix} 6 & 3 \\ -3 & 6 \end{pmatrix}$ unit mesh was suggested based on STM measurements. Comparison of the experimental LEED pattern (Figure 7.1.1c) with the LEED pattern simulated for this unit mesh (Figure 7.1.1d) shows excellent agreement and confirms that Cs phase 1 is described by a $\begin{pmatrix} 6 & 3 \\ -3 & 6 \end{pmatrix}$ matrix and is thus commensurate with respect to the underlying substrate. Furthermore, since LEED probes the surface using an electron beam with a diameter approaching 1 mm, this confirms that the adsorption phase observed by STM is the dominant packing regime across macroscopic regions of the surface.

In some STM images of the surface, bright circular protrusions, similar in shape and size to those attributed to Cs atoms, were also observed at a second site in the assembly (highlighted by the yellow circle in Figure 7.1.1b). Other images (e.g. Figure 7.1.1a) or indeed the STM previously reported for this adsorption phase,[59] do not show this second set of protrusions and instead appear to show empty pores within the molecular assembly. This could imply that Cs phase 1 is favourable for a range of Cs:TCNQ stoichiometry with the unit mesh containing four TCNQ molecules and either one or two Cs atoms. The STM suggests that both Cs sites in this interpretation are located at the centre of four TCNQ molecules arranged in a windmill with a cyano group from each molecule oriented towards the Cs atom. On inspection, the primary site appears to be better optimised for Cs-N interactions, with the molecules packed closer around the Cs than in the secondary site. This is consistent with the fact that the primary site always appears to be occupied in the STM, whereas the secondary site is only sometimes occupied.

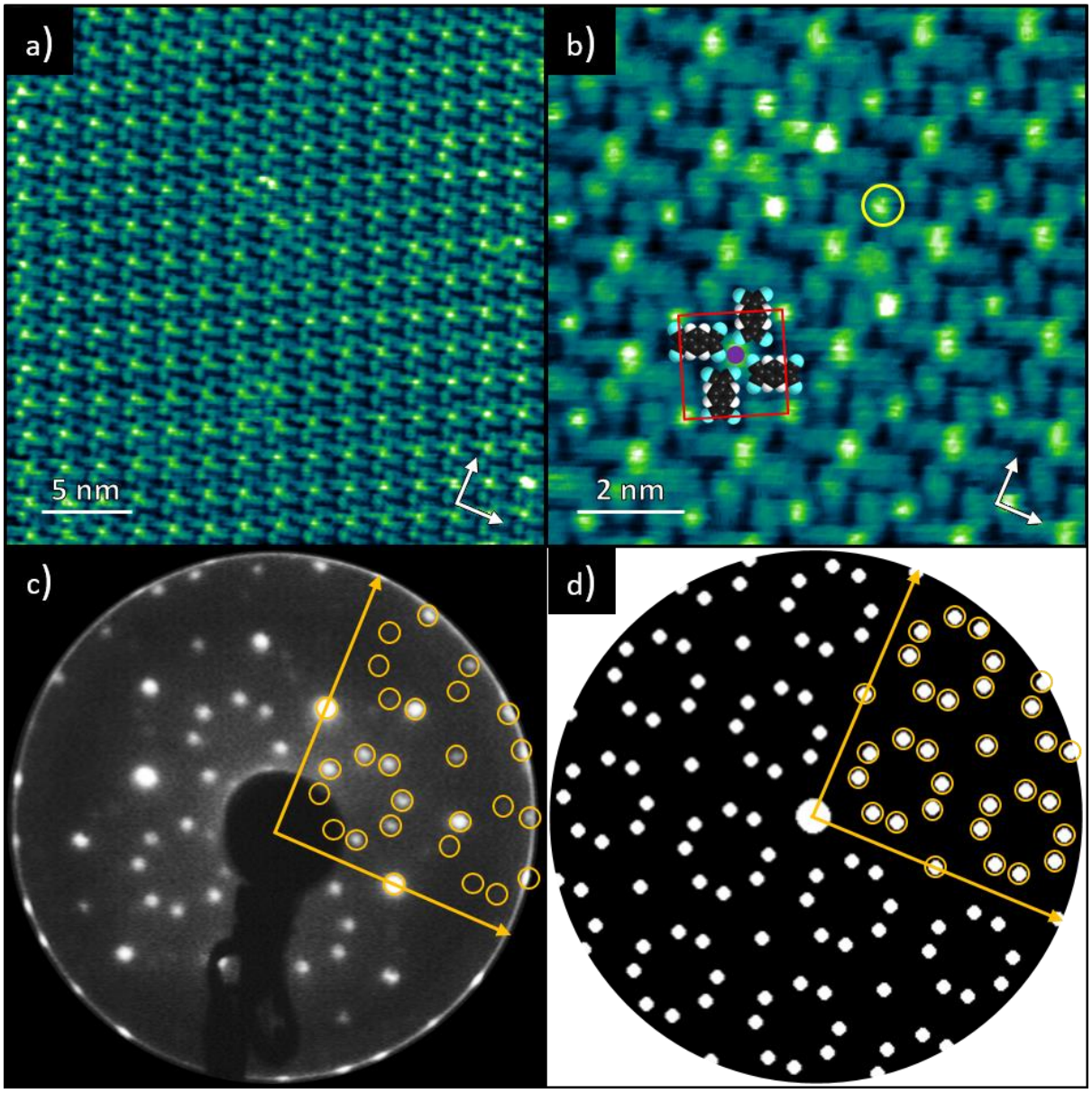

Figure 7.1.1 – STM and LEED recorded from Cs phase 1. a) – Large area STM image showing a single ordered domain (V_{samp} = -1.2 V, I = 145 pA). b) – Small area STM image (V_{samp} = -1.3 V, I = 145 pA) with scaled models of TCNQ molecules and a Cs atom (purple circle) superimposed in the assembly previously reported for this phase by Abdurakhmanova et al. [59] The surface unit mesh is indicated by the red square and the yellow circle highlights a protrusion in the STM contrast that was not observed in the previously reported STM images of this phase.[59] In both STM images, the white arrows indicate the substrate <110> directions. c) – LEED pattern measured at an electron kinetic energy of 17.0 eV. d) – Simulated LEED pattern for a commensurate $\begin{pmatrix} 6 & 3 \\ -3 & 6 \end{pmatrix}$ unit mesh. In both the experimental and simulated LEED patterns, the substrate <110> directions are shown by the yellow arrows. To aid in the comparison of the two patterns, the diffraction beams are highlighted by yellow circles in one quadrant of the LEED pattern. Note that at the electron kinetic energy used, some diffraction beams are only faintly visible.

DFT calculations, reported for this adsorption phase, identified intermolecular hydrogen bonds and molecule/substrate CN-Ag bonds as key driving factors for the observed molecular assembly.[168] In this calculated structure, the hydrogen bonds, which are formed between the cyano groups and the H atoms on the central TCNQ ring, are the main interaction between neighbouring windmill units and thus play a significant role in determining the molecular assembly.[168] This is supported by further calculations which found the structure to be unstable for the tetra-fluorinated TCNQ derivative F4-TCNQ which cannot form these hydrogen bonds.[168] If this molecular assembly is indeed able to accommodate either one or two Cs atoms per unit mesh, this would indicate that the observed molecular assembly is considerably more stable than an adsorption structure with two sites optimised for Cs-N interactions. It is interesting to note that the STM images appear to show domains with complete occupation of either one or two of the Cs sites and no domains with a partially occupied secondary Cs site. This unusual result could indicate a cooperative binding effect in which the occupation of one secondary site favours the occupation of other nearby secondary sites. Another possibility could be that the protrusions in the secondary sites are visible only under certain STM tip conditions and may not always be observed. It should also be noted that as STM is not a chemically sensitive technique, it was not possible to establish whether these protrusions do indeed correspond to Cs atoms and thus could be caused by other species, including contaminants, or could relate to some electronic or tip-related effects.

7.1.2 K/TCNQ coadsorption

Figure 7.1.2 shows STM and LEED from ordered networks (K phase 1) formed by codepositing K and TCNQ on Ag(100). STM of the surface shows a similar windmill arrangement to that of Cs phase 1, though the STM contrast does not show any features that could be attributed to K atoms. Figure 7.1.2b shows a proposed adsorption structure superimposed on the STM image with K atoms located at the centre of the windmills, based on the reported $CsTCNQ_4$ structure.[59, 168] The LEED pattern measured from K phase 1 also shows excellent agreement with a $\begin{pmatrix} 6 & 3 \\ -3 & 6 \end{pmatrix}$ unit mesh, indicating that the K phase 1 shares the same periodicity as Cs phase 1 and is commensurate with the underlying Ag(100) substrate. The fact that TCNQ coadsorption with two alkali metals, that differ in ionic radius by ~0.3 Å,[187] form commensurate structures with identical periodicity and molecular assembly could suggest that the molecule-substrate interactions have significant influence in determining the adsorption structure. DFT calculations obtained for this particular TCNQ arrangement also find that it promotes hydrogen bonding between the windmill units.[168] In the TCNQ/alkali metal windmill structures formed on the Ag(111) surface, characterised earlier in this thesis (see chapter 5), which have a 1:1 stoichiometry, the interactions between windmill units are mediated by ionic bonds, with each TCNQ molecule bonding to four alkali metal atoms and *vice versa*. In the present phase (K phase 1), which is attributed to a

$KTCNQ_4$ stoichiometry, there is no possibility of ionic interactions linking the windmill units and thus these hydrogen bonding interactions are expected to be of great importance to the stability of this assembly.

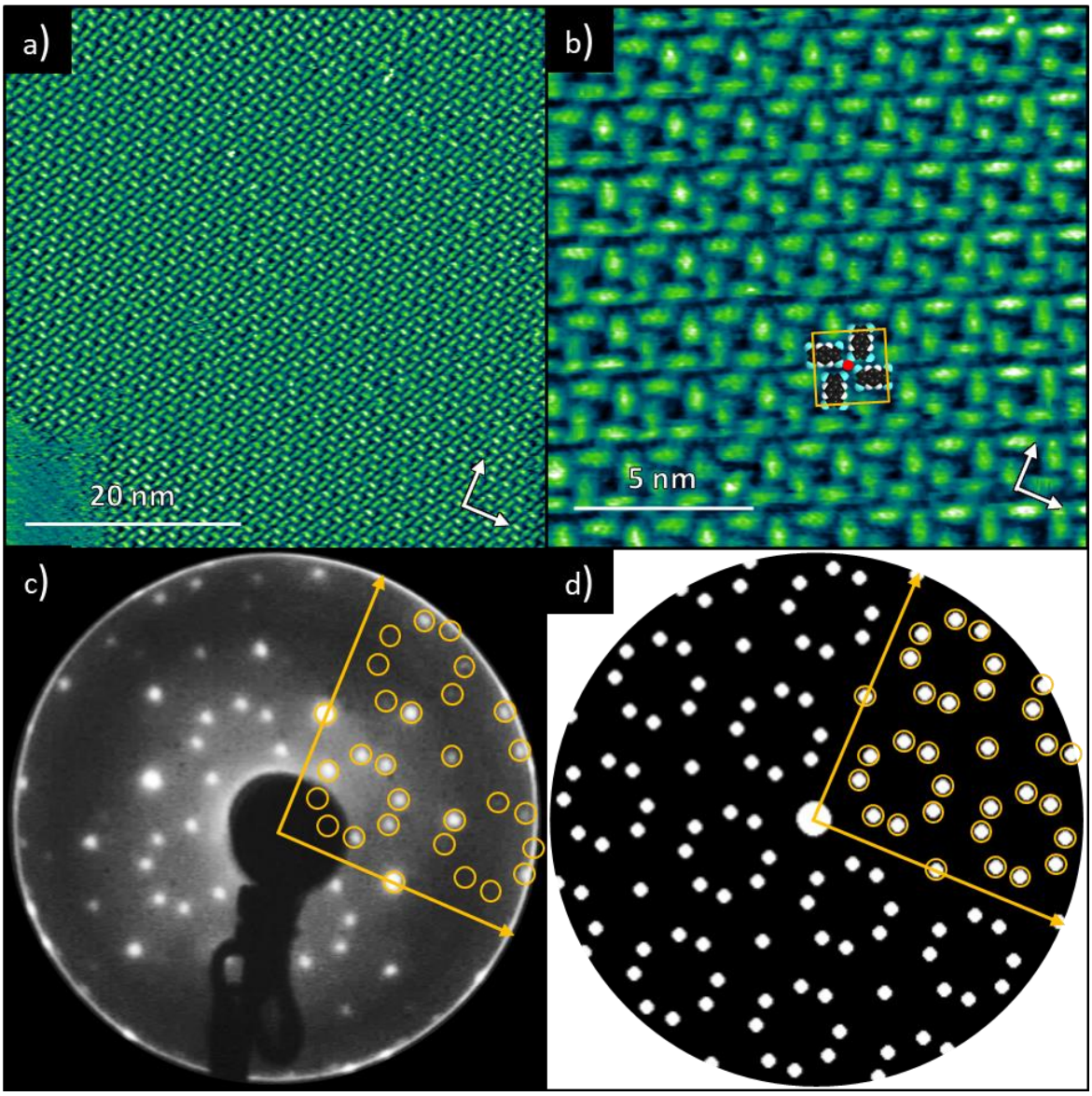

Figure 7.1.2 - STM and LEED recorded from K phase 1. a) – Large area STM image showing a single ordered domain (V_{samp} = -0.9 V, I = 250 pA). b) – Small area STM image (V_{samp} = -0.9 V, I = 250 pA) of the adsorption phase with scaled models of TCNQ molecules and a K atom (red circle) superimposed. The surface unit mesh is indicated by the yellow square. In both STM images, the white arrows indicate the substrate <110> directions. c) – LEED pattern measured at an electron kinetic energy of 18.0 eV. d) – Simulated LEED pattern for a commensurate $\begin{pmatrix} 6 & 3 \\ -3 & 6 \end{pmatrix}$ unit mesh. In both the experimental and simulated LEED patterns, the substrate <110> directions are shown by the yellow arrows. To aid in the comparison of the two patterns, the diffraction beams are highlighted by yellow circles in one quadrant of the LEED pattern. Note that at the electron kinetic energy used, some diffraction beams are only faintly visible.

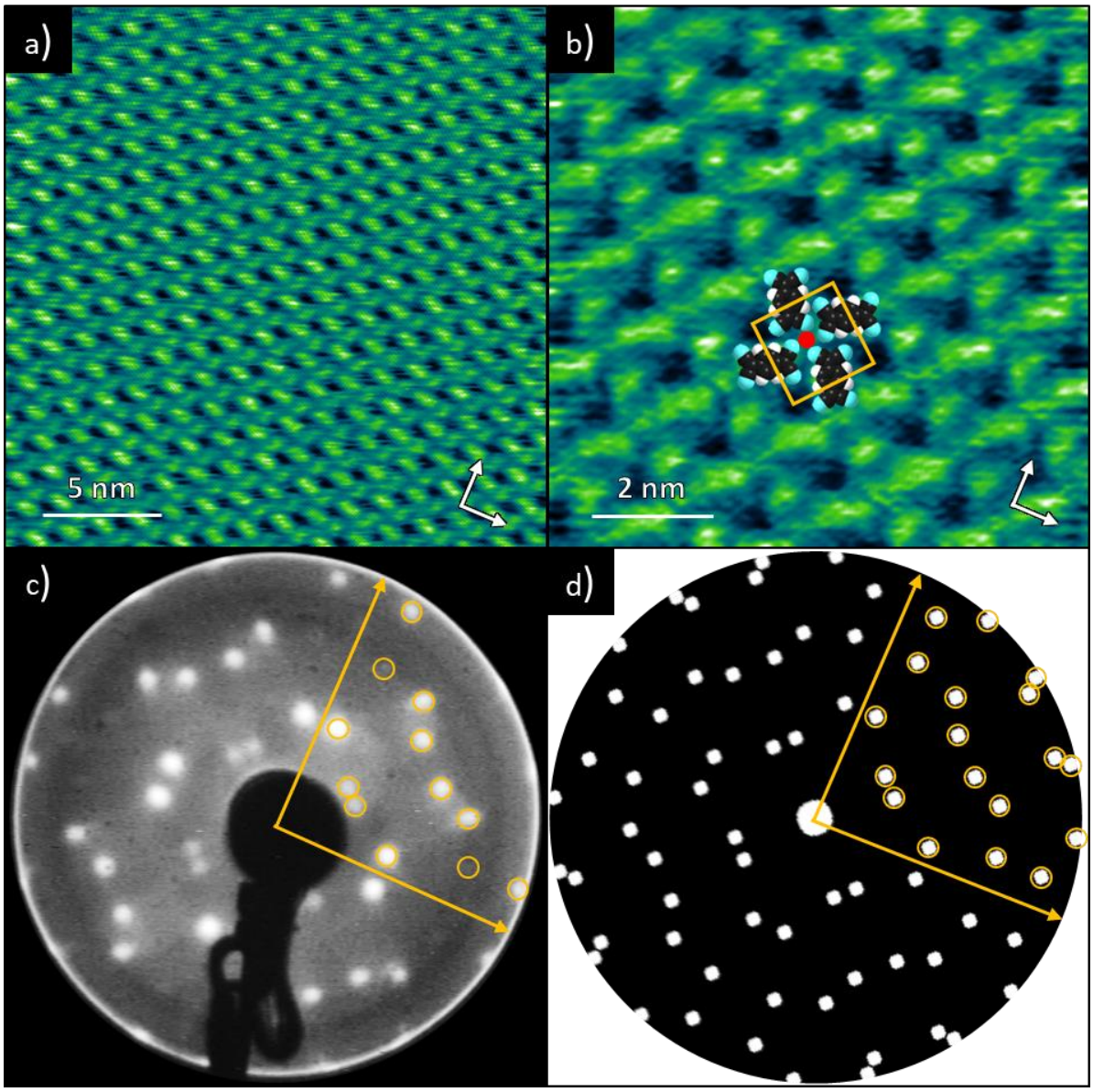

Figure 7.1.3 - STM and LEED recorded from K phase 2. a) – Large area STM image showing a single ordered domain (V_{samp} = -1.5 V, I = 200 pA). b) – Small area STM image (V_{samp} = -1.0 V, I = 250 pA) of the adsorption phase with scaled models of TCNQ molecules and a K atom (red circle) superimposed. The surface unit mesh is indicated by the yellow square. In both STM images, the white arrows indicate the substrate <110> directions. c) – LEED pattern measured at an electron kinetic energy of 16.0 eV. d) – Simulated LEED pattern for a commensurate $\begin{pmatrix} 4 & 3 \\ -3 & 4 \end{pmatrix}$ unit mesh. In both the experimental and simulated LEED patterns, the substrate <110> directions are shown by the yellow arrows. To aid in the comparison of the two patterns, the diffraction beams are highlighted by yellow circles in one quadrant of the LEED pattern. Note that at the electron kinetic energy used, some diffraction beams are only faintly visible.

Further deposition of K onto a sample of K phase 1 resulted in a transition to a different adsorption structure (K phase 2) for which STM and LEED are shown in Figure 7.1.3. STM from K phase 2 shows large ordered domains of TCNQ molecules arranged in a windmill assembly. Although the STM contrast did not show any features that could be attributed to K atoms in this structure, it was concluded that K atoms are located at the centre of the TCNQ windmill units, in line with previously characterised TCNQ/alkali metal adsorption structures, both in this work and elsewhere in the literature.[57, 59, 172] K phase 2 differs from K phase 1 as each TCNQ molecule is shared between two windmill units, resulting in a nominal $KTCNQ_2$ stoichiometry. The assembly suggests that the windmill units are linked via CN-K interactions to form an ionic network and thus intermolecular hydrogen bonding interactions are expected to be less important in stabilising this phase, although the TCNQ assembly does appear to promote hydrogen bonding between adjacent molecules in each windmill unit.

Averaging measurements from eight STM images indicates that the unit mesh of K phase 2 is defined by vector lengths b_1 = (14.4 ± 0.7) Å and b_2 = (14.5 ± 0.7 Å), an included angle of (91 ± 3)° and vector $\mathbf{b_1}$ oriented at an angle of (37 ± 4)° from the substrate <110> directions. These unit mesh dimensions are therefore consistent with a commensurate $\begin{pmatrix} 4 & 3 \\ -3 & 4 \end{pmatrix}$ matrix, which corresponds to a square unit mesh with vector lengths of 14.45 Å rotated by 36.9° relative the substrate <110> directions. Comparison of the experimental LEED pattern with the LEED pattern simulated for a $\begin{pmatrix} 4 & 3 \\ -3 & 4 \end{pmatrix}$ matrix shows excellent agreement, thus confirming the accuracy of the STM measured unit mesh.

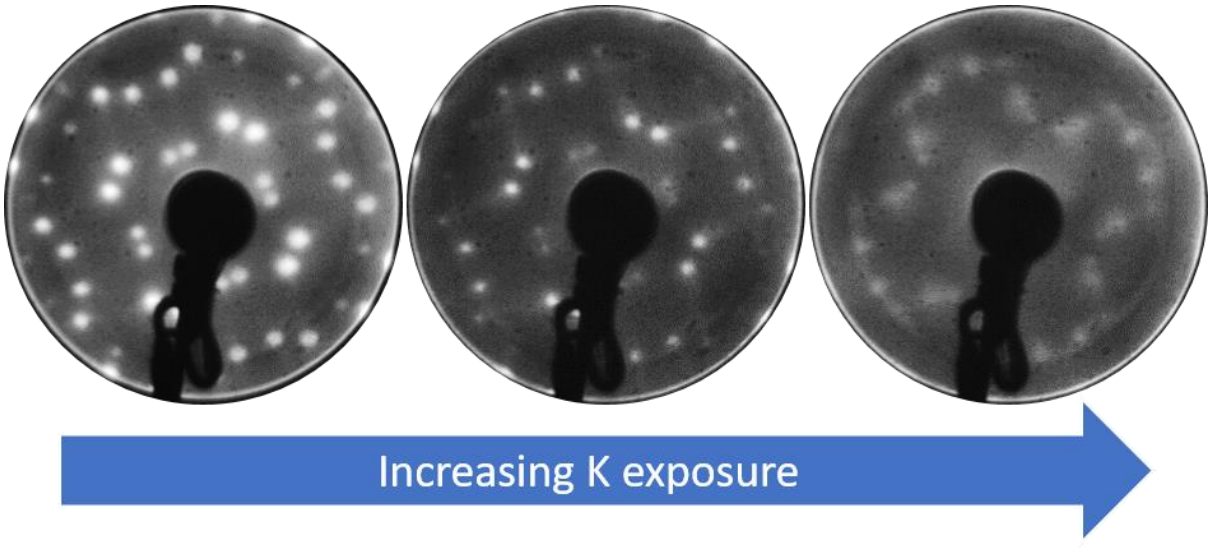

Figure 7.1.4 – LEED recorded after sequential deposition of K onto K phase 2. All LEED patterns were measured with an electron kinetic energy of 14.5 eV.

Figure 7.1.4 shows LEED recorded after further deposition of K onto K phase 2 to monitor any changes to the surface structure. With increasing K exposure, no new diffraction beams appear in the LEED. Instead, the LEED pattern become more diffuse with streaks forming between the diffraction beams. This indicates that K phase 2 remains the dominant ordered structure on the surface, however, the diffuse beams and streaks suggest the presence of disorder or mobility on the surface. One probable cause of this is that the K atoms deposited onto the surface are not incorporated into the TCNQ layer and instead are mobile on the surface. This could indicate that structures with K:TCNQ ratios larger than 1:2 are not favourable on the Ag(100) surface or that there is an activation barrier preventing their formation at ambient temperature. To investigate this further, a sample prepared by depositing excess K onto K phase 2 was annealed to overcome any potential activation barriers and allow the surface structure to rearrange. This process was monitored by LEED and is shown in Figure 7.1.5.

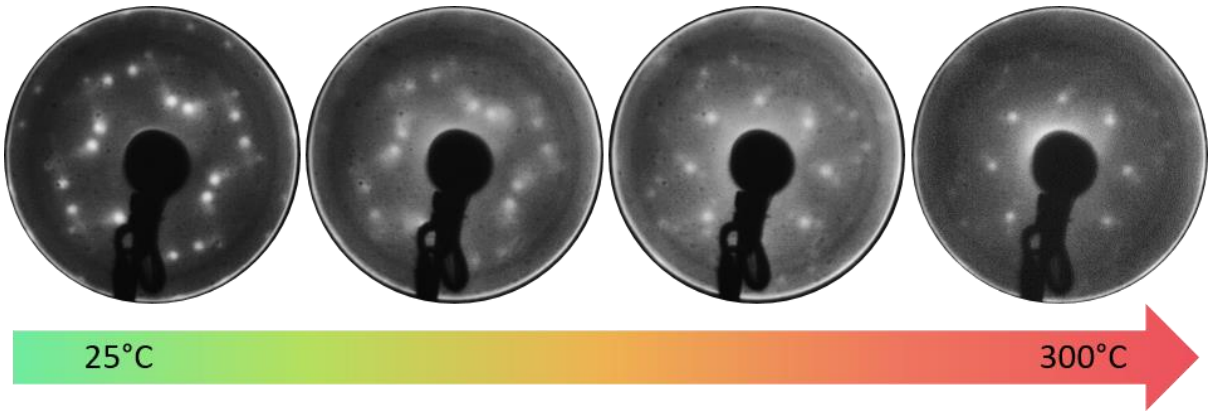

Figure 7.1.5 – LEED measured whilst annealing a sample of K phase 2 with excess K deposited on top. All LEED patterns were recorded using an electron kinetic energy of 18.0 eV.

Upon annealing the sample, the LEED shows a phase transition, with new diffraction beams (corresponding to K phase 3) appearing whilst those from K phase 2 gradually fade until, at 300 °C, only the new LEED pattern is visible. Upon cooling back to ambient temperature, the K phase 3 LEED pattern remains and the K phase 2 pattern does not reappear, indicating that the phase transition is irreversible. One interesting observation is that the K phase 3 LEED pattern has the same form as the K phase 1 LEED pattern but has a larger reciprocal mesh. This indicates that the K phase 3 has the same symmetry and azimuthal orientation as K phase 1 but with a smaller real space unit mesh. A $\begin{pmatrix} 4 & 2 \\ -2 & 4 \end{pmatrix}$ unit mesh is compatible with this observation and, indeed, the experimental LEED pattern is in excellent agreement with the LEED pattern simulated for this mesh (Figure 7.1.6), confirming this as the periodicity of K phase 3. This corresponds to a square unit mesh defined by vector lengths of 12.9 Å oriented at 26.6° to the substrate <110> directions. It is worth noting that these unit mesh dimensions

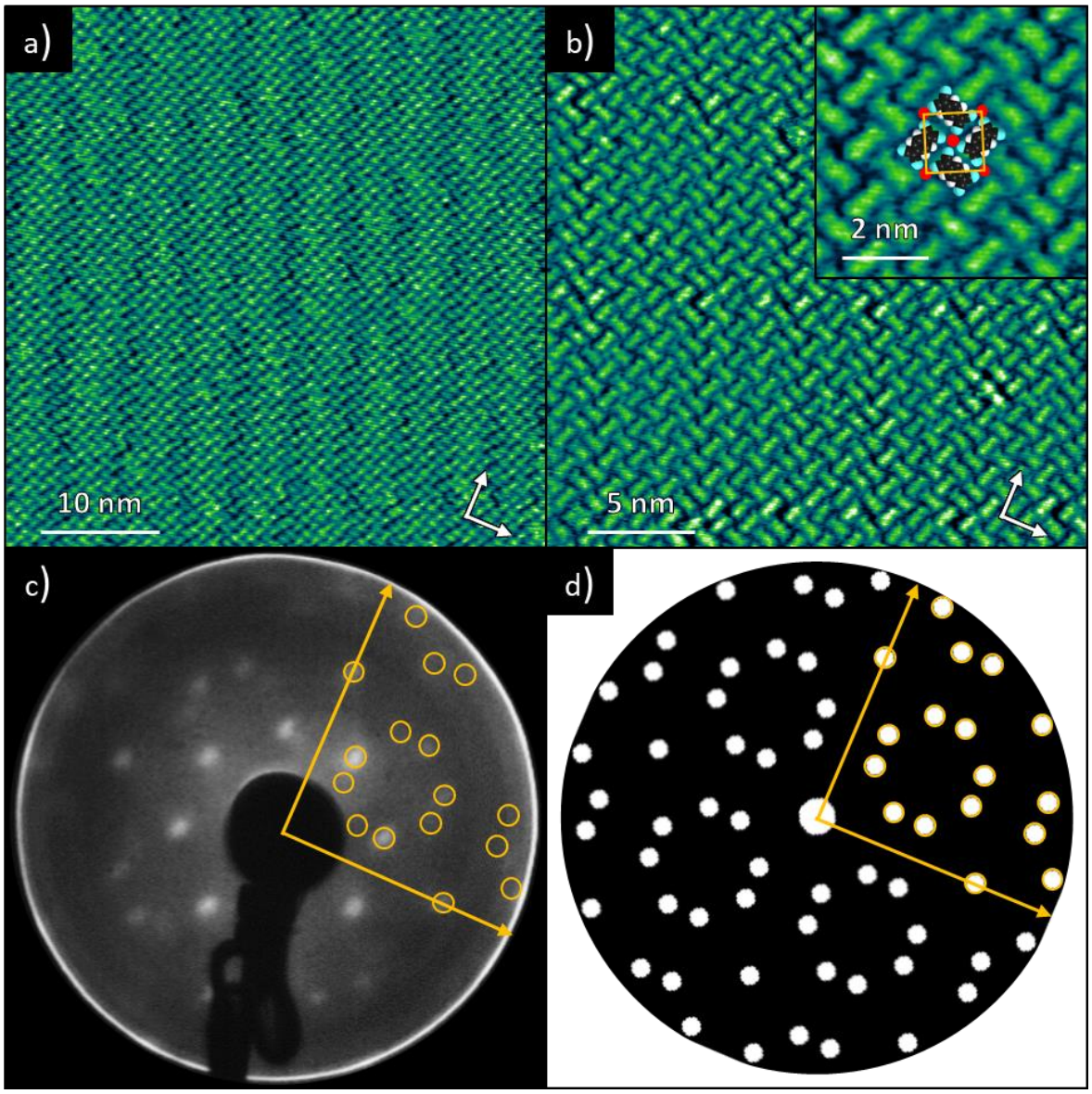

Figure 7.1.6 – STM and LEED recorded from K phase 3. a) – Large area STM image showing ordered domains with numerous dislocations. (V_{samp} = -0.8 V, I = 100 pA). b) – Selected area STM image (V_{samp} = -0.6 V, I = 300 pA). The inset shows an expanded area of the image with scaled models of TCNQ molecules and K atoms (red circles) superimposed. The surface unit mesh is indicated by the yellow square. In both STM images, the white arrows indicate the substrate <110> directions. c) – LEED pattern measured at an electron kinetic energy of 25.0 eV. d) – Simulated LEED pattern for a commensurate $\begin{pmatrix} 4 & 2 \\ -2 & 4 \end{pmatrix}$ unit mesh. In both the experimental and simulated LEED patterns, the substrate <110> directions are shown by the yellow arrows. To aid in the comparison of the two patterns, the diffraction beams are highlighted by yellow circles in one quadrant of the LEED pattern. Note that at the electron kinetic energy used, some diffraction beams are only faintly visible.

are similar to those measured for the KTCNQ windmill phase on the Ag(111) substrate, characterised earlier in this thesis (see section 5.1.1). A similar windmill structure with a 1:1 K:TCNQ stoichiometric ratio was therefore expected for K phase 3. STM of K phase 3 (Figure 7.1.6) reflects this, showing oblong protrusions, interpreted as TCNQ molecules, arranged into a windmill structure with each TCNQ molecule shared between four windmill units. Although no features were observed that could be attributed to K atoms in the STM images, it was assumed that each windmill contains a K atom at the centre in accordance with the interpretation of other similar TCNQ/alkali metal structures studied previously, both in this thesis and elsewhere in the literature.[57, 59, 172]

The STM images of the surface appear to show frequent dislocations in the form of anti-phase boundaries between relatively small domains (~5 x 10 nm) of K phase 3. As the size of these domains is smaller the transfer width of the LEED optics, it is likely that interference between the domains is significant in determining the LEED pattern. In this respect the high frequency of anti-phase domain boundaries could explain the rather diffuse nature of the observed LEED pattern. The frequent dislocations also suggests that there is some strain in the structure, possibly resulting from a mismatch between the optimal adsorption layer assembly and the geometry imposed by the underlying Ag(100) substrate. To evaluate this further, it is useful to compare K phase 3 to the similar KTCNQ structure formed on the Ag(111) surface, which is incommensurate and thus the substrate periodicity is not strictly imposed. The KTCNQ structure on Ag(111) has unit mesh dimensions of $b_1 = (13.7 \pm 0.4)$ Å and $b_2 = (13.0 \pm 0.4$ Å), therefore occupying a larger area than K phase 3 and thus suggesting that under circumstances where the substrate has a lesser directing effect, the KTCNQ windmills favour a unit mesh that is larger than the $\begin{pmatrix} 4 & 2 \\ -2 & 4 \end{pmatrix}$ mesh adopted by K phase 3 on Ag(100). This suggests that K phase 3 is significantly strained and that this is a plausible cause of the dislocations observed in the STM images.

7.1.3 Na/TCNQ coadsorption

Figure 7.1.7 shows STM and LEED measured from structures formed by codepositing Na and TCNQ on Ag(100). The STM images show domains from two coexisting ordered phases on the surface, with TCNQ molecules appearing as rounded oblong protrusions. The first of these phases (Na phase 1, outlined in yellow in Figure 7.1.7a and shown in Figure 7.1.7b) consists of TCNQ molecules, arranged in a relatively complex structure which appears to include windmill units. STM of Na phase 1 also appears to include large circular depressions, interpreted as pores within the molecular layer, but does not show any clear features that could be attributed to Na atoms. However, as the adsorption structure is different from any of the phases observed for pure TCNQ on Ag(100), it was concluded that Na must

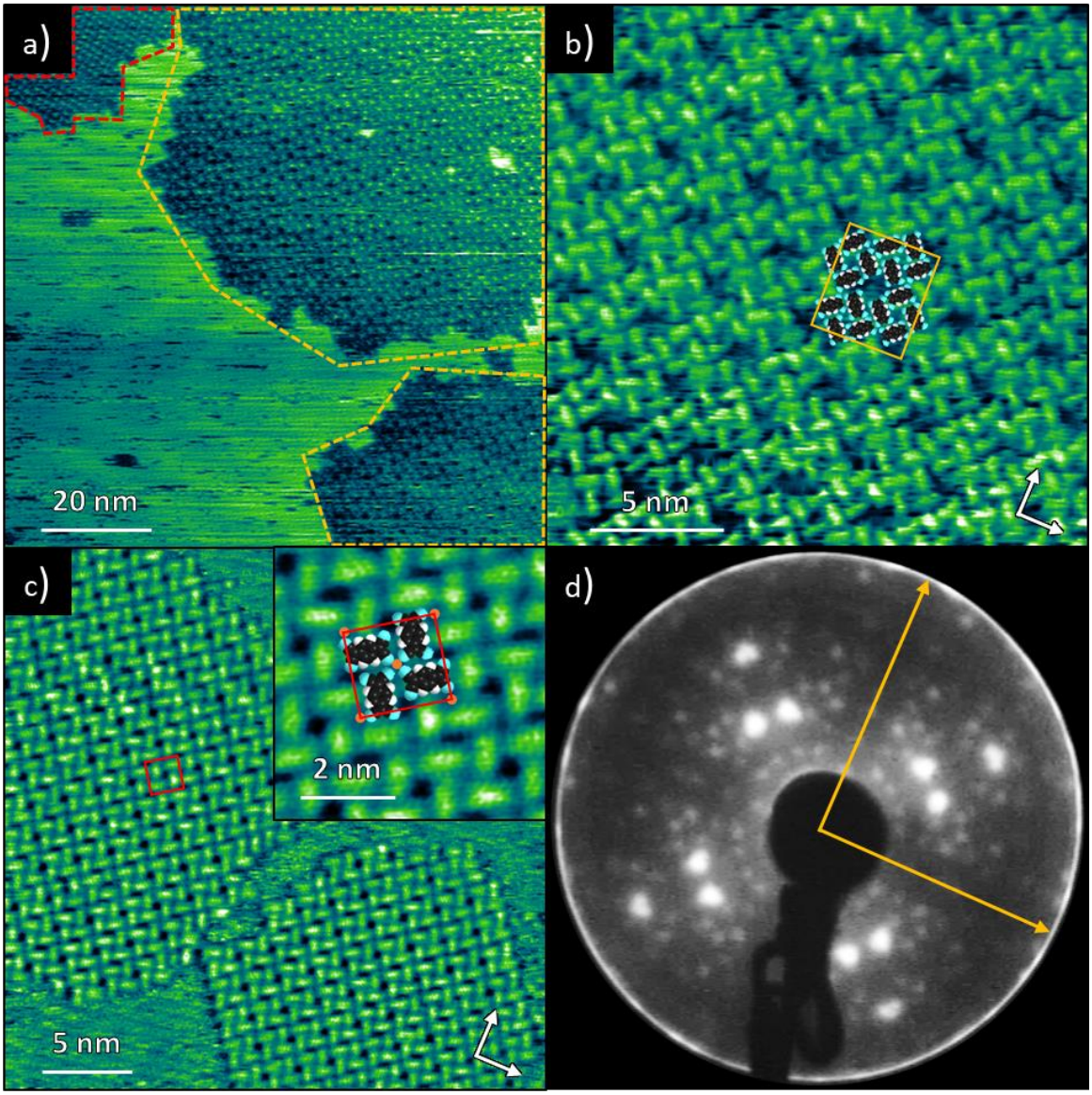

Figure 7.1.7 - STM and LEED recorded from a mixed phase sample consisting of Na phase 1 and Na phase 2. a) – Large area STM image showing domains of both ordered phases. The domains for each ordered phase are outlined in different colours, with Na phase 1 highlighted in yellow and Na phase 2 highlighted in red. (V_{samp} = -0.8 V, I = 85 pA). b) – Small area STM image showing a single ordered domain of Na phase 1. Scaled models of TCNQ molecules are superimposed in the assembly interpreted from the STM image and the surface unit mesh is indicated by the yellow rectangle. (V_{samp} = -0.8 V, I = 85 pA) c) – Small area STM image showing domains of Na phase 2. The inset shows scaled superimposed models of TCNQ molecules and Na atoms (orange circles). The surface unit mesh is indicated by the red square. In all STM images, the white arrows indicate the substrate <110> directions. d) – LEED pattern measured at an electron kinetic energy of 18.0 eV. The substrate <110> directions are shown by the yellow arrows.

be involved within this molecular assembly. The unit mesh for this assembly is indicated by the yellow rectangle in Figure 7.1.7b and was deduced to contain sixteen TCNQ molecules by overlaying scaled molecular models to fit the observed STM contrast. It was not possible to determine the number of Na

atoms within the unit mesh, due to the lack of attributable features and the complex nature of the structure. However, as further deposition of Na onto the surface favoured the formation of an $NaTCNQ_2$ structure (Na phase 2, discussed later), it was deduced that Na phase 1 must have an Na:TCNQ ratio lower than 1:2.

Unit mesh dimensions for Na phase 1 were obtained from measurements averaged from six different STM images, which gives vector lengths of $b_1 = (45 \pm 6)$ Å and $b_2 = (34.6 \pm 0.5)$ Å, an included angle of $(92 \pm 3)°$ and vector $\mathbf{b_1}$ oriented at an angle of $(0 \pm 3)°$ to the substrate <110> directions. The associated errors correspond to the standard deviation of the values averaged to give the quoted values. It should be noted that vector length b_1 has a large error range which was caused by large discrepancies between measurements taken from up and down scans[**]. As the main component of this vector is directed in the vertical axis of this image, its measured length is highly susceptible to drift occurring over the course of each scan. The quoted values were obtained by averaging over equal numbers of consecutively recorded up and down scans and thus the quoted values should account for the effects of drift over the course of the scan but, in the case of vector length b_1, produces a large associated error. Nevertheless, the unit mesh for this adsorption phase is large and therefore should produce a LEED pattern with a high density of diffraction beams. The experimentally measured LEED pattern (Figure 7.1.7d) is consistent with this, showing a large number of closely spaced diffraction beams, even at a relatively low electron kinetic energy of 18.0 eV. Due to the high density of diffraction beams and the large uncertainty of the measured vector length b_1, it was not possible to precisely assign the observed diffraction beams or to use the measured LEED pattern to confirm the accuracy of the STM measured unit mesh.

STM of Na phase 2 shows TCNQ molecules arranged into a more regular windmill structure. The structure appears to alternate between two types of windmill, with the first type showing a noticeable depression at the centre (open windmill), attributed to an unoccupied pore within the structure, whereas others are more closely packed together showing a much smaller depression at the centre (closed windmill). Similar to many of the previously studied TCNQ/alkali metal structures, the STM contrast did not show any features that could be assigned to Na atoms. However, the appearance of the closed windmills is consistent with those interpreted to be occupied by alkali metal atoms in previously characterised TCNQ/alkali metal structures, both earlier in this thesis and elsewhere in the literature.[57,

[**]The raster scans consisted of the tip sweeping left to right across the surface with the tip gradually moving either up or down (all directions relative to the STM images as they are presented). The raster scan direction alternated between consecutively captured images.

[59, 172] Overlaying scaled TCNQ and Na^+ models (using the Na^+ ionic radius of 0.99 Å)[187] over the STM contrast (Figure 7.1.7c) gives good agreement with this assignment, with the Na^+ fitting into a closely packed site surrounded by cyano groups from four TCNQ molecules. In Na phase 2, TCNQ molecules are shared between two closed windmill units, thus showing similarities to the $KTCNQ_2$ structure (K phase 2) also formed on Ag(100). This interpretation suggests a stoichiometry of $NaTCNQ_2$ for Na phase 2. Despite these similarities between Na phase 2 and K phase 2, there are also some significant differences between two phases. Most notably, the $KTCNQ_2$ structure has only two TCNQ molecules and one K atom per unit mesh whereas the unit mesh of the $NaTCNQ_2$ structure contains four TCNQ molecules and two Na atoms. This owes to a small difference in the molecular packing between the respective structures, with the pores in the 'open' windmill units of the Na phase 2 structure alternating between being oblong and circular in shape, whereas in the K phase 2, the open windmills all have the same circular shaped pores.

STM unit mesh measurements for Na phase 2, averaged from eight different images, give vector lengths of $b_1 = (18.8 \pm 0.3)$ Å and $b_2 = (18.3 \pm 1.2)$ Å with an included angle of $(91 \pm 2)°$ and the vector $\mathbf{b_1}$ rotated $(38 \pm 2)°$ from the substrate <110> directions. These values are consistent with a $\begin{pmatrix} 5 & 4 \\ -4 & 5 \end{pmatrix}$ commensurate matrix which corresponds to a square unit mesh with vector lengths of 18.5 Å rotated 38.7° from the substrate <110> directions. Due to the high density of diffraction beams from the coexisting Na phase 1, it was not possible to use the LEED to confirm the accuracy of the $\begin{pmatrix} 5 & 4 \\ -4 & 5 \end{pmatrix}$ unit mesh suggested for Na phase 2.

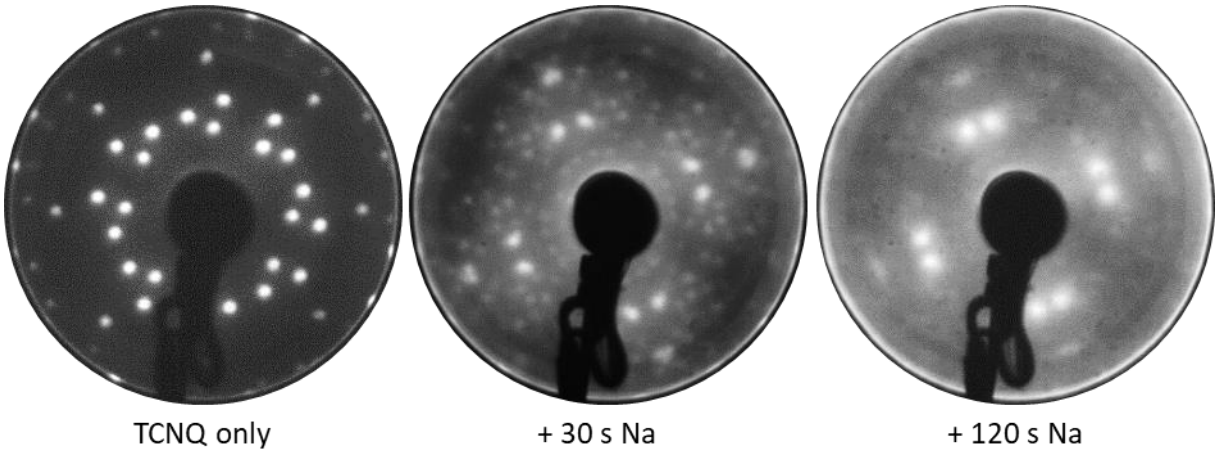

Figure 7.1.8 – Comparison of LEED patterns captured after depositing different quantities of Na onto the TCNQ/Ag(100) surface. Na was deposited on top of the $\begin{pmatrix} 1 & 4 \\ -3 & -1 \end{pmatrix}$ pure TCNQ phase in 30 s instalments. All LEED patterns were measured using an electron kinetic energy of 18.0 eV.

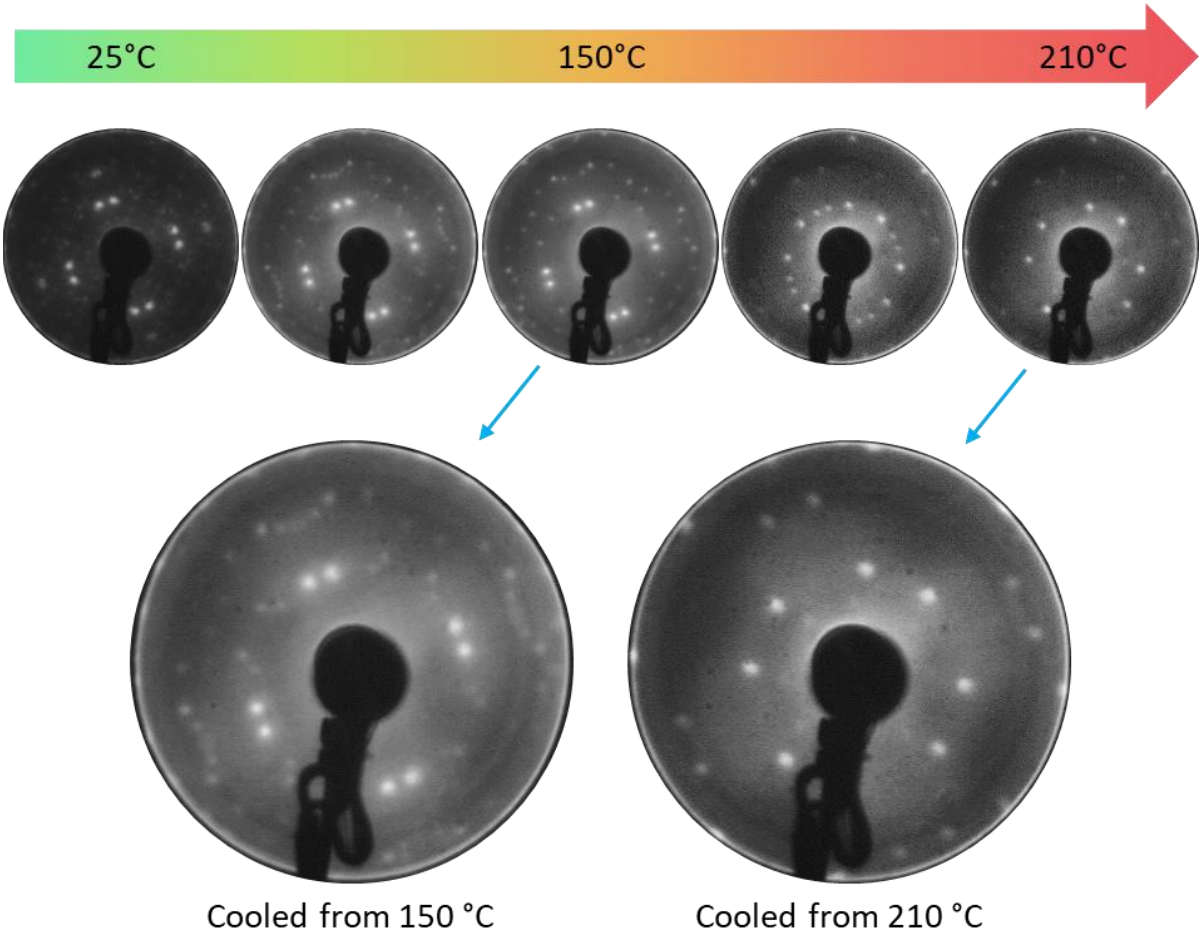

Figure 7.1.9 – LEED captured whilst annealing a mixed phase Na phase 1/Na phase 2 sample with excess Na present on the surface. After annealing to 150 °C and 210 °C, the sample was cooled to ambient temperature and the resulting LEED patterns were also captured. All LEED patterns were captured using an electron kinetic energy of 18.0 eV.

To determine whether TCNQ/Na phases could form at different stoichiometry, samples were prepared by depositing larger quantities of Na onto the initial pure TCNQ phase. This process was monitored by LEED and is shown in Figure 7.1.8, which shows that beyond the formation of a mixed Na phase 1 and Na phase 2 sample, further deposition of Na does not cause any additional phase transitions and instead results in the pre-existing LEED pattern becoming increasingly diffuse. The diffuse LEED pattern could be caused by a variety of factors including the surface becoming more disordered, the presence of high mobility species on the surface or the attenuation of diffraction beams caused by adsorbates present on top of the ordered domains. This suggests that instead of diffusing into the TCNQ adsorption layer, the excess Na atoms are mobile on the surface and/or on top of the ordered domains. For the K/TCNQ structures on Ag(100), similar observations were made and it was found that structures with higher K/TCNQ stoichiometry could be formed by annealing the sample, suggesting that there is an activation

barrier preventing the spontaneous formation of these phases at ambient temperature. A similar approach was therefore taken for the Na/TCNQ phases, monitoring the adsorption structure using LEED as a sample with excess Na was annealed (Figure 7.1.9).

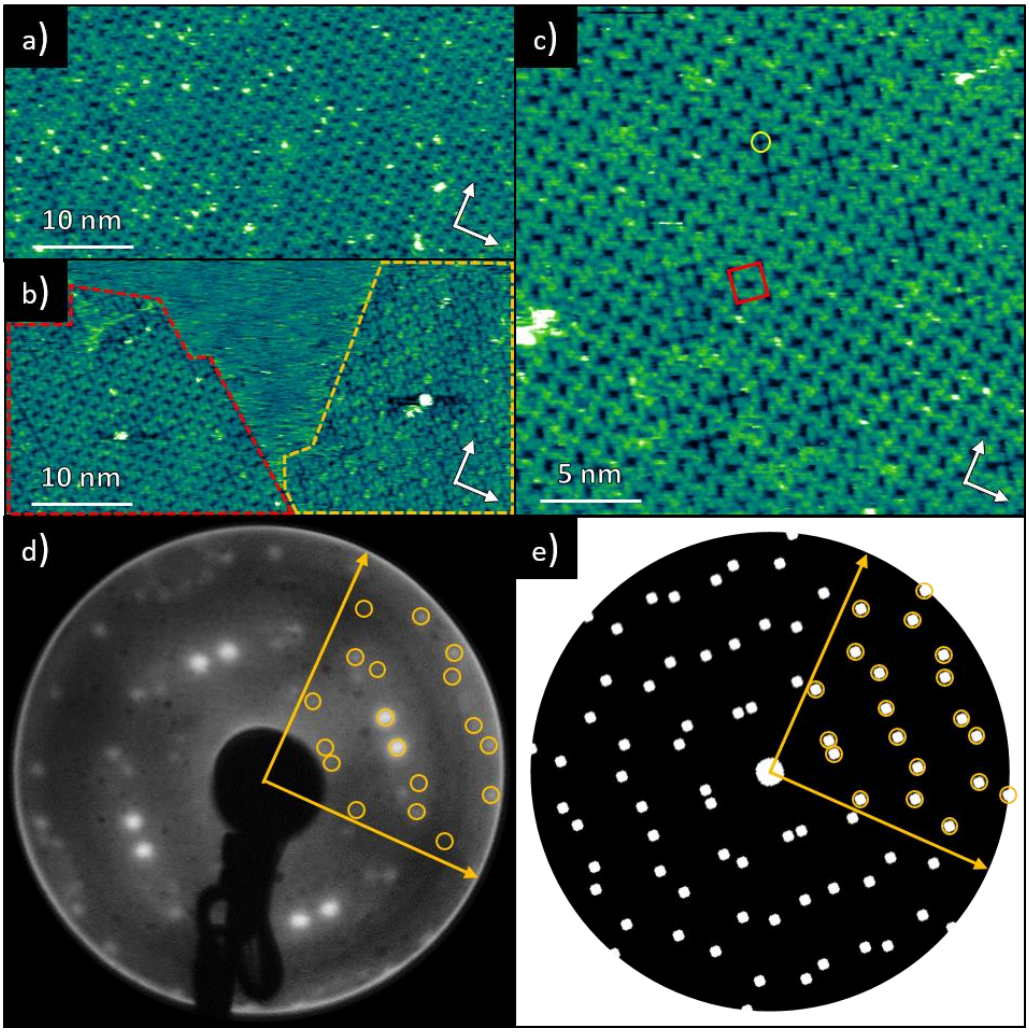

Figure 7.1.10 - STM and LEED recorded after annealing a sample of Na/TCNQ on Ag(100) to 150 °C. a) Large area STM image showing a single ordered domain of Na phase 2 (V_{samp} = -0.8 V, I = 300 pA). b) Large area STM image showing domains from Na phase 1 and Na phase 2. The domains of each ordered phase are coloured differently, with Na phase 1 outlined in yellow and Na phase 2 outlined in red. (V_{samp} = -0.4 V, I = 75 pA). c) Small area STM image showing a single ordered domain of Na phase 2. The surface unit mesh is indicated by the red square and an apparently vacant Na site is highlighted by the yellow circle (V_{samp} = -0.6 V, I = 300 pA). In all STM images, the white arrows indicate the substrate <110> directions. d) LEED pattern measured at an electron kinetic energy of 14.5 eV. e) Simulated LEED pattern for a commensurate $\begin{pmatrix} 5 & 4 \\ -4 & 5 \end{pmatrix}$ unit mesh. In both the experimental and simulated LEED patterns, the substrate <110> directions are shown by the yellow arrows. To aid in the comparison of the two patterns, the diffraction beams are highlighted by yellow circles in one quadrant of the LEED pattern. Note that at the electron kinetic energy used, some diffraction beams are only faintly visible.

The LEED captured whilst annealing the sample shows two main transitions, with the high density of diffraction beams, associated with Na phase 1, fading whilst the Na phase 2 LEED pattern remains. At an annealing temperature of 150 °C, the Na phase 1 LEED pattern is no longer visible, suggesting that only Na phase 2 is present on the surface, although upon cooling back to ambient temperature, some other very faintly visible diffraction beams reappear. Further annealing of the sample beyond 150 °C results in the appearance of a new LEED pattern (corresponding to Na phase 3, discussed later) with the Na phase 2 LEED pattern fading completely at a temperature of 210 °C. Upon cooling from 210 °C to ambient temperature the Na phase 3 LEED pattern remains and no additional diffraction beams emerge.

A sample obtained after annealing to 150 °C was measured by STM (Figure 7.1.10), which shows large domains of Na phase 2, although some domains of Na phase 1 were still present on the surface. This is consistent with the measured LEED pattern (Figure 7.1.10d) which is dominated by the Na phase 2 LEED pattern but also shows some faint additional features. The experimental LEED pattern is in excellent agreement with the LEED pattern simulated for a $\begin{pmatrix} 5 & 4 \\ -4 & 5 \end{pmatrix}$ unit mesh, thus confirming the accuracy of the STM measurements for Na phase 2. The STM contrast obtained for Na phase 2 from this sample showed circular protrusions at the centre of the windmill units. These were interpreted as Na atoms as the positions of these protrusions are consistent with the proposed model for this phase, further supporting the assigned $NaTCNQ_2$ stoichiometry. The STM images also showed that these protrusions were absent from some sites (e.g. the site marked by the yellow circle in Figure 7.1.10), which suggests that the structure contains some Na vacancies.

Figure 7.1.11 shows STM and LEED measured from the TCNQ/Na sample on Ag(100) after annealing to 210 °C. The STM shows ordered domains of oblong protrusions, interpreted as TCNQ molecules, arranged into a closely packed windmill structure (Na phase 3). Unlike Na phase 2, this phase does not include regularly distributed pores within the molecular assembly, which suggests that Na atoms are present at the centre of each windmill. There are some windmill units, scattered randomly throughout the ordered domains that feature depressions at the centre, suggesting that the structure contains some Na vacancies. In this assembly, each TCNQ molecule is shared between four windmill units, suggesting that an ionic network with a nominal 1:1 stoichiometry is formed. Averaging measurements of the unit mesh dimensions from six STM images of Na phase 3 gives vector lengths of $b_1 = (13.1 \pm 0.3)$ Å and $b_2 = (13.0 \pm 0.5)$ Å with an included angle of $(91 \pm 2)°$ and vector $\mathbf{b_1}$ rotated $(28 \pm 2)°$ from the substrate <110> directions. These dimensions are consistent with a commensurate $\begin{pmatrix} 4 & 2 \\ -2 & 4 \end{pmatrix}$ matrix, which

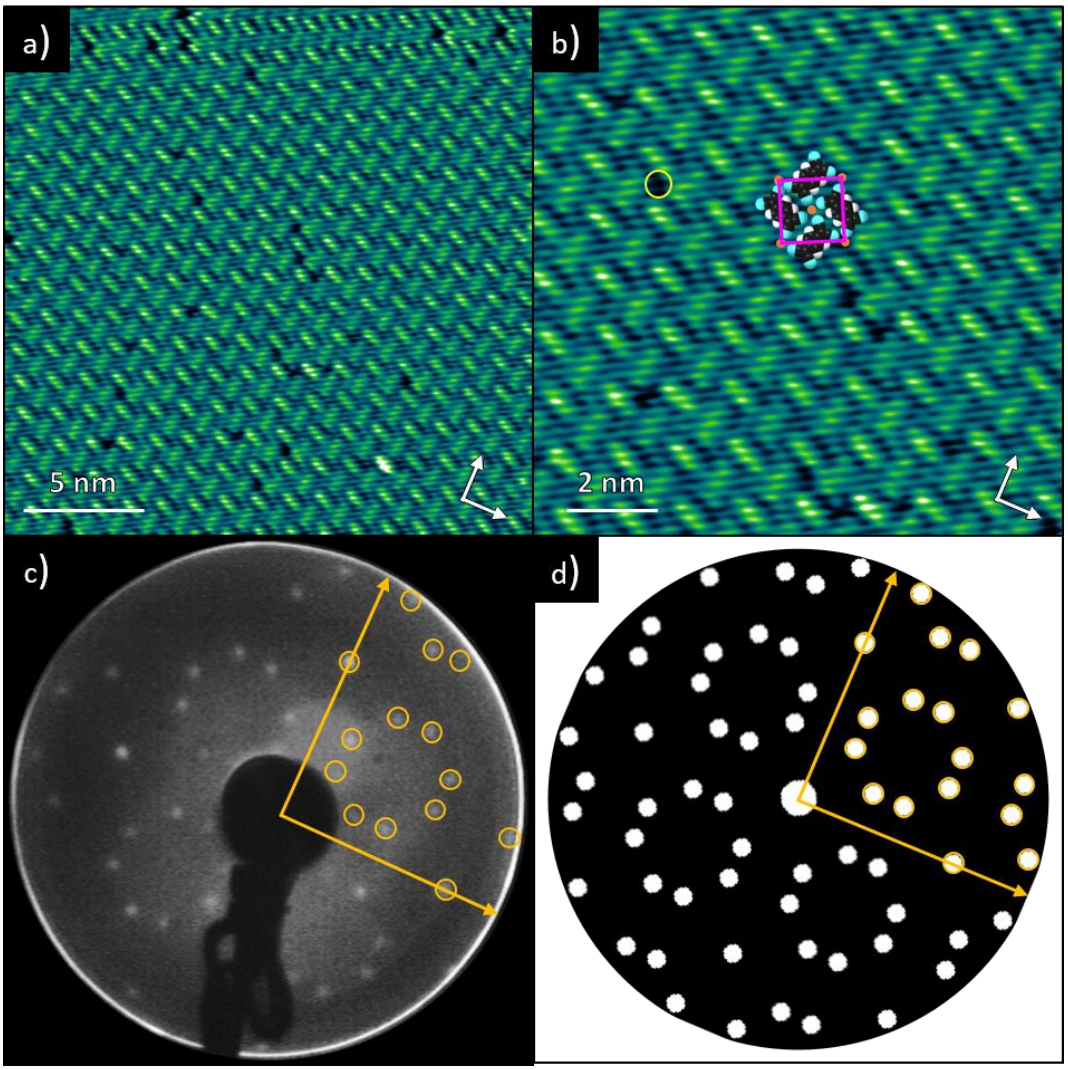

Figure 7.1.11 - STM and LEED recorded after annealing a sample of Na/TCNQ on Ag(100) to 210 °C. a) Large area STM image showing a single ordered domain of Na phase 3 (V_{samp} = -0.9 V, I = 300 pA). b) Small area STM image showing a single ordered domain of Na phase 3 with the surface unit mesh indicated by the purple square and an apparently vacant Na site is highlighted by the yellow circle. Scaled models of TCNQ and Na (using the Na^+ ionic radius of 0.99 Å) are superimposed to fit the STM contrast. (V_{samp} = -0.9 V, I = 300 pA. In both STM images, the white arrows indicate the substrate <110> directions. c) LEED pattern measured at an electron kinetic energy of 25.0 eV. d) Simulated LEED pattern for a commensurate $\begin{pmatrix} 4 & 2 \\ -2 & 4 \end{pmatrix}$ unit mesh. In both the experimental and simulated LEED patterns, the substrate <110> directions are shown by the yellow arrows. To aid in the comparison of the two patterns, the diffraction beams are highlighted by yellow circles in one quadrant of the LEED pattern. Note that at the electron kinetic energy used, some diffraction beams are only faintly visible.

corresponds to a square unit mesh with 12.9 Å vector lengths rotated by 26.6 ° to the substrate <110> directions. Comparison of the experimentally measured LEED pattern to a LEED pattern simulated for a $\begin{pmatrix} 4 & 2 \\ -2 & 4 \end{pmatrix}$ structure show excellent agreement, confirming the accuracy of the STM unit mesh

measurements. Na phase 3 therefore has identical periodicity to the K phase 3, though, unlike the KTCNQ structure, the Na phase does not show frequent dislocations in the molecular assembly. This suggests that Na phase 3 does not experience the structural strain that was attributed to the K phase 3. K phase 3, it was concluded that the strain was caused by the optimal KTCNQ assembly being larger than the periodicity imposed by the Ag(100) substrate. As Na has a smaller ionic radius than K, the TCNQ molecules can pack closer around Na than K and thus the optimal NaTCNQ assembly is more compact, allowing it to adopt a $\begin{pmatrix} 4 & 2 \\ -2 & 4 \end{pmatrix}$ periodicity without imposing significant strain on the structure.

7.2 XPS and UPS

XPS and UPS were used to probe the chemical compositions and electronic properties of the nominal $KTCNQ_4$ and $CsTCNQ_4$ phases (K phase 1 and Cs phase 1) formed on Ag(100). Figure 7.2.1 and Figure 7.2.2 show soft XPS recorded from the $KTCNQ_4$ and $CsTCNQ_4$ phases respectively. For both systems, the C 1s spectrum shows at least three distinct features, which were fitted with four components corresponding to the four chemically inequivalent C atoms within the TCNQ molecule. The relative intensities of these components were constrained (± 5%) to the expected stoichiometry of each C environment. In previously studied systems, both in this thesis and in other reports,[57, 175, 176] the C 1s spectrum of TCNQ has been shown to be characteristic of the molecular charge state. Here the C 1s spectral line shape and measured binding energies (Table 7.2.1) for both systems are consistent with a $TCNQ^-$ charge state. As TCNQ was found to already be negatively charged on the Ag(100) surface in the absence of an electron donor, it is unsurprising that the negative charge state is retained upon co-deposition of alkali metals. This result is consistent with XPS measured for the KTCNQ and CsTCNQ windmill phases measured on the Ag(111) surface (see sections 5.1.2 and 5.2.2), which also showed that the molecules adopted a $TCNQ^-$ charge state both before and after alkali metal deposition. The N 1s spectra for both the $KTCNQ_4$ and $CsTCNQ_4$ phases showed one main N component, consistent with the single N environment present within the TCNQ molecule. For both the K and Cs phases, this component was observed at a binding energy of 398.1 eV, which is also consistent with a $TCNQ^-$ charge state.[57, 175, 176] For the K phase, the K 2p spectrum showed a spin-orbit split doublet, consistent with a single K environment. Binding energies of 293.6 eV and 296.4 eV were measured for the K $2p_{3/2}$ and K $2p_{1/2}$ peaks respectively, which are consistent with values obtained for ionic K^+.[188] For the $CsTCNQ_4$ phase, a single spin-orbit split doublet was observed in the Cs 3d spectrum, although, with the relatively low intensity of the signal compared to the overlapping Ag 3s peak, other minor features may not be visible beyond the spectral noise. Binding energies of 725.0 eV and 738.8 eV were measured for the Cs $3d_{5/2}$ and Cs $3d_{3/2}$ peaks respectively, which are consistent with values obtained for

ionic Cs^+.[192] The XPS for both systems therefore indicates that the TCNQ and alkali metals are charged on the surface, consistent with the suggested ionic nature of the bonding between the two species.

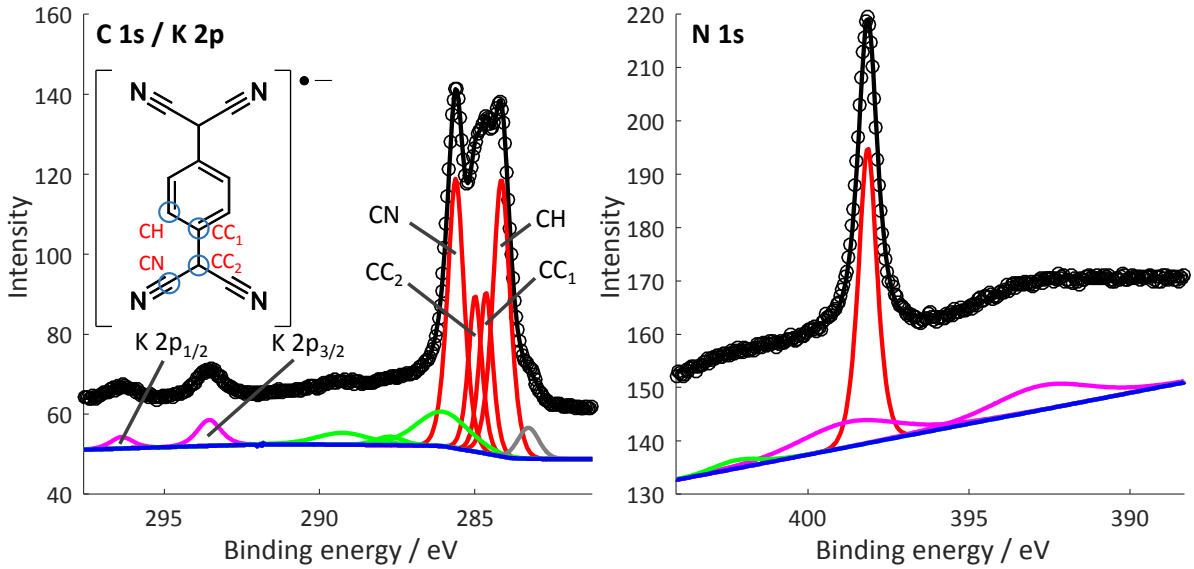

Figure 7.2.1 – Soft XPS recorded from K phase 1. The C 1s / K 2p spectrum was recorded with a photon energy of 435 eV and displays the measured intensity (black circles) along with the sum of fitted components (black line), which comprises a Shirley background (blue),[177] four main C 1s components (red), satellite features (green), a beam damage feature (grey) and a single spin-orbit split K 2p doublet (purple). The C 1s peaks are assigned to the four chemically inequivalent C environments within the TCNQ molecule, indicated in the inset schematic. The N 1s spectrum was recorded using a photon energy of 550 eV and displays the measured intensity (black circles) along with the sum of fitted components (black line), which consist of a linear background (blue), one main N 1s component (red), Ag 3d plasmon features (purple) and an additional satellite feature (green).

Table 7.2.1 – XPS measured binding energies of the main C 1s, N 1s, K 2p and Cs 3d components from K phase 1 and Cs phase 1.

Sample	Binding energy / eV								
	CH	CC_1	CC_2	CN	N	K $2p_{3/2}$	K $2p_{1/2}$	Cs $3d_{5/2}$	Cs $3d_{3/2}$
K phase 1	284.1	284.6	285.0	285.6	398.1	293.6	296.4	-	-
Cs phase 1	284.1	284.6	285.0	285.6	398.1	-	-	725.0	738.8

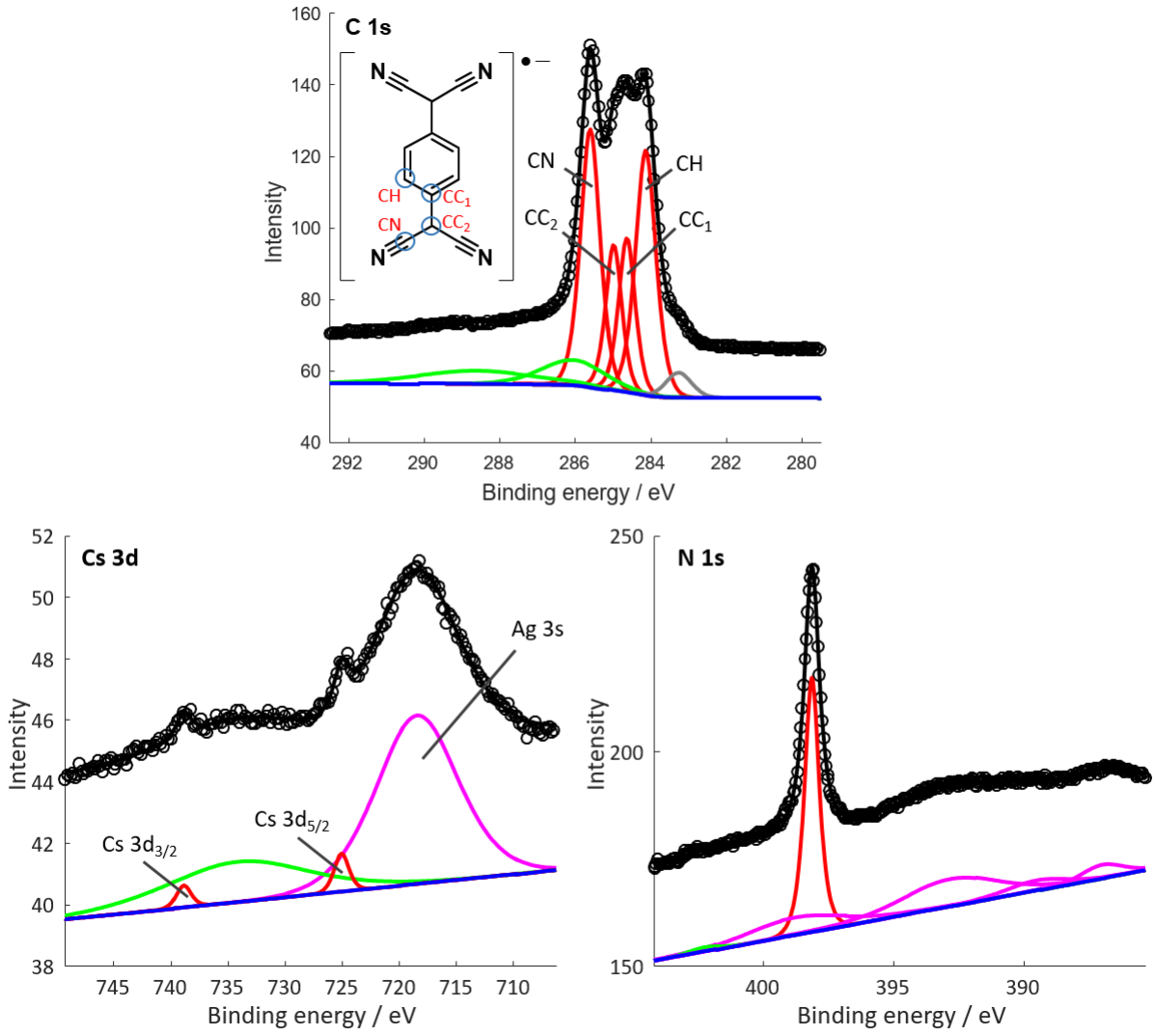

Figure 7.2.2 - Soft XPS recorded from Cs phase 1. The C 1s spectrum was recorded with a photon energy of 435 eV and displays the measured intensity (black circles) along with the sum of fitted components (black line), which comprises a Shirley background (blue),[177] four main C 1s components (red), satellite features (green) and a beam damage feature (grey). The C 1s peaks are assigned to the four chemically inequivalent C environments within the TCNQ molecule, indicated in the inset schematic. The Cs 3d spectrum was recorded using a photon energy of 900 eV and displays the measured intensity (black circles) along with the sum of fitted components (black line), which comprises a linear background (blue), one spin-orbit split doublet (red), the Ag 3s peak from the substrate (purple) and a satellite feature (green). The N 1s spectrum was recorded using a photon energy of 550 eV and displays the measured intensity (black circles) along with the sum of fitted components (black line), which comprises a linear background (blue), one main N 1s component (red), Ag 3d plasmon features (purple) and an additional satellite feature (green).

Work function measurements were obtained using UPS for the $KTCNQ_4$ and $CsTCNQ_4$ phases along with the pure TCNQ phase (low-density phase 1 as described in chapter 6) prepared prior to alkali metal deposition. The results of these measurements are shown in Table 5.1.3. As discussed in section 6.2, the adsorption of TCNQ increases the surface work function by ~0.5 eV from the typical values observed for clean Ag(100) of 4.3-4.6 eV.[198-200] This is consistent with TCNQ molecules accepting charge from the substrate, as a neutral adsorbate would be expected to decrease the work function via the 'push-back' effect and an electron donor would decrease the work function further still.[11] Upon deposition of the alkali metals to form the $KTCNQ_4$ and $CsTCNQ_4$ phases, the work function decreases by ~0.15 eV, which is consistent with the alkali metals donating electrons and becoming positively charged on the surface.

Table 7.2.2 – Work functions (Φ) measured using UPS from the TCNQ/alkali metal adsorption phases on Ag(100). Measurements were obtained using the He-IIα (hν = 40.81 eV) emission line.

Sample	**Φ / eV**
TCNQ on Ag(100)	4.95 ± 0.05
$KTCNQ_4$ on Ag(100)	4.79 ± 0.05
$CsTCNQ_4$ on Ag(100)	4.82 ± 0.05

The results of DFT calculations reported for these two phases predicted that the Cs phase would give a surface work function ~0.15 eV lower than the K phase, which was attributed to Cs having a lower ionisation energy.[168] The measurements here did not show a distinguishable difference between the $KTCNQ_4$ and $CsTCNQ_4$ phases, giving values that agree within the associated error ranges. This could indicate that the DFT calculations do not describe the system correctly, giving inaccurate work function values. One possible cause of this could be the lack of dispersion correction used in the reported DFT calculations,[168] which could result in inaccurate adsorption geometries[24, 28] and in-turn give erroneous predictions of the surface work function. However, one other important consideration in comparing the measured and predicted values is the adsorbate coverage on the surface. The DFT calculations assume a complete, defect free, layer of the TCNQ/alkali metal structures across the substrate. The absolute coverage of the TCNQ/alkali metal structures could not be confirmed by XPS, however STM obtained for samples prepared using the typical conditions to form these phases displayed areas of bare substrate or high mobility, indicative of submonolayer coverages. This suggests that the UPS measurements were also obtained from submonolayer coverages of the TCNQ/alkali metal structures, which would result in a smaller work function shift compared to the complete monolayers calculated by DFT. Furthermore, the TCNQ/alkali metal stoichiometry is also an important factor in determining the surface work function. STM images showed the presence of some alkali metal vacancies for both phases and also

suggested that additional sites in the nominal $CsTCNQ_4$ structure could be occupied by Cs atoms. The adsorption structures may therefore be able to accommodate a range of TCNQ/alkali metal stoichiometry, which would have important implications on the surface work function. Estimates of the surface composition were obtained from soft XPS for K phase 1 (see Appendix D), which suggest a 1:5 K:TCNQ ratio, consistent with a significant density of K vacancies or regions of the surface in which TCNQ is not bound to K. Due to the relatively low Cs 3d signal and the overlapping Ag 3s peak, it was not possible to reliably estimate the coverage of Cs relative to TCNQ.

7.3 NIXSW and structural models

NIXSW measurements were obtained from the nominal $KTCNQ_4$ and $CsTCNQ_4$ adsorption phases (K phase 1 and Cs phase 1) on Ag(100). The (200) reflection was used to determine the layer spacing between the constituent atoms of the TCNQ/alkali metal networks and the underlying substrate; the (111) reflection was used to obtain information on the lateral registry of the structure by triangulation.

7.3.1 $KTCNQ_4$

The NIXSW measurements obtained from K phase 1 using the (200) reflection (Table 7.3.1) show moderately high coherent fractions (0.6-0.9) for all C and N components, suggesting that the molecule occupies a small distribution of adsorption heights. The corresponding coherent positions show a downward trend from the central ring of the TCNQ molecule to the peripheral cyano groups, suggesting

Table 7.3.1 - NIXSW fitting parameters obtained from K phase 1 using the (200) reflection of the Ag(100) substrate. Separate fitting parameters were obtained for each of the photoemission components identified in Figure 7.2.1 (due to the lower energy resolution obtained with the hard X-rays used for NIXSW, components CC_1 and CC_2 were fitted together as a single component). The coherent position $D_{(200)}$ is given as $D_{(200)} = (P+1)d_{200}$ where P is the fractional coherent position and d_{200} is the spacing of the (200) lattice planes (2.043 Å). For each adsorption phase, values are averaged from eight repeat measurements over two sample preparations. Error estimates are shown in parentheses in units of 0.01.

Component	K phase 1	
	f_{co}	$D_{(200)}$ / Å
K	0.94(14)	3.88(5)
CH	0.68(10)	2.72(5)
CC	0.83(11)	2.64(5)
CN	0.69(10)	2.53(5)
N	0.76(10)	2.38(5)

that, on average, TCNQ adsorbs in a downward bending conformation with the N atoms ~0.3 Å closer to the surface than the core of the molecule. These results are closely similar to the NIXSW measured for the pure TCNQ phases on Ag(100), with all values agreeing within the associated error ranges (see Table 6.3.1), implying that K has a negligible impact on the TCNQ adsorption conformation in this phase. A high coherent fraction of (0.94 ± 0.14) was measured for K, consistent with occupation of a single adsorption height and the corresponding coherent position of (3.88 ± 0.05) Å indicates that the K atoms adsorb a considerable distance above the TCNQ molecules. The K atoms in this phase also adsorb considerably higher above the surface than in the K/TCNQ structures formed on the Ag(111) surface ((3.56 ± 0.05)Å and (3.29 ± 0.05)Å for the KTCNQ and K_2TCNQ phases respectively), which albeit on a different substrate, is consistent with the observed trend of alkali metal atoms occupying greater adsorption heights at lower alkali metal/TCNQ stoichiometric ratios.

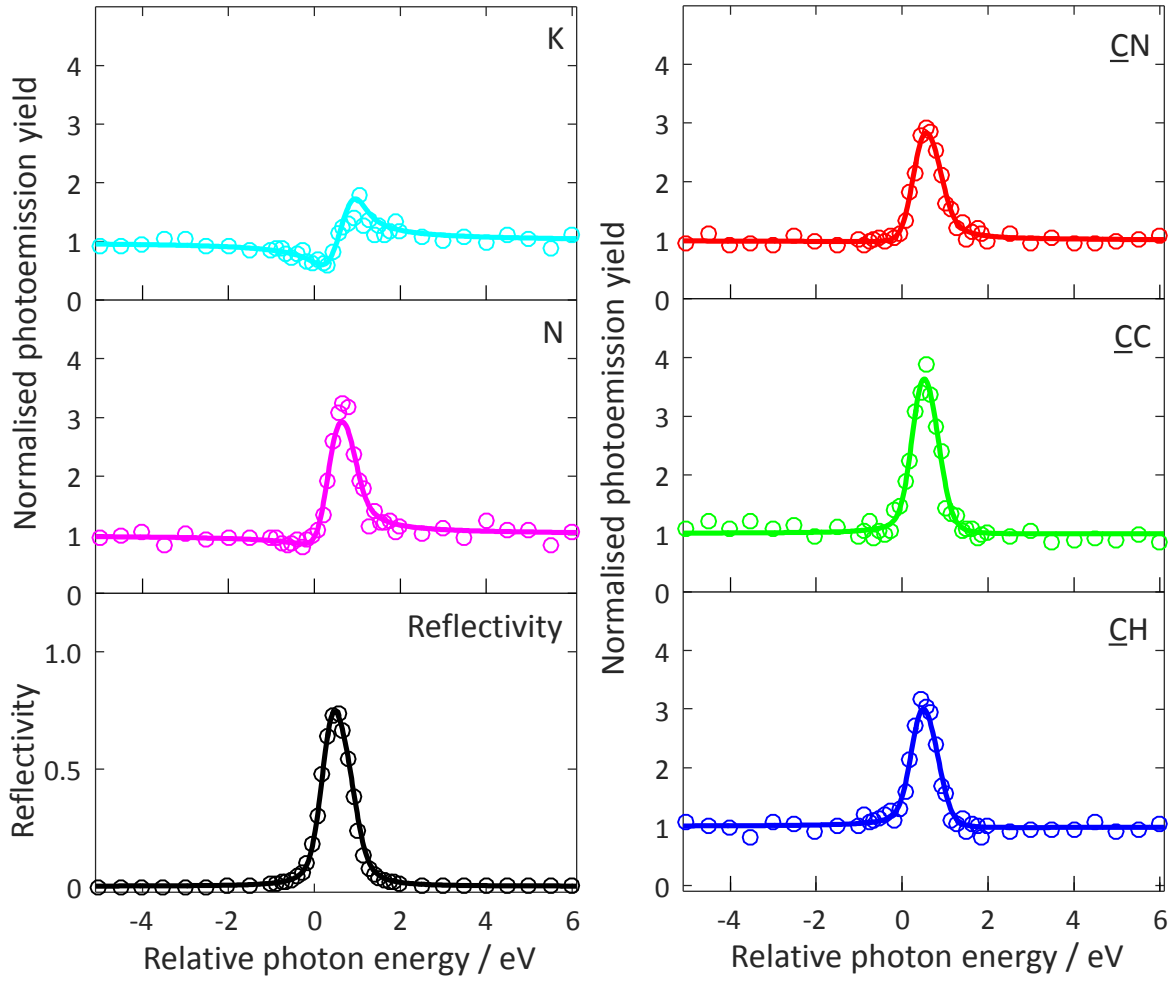

Figure 7.3.1 – Sample set of NIXSW photoemission yield curves obtained from K phase 1 using the (200) reflection of the Ag(100) substrate. Photon energies are quoted relative to the Bragg energy of 3036.0 eV. Least square fits (solid lines) to the photoemission yields (circles) were obtained to extract the coherent fractions and coherent positions.

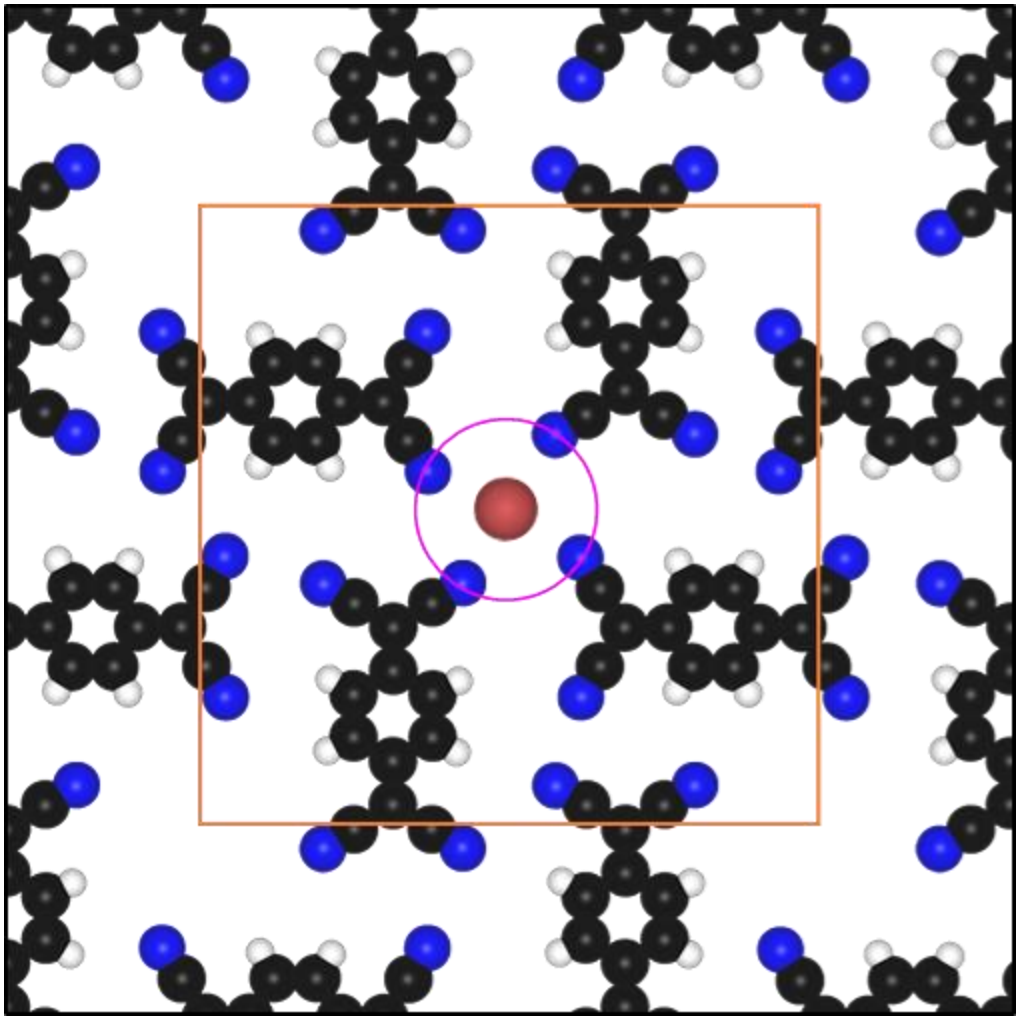

Figure 7.3.2 – Two-dimensional model of K phase 1 constructed from the contrast observed by STM. The location of K (red) was inferred from STM interpreted locations of the Cs atoms in the comparable $CsTCNQ_4$ phase reported both in this thesis and previously in the literature.[59] The orange square indicates the unit mesh. The purple circle cuts through the centre of the four N atoms surrounding the K^+ ion and has a diameter of 5.7 Å.

In the structures characterised on the Ag(111) surface, the K adsorption heights are consistent with distances expected for close contact between the cyano N atoms and K ions. To evaluate whether this is the case for K phase 1, a model of the molecular assembly was constructed based on the contrast observed in the STM images. This model is shown in Figure 7.3.2 and suggests that the K^+ ions occupy a site between four N atoms that lie on a circle 5.7 Å in diameter (purple circle). Assuming that the K^+ ions occupy the centres of these sites and using the adsorption heights measured by NIXSW, this suggests a N-K distance of 3.2 Å. This is larger than the minimum N-K distance of 2.93 Å reported from the crystal structure of bulk KTCNQ,[186] which corresponds to the the sum of the N van der Waals radius[41] and the K ionic radius.[187] This suggests that in the present adsorption phase, the K ions are not in close contact with the N atoms and instead adsorb at an elevated height above the TCNQ molecules.

This result may also explain why the NIXSW measurements for the C and N components are unchanged from the pure TCNQ phase as the K ions are too far above the surface to significantly impact on the adsorption conformation of the molecules.

The measured K height is qualitatively consistent with DFT calculations reported for this $KTCNQ_4$ structure, which predict that the alkali metals occupy an elevated height as this produces a larger positive dipole moment thus stabilising the negative dipoles generated by the TCNQ molecules more effectively.[168] There are, however some discrepancies between the calculated structure[168] and the experimental NIXSW measurements obtained here. The DFT calculations predict a K adsorption height of ~4.2 Å, which is significantly higher than the value of (3.88 ± 0.05) Å obtained from NIXSW. The DFT calculations also predict that the TCNQ molecules adopt a tilted geometry, resulting from the cyano groups at the centre of each windmill being lifted away from the surface by the K ion.[168] The calculated structure therefore does not appear to reflect the NIXSW measurements, which instead suggest that the molecules remain in the same downward bending conformation measured for the pure TCNQ phases on Ag(100). However, as only one of the four TCNQ cyano groups is lifted away from the surface in the calculated structure,[168] it could be possible that this geometry has a relatively small impact on the N coherent fraction, despite occupying two significantly different heights. To investigate whether the calculated structure[168] is qualitatively consistent with the NIXSW measurements, the model constructed in Figure 7.3.2 was used to evaluate the possible impact of this tilted geometry on the coherent fractions and positions. Using the measured K height of 3.88 Å, the N atoms surrounding the K site would need to occupy a height of ~3.2 Å to satisfy the minimum N-K separation of 2.93 Å suggested from the bulk crystal structure of KTCNQ.[186] Assuming that the other three cyano groups per molecule occupy a height of 2.36 Å (based on the heights measured by NIXSW for the pure TCNQ phase) gives an expected coherent fraction of 0.52 and a coherent position of 2.44 Å. While the coherent position predicted here is reasonably consistent with the measured value, the coherent fraction - which does not account for any reductions caused by thermal vibrations of the absorbing atoms - is significantly lower than was measured for the $KTCNQ_4$ structure. The calculated structure is therefore incompatible with the NIXSW measurements. It should be noted that dispersion corrections were not included in these DFT calculations[168] and, as van der Waals interactions are of great importance in determining the adsorption structures of organic molecules,[27-29] it is expected that dispersion corrected DFT calculations would give much better agreement with the experimental results. Nevertheless, the NIXSW measurements do show that K adopts a significantly elevated height above the molecules and is thus consistent with the dipole moment effects that were predicted by DFT.[168]

Table 7.3.2 - NIXSW fitting parameters obtained from K phase 1 using the (111) reflection of the Ag(100) substrate. Separate fitting parameters were obtained for the different C 1s photoemission components as defined in Figure 7.2.1 (due to lower resolution at the photon energies required for NIXSW, components CC_1 and CC_2 were fitted together in a single component here). The coherent positions expected for atoms occupying the two high-symmetry sites ($P_{(111)\text{ - atop}}$ and $P_{(111)\text{ -hollow}}$ for the atop and hollow sites respectively) on the Ag(100) surface are also shown in the table and are shown in fractional units as values between 0 and 1. Error estimates are shown in parentheses in units of 0.01.

Component	K phase 1			
	f_{co}	$P_{(111)}$	$P_{(111)\text{ - atop}}$	$P_{(111)\text{ - hollow}}$
K	0.35(10)	0.06(6)	0.95(3)	0.45(3)
CH	0.18(10)	0.89(5)	0.67(3)	0.17(3)
CC	0.19(10)	0.77(5)	0.65(3)	0.15(3)
CN	0.15(10)	0.01(5)	0.62(3)	0.12(3)
N	0.44(10)	0.03(6)	0.58(3)	0.08(3)

Table 7.3.2 shows NIXSW fitting parameters obtained using the (111) reflection along with the coherent positions expected for the two high symmetry sites on the Ag(100) surface (calculated using equations 6.3.1 and 6.3.2). The C components all show low coherent fractions (i.e. < 0.2), with coherent positions that are not consistent with either of the two values expected for the high-symmetry sites. The low coherent fractions indicate that the C atoms do not show any significant preference for adsorbing in either of the high-symmetry sites. As discussed previously, the coherent positions corresponding to the two high-symmetry sites should be the only possible values that can be measured using the (111) reflection, due to the symmetry of the Ag(100) surface. Consequently, the coherent positions measured here for the C components, which are not consistent with either of these values, cannot be attributed to any real structural effects. Instead, these erroneous coherent positions can be ascribed to the fact that at low coherent fractions, the modulations in the NIXSW photoemission yield profile are dominated by the reflectivity profile and thus it becomes difficult to distinguish between different coherent positions. As discussed previously, this causes coherent positions associated with low coherent fractions to be unreliable. The N component shows a larger coherent fraction of (0.44 ± 0.10) and a coherent position that is consistent with the hollow site. The measured coherent fraction is sufficiently large to imply a well-defined lateral registry but is lower than would be expected for the N atoms being centred on a high-symmetry site. This indicates that the N atoms either occupy sites that are closer to the hollow site than atop but are laterally offset from the centre of the site, or the N atoms occupy a mixture of sites above the substrate but show a preference for adsorbing closer to the hollow site rather than atop. As this phase contains four TCNQ molecules within the unit mesh, it is reasonable to expect that the

corresponding sixteen N atoms do not occupy identical sites above the substrate. Indeed, DFT calculated structures reported for this phase reflect this, with the N atoms occupying various sites above the substrate.[168] It was therefore concluded that the N atoms occupy a mixture of sites above the surface but preferentially adsorb in or close to the hollow site.

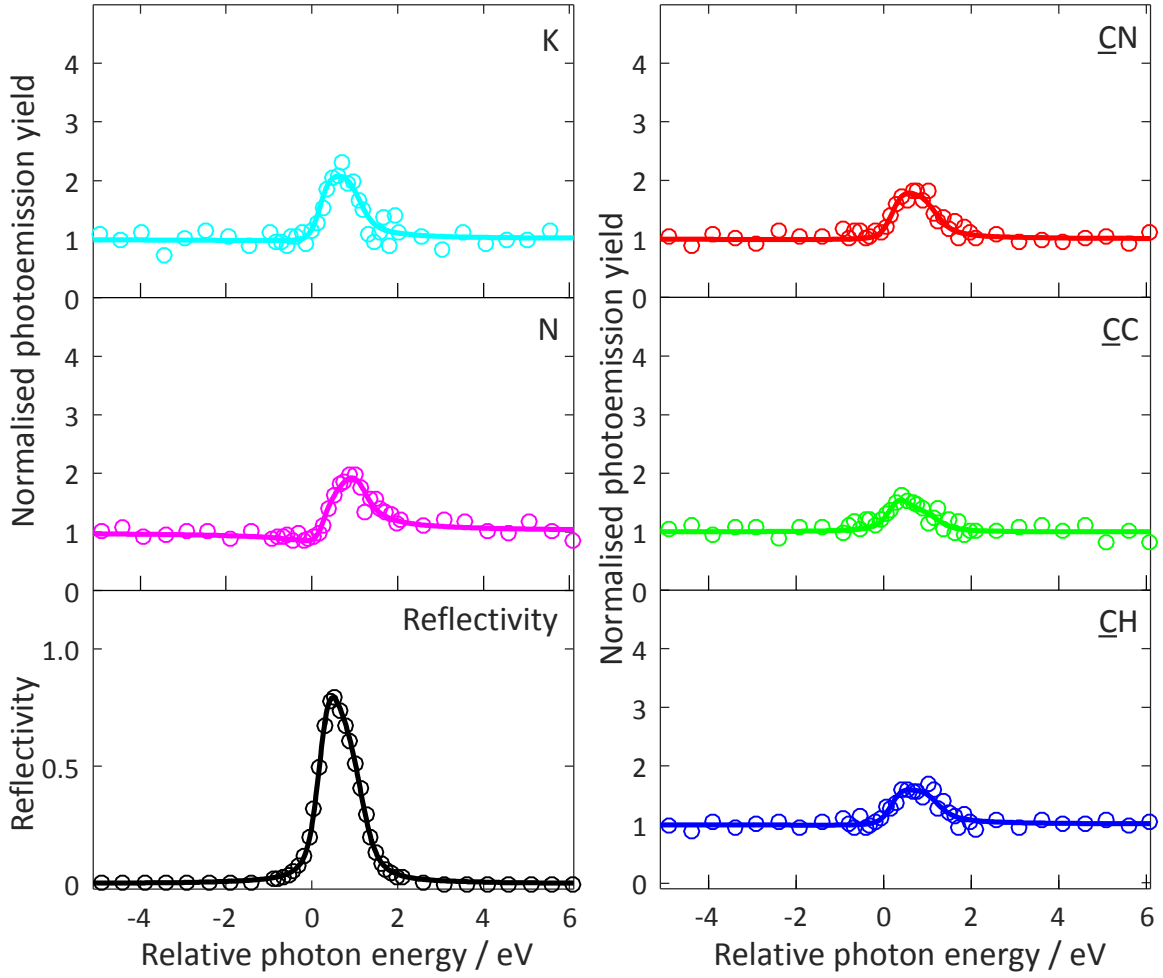

Figure 7.3.3 - Sample set of NIXSW photoemission yield curves measured from K phase 1 using the (111) reflection of the Ag(100) substrate. Photon energies are quoted relative to the Bragg energy of 2630.0 eV. Least square fits (solid lines) to the photoemission yields (circles) were obtained to extract the coherent fractions and coherent positions.

The K component shows a relatively low coherent fraction of (0.35 ± 0.10) in the (111) reflection, with a coherent position that is more consistent with the atop site than the hollow site. As there is only one K atom within the unit mesh, all of the K atoms within the structure must occupy the same site and thus the low coherent fraction suggests that the K atoms are not centred on the atop site. As K adsorbs at an elevated height of (3.88 ± 0.05) Å in this phase, its registry to the substrate is unlikely to have any significant impact on the stability of the structure and thus it is reasonable that K does not occupy a

high symmetry site. However, as the registry to the substrate is expected to be dictated by interactions between the TCNQ cyano groups and the substrate and because it is these cyano groups that define a fourfold rotationally symmetric site that K occupies, it could also be reasonably expected that K would occupy a high-symmetry site. Rather than being offset laterally from the atop site, it could be possible that the low coherent fraction is caused large vibrational amplitudes parallel to the surface. Previously reported quantitative LEED measurements suggest that K exhibits anisotropic vibrations when adsorbed on Ag, with measurements recorded at a temperature of 35 K for K adsorbed on Ag(111) showing rms vibrational amplitudes of 0.15 Å perpendicular to the surface and 0.50 Å parallel to the surface.[190] If equally large vibrations were present in the $KTCNQ_4$ adsorption phase, they would still be insufficient to reduce the coherent fraction to the experimentally measured value. However, it may also be possible that at ambient temperatures, at which the NIXSW measurements were recorded, that these vibrational amplitudes could be even larger and thus be sufficient to account for the low K coherent fraction. It should also be noted that it is not known whether K exhibits these large vibrational amplitudes within the networks formed with TCNQ and further analysis would be required to fully assess the impact of thermal vibrations on the coherent fractions.

7.3.2 $CsTCNQ_4$

NIXSW measurements obtained using the (200) reflection for Cs phase 1 (Table 7.3.3) show closely similar results to K phase 1. The C and N components show moderate coherent fractions (0.6 – 0.8) with a general downward trend in the coherent position going from the central ring of the molecule to

Table 7.3.3 - NIXSW fitting parameters obtained from Cs phase 1 using the (200) reflection of the Ag(100) substrate. Separate fitting parameters were obtained for each of the photoemission components identified in Figure 7.2.2 (due to the lower energy resolution obtained with the hard X-rays used for NIXSW, components CC_1 and CC_2 were fitted together as a single component). The coherent position $D_{(200)}$ is given as $D_{(200)} = (P+1)d_{200}$ where P is the fractional coherent position and d_{200} is the spacing of the (200) lattice planes (2.043 Å). For each adsorption phase, values are averaged from eight repeat measurements over two sample preparations. Error estimates are shown in parentheses in units of 0.01.

Component	Cs phase 1	
	f_{co}	$D_{(200)}$ / Å
Cs	0.74(10)	4.08(5)
CH	0.63(10)	2.74(5)
CC	0.80(10)	2.63(5)
CN	0.71(10)	2.53(5)
N	0.78(10)	2.38(5)

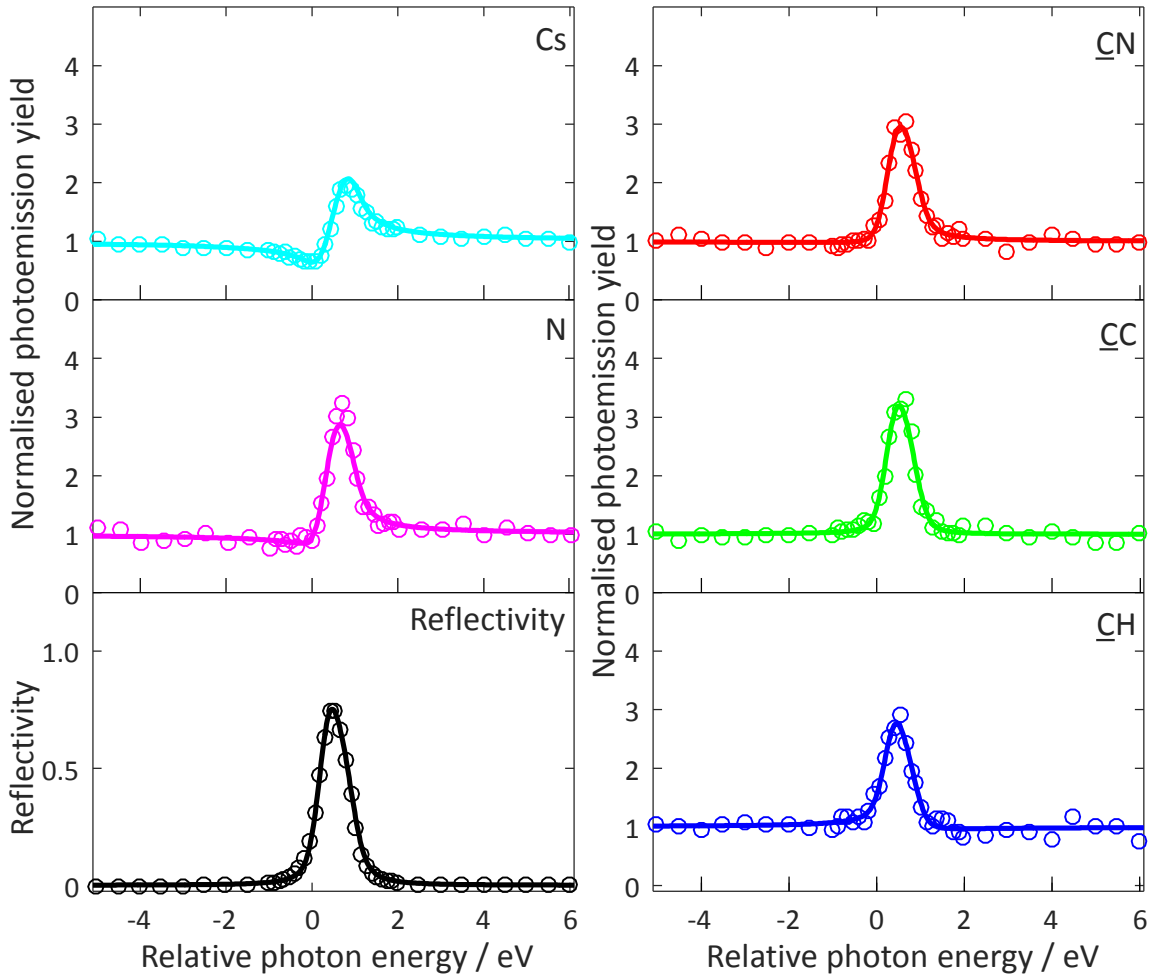

Figure 7.3.4 - Sample set of NIXSW photoemission yield curves obtained from Cs phase 1 using the (200) reflection of the Ag(100) substrate. Photon energies are quoted relative to the Bragg energy of 3036.0 eV. Least square fits (solid lines) to the photoemission yields (circles) were obtained to extract the coherent fractions and coherent positions.

the peripheral cyano groups. The measured values agree, within the associated error ranges, with the NIXSW measurements obtained for the pure TCNQ phase (low-density phase 1 as described in chapter 6, see Table 6.3.1) and K phase 1, suggesting that TCNQ adopts the same conformation, in which the cyano groups bend down towards the substrate. The Cs component shows a moderately high coherent fraction of (0.74 ± 0.10), which is slightly lower than values typically attributed to a single adsorption height and could indicate that there is a relatively small but significant distribution of adsorption heights. The corresponding coherent position of (4.08 ± 0.05) Å indicates that the Cs ions adsorb a considerable distance above the TCNQ molecules. Using the same model constructed for the K phase 1 shown in Figure 7.3.2, the adsorption heights measured by NIXSW suggest a N-Cs distance of 3.32 Å. This is larger than the minimum N-Cs distance of 3.07 Å reported for the bulk crystal structure of Cs_2TCNQ_3,[194] which is consistent with the sum of the N van der Waals radius[41] and the Cs

ionic radius.[187] This suggests that in Cs phase 1, the Cs ions are not in close contact with the N atoms and instead adsorb at an elevated height above the TCNQ molecules, similar to K phase 1. This result is also consistent with the NIXSW measured for the C and N components remaining unchanged from the pure TCNQ phase as the Cs ions are seemingly too far above the surface to impact on the adsorption conformation of the molecule.

The NIXSW measurements indicate that, in their respective structures, Cs adsorbs (0.2 ± 0.1) Å above the surface than K. This result is consistent with DFT calculations reported for these phases, which suggest that because Cs has a lower ionisation potential than K, it is more effective at stabilising the dipoles generated by the TCNQ molecules and achieves this by adsorbing higher above the surface to produce a larger dipole moment of opposing polarity.[168] However, similar to K phase 1, there are some discrepancies between the NIXSW measurements and the DFT calculations[168] for Cs phase 1. The DFT calculations predict a Cs adsorption height of ~4.9 Å and that the TCNQ molecules adsorb in a tilted geometry, with the cyano groups at the centre of each windmill unit lifted from the surface.[168] In contrast to this, the NIXSW measurements show a significantly lower Cs adsorption height of (4.08 ± 0.05) Å and give measured coherent fractions that are not consistent with the predicted tilted geometry. As discussed previously, these DFT calculations[168] did not include dispersion corrections and thus would not give an accurate description of the van der Waals forces that are of great importance in determining the adsorption structures of organic molecules.[27-29] It is therefore expected that dispersion corrected DFT calculations would give better agreement with the experimental NIXSW results. Nonetheless, the NIXSW does show that the Cs ions adsorb at an elevated height above the molecules that is higher than the K ions in the equivalent adsorption phase, which is qualitatively consistent with the dipole moment effects predicted by the DFT calculations.

Table 7.3.4 - NIXSW fitting parameters measured from Cs phase 1 using the (111) reflection of the Ag(100) substrate. The coherent positions expected for atoms occupying the two high-symmetry sites ($P_{(111)\text{ - atop}}$ and $P_{(111)\text{ -hollow}}$ for the atop and hollow sites respectively) on the Ag(100) surface are also shown in the table and are given in fractional units as values between 0 and 1. Error estimates are shown in parentheses in units of 0.01.

Component	Cs phase 1			
	f_{co}	$P_{(111)}$	$P_{(111)\text{ - atop}}$	$P_{(111)\text{ - hollow}}$
Cs	0.30(10)	0.49(4)	0.00(3)	0.50(3)
N	0.41(10)	0.02(6)	0.58(3)	0.08(3)

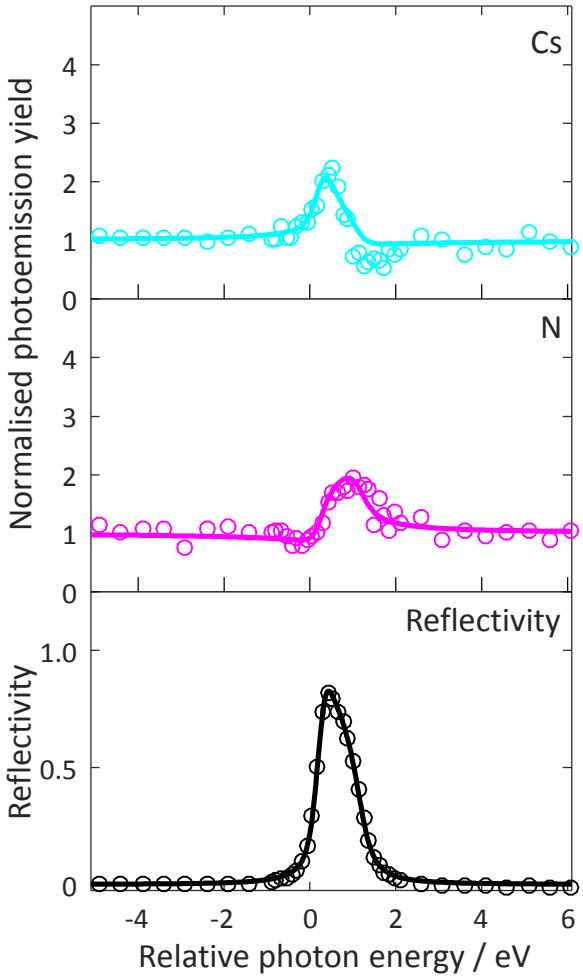

Figure 7.3.5 - Sample set of NIXSW photoemission yield curves measured from Cs phase 1 using the (111) reflection of the Ag(100) substrate. Photon energies are quoted relative to the Bragg energy of 2630.0 eV. Least square fits (solid lines) to the photoemission yields (circles) were obtained to extract the coherent fractions and coherent positions.

Table 7.3.4 shows NIXSW fitting parameters obtained from Cs phase 1 using the (111) reflection of the Ag(100) substrate, along with the coherent positions expected for the hollow and atop sites. As the C atoms were not expected to show any specific preference for adsorption sites, which was the case for the pure TCNQ phases and K phase 1, only the N and Cs components were measured in the (111) reflection. For N, a coherent fraction of (0.41 ± 0.10) and a coherent position that is consistent with the hollow site was measured. The coherent fraction is lower than would be expected for the N atoms being centred on a high-symmetry site but is high enough to suggest a well-defined registry with the underlying substrate. As with K phase 1, the low coherent fraction could suggest that the N atoms occupy sites that are laterally offset from the high symmetry sites or that the N atoms occupy a mixture of different adsorption sites but overall show a preference for the hollow site. The latter is consistent

with the structure predicted by DFT calculations reported for this phase, which suggest that the N atoms occupy a variety of sites above the substrate.[168]

The Cs component shows a relatively low coherent fraction of (0.30 ± 0.10) with a corresponding coherent position of (0.49 ± 0.04), which is consistent with the hollow site. The low coherent fraction measured here could indicate that the Cs atoms occupy a site above the substrate that is laterally offset from the hollow-site. As Cs occupies an elevated height above the surface, it is unlikely that the Cs has a significant impact on the surface registry of the adsorption structure so it is reasonable to expect that Cs would not necessarily occupy a high-symmetry site. However, as the registry to the substrate is expected to be dictated by interactions between the TCNQ cyano groups and the substrate and because it is these cyano groups that define a fourfold rotationally symmetric site that Cs occupies, there is also a reasonable argument for Cs to occupy a high-symmetry site. If this is the case, the low coherent fraction would imply that the Cs ions exhibit rather large vibrational amplitudes parallel to the surface. Quantitative LEED measurements suggest that alkali metals exhibit anisotropic vibrations with considerably large vibrational amplitudes parallel to the surface,[193] though it is unknown whether Cs would exhibit similarly large vibrational amplitudes within the networks formed with TCNQ and thus further analysis is needed to determine the impact that these would have on the coherent fraction.

Comparing the (111) reflection NIXSW measurements for the alkali metal components in the K phase 1 and Cs phase 1 structures shows a difference, with the coherent position for K being consistent with the atop site whereas the value for Cs was consistent with the hollow site. As the STM of both phases revealed similar packing motifs, this result could suggest that the substrate registry of the respective structures is different between the two phases. In both cases, the corresponding coherent fractions were low, which could be due to the alkali metal atoms adsorbing far from the centres of these high-symmetry sites and therefore the difference in registry between the two phases may only be small. Nonetheless, the NIXSW results do highlight that, although the K and Cs phases share the same periodicity, there is a difference in their lateral geometry.

7.4 General discussion and conclusions

The $CsTCNQ_4$ structure formed on the Ag(100) surface, reported by Abdurakhmanova *et al.*[59] was successfully reproduced and a variety of previously unreported adsorption phases were also identified by STM and LEED for TCNQ coadsorbed with K or Na on Ag(100). The different structures observed for K and Na were attributed to different alkali metal/TCNQ stoichiometric ratios. The structures available for Cs/TCNQ on Ag(100) were not explored beyond the previously reported $CsTCNQ_4$ structure. The STM results did suggest that the nominal $CsTCNQ_4$ structure could be favourable for a

Cs:TCNQ ratio of up to 1:2, with bright protrusions similar in appearance to those attributed to Cs observed in a second site within the adsorption structure. To further explore this possibility, the effect of further Cs deposition on the adsorption structure should be investigated to determine whether different adsorption structures are accessible at higher Cs/TCNQ ratios. This investigation would ideally be accompanied by measurements of surface composition and relative coverages on the surface, which could be achieved with XPS or Auger electron spectroscopy. With the exception of one rather complex Na/TCNQ adsorption phase (Na phase 1), all of the alkali metal/TCNQ phases on Ag(100) were found to have square commensurate unit meshes.

STM and LEED measurements of the adsorption phase formed at a nominal $KTCNQ_4$ stoichiometry (K phase 1) shows the same $\begin{pmatrix} 6 & 3 \\ -3 & 6 \end{pmatrix}$ periodicity as the previously reported $CsTCNQ_4$ structure and exhibits a similar windmill packing motif.[59] In work published by Floris *et al.* DFT calculations were performed for the $CsTCNQ_4$ structure based on previously reported STM results[59] and also investigated the effects of other hypothetical TCNQ/alkali metal structures by replacing Cs with other alkali metals (namely K, Na and Li).[168] The measurements presented in this chapter confirmed that such a $KTCNQ_4$ phase can be formed, though an equivalent phase was not observed for $NaTCNQ_4$. This result is consistent with the aforementioned DFT calculations, which indicated that the $\begin{pmatrix} 6 & 3 \\ -3 & 6 \end{pmatrix}$ windmill structure was unstable for Na.[168] Due to their close similarity, the $KTCNQ_4$ and $CsTCNQ_4$ structures were ideal for comparison of the structural and electronic influence of the different alkali metals on the interface. To this effect, these phases were measured by XPS, UPS and NIXSW to probe the electronic and structural properties of the surface for the different alkali metals. This comparison could potentially be expanded by investigating adsorption structures formed by Rb and TCNQ on Ag(100). As Rb is an alkali metal with an ionic radius between that of K and Cs,[187] it is highly plausible that a similar $\begin{pmatrix} 6 & 3 \\ -3 & 6 \end{pmatrix}$ $RbTCNQ_4$ phase could also be formed. This would be advantageous as it would provide an additional data point for comparing the trend in the alkali metal's influence on the surface properties.

XPS of the $KTCNQ_4$ and $CsTCNQ_4$ phases indicated that the molecules adopt a $TCNQ^-$ charge state. The XPS binding energies for K 2p and Cs 3d are also consistent with the alkali metals donating electrons and becoming positively charged on the surface. Estimates of the K/TCNQ stoichiometry were obtained by XPS, which gave a 1:5 ratio and thus suggested that a significant density of vacant K sites were present on the surface. UPS measurements were obtained to compare the surface work function between the two phases. It was expected that a larger work function shift would be observed for the $CsTCNQ_4$ phase compared to the $KTCNQ_4$ phase, however the measured values did not show a significant difference between the two phases. The absolute alkali metal coverage is very low in these

adsorbate structures and thus the overall work function shift is relatively small. As a result, it is plausible that any differences in the relative work function shifts between different alkali metals in this structure would be too small to resolve. Another important consideration is that the relative coverages and stoichiometry of the two phases would need to be consistent to obtain a reliable comparison and thus, in future measurements, accurate determination of the surface coverage should be obtained alongside the work function measurements. Alternatively, structures with a larger alkali metal/TCNQ stoichiometric ratio would be expected to give a larger work function shift and thus any differences in work function caused by the different alkali metals would be easier to distinguish, as was demonstrated for the K/TCNQ and Cs/TCNQ structures formed on Ag(111) (see chapter 5).

The NIXSW measurements showed that in the $CsTCNQ_4$ and $KTCNQ_4$ structures, the alkali metal ions adsorb at elevated heights above the surface that are not consistent with the ions simply resting on top of the TCNQ cyano groups. Instead, this indicates the presence of a driving force for the alkali metal ions to adopt an increased height above the surface, consistent with dipole moment effects predicted in DFT calculations of these phases.[168] Furthermore, the NIXSW measurements also showed the same trend in alkali metal heights predicted by DFT calculations reported for these phases,[168] with Cs adsorbing significantly higher above the surface than K in the corresponding structures. This was attributed to Cs having a lower ionisation energy than K, enabling it to stabilise the negative dipoles generated by the TCNQ molecules more effectively, which is achieved by Cs adsorbing further above the surface thus producing a larger positive dipole moment.[168] The experimental NIXSW measurements therefore demonstrate that the structural features predicted by DFT and ascribed to the aforementioned dipole effects,[168] are indeed present within the TCNQ/alkali metal adsorption structures.

Despite showing good qualitative agreement with the predicted trends in alkali metal adsorption height, there are some discrepancies between the DFT calculated adsorption structures[168] and the NIXSW measurements. The DFT calculations predict that the four cyano groups around the alkali metal ion are lifted from the substrate, resulting in TCNQ adsorbing in a tilted geometry.[168] The NIXSW measurements indicate that the TCNQ molecules retain the same bent geometry as observed in the pure TCNQ on Ag(100) phases, in which the cyano groups point down towards the substrate and are not lifted by the alkali metal ions. In addition to this, the measured alkali metal adsorption heights are significantly lower than those predicted by DFT.[168] One possible cause for the discrepancies between the calculated structures and the NIXSW measurements was identified as the lack of dispersion corrections included in the calculations.[168] To better complement the NXISW measurements, calculated structures should be obtained using dispersion corrected DFT codes. The NIXSW measurements presented in this chapter could be used to identify the dispersion correction that best reproduces the

experimentally measured structure. In turn, the dispersion corrected DFT calculations could then be used to gain further insight into the key interactions that occur within the alkali metal/TCNQ structures.

NIXSW measurements obtained using the (111) reflection indicated that, similar to the pure TCNQ phase, the N atoms in both phases show a preference towards adsorbing in, or close to, the fourfold hollow sites of the Ag(100) substrate. The low measured coherent fractions were interpreted as being caused by the N atoms within the structure occupying a variety of different sites, with the coherent position indicating an overall preference for the hollow site. The C atoms did not show any specific preference for either site as very low coherent fractions were measured for all C components. In both the $CsTCNQ_4$ and $KTCNQ_4$ structures, NIXSW of the alkali metals gave low coherent fractions, with the coherent position measured for Cs consistent with the fourfold hollow site, whereas the value measured for K is consistent with the atop site. This result indicates that despite the two phases sharing the same commensurate periodicity, there are some differences in the lateral registry. The low coherent fractions are consistent either with the alkali metal not being centred on a high-symmetry site or due to large vibrational amplitudes parallel to the surface. Anisotropic vibrations with a large amplitude parallel to the surface have been reported from quantitative LEED measurements for K and Cs on Ag(111),[190, 193] and such vibrations could therefore be a significant contributing factor to the low coherent fractions. However, the vibrational amplitudes reported for alkali metals on Ag(111)[190, 193] would not be sufficient to entirely account for the low measured coherent fractions. It is also unknown whether the alkali metal ions would exhibit similar behaviour within the networks formed with the TCNQ molecules and as a result, further analysis would need to be performed to establish the cause of the low coherent fractions.

8. Conclusions and outlook

The adsorption structures formed by TCNQ, both with and without coadsorbed alkali metals, on the (111) and (100) surfaces of Ag were characterised using a variety of complementary surface science techniques. For each system, a wide array of adsorption phases were formed by changing the preparation conditions, such as the TCNQ/alkali metal stoichiometry, the TCNQ coverage or by heating the sample. STM and LEED were used to identify these adsorption phases by determining the lateral periodicity and molecular assemblies that define them. Precise quantitative structural measurements were obtained from a subset of these adsorption phases using the NIXSW technique. UPS and XPS measurements were also obtained to probe the electronic properties of the surface, including the surface work function and adsorbate charge states, which were then related to the measured structures. For some of the commensurate phases, dispersion corrected DFT calculations (performed by collaborators as detailed in section 2.8.8) were obtained to provide useful comparisons with the experimental measurements.

A key motivation of the work presented in this thesis was to use experimental techniques to investigate the results of DFT calculations performed for TCNQ/alkali metal networks adsorbed on Ag.[168] These calculations predict that the alkali metal ions occupy elevated heights above the TCNQ molecules as this, together with its image charge, generates a larger dipole moment that more effectively counteracts the oppositely polarised dipole moments generated by negatively charged TCNQ molecules.[168] As ionisation energy decreases with increasing alkali metal size, larger alkali metals can counter the TCNQ dipoles more effectively, which is achieved by them adsorbing further above the surface and causes a larger shift to the surface work function.[168] These effects were investigated in this thesis through characterisation of the structural and electronic properties of TCNQ/alkali metal networks formed on the Ag(100) and Ag(111) surfaces. On both substrates, a variety of different adsorption phases were formed by codepositing TCNQ with Cs, K and Na at a range of TCNQ/alkali metal stoichiometry. NIXSW measurements obtained from a subset of these adsorption phases revealed that the alkali metals do indeed adsorb above the TCNQ molecules and are significantly further above the surface than when the alkali metals were deposited alone on the surface. Moreover, increasing the relative coverage of the alkali metals results in them adsorbing closer to the surface and, in analogous Cs/TCNQ and K/TCNQ adsorption phases, Cs adsorbed at a greater height and generated a larger work function shift than K. The structural outcomes predicted by DFT to be caused by the interactions of surface dipoles[168] were therefore observed using experimental techniques for TCNQ/alkali metal networks formed on the Ag(111) and Ag(100) surfaces and thus support the claim that these dipoles have an important influence on the structural and electronic properties of the interface. The UPS measurements also showed that a

considerably large range (~1.5 eV) of work function values are achievable by varying the amount and type of alkali metal deposited onto the TCNQ layer. This large range of work function values is achievable within an adsorbed layer that is only one molecule thick, which is a highly desirable property for charge transport layers used in OEDs.[3, 64, 150, 151] The results here highlight that these TCNQ/alkali metal networks could be promising candidates for such applications. However, with only limited data, it is unclear whether this achievable range of work functions values is continuous and a more detailed investigation of how the work function varies as a function of the TCNQ/alkali metal stoichiometry would need to be conducted. Furthermore, to be incorporated into OEDS, these TCNQ/alkali metal networks would need to be stable and resistant to degradation under ambient conditions[9] and therefore the behaviour of these networks under ambient conditions would also need to be investigated.

On the Ag(111) surface, TCNQ adsorbs with the core of the molecule near-parallel to the substrate with some cyano groups pointing up and others pointing down. This was found to be a direct consequence of Ag adatoms from the substrate being incorporated into the TCNQ layer. This result differs significantly from the conventional wisdom in the literature, which suggests that TCNQ adopts a considerably bent conformation, with all four cyano groups pointing down towards the substrate, when adsorbed on coinage metal surfaces.[17, 128, 164, 165] This conventional wisdom is largely based on the results of STM combined with DFT calculations that do not include dispersion corrections to account for vdW interactions.[17, 128, 164] The results presented in this thesis showed that obtaining both experimental quantitative structural measurements and dispersion corrected DFT calculations were essential in determining the adsorption structure of TCNQ on Ag(111) and also highlighted some pitfalls of the approach commonly used in the literature of relying only on STM and DFT to resolve adsorption structures.[54, 164, 165, 184]

These previous studies of TCNQ adsorption structures typically consist of using STM to identify the lateral ordering and assembly of the molecules on the surface and use DFT calculations to optimise the geometry of the structure interpreted from the STM contrast. In some cases,[54, 61] Tersoff-Hamann simulations[132] are also used to ascertain the extent to which the calculated structures agree with the experimental STM images. Due to the nature of STM, which maps information of the surface electronic structure, there is no reliable one-to-one correspondence of protrusions in the image contrast with atoms on the surface. Consequently, this could lead to the incorrect interpretation of adsorption structures if important components of the structure are not clearly visible in STM images. The results for TCNQ on Ag(111) demonstrated this as the STM images did not show any evidence of Ag adatoms and DFT-D calculations that did not include adatoms yielded a significantly bent conformation that is incompatible with the experimental NIXSW results. Moreover, Tersoff-Hamann simulations[132] of the DFT-D

structures calculated both with and without adatoms showed good qualitative agreement with the experimentally measured STM images, with no clear features visible at the locations of the adatoms, illustrating that these simulations do not give a reliable indication that the correct structure has been calculated. It is therefore conceivable that without the quantitative experimental structural measurements, the presence of adatoms in this structure would have been missed. It was also noted that the bent conformation calculated for TCNQ on Ag(111) in the absence of adatoms is comparable to TCNQ adsorption conformations predicted by DFT on other substrates on which the possible involvement of substrate adatoms was not explored.[17, 128, 164, 165] It is therefore plausible that substrate adatoms are also present in these previously reported TCNQ adsorption phases[17, 128, 164, 165] and consequently, these systems require a more thorough investigation. More generally, the issue of relying on only STM and DFT to resolve adsorption structures is not unique to systems involving TCNQ and related molecules. Indeed, there are numerous examples[38, 56, 184, 203-205] of this across a wide range of adsorbates and surfaces, whilst there remains a dearth of experimental quantitative structural studies. It is reasonable to speculate that the structural conclusions from a significant proportion of STM and DFT studies may be incorrect and this highlights a greater need for experimental structure determination, using techniques such as NIXSW, to fully understand these interfaces.

NIXSW measurements of the head-to-tail type adsorption phases formed by TCNQ on Ag(100) showed that the molecule does adopt a significantly bent conformation, which could indicate a lack of substrate adatom involvement. As the molecular conformation alone provides insufficient evidence to ascertain whether adatoms are present within the adsorption structure, dispersion corrected DFT calculations should be obtained for the commensurate head-to-tail phase to investigate this further. STM images of the windmill adsorption phases formed after annealing the sample did show some evidence of Ag adatoms within the TCNQ layer and suggested that such participation of Ag adatoms in TCNQ structures on Ag(100) could be thermally activated. However, due to the previously discussed deficiencies of STM, quantitative structural measurements would need to be obtained for these windmill adsorption phases to confirm this. An obvious way to achieve this would be to adopt the same approach used for the Ag(111) surface, recording NIXSW measurements and comparing the results with dispersion corrected DFT calculations. Whilst this approach was successful in identifying the presence of adatoms on Ag(111), it may be possible to identify any involvement of Ag adatoms in the surface structure more directly using surface X-ray diffraction. As Ag atoms are significantly heavier than the constituent atoms of the TCNQ molecule, they have a much larger X-ray scattering factor and consequently would dominate the diffracted amplitude if they are present in the adsorption structure.[206]

Another important aspect of calculating accurate adsorption structures with DFT is the need for an appropriate dispersion correction to describe vdW interactions that are of great significance for organic adsorbate systems. One issue with current dispersion corrections is that they can be largely system dependent and thus is difficult possible to determine *a priori* which one is best to use.[27, 131, 207] This was demonstrated in calculations obtained for TCNQ on Ag(111) for which the predicted molecule-substrate spacing varied by as much as 0.7 Å depending on the correction that was used. In this thesis the NIXSW measurements were used as an empirical reference point with which to compare the structures calculated using different dispersion corrections, providing a basis to identify the best dispersion correction for the given system. In fact, dispersion corrected functionals are typically benchmarked through similar comparisons to experimentally measured structural parameters, often obtained from NIXSW measurements.[23, 24, 30, 35] In this regard, the NIXSW measurements recorded in this thesis could also serve as empirical reference points for future benchmarking of DFT dispersion corrections. The TCNQ/alkali metal networks or TCNQ structures that include Ag adatoms could be of particular interest for this purpose as recent work in the literature has been dedicated to improving dispersion corrections for materials that contain ions.[143, 208] Thus far, these dispersion correction parameters for ionic systems have not been tested in the context of hybrid metal-organic interfaces and, consequently, the NIXSW measurements presented in this thesis would be a useful point of comparison. Indeed, the dispersion corrected DFT calculations shown in this thesis for the K_2TCNQ phase used C_6 and polarisability coefficients derived from these recent improvements for ionic systems.[143, 208] The results of these calculations show excellent agreement with the experimental NIXSW results, suggesting that these parameters give a good description of vdW forces in the studied system. This comparison of theory and experiment could also be expanded to the other commensurate TCNQ/alkali metal structures that were measured by NIXSW and the numerous other commensurate phases that were identified by STM and LEED.

A common problem that is faced when determining surface structures using the NIXSW technique, is the issue of low coherent fractions. It is generally accepted that coherent fractions of 0.8 or greater are consistent with a single adsorption height, with small reductions from the theoretical maximum value of unity attributed to incoherence caused by thermal vibrations of the substrate and absorber atoms.[21, 98] In this situation, the associated coherent position can simply be attributed to the single adsorption height adopted by the absorbing atoms. Coherent fractions lower than 0.8 complicate the interpretation of NIXSW measurements as they indicate that the absorbing atoms contributing to the measurement occupy a significant distribution of heights, with the associated coherent position corresponding to a weighted average of this distribution.[21, 98] Low coherent fractions can be caused by several factors, including static and dynamic disorder in the surface or the co-occupation of two or more sites with

distinctly different adsorption heights, and therefore to understand the context of the coherent position, the cause(s) of the low coherent fraction must be identified.[21, 98] Despite this, there are numerous examples in the literature where coherent fractions that are significantly lower than 0.8 are reported without giving a credible rationale to explain why a low value is measured.[23, 169, 209-212] In these examples, the low coherent fraction is typically attributed, without full justification, to thermal vibrations or some unspecified disorder, with the absorbing atoms otherwise assumed to occupy a uniform height corresponding to the measured coherent position.[23, 169, 209-212] Coherent fractions of ~0.4-0.6 are often interpreted in this way; [23, 169, 210-212] there are even some instances of this for values of 0.2 or lower.[209] Vibrational motion alone would require questionably large amplitudes (i.e. rms vibrational amplitudes of >0.3 Å) to reduce the coherent fraction to values below 0.6 and so the possibility that these low values could instead be caused by co-occupation of at least two distinct contributing heights should also be considered but is often neglected. [23, 169, 209-211] However, even in situations where static disorder can largely be excluded (such as nominally planar molecules adsorbed in apparent flat-lying geometries on large surface terraces), low coherent fractions are still sometimes recorded.[212, 213] Clearly the causes of low coherent fractions and their significance are not well understood in the literature and require further investigation.

Low coherent fractions were recorded for a significant portion of the adsorption structures measured in this thesis. For TCNQ on Ag(111), dispersion corrected DFT calculations aided the interpretation of the NIXSW measurements, demonstrating that structural models including Ag adatoms reproduced the experimentally measured trends in coherent fractions as well as the coherent positions. Conversely, for the K_2TCNQ head-to-tail structure formed on Ag(111), dispersion corrected DFT calculations did not present any structural explanation for the reduced coherent fractions that were measured, though the calculated models did show excellent agreement with the measured coherent positions. This was interpreted as an indication that the low coherent fractions are not caused by the co-occupation of multiple adsorption heights but instead are caused by vibrational effects. It was noted that due to the structure of the molecule, a relatively small rms rotational amplitude (~3°) could account for the low coherent fractions. The examples here demonstrate that complementing NIXSW measurements with dispersion corrected DFT calculations provides useful insight into possible structural causes of low coherent fractions. Indeed, many of the adsorption phases studied with NIXSW in this thesis were not accompanied with dispersion corrected DFT calculations, which severely limited the ability to interpret the low coherent fractions. It follows that dispersion corrected DFT calculations should be employed where possible for all NIXSW measurements that feature low coherent fractions. However, due to the requirement of periodic boundary conditions for DFT calculations, only commensurate structures can be explicitly modelled. Incommensurate structures therefore present an issue, but it may be possible to

gain some insight with suitable approximations, such as constraining the model to a similar commensurate structure[56] or explicitly modelling finite clusters of the incommensurate structure that are isolated from their periodically repeated images.[214, 215]

To provide even further insight into the causes of low coherent fractions, it would be useful to also characterise the vibrational dynamics of the surface structure. To this effect, Mercurio *et al.* modelled anharmonic vibrational modes from azobenzene on Ag(111) to investigate the impact they have on NIXSW measurements.[216] These calculations predict that the vibrations cause a small (5-10%) reduction in the coherent fraction but also that, due to the anharmonicity, the vibrations cause significant shifts (>0.1 Å) in the average heights of the atoms.[216] A more complete model of the vibrational dynamics could be provided by *ab-initio* molecular dynamics (AIMD) simulations,[217] which so far have not been used to investigate temperature effects in NIXSW. Due to their high computational cost, AIMD simulations are limited to systems that can be modelled with a relatively small number of atoms, though an example of these calculations has been reported for small molecule adsorbates of comparable size to TCNQ.[218] In addition to these theoretical approaches, the effect of thermal vibrations could also be investigated experimentally by conducting temperature-dependent NIXSW experiments on an otherwise well-characterised interface for which the structural phase does not change with temperature. In this scenario, the coherent fraction would be expected to decrease with increasing temperature if the vibrational modes have significant amplitudes.

Appendices

Appendix A – List of publications

List of articles resulting from work performed during the PhD period that have been/will be published:

- P.J. Blowey, R.J. Maurer, L.A. Rochford, D.A. Duncan, P.T.P. Ryan, T.-L. Lee, P.K. Thakur, G. Costantini, D.P. Woodruff, *Testing the potential of two-dimensional charge-transfer networks to control the electronic structure of metal-organic interfaces*, in preparation.
- P.J. Blowey, R.J. Maurer, L.A. Rochford, D.A. Duncan, D.A. Warr, J. Lawrence, T.-L. Lee, P.K. Thakur, G. Costantini, D.P. Woodruff, *Conformational adsorption changes of electron acceptor molecules on metal surfaces*, in preparation.
- P.J. Blowey, R.J. Maurer, L.A. Rochford, D.A. Duncan, D.A. Warr, P.T.P. Ryan, T.-L. Lee, P.K. Thakur, G. Costantini, D.P. Woodruff, *The structure of TCNQ/alkali metal charge-transfer networks on metal surfaces*, in preparation.
- L.A. Rochford, P.J. Blowey, D.A. Duncan, D.-H. Kang, T.-L. Lee, G. Costantini, R.J. Maurer, K. Reuter, D.P. Woodruff, *The structure of VOPc on Cu(111): does V=O point up, down, or both?*, in preparation.
- P.J. Blowey, S. Velari, L.A. Rochford, D.A. Duncan, D.A. Warr, T.-L. Lee, A. De Vita, G. Costantini, D.P. Woodruff, *Re-evaluating how charge transfer modifies the conformation of adsorbed molecules*, accepted by Nanoscale.
- P.T.P. Ryan, Z. Jakub, J. Balajika, J. Hulva, M. Meier, J.T. Küchle, P.J. Blowey, P.K. Thakur, C. Franchini, D.J. Payne, D.P. Woodruff, L.A. Rochford, F. Allegretti, T.-L. Lee, G.S. Parkinson, D.A. Duncan, *Direct measurement of Ni incorporation into Fe_3O_4(001)*, Physical Chemistry Chemical Physics, (2018), advance article.
- T.W. White, D.A. Duncan, S. Fortuna, Y.-L. Wang, B. Moreton, T.-L. Lee, P.J. Blowey, G. Costantini, D.P. Woodruff, *A structural investigation of the interaction of oxalic acid with Cu(110)*, Surface Science, 668 (2018), 134-143.
- P.J. Blowey, L.A. Rochford, D.A. Duncan, D.A. Warr, T.-L. Lee, D.P. Woodruff, G. Costantini, *Probing the interplay between geometric and electronic structure in a two-dimensional K-TCNQ charge transfer network*, Faraday Discussions, 204 (2017), 97-110.
- T. Suzuki, J. Lawrence, M. Walker, J.M. Morbec, P.J. Blowey, K. Yagyu, P. Kratzer, G. Costantini, *Indium coverage of the Si(111)-$\sqrt{7} \times \sqrt{3}$-In surface*, Physical Review B, 96 (2017), 035412.

- P.S. Deimel, R.M. Bababrik, B. Wang, P.J. Blowey, L.A. Rochford, P.K. Thakur, T.-L. Lee, M.-L. Bocquet, J.V. Barth, D.P. Woodruff, D.A. Duncan, F. Allegretti, *Direct quantitative identification of the "surface trans-effect"*, Chemical Science, 7 (2016), 5647-5656.

Appendix B – TCNQ on Ag(111) Boltzmann distribution

The adsorption energies (E_{ads}) obtained from DFT-D models calculated for phase II TCNQ surface structure on Ag(111) were obtained by determining the difference in total energy between the final calculated structure and the sum of the separate constituent components. For the phase II surface structure, which includes three TCNQ molecules per unit mesh, the adsorption energy per unit mesh is given by:

$$E_{ads} = E_{model} - (E_{slab} + 3E_{TCNQ} + nE_{Ag}) \quad \text{[B.1]}$$

where E_{model} is the total energy of the final calculated structure, E_{slab} is the total energy of the clean Ag(111) slab, E_{TCNQ} is the total energy of gas phase TCNQ (modelled as a TCNQ molecule isolated by vacuum), E_{Ag} is the total energy per atom calculated for bulk Ag and n is the number of Ag adatoms included in the final calculated structure. The nE_{Ag} term is included to account for the different numbers of Ag atoms within the models, using the energy of a bulk Ag atom as a reference level for adatom formation.[219]

Table B.1 – DFT-D calculated energies of the separate constituent components used as initial state references for the calculated models.

Component	Total energy / eV
E_{TCNQ}	-3106.79
E_{Ag}	-1292.16
E_{slab}	-139508.70

Table B.2 – Total energies from the DFT-D models for TCNQ on Ag(111) and the adsorption energies calculated for each model. Relative adsorption energies are also given by subtracting E_{ads} for the 2 ββ model from E_{ads} for each model.

Model	E_{model} / eV	E_{ads} / eV	Relative energy / eV
0	-148840.155	-11.068	-0.004
1 α	-150132.439	-11.169	-0.105
1 β	-150132.384	-11.114	-0.050
2 αβ	-151424.632	-11.180	-0.116
2 ββ	-151424.516	-11.064	0.000
3	-152716.758	-11.124	-0.059

The relative occupancy of each model (shown in Table B.3) was estimated by calculating a Boltzmann distribution from the relative adsorption energies shown in Table B.2. The fractional occupation of each structural model is given by:

$$\frac{N_i}{N} = \frac{g_i exp(-E_{ads,i}/k_B T)}{\sum_j g_j exp(-E_{ads,j}/k_B T)} \qquad [B.2]$$

where N_i is the population coefficient for model i, N is the sum of population coefficients for all models, g is the degeneracy, k_B is the Boltzmann constant and T is the temperature.

Table B.3 – Occupancies (expressed as a percentage) calculated for T = 300 K from the different DFT-D models. The degeneracy gives the number of unique but symmetrically equivalent adatom configurations possible for each model.

Model	Relative energy / eV	Degeneracy	N_i	Occupancy / %
0	-0.004	1	1.171	0.45
1 α	-0.105	1	58.25	22.26
1 β	-0.050	2	13.67	5.22
2 αβ	-0.116	2	177.6	67.87
2 ββ	0.000	1	1.000	0.38
3	-0.059	1	9.969	3.81

Appendix C – DFT and vdW-DF structures calculated for TCNQ on Ag(111)

In section 4.3, structural models calculated for TCNQ on Ag(111) using the DFT-D dispersion correction proposed by Grimme[27] were used to aid in the interpretation of the experimental NIXSW results. Structural models were also calculated using the vdW-DF dispersion correction of Dion *et al.*[29] as well as without dispersion corrections, which both yield adsorption heights that are much larger than the NIXSW measurements suggest. Table C.1 shows NIXSW parameters expected from the atomic coordinates of the models calculated using the vdW-DF method and without dispersion corrections.

Table C.1 – Expected coherent fractions (f) and coherent positions ($D_{(111)}$) obtained from the atomic coordinates of the various pure DFT and vdW-DF dispersion corrected structural models. Adatom models are listed in the left-hand column stating the number of adatoms and the sites occupied. The $D_{(111)}$ values are taken relative to the average height of the outermost Ag layer.

	f				***D*$_{(111)}$ / Å**			
DFT								
Adatoms	CH	CC	CN	N	CH	CC	CN	N
0	0.96	0.94	0.99	0.98	3.30	3.12	2.72	2.38
1 α	0.95	0.94	0.79	0.52	3.29	3.15	2.83	2.44
1 β	0.96	0.94	0.81	0.59	3.34	3.20	2.84	2.42
2 αβ	0.99	0.97	0.73	0.23	3.31	3.21	2.98	2.68
2 ββ	0.93	0.97	0.78	0.36	3.39	3.27	2.97	2.52
3	0.87	0.96	0.71	0.12	3.45	3.36	3.13	2.88
vdW-DF								
Adatoms	CH	CC	CN	N	CH	CC	CN	N
0	0.99	0.96	0.98	0.94	3.45	3.29	2.93	2.61
1 α	0.97	0.94	0.78	0.49	3.47	3.35	3.06	2.69
1 β	0.99	0.96	0.81	0.53	3.46	3.34	3.02	2.62
2 αβ	0.99	0.97	0.75	0.20	3.47	3.39	3.20	3.04
2 ββ	0.98	0.96	0.73	0.31	3.53	3.44	3.20	3.00
3	0.98	0.99	0.82	0.46	3.53	3.48	3.35	3.30

Appendix D – Determining surface stoichiometry using soft XPS

The stoichiometry of the TCNQ/alkali metal networks were estimated by comparing core-level photoemission intensities, accounting for the differences in photoionisation cross-sections of the different core-levels.

The cross-sections were corrected for the angular distribution of photoemission using:

$$\sigma_{corr} = \sigma_i(1 + \beta P_2(\cos\theta)) \quad [D.1]$$

where σ_i is the photoemission cross-section, β is the dipole asymmetry parameter, $P_2(cos\theta)$ is the second order Legendre polynomial and θ is the angle between the photon polarisation vector and the photoelectron emission direction. For the experimental geometry used $\theta = 0°$. Expanding $P_2(cos\theta)$ and substituting 1 for cos(0) the equation can be expressed as:

$$\sigma_{corr} = \sigma_i(1 + \beta) \quad [D.2]$$

Corrected photoionisation cross-sections were determined for the C 1s, K 2p and Cs 3d core-levels at the photon energies used to record the XP spectra presented in this thesis. These values are shown in Table D.1.

Table D.1 – Photoionisation cross-sections (σ), dipole asymmetry parameters (β) and angular distribution corrected photoionisation cross-sections (σ_{corr}) at the photon energies used to measure XPS in this thesis. The cross-sections and dipole asymmetry parameters were obtained from atomic and nuclear data tables.[93, 94]

Core-level	Photon energy / eV	σ / Mbarn	β	σ_{corr} / Mbarn
C 1s	435	0.38	2.00	1.14
K 2p	435	1.51	1.34	3.53
C 1s	850	0.07	2.00	0.20
Cs 3d	850	2.20	0.46	3.21

To normalise the measured XPS signal, the integrated photoemission peak areas are divided by the appropriate σ_{corr} value. To account for each TCNQ molecule containing twelve carbon atoms, the C 1s intensities were also divided by twelve. This can be expressed as:

$$I_{norm} = \frac{I}{\sigma_{corr} \times n} \qquad [D.3]$$

where I_{norm} is the peak intensity normalised for cross-section, asymmetry and number of atoms per molecule, I is the integrated photoemission peak intensity and n is the number of atoms of a given element per molecule (where applicable). The surface stoichiometry was then estimated as the ratio of these normalised photoemission peak areas. Measured XPS peak areas obtained from the K/TCNQ and Cs/TCNQ adsorption phases, the corresponding normalised peak areas and estimated surface stoichiometry are shown in Table D.2 and Table D.3.

Table D.2 – Integrated peak areas (I) measured from high-resolution soft XPS (hv = 435 eV) recorded from the K/TCNQ adsorption phases on Ag(111) and Ag(100). The peak areas were normalised (I_{norm}) as described in equation D.3 and the ratio of these normalised peak areas were used to estimate the K/TCNQ ratio. Measurements were obtained from two separate samples for each phase.

Phase	Preparation	I_{K2p}	I_{C1s}	$I_{norm,K2p}$	$I_{norm,C1s}$	K/TCNQ ratio
K/TCNQ windmill Ag(111)	1	23.5	97.6	6.7	7.1	0.9
	2	38.0	189.6	10.8	13.9	0.8
K/TCNQ head-to-tail Ag(111)	1	9.55	11.1	2.0	0.8	2.5
	2	2.58	4.4	0.7	0.3	2.3
K phase 1 Ag(100)	1	13.1	288.3	3.7	21.1	0.2
	2	9.1	178	2.6	13.0	0.2

Table D.3 – Integrated peak areas (I) measured from soft XPS survey scans (hv = 850 eV) recorded from the Cs/TCNQ adsorption phases on Ag(111). The peak areas were normalised (I_{norm}) as described in equation D.3 and the ratio of these normalised peak areas were used to estimate the Cs/TCNQ stoichiometry. Measurements were obtained from two separate samples for each phase.

Phase	Preparation	I_{Cs3d}	I_{C1s}	$I_{norm,Cs3d}$	$I_{norm,C1s}$	Cs/TCNQ ratio
Cs/TCNQ windmill Ag(111)	1	1.44	0.78	0.45	0.33	1.4
	2	1.95	0.94	0.61	0.39	1.5
Cs/TCNQ head-to-tail Ag(111)	1	3.12	1.13	0.97	0.47	2.0
	2	2.75	1.07	0.85	0.45	1.9

As the high-resolution Cs 3d XPS from the Cs/TCNQ phases on Ag(111) were measured using a different pass energy to the C 1s and N 1s spectra, no meaningful comparison could be obtained from their relative peak intensities. Consequently, lower resolution survey spectra were used instead to obtain estimates of the surface composition. The C 1s and Cs 3d regions of these survey spectra for the two Cs/TCNQ phases on Ag(111) are shown in Figure D.1.

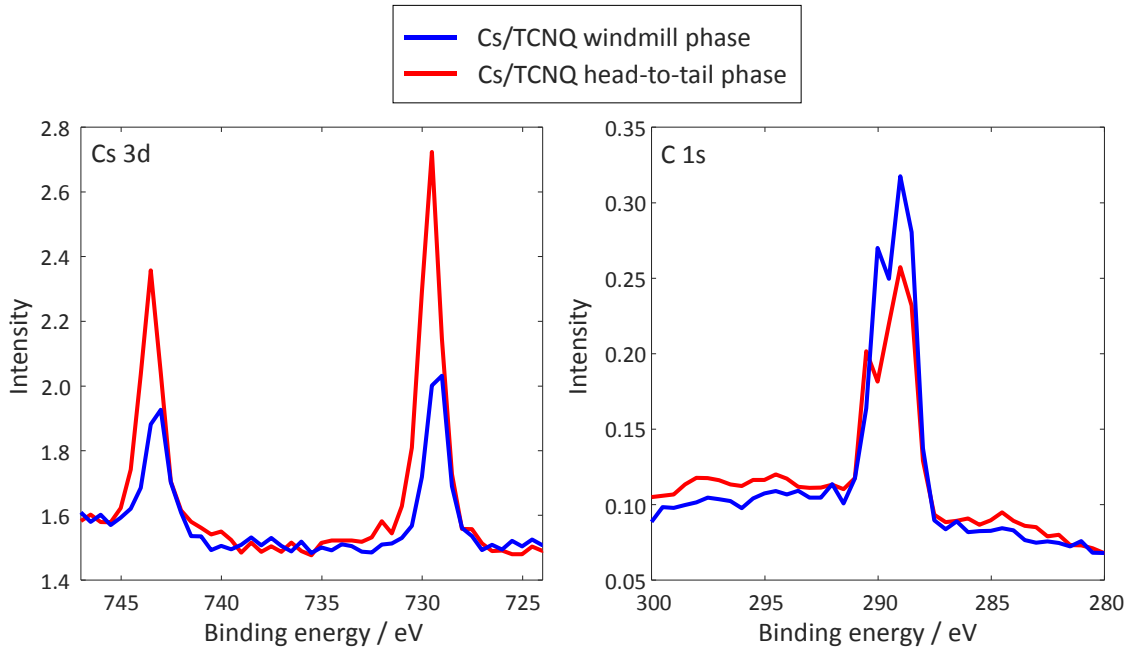

Figure D.1 – The Cs 3d and C 1s regions from soft XPS survey scans obtained from the Cs/TCNQ phases on the Ag(111) surface. The survey spectra were recorded at a photon energy of 850 eV.

Appendix E – NIXSW non-dipole correction parameters

For NIXSW experiments, non-dipole corrections were applied when fitting the photoemission yield curves. The forward-backward asymmetry parameter Q was calculated using the following expression:

$$Q = \frac{(\delta + \gamma cos^2\theta) sin\theta cos\varphi}{\left(1 + \left(\frac{\beta}{2}\right)(3cos^2\theta - 1)\right)} \quad [E.1]$$

where β, γ and δ are the asymmetry parameters discussed in section 2.6, θ is the angle between the X-ray polarisation vector and the direction of emission towards the electron detector and φ is the angle between the photon propagation direction and the projection of emission direction in the plane perpendicular to the X-ray polarisation vector. In the experimental geometry used at I09, the electron analyser was mounted at 90° to the incident X-ray beam, with the X-ray polarisation vector pointing towards the analyser. As all emission was detected within the plane containing the X-ray polarisation vector and the photon propagation direction, the angle φ was 0° for all experiments. The electron analyser used has a 60° angular acceptance range, though when operating at normal incidence to the surface (using the Bragg reflection from planes parallel to the crystal surface), photoemission could only be detected from half of the angular acceptance range as the remaining half was not in line-of-sight of the crystal surface. The direction of the detector was approximated as the middle of the half of the acceptance range 'visible' to the crystal surface and thus a value of θ = 15° was used. When using the reflections from planes not parallel to the crystal surface, such as the (111) reflection of the Ag(100) substrate, the full angular acceptance range of the detector was in view of the crystal surface and thus the centre of the analyser corresponds to θ = 0°, which gives a Q value of 0.

The β, γ and δ asymmetry parameters were interpolated from calculated values given for the different core-levels studied using NIXSW,[107] to give values corresponding to the photon energies used for the (111) and (200) reflections of Ag. The corresponding Q values used in this thesis are summarised in Table E. 1.

Table E. 1 – Q values used to apply corrections for non-dipole effects to NIXSW measurements obtained in this thesis.

Core level	Q value for (111) reflection of Ag(111)	Q value for (200) reflection of Ag(100)
C 1s	0.0922	0.1010
N 1s	0.0889	0.0974
K 2p	0.1038	0.1153
Cs 3d	0.0602	0.0754

Bibliography

1. J. H. Burroughes, D. D. C. Bradley, A. R. Brown, R. N. Marks, K. Mackay, R. H. Friend, P. L. Burns and A. B. Holmes, *Nature*, 1990, **347**, 539-541.

2. M. A. Baldo, D. F. O'Brien, Y. You, A. Shoustikov, S. Sibley, M. E. Thompson and S. R. Forrest, *Nature*, 1998, **395**, 151-154.

3. P. Peumans, A. Yakimov and S. R. Forrest, *J. Appl. Phys.*, 2003, **93**, 3693-3723.

4. J. Peet, A. J. Heeger and G. C. Bazan, *Acc. Chem. Res.*, 2009, **42**, 1700-1708.

5. G. J. Hedley, A. Ruseckas and I. D. W. Samuel, *Chem. Rev.*, 2017, **117**, 796-837.

6. M. Muccini, *Nat. Mater.*, 2006, **5**, 605-613.

7. H. Sirringhaus, *Adv. Mater.*, 2014, **26**, 1319-1335.

8. H. E. Katz and J. Huang, *Annu. Rev. Mater. Res*, 2009, **39**, 71-92.

9. S. R. Forrest, *Nature*, 2004, **428**, 911-918.

10. S. Scholz, D. Kondakov, B. Lüssem and K. Leo, *Chem. Rev.*, 2015, **115**, 8449-8503.

11. S. Braun, W. R. Salaneck and M. Fahlman, *Adv. Mater.*, 2009, **21**, 1450-1472.

12. H. Ishii, K. Sugiyama, E. Ito and K. Seki, *Adv. Mater.*, 1999, **11**, 605-+.

13. C. R. McNeill, *J. Polym. Sci., Part B: Polym. Phys.*, 2011, **49**, 909-919.

14. J. Rivnay, S. C. B. Mannsfeld, C. E. Miller, A. Salleo and M. F. Toney, *Chem. Rev.*, 2012, **112**, 5488-5519.

15. M. Mas-Torrent and C. Rovira, *Chem. Rev.*, 2011, **111**, 4833-4856.

16. G. Mercurio, O. Bauer, M. Willenbockel, N. Fairley, W. Reckien, C. H. Schmitz, B. Fiedler, S. Soubatch, T. Bredow, M. Sokolowski and F. S. Tautz, *Phys. Rev. B*, 2013, **87**, 045421.

17. T.-C. Tseng, C. Urban, Y. Wang, R. Otero, S. L. Tait, M. Alcamí, D. Écija, M. Trelka, J. M. Gallego, N. Lin, M. Konuma, U. Starke, A. Nefedov, A. Langner, C. Wöll, M. Á. Herranz, F. Martín, N. Martín, K. Kern and R. Miranda, *Nat. Chem.*, 2010, **2**, 374-379.

18. B. D. Ratner and D. G. Castner, in *Surface Analysis – The Principal Techniques*, John Wiley & Sons, Ltd, 2009, pp. 47-112.

19. F. Jona, J. A. Strozier and P. M. Marcus, in *The Structure of Surfaces*, eds. M. A. Van Hove and S. Y. Tong, Springer Berlin Heidelberg, Berlin, Heidelberg, 1985, pp. 92-99.

20. P. W. Palmberg, *J. Vac. Sci. Technol., A*, 1994, **12**, 946-952.

21. D. P. Woodruff, *Rep. Prog. Phys.*, 2005, **68**, 743.

22. D. P. Woodruff and A. M. Bradshaw, *Rep. Prog. Phys.*, 1994, **57**, 1029.

23. C. Burker, N. Ferri, A. Tkatchenko, A. Gerlach, J. Niederhausen, T. Hosokai, S. Duhm, J. Zegenhagen, N. Koch and F. Schreiber, *Phys. Rev. B*, 2013, **87**, 5.

24. G. Mercurio, E. R. McNellis, I. Martin, S. Hagen, F. Leyssner, S. Soubatch, J. Meyer, M. Wolf, P. Tegeder, F. S. Tautz and K. Reuter, *Phys. Rev. Lett.*, 2010, **104**, 036102.

25. A. J. Cohen, P. Mori-Sánchez and W. Yang, *Chem. Rev.*, 2012, **112**, 289-320.

26. A. Jain, Y. Shin and K. A. Persson, *Nat. Rev. Mater.*, 2016, **1**, 15004.

27. S. Grimme, *Wiley Interdiscip. Rev. Comput. Mol. Sci.*, 2011, **1**, 211-228.

28. S. Grimme, J. Antony, S. Ehrlich and H. Krieg, *J. Chem. Phys.*, 2010, **132**, 154104.

29. M. Dion, H. Rydberg, E. Schröder, D. C. Langreth and B. I. Lundqvist, *Phys. Rev. Lett.*, 2004, **92**, 246401.

30. A. Tkatchenko, L. Romaner, O. T. Hofmann, E. Zojer, C. Ambrosch-Draxl and M. Scheffler, *MRS Bull.*, 2010, **35**, 435-442.

31. R. A. DiStasio, Jr., V. V. Gobre and A. Tkatchenko, *J. Phys.: Condens. Matter*, 2014, **26**, 213202.

32. V. G. Ruiz, W. Liu, E. Zojer, M. Scheffler and A. Tkatchenko, *Phys. Rev. Lett.*, 2012, **108**, 146103.

33. A. Tkatchenko, R. A. DiStasio, R. Car and M. Scheffler, *Phys. Rev. Lett.*, 2012, **108**, 236402.

34. R. J. Maurer, V. G. Ruiz, J. Camarillo-Cisneros, W. Liu, N. Ferri, K. Reuter and A. Tkatchenko, *Prog. Surf. Sci.*, 2016, **91**, 72-100.

35. W. Liu, A. Tkatchenko and M. Scheffler, *Acc. Chem. Res.*, 2014, **47**, 3369-3377.

36. F. Jona, J. J. A. Strozier and W. S. Yang, *Rep. Prog. Phys.*, 1982, **45**, 527.

37. R. Feidenhans'l, *Surf. Sci. Rep.*, 1989, **10**, 105-188.

38. R. Otero, J. M. Gallego, A. L. V. de Parga, N. Martín and R. Miranda, *Adv. Mater.*, 2011, **23**, 5148-5176.

39. J. V. Barth, G. Costantini and K. Kern, *Nature*, 2005, **437**, 671-679.

40. J. E. Lennard-Jones, *Trans. Faraday Soc.*, 1932, **28**, 333-359.

41. A. Bondi, *J. Phys. Chem.*, 1964, **68**, 441-451.

42. B. Cordero, V. Gomez, A. E. Platero-Prats, M. Reves, J. Echeverria, E. Cremades, F. Barragan and S. Alvarez, *Dalton Trans.*, 2008, **0**, 2832-2838.

43. P. M. Morse, *Phys. Rev.*, 1929, **34**, 57-64.

44. G. Attard and C. Barnes, *Surfaces*, Oxford University Press, 1998.

45. A. Hauschild, R. Temirov, S. Soubatch, O. Bauer, A. Scholl, B. C. C. Cowie, T. L. Lee, F. S. Tautz and M. Sokolowski, *Phys. Rev. B*, 2010, **81**, 12.

46. S. Duhm, A. Gerlach, I. Salzmann, B. Bröker, R. L. Johnson, F. Schreiber and N. Koch, *Org. Electron.*, 2008, **9**, 111-118.

47. J. A. Theobald, N. S. Oxtoby, M. A. Phillips, N. R. Champness and P. H. Beton, *Nature*, 2003, **424**, 1029-1031.

48. F. Huang and E. V. Anslyn, *Chem. Rev.*, 2015, **115**, 6999-7000.

49. R. Otero, M. Schöck, L. M. Molina, E. Lægsgaard, I. Stensgaard, B. Hammer and F. Besenbacher, *Angew. Chem. Int. Ed.*, 2005, **44**, 2270-2275.

50. D. A. Duncan, W. Unterberger, K. A. Hogan, T. J. Lerotholi, C. L. A. Lamont and D. P. Woodruff, *Surf. Sci.*, 2010, **Vol.604**, 47-53.

51. I. Kröger, B. Stadtmüller, C. Wagner, C. Weiss, R. Temirov, F. S. Tautz and C. Kumpf, *J. Chem. Phys.*, 2011, **135**, 234703.

52. H. Grönbeck, A. Curioni and W. Andreoni, *J. Am. Chem. Soc.*, 2000, **122**, 3839-3842.

53. X.-Q. Shi, M. A. Van Hove and R.-Q. Zhang, *Phys. Rev. B*, 2012, **85**, 075421.

54. M. N. Faraggi, N. Jiang, N. Gonzalez-Lakunza, A. Langner, S. Stepanow, K. Kern and A. Arnau, *J. Phys. Chem. C*, 2012, **116**, 24558-24565.

55. V. Y. Kutsenko, Y. Y. Lopatina, L. Bossard-Giannesini, O. A. Marchenko, O. Pluchery and S. V. Snegir, *Nanotechnology*, 2017, **28**, 235603.

56. C. Zwick, A. Baby, M. Gruenewald, E. Verwüster, O. T. Hofmann, R. Forker, G. Fratesi, G. P. Brivio, E. Zojer and T. Fritz, *ACS Nano*, 2016, **10**, 2365-2374.

57. C. Wackerlin, C. Iacovita, D. Chylarecka, P. Fesser, T. A. Jung and N. Ballav, *Chem. Commun.*, 2011, **47**, 9146-9148.

58. T.-C. Tseng, N. Abdurakhmanova, S. Stepanow and K. Kern, *J. Phys. Chem. C*, 2011, **115**, 10211-10217.

59. N. Abdurakhmanova, A. Floris, T.-C. Tseng, A. Comisso, S. Stepanow, A. De Vita and K. Kern, *Nat. Commun.*, 2012, **3**, 940.

60. J. Rodríguez-Fernández, K. Lauwaet, M. Á. Herranz, N. Martín, J. M. Gallego, R. Miranda and R. Otero, *J. Chem. Phys.*, 2015, **142**, 101930.

61. S. Bedwani, D. Wegner, M. F. Crommie and A. Rochefort, *Phys. Rev. Lett.*, 2008, **101**, 216105.

62. E. Torres, P. U. Biedermann and A. T. Blumenau, *Int. J. Quantum Chem*, 2009, **109**, 3466-3472.

63. A. Opitz, J. Frisch, R. Schlesinger, A. Wilke and N. Koch, *J. Electron. Spectrosc. Relat. Phenom.*, 2013, **190**, 12-24.

64. S. Lattante, *Electronics*, 2014, **3**, 132.

65. M. Oehzelt, K. Akaike, N. Koch and G. Heimel, *Sci. Adv.*, 2015, **1**.

66. N. Koch, A. Gerlach, S. Duhm, H. Glowatzki, G. Heimel, A. Vollmer, Y. Sakamoto, T. Suzuki, J. Zegenhagen, J. P. Rabe and F. Schreiber, *J. Am. Chem. Soc.*, 2008, **130**, 7300-7304.

67. V. Sahni and K. P. Bohnen, *Phys. Rev. B*, 1985, **31**, 7651-7661.

68. C. Tengstedt, M. Unge, M. P. de Jong, S. Stafström, W. R. Salaneck and M. Fahlman, *Phys. Rev. B*, 2004, **69**, 165208.

69. M. Willenbockel, D. Luftner, B. Stadtmuller, G. Koller, C. Kumpf, S. Soubatch, P. Puschnig, M. G. Ramsey and F. S. Tautz, *PCCP*, 2015, **17**, 1530-1548.

70. B. Stadtmueller, D. Lueftner, M. Willenbockel, E. M. Reinisch, T. Sueyoshi, G. Koller, S. Soubatch, M. G. Ramsey, P. Puschnig, F. S. Tautz and C. Kumpf, *Nat. Commun.*, 2014, **5**.

71. R. G. Musket, W. McLean, C. A. Colmenares, D. M. Makowiecki and W. J. Siekhaus, *Appl. Surf. Sci.*, 1982, **10**, 143-207.

72. J. Verhoeven, in *Surface Contamination: Genesis, Detection, and Control*, ed. K. L. Mittal, Springer US, Boston, MA, 1979, pp. 499-512.

73. M. Mozetič, K. Ostrikov, D. N. Ruzic, D. Curreli, U. Cvelbar, A. Vesel, G. Primc, M. Leisch, K. Jousten, O. B. Malyshev, J. H. Hendricks, L. Kövér, A. Tagliaferro, O. Conde, A. J. Silvestre, J. Giapintzakis, M. Buljan, N. Radić, G. Dražić, S. Bernstorff, H. Biederman, O. Kylián, J. Hanuš, S. Miloševič, A. Galtayries, P. Dietrich, W. Unger, M. Lehocky, V. Sedlarik, K. Stana-Kleinschek, A. Drmota-Petrič, J. J. Pireaux, J. W. Rogers and M. Anderle, *J. Phys. D: Appl. Phys.*, 2014, **47**, 153001.

74. S. Kowarik, A. Gerlach and F. Schreiber, *J. Phys.: Condens. Matter*, 2008, **20**, 184005.

75. A. Yamashita and T. Hayashi, *Adv. Mater.*, 1996, **8**, 791-799.

76. C. Davisson and L. H. Germer, *Phys. Rev.*, 1927, **30**, 705-740.

77. D. P. Woodruff, *Modern Techniques of Surface Science*, Cambridge University Press, Cambridge, 3 edn., 2016.

78. M. P. Seah and W. A. Dench, *Surf. Interface Anal.*, 1979, **1**, 2-11.

79. V. M. Bermudez, *J. Vac. Sci. Technol., A*, 1987, **5**, 2975-2976.

80. K. Heinz, *Surf. Sci.*, 1980, **99**, 440-452.

81. G. Binnig and H. Rohrer, *Helv. Phys. Acta*, 1982, **55**, 726-735.

82. C. J. Chen, *Introduction to Scanning Tunneling Microscopy*, OUP Oxford, 2008.

83. D. Bonnell, *Scanning Probe Microscopy and Spectroscopy: Theory, Techniques, and Applications*, Wiley, 2000.

84. C. Bai, *Scanning Tunneling Microscopy and Its Application*, Springer, 2000.

85. A. Della Pia and G. Costantini, in *Surface Science Techniques*, eds. G. Bracco and B. Holst, Springer Berlin Heidelberg, Berlin, Heidelberg, 2013, pp. 565-597.

86. G. Binnig and H. Rohrer, *Rev. Mod. Phys.*, 1987, **59**, 615-625.

87. J. E. Griffith and G. P. Kochanski, *Annu. Rev. Mater. Sci.*, 1990, **20**, 219-244.

88. N. D. Lang, *Phys. Rev. B*, 1986, **34**, 5947-5950.

89. H. Hertz, *Ann. Phys. (Berl.)*, 1887, **267**, 983-1000.

90. A. Einstein, *Ann. Phys. (Berl.)*, 1905, **322**, 132-148.

91. D. P. Woodruff and T. A. Delchar, *Modern Techniques of Surface Science*, Cambridge University Press, Cambridge, 2 edn., 1994.

92. H. L. Skriver and N. M. Rosengaard, *Phys. Rev. B*, 1992, **46**, 7157-7168.

93. J. J. Yeh and I. Lindau, *At. Data Nucl. Data Tables*, 1985, **32**, 1-155.

94. J.-J. Yeh, *Atomic calculation of photoionization cross-sections and asymmetry parameters*, Gordon & Breach Science Publishers, 1993.

95. N. M. D. Brown, J. A. Hewitt and B. J. Meenan, *Surf. Interface Anal.*, 1992, **18**, 187-198.

96. J. Zegenhagen, in *Surface Science Techniques*, eds. G. Bracco and B. Holst, Springer Berlin Heidelberg, 2013, vol. 51, ch. 9, pp. 249-275.

97. A. Kazimirov and J. Zegenhagen, *The X-Ray Standing Wave Technique*, World Scientific, 2013.

98. D. P. Woodruff, *Prog. Surf. Sci.*, 1998, **57**, 1-60.

99. J. Zegenhagen, *Surf. Sci. Rep.*, 1993, **18**, 202-271.

100. B. W. Batterman, *Phys. Rev.*, 1964, **133**, A759-A764.

101. B. W. Batterman and H. Cole, *Rev. Mod. Phys.*, 1964, **36**, 681-717.

102. W. H. Bragg and W. L. Bragg, *Proc. R. Soc. London, Ser. A*, 1913, **88**, 428-438.

103. C. G. Darwin, *Philos. Mag.*, 1914, **27**, 315-333.

104. P. P. Ewald, *Ann. Phys. (Leipzig)*, 1916, **354**, 117-143.

105. M. v. Laue, *Ergeb. Exakt. Naturw.*, 1931, **10**, 133.

106. J. C. Slater, *Rev. Mod. Phys.*, 1958, **30**, 197-222.

107. M. B. Trzhaskovskaya, V. I. Nefedov and V. G. Yarzhemsky, *At. Data Nucl. Data Tables*, 2001, **77**, 97-159.

108. B. W. Batterman, *Phys. Rev. Lett.*, 1969, **22**, 703-705.

109. T. Ohta, Y. Kitajima, H. Kuroda, T. Takahashi and S. Kikuta, *Nucl. Instrum. Methods Phys. Res., Sect. A*, 1986, **246**, 760-762.

110. D. P. Woodruff, D. L. Seymour, C. F. McConville, C. E. Riley, M. D. Crapper, N. P. Prince and R. G. Jones, *Phys. Rev. Lett.*, 1987, **58**, 1460-1462.

111. G. van Straaten, M. Franke, F. C. Bocquet, F. S. Tautz and C. Kumpf, *J. Electron. Spectrosc. Relat. Phenom.*, 2018, **222**, 106-116.

112. J. J. Lee, C. J. Fisher, D. P. Woodruff, M. G. Roper, R. G. Jones and B. C. C. Cowie, *Surf. Sci.*, 2001, **494**, 166-182.

113. I. A. Vartanyants and J. Zegenhagen, *Solid State Commun.*, 1999, **113**, 299-320.

114. F. C. Bocquet, G. Mercurio, M. Franke, G. van Straaten, S. Weiß, S. Soubatch, C. Kumpf and F. S. Tautz, *Comput. Phys. Commun.*, 2018.

115. Jeff Greeley, Jens K. Nørskov and M. Mavrikakis, *Annu. Rev. Phys. Chem.*, 2002, **53**, 319-348.

116. J. K. Nørskov, F. Abild-Pedersen, F. Studt and T. Bligaard, *Proc. Natl. Acad. Sci. U.S.A.*, 2011, **108**, 937.

117. M. C. Payne, M. P. Teter, D. C. Allan, T. A. Arias and J. D. Joannopoulos, *Rev. Mod. Phys.*, 1992, **64**, 1045-1097.

118. M. Born and R. Oppenheimer, *Ann. Phys. (Berl.)*, 1927, **389**, 457-484.

119. V. Fock, *Z. Phys.*, 1930, **61**, 126-148.

120. D. R. Hartree, *Math. Proc. Camb. Philos. Soc.*, 1928, **24**, 426-437.

121. C. J. Cramer, *Essentials Of Computational Chemistry: Theories And Models*, John Wiley & Sons, 2 edn., 2005.

122. P. Hohenberg and W. Kohn, *Phys. Rev.*, 1964, **136**, B864-B871.

123. W. Kohn and L. J. Sham, *Phys. Rev.*, 1965, **140**, A1133-A1138.

124. D. C. Langreth and M. J. Mehl, *Phys. Rev. B*, 1983, **28**, 1809-1834.

125. V. Blum, R. Gehrke, F. Hanke, P. Havu, V. Havu, X. Ren, K. Reuter and M. Scheffler, *Comput. Phys. Commun.*, 2009, **180**, 2175-2196.

126. D. Vanderbilt, *Phys. Rev. B*, 1990, **41**, 7892-7895.

127. F. Bloch, *Z. Phys.*, 1929, **52**, 555-600.

128. J. I. Martínez, E. Abad, F. Flores and J. Ortega, *Phys. Status Solidi B*, 2011, **248**, 2044-2049.

129. A. Della Pia, M. Riello, D. Stassen, T. S. Jones, D. Bonifazi, A. De Vita and G. Costantini, *Nanoscale*, 2016, **8**, 19004-19013.

130. N. Marom, A. Tkatchenko, M. Rossi, V. V. Gobre, O. Hod, M. Scheffler and L. Kronik, *J. Chem. Theory Comput.*, 2011, **7**, 3944-3951.

131. H. Schröder, J. Hühnert and T. Schwabe, *J. Chem. Phys.*, 2017, **146**, 044115.

132. J. Tersoff and D. R. Hamann, *Phys. Rev. B*, 1985, **31**, 805-813.

133. H. Lin, J. M. C. Rauba, K. S. Thygesen, K. W. Jacobsen, M. Y. Simmons and W. A. Hofer, *Frontiers of Physics in China*, 2010, **5**, 369-379.

134. K. E. Hermann and M. A. Van Hove, LEEDpat, 2014, http://www.fhi-berlin.mpg.de/KHsoftware/LEEDpat/index.html

135. D. Nečas and P. Klapetek, *Cent. Eur. J. Phys.*, 2012, **10**, 181-188.

136. C. Kittel, *Introduction to Solid State Physics*, John Wiley & Sons, 8 edn., 2004.

137. N. Mannella, S. Marchesini, A. W. Kay, A. Nambu, T. Gresch, S. H. Yang, B. S. Mun, J. M. Bussat, A. Rosenhahn and C. S. Fadley, *J. Electron. Spectrosc. Relat. Phenom.*, 2004, **141**, 45-59.

138. T. J. Reber, N. C. Plumb, J. A. Waugh and D. S. Dessau, *Rev. Sci. Instrum.*, 2014, **85**, 043907.

139. P. Giannozzi, S. Baroni, N. Bonini, M. Calandra, R. Car, C. Cavazzoni, D. Ceresoli, G. L. Chiarotti, M. Cococcioni, I. Dabo, A. Dal Corso, S. de Gironcoli, S. Fabris, G. Fratesi, R. Gebauer, U. Gerstmann, C. Gougoussis, A. Kokalj, M. Lazzeri, L. Martin-Samos, N. Marzari, F. Mauri, R. Mazzarello, S. Paolini, A. Pasquarello, L. Paulatto, C. Sbraccia, S. Scandolo, G. Sclauzero, A. P. Seitsonen, A. Smogunov, P. Umari and R. M. Wentzcovitch, *J. Phys.: Condens. Matter*, 2009, **21**, 395502.

140. J. P. Perdew, K. Burke and M. Ernzerhof, *Phys. Rev. Lett.*, 1996, **77**, 3865-3868.

141. S. Grimme, *J. Comput. Chem.*, 2006, **27**, 1787-1799.

142. V. Barone, M. Casarin, D. Forrer, M. Pavone, M. Sambi and A. Vittadini, *J. Comput. Chem.*, 2008, **30**, 934-939.

143. T. Gould and T. Bučko, *J. Chem. Theory Comput.*, 2016, **12**, 3603-3613.

144. H. J. Monkhorst and J. D. Pack, *Phys. Rev. B*, 1976, **13**, 5188-5192.

145. J. B. Torrance, *Acc. Chem. Res.*, 1979, **12**, 79-86.

146. Z. G. Soos, *Annu. Rev. Phys. Chem.*, 1974, **25**, 121-153.

147. J. Ferraris, D. O. Cowan, V. Walatka and J. H. Perlstein, *J. Am. Chem. Soc.*, 1973, **95**, 948-949.

148. H. Alves, R. M. Pinto and E. S. Maçôas, *Nat. Commun.*, 2013, **4**, 1842.

149. C.-L. Hsu, C.-T. Lin, J.-H. Huang, C.-W. Chu, K.-H. Wei and L.-J. Li, *ACS Nano*, 2012, **6**, 5031-5039.

150. X. Zhou, J. Blochwitz, M. Pfeiffer, A. Nollau, T. Fritz and K. Leo, *Adv. Funct. Mater.*, 2001, **11**, 310-314.

151. J. Blochwitz, M. Pfeiffer, T. Fritz and K. Leo, *Appl. Phys. Lett.*, 1998, **73**, 729-731.

152. E. Menard, V. Podzorov, S. H. Hur, A. Gaur, M. E. Gershenson and J. A. Rogers, *Adv. Mater.*, 2004, **16**, 2097-2101.

153. C.-a. Di, G. Yu, Y. Liu, Y. Guo, W. Wu, D. Wei and D. Zhu, *PCCP*, 2008, **10**, 2302-2307.

154. C.-a. Di, Y. Liu, G. Yu and D. Zhu, *Acc. Chem. Res.*, 2009, **42**, 1573-1583.

155. F. Guillain, J. Endres, L. Bourgeois, A. Kahn, L. Vignau and G. Wantz, *ACS Appl. Mater. Interfaces*, 2016, **8**, 9262-9267.

156. I. F. Torrente, K. J. Franke and J. I. Pascual, *Int. J. Mass spectrom.*, 2008, **277**, 269-273.

157. R. E. Long, R. A. Sparks and K. N. Trueblood, *Acta Crystallogr.*, 1965, **18**, 932-939.

158. S. Barja, M. Garnica, J. J. Hinarejos, A. L. Vazquez de Parga, N. Martin and R. Miranda, *Chem. Commun.*, 2010, **46**, 8198-8200.

159. D. Gerbert and P. Tegeder, *J. Phys. Chem. Lett.*, 2017, **8**, 4685-4690.

160. D. Gerbert, F. Maaß and P. Tegeder, *J. Phys. Chem. C*, 2017, **121**, 15696-15701.

161. B. Milián, R. Pou-Amérigo, R. Viruela and E. Ortí, *J. Mol. Struct. (Theochem.)*, 2004, **709**, 97-102.

162. M. J. Capitán, C. Navío, J. I. Beltrán, R. Otero and J. Álvarez, *J. Phys. Chem. C*, 2016, **120**, 26889-26898.

163. V. Feyer, M. Graus, P. Nigge, G. Zamborlini, R. G. Acres, A. Schöll, F. Reinert and C. M. Schneider, *J. Electron. Spectrosc. Relat. Phenom.*, 2015, **204**, 125-131.

164. S. Barja, D. Stradi, B. Borca, M. Garnica, C. Díaz, J. Rodriguez-García, M. Alcamí, A. Vázquez de Parga, F. Martín and R. Miranda, *J. Phys.: Condens. Matter*, 2013, **25**, 484007.

165. D. Stradi, B. Borca, S. Barja, M. Garnica, C. Diaz, J. M. Rodriguez-Garcia, M. Alcami, A. L. Vazquez de Parga, R. Miranda and F. Martin, *RSC Adv.*, 2016, **6**, 15071-15079.

166. M. M. Kamna, T. M. Graham, J. C. Love and P. S. Weiss, *Surf. Sci.*, 1998, **419**, 12-23.

167. J. R. Fernandez, PhD, Universidad Autónoma de Madrid, 2014.

168. A. Floris, A. Comisso and A. De Vita, *ACS Nano*, 2013, **7**, 8059-8065.

169. L. Romaner, G. Heimel, J.-L. Brédas, A. Gerlach, F. Schreiber, R. L. Johnson, J. Zegenhagen, S. Duhm, N. Koch and E. Zojer, *Phys. Rev. Lett.*, 2007, **99**, 256801.

170. T.-C. Tseng, C. Lin, X. Shi, S. L. Tait, X. Liu, U. Starke, N. Lin, R. Zhang, C. Minot, M. A. Van Hove, J. I. Cerdá and K. Kern, *Phys. Rev. B*, 2009, **80**, 155458.

171. X. Q. Shi, C. Lin, C. Minot, T.-C. Tseng, S. L. Tait, N. Lin, R. Q. Zhang, K. Kern, J. I. Cerdá and M. A. Van Hove, *J. Phys. Chem. C*, 2010, **114**, 17197-17204.

172. T. R. Umbach, I. Fernández-Torrente, M. Ruby, F. Schulz, C. Lotze, R. Rurali, M. Persson, J. I. Pascual and K. J. Franke, *New J. Phys.*, 2013, **15**, 083048.

173. R. Heckingbottom, *Surf. Sci.*, 1969, **17**, 394-401.

174. C. Park, G. A. Rojas, S. Jeon, S. J. Kelly, S. C. Smith, B. G. Sumpter, M. Yoon and P. Maksymovych, *Phys. Rev. B*, 2014, **90**, 7.

175. R. Precht, R. Hausbrand and W. Jaegermann, *PCCP*, 2015, **17**, 6588-6596.

176. R. Precht, S. Stolz, E. Mankel, T. Mayer, W. Jaegermann and R. Hausbrand, *PCCP*, 2016, **18**, 3056-3064.

177. D. A. Shirley, *Phys. Rev. B*, 1972, **5**, 4709-4714.

178. E. A. Soares, V. B. Nascimento, V. E. de Carvalho, C. M. C. de Castilho, A. V. de Carvalho, R. Toomes and D. P. Woodruff, *Surf. Sci.*, 1999, **419**, 89-96.

179. K. P. Bohnen and D. M. Kolb, *Surf. Sci.*, 1998, **407**, L629-L632.

180. T. Katayama, K. Mukai, S. Yoshimoto and J. Yoshinobu, *J. Phys. Chem. Lett.*, 2010, **1**, 2917-2921.

181. K. Momma and F. Izumi, *J. Appl. Crystallogr.*, 2011, **44**, 1272-1276.

182. N. H. de Leeuw and C. J. Nelson, *J. Phys. Chem. B*, 2003, **107**, 3528-3534.

183. T. Classen, G. Fratesi, G. Costantini, S. Fabris, L. Stadler Frank, C. Kim, S. de Gironcoli, S. Baroni and K. Kern, *Angew. Chem. Int. Ed.*, 2005, **44**, 6142-6145.

184. Z. Feng, S. Velari, A. Cossaro, C. Castellarin-Cudia, A. Verdini, E. Vesselli, C. Dri, M. Peressi, A. De Vita and G. Comelli, *ACS Nano*, 2015, **9**, 8697-8709.

185. I. Horcas, R. Fernández, J. M. Gómez-Rodríguez, J. Colchero, J. Gómez-Herrero and A. M. Baro, *Rev. Sci. Instrum.*, 2007, **78**, 013705.

186. M. Konno, T. Ishii and Y. Saito, *Acta Crystallogr. Sect. B: Struct. Sci.*, 1977, **33**, 763-770.

187. R. Shannon, *Acta Crystallogr. Sect. A: Found. Crystallogr.*, 1976, **32**, 751-767.

188. W. E. Morgan, J. R. Van Wazer and W. J. Stec, *J. Am. Chem. Soc.*, 1973, **95**, 751-755.

189. J. F. Moulder, W. F. Stickle, P. E. Sobol and K. D. Bomben, *Handbook of X-ray Photoelectron Spectroscopy: A Reference Book of Standard Spectra for Identification and Interpretation of XPS Data*, Physical Electronics, 1995.

190. G. S. Leatherman, R. D. Diehl, P. Kaukasoina and M. Lindroos, *Phys. Rev. B*, 1996, **53**, 10254-10260.

191. J. Murgich, *J. Chem. Phys.*, 1979, **70**, 1198-1200.

192. S. J. Yang and C. W. Bates, *Appl. Phys. Lett.*, 1980, **36**, 675-677.

193. M. Caragiu, G. S. Leatherman, R. D. Diehl, P. Kaukasoina and M. Lindroos, *Surf. Sci.*, 1999, **441**, 84-90.

194. C. J. J. Fritchie and P. J. Arthur, *Acta Crystallogr.*, 1966, **21**, 139-145.

195. S. C. B. Mannsfeld and T. Fritz, *Phys. Rev. B*, 2004, **69**, 075416.

196. S. C. B. Mannsfeld and T. Fritz, *Phys. Rev. B*, 2005, **71**, 235405.

197. I. Kröger, B. Stadtmüller, C. Stadler, J. Ziroff, M. Kochler, A. Stahl, F. Pollinger, T.-L. Lee, J. Zegenhagen, F. Reinert and C. Kumpf, *New J. Phys.*, 2010, **12**, 083038.

198. H. B. Nielsen, U. Burghaus, G. Broström and E. Matthias, *Vacuum*, 1990, **41**, 558-560.

199. A. W. Dweydari and C. H. B. Mee, *Phys. Status Solidi A*, 2006, **27**, 223-230.

200. G. N. Derry, M. E. Kern and E. H. Worth, *Journal of Vacuum Science & Technology A*, 2015, **33**, 060801.

201. H. Li, J. Quinn, Y. S. Li, D. Tian, F. Jona and P. M. Marcus, *Phys. Rev. B*, 1991, **43**, 7305-7307.

202. M. S. Kariapper, C. J. Fisher, D. P. Woodruff, A. S. Y. Chan and R. G. Jones, *Surf. Sci.*, 2008, **602**, 650-659.

203. M. El Garah, Y. Makoudi, F. Palmino, E. Duverger, P. Sonnet, L. Chaput, A. Gourdon and F. Cherioux, *ChemPhysChem*, 2009, **10**, 3190-3193.

204. M. N. Faraggi, C. Rogero, A. Arnau, M. Trelka, D. Écija, C. Isvoranu, J. Schnadt, C. Marti-Gastaldo, E. Coronado, J. M. Gallego, R. Otero and R. Miranda, *J. Phys. Chem. C*, 2011, **115**, 21177-21182.

205. M. Casarin, M. D. Marino, D. Forrer, M. Sambi, F. Sedona, E. Tondello, A. Vittadini, V. Barone and M. Pavone, *J. Phys. Chem. C*, 2010, **114**, 2144-2153.

206. J. B. Pendry, K. Heinz and W. Oed, *Phys. Rev. Lett.*, 1988, **61**, 2953-2956.

207. W. Hujo and S. Grimme, *PCCP*, 2011, **13**, 13942-13950.

208. T. Gould, S. Lebègue, J. G. Ángyán and T. Bučko, *J. Chem. Theory Comput.*, 2016, **12**, 5920-5930.

209. G. Heimel, S. Duhm, I. Salzmann, A. Gerlach, A. Strozecka, J. Niederhausen, C. Burker, T. Hosokai, I. Fernandez-Torrente, G. Schulze, S. Winkler, A. Wilke, R. Schlesinger, J. Frisch, B. Broker, A. Vollmer, B. Detlefs, J. Pflaum, S. Kera, K. J. Franke, N. Ueno, J. I. Pascual, F. Schreiber and N. Koch, *Nat. Chem.*, 2013, **5**, 187-194.

210. S. K. M. Henze, O. Bauer, T. L. Lee, M. Sokolowski and F. S. Tautz, *Surf. Sci.*, 2007, **601**, 1566-1573.

211. A. Gerlach, T. Hosokai, S. Duhm, S. Kera, O. T. Hofmann, E. Zojer, J. Zegenhagen and F. Schreiber, *Phys. Rev. Lett.*, 2011, **106**, 156102.

212. J. D. Baran, J. A. Larsson, R. A. J. Woolley, Y. Cong, P. J. Moriarty, A. A. Cafolla, K. Schulte and V. R. Dhanak, *Phys. Rev. B*, 2010, **81**, 075413.

213. C. Bürker, A. Franco-Cañellas, K. Broch, T. L. Lee, A. Gerlach and F. Schreiber, *J. Phys. Chem. C*, 2014, **118**, 13659-13666.

214. J. Chen, H. Zhang, X. Liu, C. Yuan, M. Jia, Z. Luo and J. Yao, *PCCP*, 2016, **18**, 7190-7196.

215. G.-C. Wang, L. Jiang, X.-Y. Pang and J. Nakamura, *J. Phys. Chem. B*, 2005, **109**, 17943-17950.

216. G. Mercurio, R. J. Maurer, W. Liu, S. Hagen, F. Leyssner, P. Tegeder, J. Meyer, A. Tkatchenko, S. Soubatch, K. Reuter and F. S. Tautz, *Phys. Rev. B*, 2013, **88**, 035421.

217. T. D. Kühne, *Wiley Interdiscip. Rev. Comput. Mol. Sci.*, 2014, **4**, 391-406.

218. R. J. Maurer, W. Liu, I. Poltavsky, T. Stecher, H. Oberhofer, K. Reuter and A. Tkatchenko, *Phys. Rev. Lett.*, 2016, **116**, 146101.

219. M. Scheffler and C. Stampfl, *Theory of Adsorption on Metal Substrates*, Elsevier, Amsterdam, 2000.